

ABSTRACT

OZCAM, ALI EVREN. Modification and Characterization of Polymeric Surfaces for Targeted Functionality. (Under the direction of Jan Genzer and Richard J. Spontak.)

We have investigated the surface modification of polymeric materials as a viable means by which to create novel functional surfaces for use in a wide range of (nano)technologies, including the development of nanocomposites.

Improvement of the barrier properties of rPET is the overarching theme of this project. It is known that inorganic fillers introduced into a polymer matrix tend to decrease gas permeation by increasing the diffusive path length of penetrant species through the material. Nanoclays as filler materials are ideal for this purpose because of the high aspect ratio of the clay platelets. Therefore, we have sought to generate rPET/clay nanocomposites by two different protocols in this study: attachment of natural clay platelets on functionalized rPET surface, and mechanical alloying of rPET flakes with natural clay platelets.

We have shown that PET surfaces can be chemically modified while avoiding chemical degradation. Specifically, we find that brief exposure of PET substrates to ultraviolet/ozone (UVO) generates a large surface concentration of hydrophilic moieties.

Chemical surface modification routes have also been explored due to the irregular and 3D nature of rough rPET flakes. Polyethyleneimine (PEI), as “molecular glue”, increases the adsorption of clay platelets on modified rPET surface. Subsequent characterization reveals that the presence of PEI molecules permits adsorption of 1-2 clay platelets/layer on the modified rPET surface. Extrusion of these surface-modified materials yields polymer/clay nanocomposites, but the high melting point of PET causes considerable degradation under non-optimized conditions. Hence, we have substituted rPET with a low melting

poly(ethylene-*co*-octene) to perform PEI and clay adsorption multiple times and thus adjust the concentration of clay platelets in the polymer matrix. The presence of clay platelets results in a decrease in O₂ and CO₂ permeabilities, which compares favorably with calculations from the Nielsen model. In addition, the thermal stability of the nanocomposites increases with increasing clay loading due to the presence of the inorganic platelets.

Electrospun PET fiber surfaces have also been chemically functionalized with polymer brushes composed of poly(*N*-isopropyl acrylamide) (PNIPAAm), poly(dimethylaminoethyl methacrylate) (PDMAEMA) and poly(hydroxyethyl methacrylate) (PHEMA) via surface-initiated polymerization. These fibers can be used as functional filters to 1) capture metal salts or cyanide ions from water, 2) prepare antibacterial or antifouling fibers, and 3) produce fibers responsive to temperature or pH.

We have also investigated the formation of rPET/clay nanocomposites via mechanical alloying by using high-energy ball milling as an alternative route to melt processing. Solid-state mechanical alloying was conducted using natural clay and rPET at ambient temperature. Specifically, polymer and clay powders were mixed in a steel vial in the presence of steel balls designed to induce considerable and repeated shear, fracture and welding and thus exfoliate the clay platelets in the rPET matrix. The molecular weight of mechanically milled rPET and virgin-PET is found to decrease with increasing milling time, reaching ≈45% of their original values after 16 h of milling. Characterization of the resulting nanocomposites by x-ray diffractometry and transmission electron microscopy confirm exfoliation of clay platelets irregardless of milling time.

The development of a universal polymer coating has been achieved by chemically coupling trichlorosilane (TCS) to the vinyl groups of poly(vinylmethyl siloxane) (PVMS) via

hydrosilylation. The resultant PVMS-TCS coating can be deposited as a functional organic layer on a variety of substrates ranging from hydrophobic to hydrophilic. Spin-coating PVMS-TCS onto a substrate yields a uniform coating layer and exposing the coating to minute amounts of moisture generates a large density of surface-bound hydroxyl groups. Moreover, treating the PVMS-TCS substrates with UVO further increases the density of hydroxyl groups on the surface. The elastic modulus of the coating can be regulated by adjusting the TCS concentration. Several case studies demonstrating the remarkable properties of these PVMS-TCS functional coatings are presented.

Decreasing supplies of fresh water and increasing population necessitate the development of water cleaning technologies that would expedite the removal of pollutants. To assist water purification processes, we have synthesized functionalized macromolecules that contribute to decontamination by scavenging detrimental chemicals. Epitomizing this role, the thioimide unit enables chemical flexibility that facilitates reversible catch-release of the ions on the basis of subtle reduction-oxidation environmental changes. Chemical tunability of the thioimide moiety enables synthesis of thioimide-based monomers and post-polymerization modification agents. Two distinct synthetic pathways, polymerization and post-polymerization modification, have been explored, leading to functional thioimide-based macromolecules. The presence of thioimide units on macromolecular chains decreases the concentration of cyanide ions in water from 24 to 3 ppm in less than 1 h.

Surface Modification and Characterization of Polymeric Materials
for Targeted Functionality

by
Ali Evren Özçam

A dissertation submitted to the Graduate Faculty of
North Carolina State University
in partial fulfillment of the
requirements for the degree of
Doctor of Philosophy

Chemical Engineering

Raleigh, North Carolina

2011

APPROVED BY:

Richard J. Spontak
Chair of Advisory Committee

Jan Genzer
Co-chair of Advisory Committee

Saad A. Khan

Orlin D. Velev

Russell E. Gorga

DEDICATION

To Mom and Sisters...

BIOGRAPHY

Ali Evren Özçam was born on September 30th, 1982 in Izmir, Turkey. He attended Buca Anadolu Lisesi for high school and upon graduation he started his undergraduate studies at Department of Chemical Engineering at Middle East Technical University.

He graduated from Department of Chemical Engineering as the 1st ranking student among 102 graduates in 2005. He joined the Department of Chemical and Biomolecular Engineering at North Carolina State University in August 2005 to pursue a philosophy of doctorate degree in polymer science.

He worked as a PhD intern at Global Chemical Technology Division for Procter and Gamble Company in 2007 summer. Evren spent his 2008 and 2010 summers as a guest researcher in the research group of Jiri Srogl at the Institute of Organic Chemistry and Biochemistry of the Czech Academy of Sciences, Prague Czech Republic. He worked on synthesis, polymerization, post-polymerization modification and characterization of functional thio-imide molecules for water purification technologies.

He will be working as a post-doctoral researcher in the research group of Nitash P. Balsara at University of California Berkeley upon completion of his PhD.

ACKNOWLEDGMENTS

First and most importantly, I need to thank my advisors, Professors Jan Genzer and Richard Spontak, for their guidance, support, motivation, and teaching. I am grateful to the President and CEO of United Resource Recovery Corporation, Mr. Carlos Gutierrez, for the financial support provided throughout the course of my Ph.D. I likewise thank my committee members — Professors Saad Khan, Orlin Velez and Russell Gorga — for their guidance and comments. I particularly thank Professors Saad Khan, Wesley Henderson and Michael Dickey for letting me use analytical instruments in their laboratories. I would also like to thank Dr. Kirill Efimenko for being a friend and collaborator, as well as Dr. Jiri Srogl and Adam Henke from whom I learned valuable synthetic chemistry skills. Lastly, I need to recognize (with much appreciation) Drs. Salomon Turgman and Omer Gozen for being great friends, colleagues and partners!!

It was a genuine pleasure to work, discuss and share scientific experiences with my group members and other Ph.D. students in the Department of Chemical & Biomolecular Engineering: Dr. Arjun Krishnan, Kristen Roskov, Anand Patel, Casey Galvin, Erich Bain, Pruthesh Vargantwar, Professor Julie Willoughby, Dr. Carl Saquing, Chris Aberg, Dr. Hyun-Kwan Yang, Dr. Young Kuk Jhon, Dr. Shafi Arifuzzaman, Kiran Goli, Dr. Dave Frankowski, Dr. Josh Manasco, Dr. Xiao-Yu Sun, Dr. Michelle Bowman, Dr. Sachin Talwar, Dr. Joan Patterson, Dr. Vinayak Rastogi, Chris Bonino, Sara Arvidson and Christina Tang.

Finally, I would like to thank my great friends for the fun and joy they provided during my Ph.D. These include, but are not limited to, Mehmet, Ozan, Melda, Murat, Hulusi,

Erdogan, Bora, Alp, Egemen, Ergin, Rico, Emir, Erdem, Can Sezer, Baha, Alex, Rachel, and many others!!! None of this would have been possible without the ongoing support and confidence provided by my family, to whom I am eternally grateful. Thank you all!

TABLE OF CONTENTS

LIST OF TABLES	xii
LIST OF FIGURES	xiii
CHAPTER 1: INTRODUCTION AND MOTIVATION.....	1
1.1. BACKGROUND	1
1.2.SURFACE MODIFICATION OF RECYCLED POLY(ETHYLENE TEREPHTHALATE) (rPET) FLAKES	2
1.3. SURFACE MODIFICATION OF SILICONE ELASTOMER NETWORKS	10
1.4.SYNTHESIS OF FUNCTIONAL COPOLYMERS AND POST-POLYMERIZATION MODIFICATION REACTIONS FOR WATER PURIFICATION.....	14
1.5. REFERENCES.....	16
1.6. FIGURES.....	19
CHAPTER 2: MODIFICATION OF POLY(ETHYLENE TEREPHTHALATE) (PET) SURFACES WITH SELF-ASSEMBLED MONOLAYERS OF ORGANOSILANE PRECURSORS	24
2.1. INTRODUCTION.....	24
2.2. EXPERIMENTAL.....	27
2.2.1. FILM PREPARATION	27
2.2.2. ULTRAVIOLET/OZONE (UVO) TREATMENT.....	28
2.2.3. SEMIFLUORINATED SELF-ASSEMBLED MONOLAYER FORMATION	28
2.2.4. WATER CONTACT ANGLE MEASUREMENTS	29
2.2.5. ATOMIC FORCE MICROSCOPY	29
2.2.6. ELLIPSOMETRY.....	30
2.2.7. X-RAY PHOTOELECTRON SPECTROSCOPY	30
2.2.8. NEXAFS SPECTROSCOPY.....	31
2.3. RESULTS AND DISCUSSION	32
2.4. CONCLUSIONS	42
2.5. REFERENCES.....	44
2.6. FIGURES.....	47
CHAPTER 3: MODIFICATION OF RECYCLED POLY(ETHYLENE TEREPHTHALATE) (RPET) FLAKES WITH POLYELECTROLYTES.....	58

3.1. INTRODUCTION.....	58
3.2. EXPERIMENTAL.....	64
3.2.1. MATERIALS.....	64
3.2.2. THIN PET FILM PREPARATION.....	65
3.2.3. POLYELECTROLYTE AND CLAY ADSORPTION ON PET SURFACE	65
3.2.4. POLYELECTROLYTE AND CLAY ADSORPTION ON PDMS NETWORK AND POLY(ETHYLENE-OCTENE) SURFACE	66
3.2.5. ELLIPSOMETRY.....	67
3.2.6. WATER CONTACT-ANGLE MEASUREMENTS	68
3.2.7. X-RAY PHOTOELECTRON SPECTROSCOPY	68
3.2.8. MELT PROCESSING OF RPET FLAKES	68
3.2.9. MELT RHEOLOGY.....	69
3.2.10. FOURIER TRANSFORM INFRARED SPECTROSCOPY	69
3.2.11. ATOMIC FORCE MICROSCOPY	70
3.2.12. GAS PERMEATION.....	70
3.2.12. THERMOGRAVIMETRIC ANALYSIS	71
3.3. RESULTS AND DISCUSSION	72
3.4. CONCLUSIONS	79
3.5. REFERENCES.....	81
3.6. TABLES AND FIGURES	84
CHAPTER 4: RESPONSIVE PET NANO/MICROFIBERS VIA SURFACE- INITIATED POLYMERIZATION	103
4.1. INTRODUCTION.....	103
4.2. EXPERIMENTAL.....	106
4.3. RESULTS AND DISCUSSION	108
4.4. CONCLUSIONS	113
4.5. REFERENCES.....	115
4.6. FIGURES.....	118
CHAPTER 5: GENERATION OF FUNCTIONAL NANO/MICRO FIBERS THROUGH SURFACE-INITIATED POLYMERIZATION	123
5.1. INTRODUCTION.....	123
5.2. EXPERIMENTAL.....	128
5.2.1. MATERIALS.....	128
5.2.2. INSTRUMENTATION	129
5.2.3. PET SURFACE MODIFICATION AND POLYMER BRUSH GROWTH	130

5.2.4. TESTING ANTIBACTERIAL BEHAVIOR OF PET FIBERS WITH GRAFTED PDMAEMA BRUSHES	132
5.2.5. TESTING PROTEIN RESISTANCE OF PET FIBERS WITH GRAFTED PHEMA BRUSHES.....	132
5.3. RESULTS AND DISCUSSION	133
5.4. CONCLUSIONS AND FUTURE WORK.....	142
5.5. REFERENCES.....	144
5.6 TABLES AND FIGURES	149
CHAPTER 6: MECHANICAL ALLOYING OF POLY(ETHYLENE TEREPHTHALATE) (PET) WITH LAYERED SILICATES	160
6.1. INTRODUCTION.....	160
6.2. EXPERIMENTAL.....	164
6.2.1. MATERIALS.....	164
6.2.2. BALL MILLING	165
6.2.3. SOLUTION VISCOSITY.....	165
6.2.4. DIFFERENTIAL SCANNING CALORIMETRY.....	166
6.2.5. THERMOGRAVIMETRIC ANALYSIS	166
6.2.6. X-RAY DIFFRACTION	166
6.2.7. ELECTRON MICROSCOPY.....	167
6.3. RESULTS AND DISCUSSION	167
6.4. CONCLUSION AND FUTURE WORK	171
6.5. REFERENCES.....	174
6.6. FIGURES.....	177
CHAPTER 7: UNIVERSAL COATINGS BASED ON FUNCTIONAL SILICONES 184	
7.1. INTRODUCTION.....	184
7.2. EXPERIMENTAL.....	192
7.2.1. MATERIALS.....	192
7.2.2. FILM PREPARATION	193
7.2.3. PVMS-TCS COUPLING REACTIONS AND MODIFICATIONS	194
7.2.4. PVMS-TCS THIN FILM FORMATION	196
7.2.5. WATER CONTACT ANGLE MEASUREMENTS	196
7.2.6. X-RAY PHOTOELECTRON SPECTROSCOPY	197
7.2.7. FOURIER TRANSFORM INFRARED SPECTROSCOPY.....	197
7.2.8. ULTRAVIOLET/OZONE TREATMENT.....	198
7.2.9. FORMATION OF SEMIFLUORINATED SELF-ASSEMBLED MONOLAYERS	198

7.2.10. SCANNING ELECTRON MICROSCOPY	199
7.2.11. SPECTROSCOPIC ELLIPSOMETRY	199
7.2.12. NEAR-EDGE X-RAY ABSORPTION FINE STRUCTURE.....	200
7.2.13. NANOINDENTATION.....	201
7.3. RESULTS AND DISCUSSION	202
7.3.1. PVMS-TCS COATING ON PDMS NETWORK SUBSTRATES	204
7.3.2. PVMS-TCS COATING ON PET SUBSTRATES	210
7.3.3. SURFACE INITIATED POLYMERIZATION ON PET, PP AND SiO _x SURFACES	219
7.4. CONCLUSION AND FUTURE WORK	220
7.5. REFERENCES.....	227
7.6. FIGURES.....	229
7.7. APPENDIX.....	257
7.7.1. SYNTHESIS OF PVMS	257
7.7.2. PREPARATION OF SILOXANE NETWORKS.....	258
CHAPTER 8: COPOLYMERIZATION STUDIES OF FUNCTIONAL THIOIMIDE MOLECULES	260
8.1. INTRODUCTION.....	260
8.2. EXPERIMENTAL.....	263
8.2.1. MATERIALS.....	263
8.2.2. INSTRUMENTATION	266
8.2.3. CONTROL EXPERIMENTS WITH MODEL CONTROL-SN COMPOUND	267
8.2.4. POLYMERIZATION REACTIONS.....	268
8.2.4.1. COPOLYMERIZATION OF SN2P AND PHENYLACRYLAMIDE	268
8.2.4.2. SURFACE INITIATED COPOLYMERIZATION OF SN2P AND PHENYLACRYLAMIDE	269
8.2.4.3. COPOLYMERIZATION OF NIPAAM WITH SN2U, SN2P, SN3U AND SN3P	270
8.2.5. DEPROTECTION OF PNIPAAM-CO-SN3P COPOLYMERS FROM T-BUTYL GROUPS.....	270
8.3. RESULTS AND DISCUSSION	271
8.3.1. CONTROL EXPERIMENTS WITH MODEL CONTROL-SN COMPOUND	271
8.3.2. COPOLYMERIZATION OF SN2P AND PHENYLACRYLAMIDE IN BULK .	273
8.3.2.1. HOMOPOLYMERIZATIONS OF SN2P AND PHAAM	274
8.3.2.2. COPOLYMERIZATIONS OF SN2P MONOMER WITH PHAAM	275
8.3.3. SURFACE INITIATED COPOLYMERIZATION OF SN2P AND PHENYLACRYLAMIDE	278

8.3.3.1. GROWING PPHAAM AND POLY(PHAAM-CO-SN2P) BRUSHES FROM SILICON WAFERS	278
8.3.4. COPOLYMERIZATION OF NIPAAM WITH SN2U, SN2P, SN3U AND SN3P	281
8.3.4.1. HOMOPOLYMERIZATION OF NIPAAM, SN3U AND SN3P MONOMERS.	281
8.3.4.2. COPOLYMERIZATION OF NIPAAM WITH SN2U, SN2P, SN3U AND SN3P MONOMERS.....	283
8.3.5. DEPROTECTION OF PNIPAAM-CO-SN3P COPOLYMERS FROM T-BUTYL GROUPS.....	285
8.4. CONCLUSION AND FUTURE WORK	286
8.5. REFERENCES.....	291
8.6. TABLES AND FIGURES	292
8.7. APPENDIX.....	329
CHAPTER 9: POST-POLYMERIZATION MODIFICATION STUDIES WITH FUNCTIONAL THIOIMIDE MOLECULES	331
9.1. INTRODUCTION.....	331
9.2. EXPERIMENTAL	334
9.2.1. MATERIALS.....	334
9.2.2. INSTRUMENTATION	336
9.2.3. POLYMERIZATION AND POST-MODIFICATION REACTIONS.....	338
9.2.3.1. POLYMERIZATION OF PDMAEMA.....	338
9.2.3.2. POLYMERIZATION OF PDMAEMA BRUSHES.....	338
9.2.3.3. POLYMERIZATION OF PROPARGYL METHACRYLATE.....	339
9.2.3.4. POST-MODIFICATION OF PDMAEMA WITH SN BASED QUARTERNIZATION AGENTS	340
9.2.3.5. POST-MODIFICATION OF PDMAEMA BRUSHES WITH SN BASED QUARTERNIZATION AGENTS	341
9.2.3.6. POST-MODIFICATION OF PPMA WITH ORGANIC AZIDES.....	341
9.2.3.7. CAPTURING OF CYANIDE IONS WITH qPDMAEMA-SN.....	342
9.3. RESULTS AND DISCUSSIONS.....	342
9.3.1. POST-MODIFICATION OF PDMAEMA BRUSHES ON SILICON WAFER AND PET FIBERS WITH QSN1U VIA QUARTERNIZATION	342
9.3.2. POST-MODIFICATION OF PDMAEMA IN BULK WITH qSN3U VIA QUARTERNIZATION.....	348
9.3.3. POST-MODIFICATION OF PPMA WITH AZIDE-SN3U VIA CLICK REACTION	350
9.3.4. CAPTURING OF CYANIDE IONS WITH qPDMAEMA-SN.....	351
9.4. CONCLUSION AND FUTURE WORK	352

9.5. REFERENCES.....	356
9.6. TABLES AND FIGURES	358
9.7 APPENDIX.....	378
9.7.1. SYNTHESIS OF N-BENZYL-2-CHLORO-5-NITROBENZAMIDE	378
9.7.2. SYNTHESIS OF N-BENZYL-2-TERT-BUTYLSULFANYL-BENZAMIDE.....	378
9.7.3. SYNTHESIS OF 5-AMINE-N-BENZYL-2-TERT-BUTYLSULFANYL-5-NITROBENZAMIDE.....	379
9.7.4. SYNTHESIS OF N-BENZYL-2-TERT-BUTYLSULFANYL-5-(2-CHLORO-ACETYLAMINO)-BENZAMIDE.....	379
9.7.5. SYNTHESIS OF N-(2-BENZYL-3-OXO-2,3-DIHYDRO-BENZO[d]ISOTHIAZOL-5-YL)-2-CHLORO-ACETAMIDE	379
CHAPTER 10: SUMMARY AND OUTLOOK.....	381
10.1. SUMMARY	381
10.2. OUTLOOK.....	386

LIST OF TABLES

Table 3.1. Classifications of layered silicate crystals	84
Table 5.1. Atomic concentration of PET fiber surface with grafted PDMAEMA and PHEMA brushes	149
Table 5.2. Atomic concentration of PET fiber surface with grafted PDMAEMA brushes after quarternization post-polymerization modification reactions	150
Table 5.3. Atomic concentration of PET fiber surface with grafted PHEMA brushes after fluorination post-polymerization modification reactions.....	151
Table 8.1. Composition of the polymerizations performed	292
Table 8.2. Molecular weight and its distribution of the synthesized polymers	293
Table 8.3. N:C and N:S ratios of the copolymers determined with XPS.....	294
Table 8.4. Measured thickness and refractive index of polymer brushes	295
Table 8.5. Calculated refractive indexes of monomers.....	296
Table 8.6. Atomic percentages of PPhAAM and 9.1% SN2P polymer brush measured with XPS	297
Table 9.1. Thickness and optical constants of PDMAEMA brushes before and after attaching qSN1P.....	358
Table 9.2. Atomic concentrations of qSN1U modified PDMAEMA brushes on silicon wafer and theoretical atomic percentages	359
Table 9.3. Calculated refractive indices and molecular weights of qSN1U, fluorinated thiol and THF	360
Table 9.4. Atomic percentages of samples after exposed to fluorinated thiol in ethanol ...	361

LIST OF FIGURES

Figure 1.1. Production rate of plastics and distribution of polymer usage areas.	19
Figure 1.2. CO ₂ retention times of the bottles produced from rPET and vPET.	20
Figure 1.3. The silicone backbone with the bond angles (θ) and the bond length (L) identified. If both R groups are methyl, the polymer is referred to as poly(dimethylsiloxane) (PDMS).....	21
Figure 1.4. Cross-linking of silicone chains to form a silicone elastomer network (SEN). 22	
Figure 1.5. Generalized structure of a thioimide compound.	23
Figure 2.1. Thickness of PET at various stages of surface treatment. The original thickness decreases with increasing UVO treatment time (a) and decreases further after subsequent sonication (b). The total amount of PET removed from the sample is shown in (c).	47
Figure 2.2. Static water contact angle (top), oxygen content (middle), and carbon content (bottom) as functions of UVO treatment time immediately after UVO treatment (black squares) and after UVO followed by sonication (red triangles). The contact angle was measured by the contact angle goniometer and the elemental compositions were determined by XPS.	48
Figure 2.3. High resolution XPS spectra of PET samples in the oxygen (before break) and carbon (after break) treated with UVO for various times.	49
Figure 2.4. Atomic percentages of various chemical functionalities present in the PET-UVO specimens, determined by XPS, as a function of the UVO treatment time before (black squares) and after (red triangles) sonication. The lines are meant to guide the eye.	50
Figure 2.5. AFM images of PET surfaces treated with UVO for various times (in min): a) 0, b) 2, c) 8, and d) 30. The left and right panels in parts (b)-(d) correspond to the image taken from samples before and after sonication, respectively. The height scale r ranges from 0 (dark brown) to 30 nm (white).	51
Figure 2.6. Water contact angles of PET-UVO/tF8H2 (squares) and SiO _x /tF8H2 (triangles) samples as function of UVO treatment time.	52
Figure 2.7. Fluorine K-edge PEY NEXAFS spectra collected from PET modified with UVO for various times ranging from 1 to 30 min and covered with tF8H2 SAM.	53
Figure 2.8. Carbon K-edge PEY NEXAFS spectra collected from PET modified with UVO for various times ranging from 1 to 30 min and covered with tF8H2 SAM. The PEY NEXAFS spectra for samples treated for UVO times longer than 1 min have been shifted vertically by 0.3 (with respect to the preceding spectrum) on a relative intensity scale. The dotted lines below each spectrum denote the PEY NEXAFS intensity corresponding to the pre-edge intensity signal for that spectrum.	54
Figure 2.9. a) PEY NEXAFS spectrum from PET-UVO (black dashed line) and PET-UVO covered with tF8H2 SAM (red solid line). In both cases the UVO time was 6 min. b)	

Difference PEY NEXAFS intensity obtained by subtracting the PET-UVO spectrum (dashed line in part a) from the PET-UVO/tF8H2 spectrum (solid line in part a).	55
Figure 2.10. Edge-jump in PEY NEXAFS intensity from difference spectra (cf. Figure 9) determined at 320 eV as a function of UVO treatment time (blue triangles). Scaling coefficient (K) values as defined in the text as a function of UVO treatment time (red squares).	56
Figure 2.11. Normalized PEY NEXAFS spectra collected from PET-UVO/tF8H2 specimens at the carbon K-edge in two different sample orientations θ (defined as the angle between the surface normal and the electric vector of the incident x-ray beam): 20° (black) and 90° (red). The PET was treated with UVO for various times ranging from 2 (top) to 8 (bottom) min.....	57
Figure 3.1. The effect aspect ratio (a, b and c) and orientation (d) on the tortuosity factor. ..	85
Figure 3.2. Chemical structure of 2:1 layered silicates. ^[10]	86
Figure 3.3. Different morphologies of polymer/clay composites. ^[10]	87
Figure 3.4. Degradation behavior of various clays in air atmosphere (C30B, C15A and C10A are the organically modified clays of Southern Clay Products. C30B is natural montmorillonite modified with methyl, tallow, bis-2-hydroxyethyl quaternary ammonium, C15A is natural montmorillonite modified with dimethyl, dehydrogenated tallow quaternary ammonium, C10A is natural montmorillonite modified with dimethyl, benzyl, hydrogenated tallow quaternary ammonium). The dashed line represent the range of melt processing temperature of PET.....	88
Figure 3.5. The proposed starting point for rPET/clay nanocomposite formation.	89
Figure 3.6. Surface topography of PET soft drink bottle (a) and rPET flake (b). The scale bar is 2 μm for both images.	90
Figure 3.7. Schematic representation of polyelectrolyte adsorption on PET flake surface with subsequent clay platelet adsorption.	91
Figure 3.8. Water contact angle of PET surface after polyelectrolyte (a) and subsequent clay (b) adsorption as a function of polyelectrolyte deposition time for PAH (■), PEI25 (●) and PEI60 (▲). Green and pink lines represent the water contact angle values of bare PET thin film and PET thin film exposed to clay suspension in DI water, respectively.	92
Figure 3.9. Thickness of the polyelectrolyte (a) and clay (b) layers after polyelectrolyte and subsequent clay adsorption as a function of polyelectrolyte deposition time for PAH (■), PEI25 (●) and PEI60 (▲).....	93
Figure 3.10. Surface composition of rPET (a) and PEI treated rPET surface (b).....	94
Figure 3.11. Surface composition of rPET surface exposed to clay suspension (a) and PEI60 treated rPET surface exposed to clay suspension (b).....	95
Figure 3.12. FT-IR spectra collected on a rPET flake and the inset shows the ratio of FT-IR peak areas located at 1200 and 750 cm^{-1} before (red columns) and after extrusion (green columns) for rPET, rPET/PEI60 and rPET/PEI60/MMT flakes.	96
Figure 3. 13. Carbon dioxide (■) and oxygen (●) permeability through PDMS network as a function of PEI60/clay layers.....	97

Figure 3. 14. Percentage of remaining inorganic residue after pyrolysis modified LLDPE as a function of processing cycles for PEI60/clay (■) and PEI60 (●).	98
Figure 3. 15. Oxygen (left) and carbon dioxide (right) permeabilities through LLDPE as a function of processing cycles for PEI60/clay (■) and PEI60 (●).	99
Figure 3. 16. The comparison of experimentally obtained permeabilities (■) of oxygen and carbon dioxide with calculated with Nielsen model based on the inorganic residue concentration determined from TGA for the clay aspect ratios of 50 (□), 100 (○) and 200 (Δ).	100
Figure 3. 17. FT-IR spectra of virgin LLDPE (black line), PEI60 (red line) and PEI60/clay (blue line) treated and melt processed LLDPE films.	101
Figure 3. 18. Onset degradation temperature measured by TGA experiments for LLDPE membrane treated with PEI60/clay (■) and PEI60 (●).	102
Figure 4.1. Sequence of surface modification steps employed in this study to functionalize electrospun PET microfibers with thermoresponsive PNIPAAm brushes. The steps require deposition and amidation of APTES (a), followed by hydrolysis of the ethoxysilane groups on APTES to form silanol groups (b), which permit attachment of BMPUS (c) and subsequent ATRP of NIPAAm to yield PNIPAAm brushes (d). The top and bottom SEM images display PET and PET-PNIPAAm microfibers, respectively.	118
Figure 4.2. FTIR spectra of (a) as-spun PET, (b) PET-SiOH and (c) PET-PNIPAAm microfibers. Spectra arranged in the same order in the expanded views reveal the appearance of peaks associated with the formation of secondary amide moieties (dotted lines; see text for assignments).	119
Figure 4.3. XPS spectra of (a) PET-SiOH microfibers and (b) PET-PNIPAAm microfibers. The survey scans confirm the presence of N upon amidation of PET by APTES in (a) and PNIPAAm brush formation in (b). The high-resolution insets show the C _{1s} peak (≈ 285 eV) before (a) and after (b) PNIPAAm brush growth.	120
Figure 4.4. Cyclic WCA measurements of as-spun PET (●) and PET-PNIPAAm (○) microfibers at temperatures (in °C) below and above the T _c of PNIPAAm in water: (a) 25, (b) 60, (c) 25, and (d) 60. The error bars correspond to one standard deviation in the data.	121
Figure 4.5. SEM images acquired from PET-PNIPAAm microfibers exposed to aqueous suspensions of Au nanoparticles at temperatures (labeled) below and above the T _c of PNIPAAm. The illustrations in the insets (not drawn to scale) portray the conformation of the PNIPAAm brush at each temperature.	122
Figure 5.1. Surface modification and polymer brush growth steps on PET fibers. Two polymers were grafted to the PET surface: PHEMA (R=(CH ₂) ₂ OH) and PDMAEMA (R=(CH ₂) ₂ N(CH ₃) ₂).	152
Figure 5.2. Morphology of PET fibers after PDMAEMA (a) and PHEMA (b) brush growth.	153
Figure 5.3. FT-IR spectra of PDMAEMA (a) and PHEMA (b) brushes on PET fibers (solid blue line) along with PDMAEMA and PHEMA homopolymers (solid black line) and PET fiber (dotted black line).	154

Figure 5.4. PET fiber (a), PDMAEMA brush attached to PET fiber (b) and PHEMA brush attached to PET fiber (c).	155
Figure 5.5. Morphology PDMAEMA (a) and PHEMA (a) brushes on PET fibers after quarternization and fluorination reactions, respectively.	156
Figure 5.6. FT-IR spectra of PDMAEMA (a) and PHEMA (b) brushes on PET fibers along with PDMAEMA and PHEMA homo-polymers and PET fiber before and after quarternization and fluorination reactions.	157
Figure 5.7. Mechanism of bacterial lysis upon interaction with quarternized PDMAEMA (a), photos of agar plates those shows the number of colony forming units after incubation at 37 C for 18 hours (b) and number of CFUs on agar plates after exposing the bacteria to qPDMAEMA brushes on PET fibers. The red line is the initial number of <i>E. coli</i> exposed to qPDMAEMA brushes on PET fibers (c) (Scheme in Figure 7.a was obtained from ref. 72).	158
Figure 5.8. Surface nitrogen concentration on modified PET fibers and flat substrates and corresponding thickness after fibrinogen adsorption experiments.	159
Figure 6.1. Fundamental principle of high-energy-mechanical-milling.	177
Figure 6.2. Change in molecular weight of rPET (■) and vPET (●) as a function of milling time.	178
Figure 6.3. Crystallinity of (a) vPET, (b) rPET, (c) vPET+5%Na ⁺ MMT and (d) rPET+5%Na ⁺ MMT as a function of milling time.	179
Figure 6.4. Weight-loss of rPET and vPET, as well as vacuum-oven dried rPET and vPET (see legend). The solid and dashed lines represent the weight loss and the derivative of the weight loss, respectively.	180
Figure 6.5. Summary of thermal degradation behavior of mechanically milled rPET (■) and vPET (●) mechanically alloyed rPET/clay (□) and vPET/clay (○) samples: (a) residue after complete pyrolyzing all organics (b) onset degradation temperatures and (c) 2 nd peak degradation temperatures.	181
Figure 6.6. XRD patterns of as received Na ⁺ MMT, 5% (w/w) physical mixture of Na+ MMT and 2 hr milled rPET, 2, 5, 8 and 16 h mechanically alloyed 5% Na ⁺ MMT and rPET mixture.....	182
Figure 6.7. TEM micrographs of mechanically alloyed 5% (w/w) Na ⁺ MMT and rPET for 2 hours (a) and (b) and 16 hours (c) and (d).	183
Figure 7.1. The silicone backbone with the bond angles and the bond length. If both R groups are methyl the polymer is called poly(dimethylsiloxane) (PDMS).	229
Figure 7.2. Linking silicone chains with each other to form the silicone elastomer networks (SENs).....	230
Figure 7.3. Possible routes to form bi-layers of silicone networks.....	231
Figure 7.4. Coupling of trichlorosilane (TCS) molecule to vinyl groups of PVMS via the hydrosilylation reaction.	232
Figure 7.5. The chemical structure of PVMS-TCS/PVMS random copolymer (a), the percentage of reacted vinyl groups with the TCS molecules as a function of the vinyl:TCS ratio (b) and optical images of PVMS-TCS coated PDMS network with PVMS-TCS that has different percentages of the coupled vinyl groups. The red, orange	

and pink dots in Figure 7.3b correspond to the optical images of the same color frame in Figure 7.3c.	233
Figure 7.6. The thickness on the PVMS-TCS layer as a function of the concentration of PVMS-TCS in spin-coating solution and vinyl:TCS ratio (■). The lines are meant to guide the eye.	234
Figure 7.7. Optical microscopy images of spin-coated PVMS-TCS on PDMS network as a function of Vinyl:TCS ratio.	235
Figure 7.8. The modulus on the PVMS-TCS layer as a function of the concentration of PVMS-TCS in spin-coating solution and vinyl:TCS ratio (■). The lines are meant to guide the eye.	236
Figure 7.9. Oxygen permeation through the PVMS, PDMS and PVMS-TCS coated PDMS networks. PVMS-TCS layer was ≈ 150 nm, the vinyl:TCS ratio = 7. The values reported represent the average of 3 measurements, the error bars were calculated as “standard error”.....	237
Figure 7.10. Water contact angle of PVMS-TCS coated PDMS networks as a function of vinyl : TCS ratio before (a) and after 10 minutes of UVO treatment for 0.5 (■), 1 (■), 3 (■), and 5% (■) PVMS-TCS concentration in spin-coating solution. The grey and light blue rectangles are the water contact angle range for bare PDMS and PVMS, respectively before and after 10 minutes of UVO treatment.	238
Figure 7.11. FT-IR spectra of PDMS (thick black line), PVMS-TCS/PDMS laminates (from 0.5 (red line), 1 (blue line), 3 (dark yellow line) and 5% (purples line) PVMS-TCS copolymer in spin-coating solution) and bare PVMS (thick olive line) before (a) and after 10 minutes (b) of UVO treatment.	239
Figure 7.12. Surface nitrogen concentration (a) and modulus (b) of PVMS (●) and PVMS-TCS (■) coated PDMS network after attaching thiol-terminated peptide via thiol-ene addition reaction.....	240
Figure 7.13. Reaction scheme depicting the pre-modification of PVMS-TCS coating.....	241
Figure 7.14. Chemical structure of functional coatings and their corresponding wettabilities.	242
Figure 7.15. FT-IR spectra of PET film (black line), PVMS network (green line), ≈ 200 nm PVMS-TCS layer on PET film (blue line) and $\approx 1 \mu\text{m}$ PVMS-TCS layer on PET film (red line).	243
Figure 7.16. Water contact angle of PET films (a), PVMS-TCS/PET and PVMS-TCS/SiOx films (b) as a function of the UVO treatment time.	244
Figure 7.17. Atomic concentrations of oxygen (a), carbon (b) and silicon (c) for PET (●), PVMS-TCS/PET (▲) and PVMS network (□) as a function of the UVO treatment time.	245
Figure 7.18. HR-XPS silicon (a), oxygen (b) and carbon (c) spectra of bare PVMS (black line) and UVO treated PVMS-TCS/PET as a function of UVO treatment time: 0(red line), 1 (blue line), 3 (dark yellow line), 5 (navy line), 10 (purple line), 15 (wine line) and 30 (olive line) minutes of UVO treatment. The dashed lines are guides to eye,	

which are centered at the peak maximas of Si 2p, O 1s and C 1s spectra of PVMS-TCS/PET.....	246
Figure 7.19. Surface topography of PET (a) and PVMS-TCS coated PET films (b) as a function of the UVO treatment time.....	247
Figure 7.20. Water contact angle of fluorinated PET (●), PVMS-TCS coated PET (▲) and silicon wafer (■) as a function of the UVO treatment time of PET and PVMS-TCS/PET substrates.....	248
Figure 7.21. Carbon K-edge PEY NEXAFS spectra collected at $\theta = 50^\circ$ from PVMS-TCS/PET modified with UVO for various times ranging from 1 to 30 minutes and covered with tF8H2 SAM. The short dashed line at the post-edge coincides with the pre-edge PEY intensity.....	249
Figure 7.22. Proposed mechanism of removal of fluorinated t-F8H2 silanes for UVO-treated PET.....	250
Figure 7.23. NEXAFS spectra of UVO treated and fluorinated PET (a) PVMS-TCS/PET (b) films.....	251
Figure 7.24. Wettability of different material surfaces before and after coating and 5 minutes of UVO treatment.....	252
Figure 7.25. Coupling of azo based free radical polymerization initiator to PVMS-TCS..	253
Figure 7.26. FT-IR spectra of PVMS-TCS-azo/PP (green line), PMMA (black line), PVMS-TCS-azo/PET-PMMA (blue line) and PVMS-TCS-azo/PP-PMMA (red line) plotted in graph (a) and surface tethered PMMA chains grown on silicon wafers from PVMS-TCS-azo coating. The thin black lines are the IR spectra of corresponding substrates (PP and PET) and the dashed lines are guide to eye for the IR peaks of PMMA.....	254
Figure 7.27. Incorporation of nanoparticles in PVMS-TCS copolymer solution would increase the hardness and barrier properties of the coating.....	255
Figure 7.28. Bi-axial buckles formed on PDMS network via immersion of swelled PDMS network in PVMS-TCS copolymer solution.....	256
Figure 8.1. Polymers anchored to the surface of a fiber are endowed with thioimide functionality. After oxidation, the ring opens up and the thioimide is ready to scavenge a heavy metal of a toxin (phosphate or cyanide). This process is associated with a color change. Capturing of heavy metals/toxins is associated with de-coloring. The metals/toxins can be removed from the polymeric materials by mild oxidation. The system returns to the original state and can be reused in the recovery process.....	298
Figure 8.2. Structure of SN compound.....	299
Figure 8.3. Direct polymerization of functional polymer (a) and polymerization of “reactive” polymer for post-polymerization reaction and subsequent attachment of desired functionality.....	300
Figure 8.4. Azo-based polymerization initiator for surface-initiated polymerization.....	301
Figure 8.5. HPLC chromatogram of control-SN molecule in DMF in the presence of FRP initiator and naphthalene at 75 °C for 0 hour (black line), 6 hours (red line) and 46 hours (blue line). The peaks located at 3.09 and 3.68 minutes correspond to control-SN and naphthalene respectively.....	302

Figure 8.6. HPLC chromatogram of control-SN molecule in DMF in the presence of SN3U monomer, FRP initiator and naphthalene at 75 °C for 0 hour (black like), 2 hours (red line), 3.5 hours (blue line) and 22 hours (purple line). The peaks located at 2.96, 3.09 and 3.68 minutes correspond to SN3U monomer, control-SN and naphthalene respectively.	303
Figure 8.7. HPLC chromatograms of SN3U (left) and SN3P monomers (right) for 0 hour (black line) and 40 hours (red line) in DMF at 75 °C. The peaks located at 2.96, 3.11, 3.49 and 3.68 min correspond to SN3U monomer, impurities in SN3U monomer, SN3P monomer and naphthalene respectively.	304
Figure 8.8. Polymerization scheme of SN2P and PhAAm.	305
Figure 8.9. Differential refractive index (DRI) and light scattering data of SN2P monomer (black line) and dried polymerization mixture (red line).	306
Figure 8.10. FT-IR spectra of SN2P monomer (black line) and dried polymerization mixture of 100% SN2P (red line).	307
Figure 8.11. NMR spectra of dried polymerization mixture of 100% SN2P collected in d-acetone.	308
Figure 8.12. NMR spectra of 9.1% SN2P copolymer measured in d-acetone.	309
Figure 8.13. DSC thermograms of PPhAAm (black line), 4.8% SN2P (red line) and 9.1% SN2P (blue line) containing copolymers synthesized in DMF at 75 °C (exotherm is up).	310
Figure 8.14. Simulated values of refractive indices for SN2P (▲), PhAAm (■) and SN2U (●) as a function of monomeric repeat units.	311
Figure 8.15. FT-IR spectra of 9.1% SN2P-PAAm copolymer, PPhAAm brush and their difference.	312
Figure 8.16. Original (left) and normalized (right) SEC chromatograms of the polymerization mixtures from brush growth and monomers. SN2P monomer (black line), PhAAm monomer (red line), from PPhAAm brush polymerization solution (dark yellow line), from 9.1 SN2P brush polymerization solution (blue line) and heated PhAAm solution (olive line).	313
Figure 8.17. HPLC chromatograms of SN3U homopolymerization mixture in DMF at 75 °C for 0 black line), 2 (red line), 4.5 (blue line) and 24 hours (purple line). The peaks located at 2.96, 3.11, 3.49 and 3.68 min correspond to SN3U monomer, impurities in SN3U monomer and naphthalene respectively.	314
Figure 8.18. ¹ H-NMR spectra of PNIPAAm (black line), 10% SN3U (red line), 30% SN3U (blue line) containing copolymer and SN3U homopolymer (green line).	315
Figure 8.19. FT-IR spectra of SN3U homopolymer.	316
Figure 8.20. HPLC chromatograms of SN3P homopolymerization mixture in DMF at 75 °C for 0 black line), 2 (red line), 4.5 (blue line) and 24 hours (purple line). The peaks located at 3.47 and 3.68 min correspond to SN3P monomer and naphthalene respectively.	317
Figure 8.21. HPLC chromatograms of 10% SN3U and 90% NIPAAm polymerization mixture for 0 (black line), 2 (red line), 5 (blue line), 7 (purple line) and 23 hours (olive	

line). The peaks located at 1.14, 2.98 and 2.68 minutes correspond to NIPAAm, SN3U and naphthalene respectively.	318
Figure 8.22. HPLC chromatograms of 10% SN3P and 90% NIPAAm polymerization mixture for 0 (black line), 2 (red line), 4 (blue line) and 20 hours (olive line). The peaks located at 1.14, 3.47 and 2.68 minutes correspond to NIPAAm, SN3P and naphthalene respectively.	319
Figure 8.23. HPLC chromatogram of 30% SN3P and 70% NIPAAm polymerization mixture for 0 (black line), 3 (red line), 7 (blue line), 10 (purple line) and 22 hours (olive line). The peaks located at 1.14, 3.47 and 2.68 minutes correspond to NIPAAm, SN3P and naphthalene respectively.	320
Figure 8.24. ¹ H-NMR spectra of 50% wt SN3P containing NIPAAm-co-SN3P copolymer before (black line) and after (red line) deprotection reaction.	321
Figure 8.25. FT-IR spectra of 50% SN3P containing NIPAAm-co-SN3P copolymer before (black line) and after (red line) deprotection reaction.	322
Figure 8.26. Synthesis of PAAm from aniline and acryloyl chloride.	323
Figure 8.27. Reaction step 1.	324
Figure 8.28. Byproduct of reaction step 1.	325
Figure 8.29. Reaction step 2.	326
Figure 8.30. Reaction step 3.	327
Figure 8.31. Reaction step 4.	328
Figure 9.1. Free radical and atom transfer radical polymerization initiators for surface initiated.	362
Figure 9.2. FT-IR spectra of 100nm PDMAEMA brush on silicon wafer (black line), qSN1U attached to 100nm (blue line) and 200nm (red line) PDMAEMA brush on silicon wafer.	363
Figure 9.3. Reaction scheme of activating SN bond of qSN1U.	364
Figure 9.4. Differential refractive index and UV absorbance data of qSN1U (black line) and qSN1U after attachment of fluorinated thiol (red line).	365
Figure 9.5. FT-IR spectra of PDMAEMA brushes on PET fibers before (black line) and after qSN1U modification (red line).	366
Figure 9.6. Reaction scheme of quarternization reaction of PDMAEMA and qSN3U.	367
Figure 9.7. Reaction scheme of quarternization reaction of PDMAEMA and qSN3U.	368
Figure 9.8. ¹ H-NMR spectra of PDMAEMA before (black line) and after (red line) quarternization reaction with qSN3U.	369
Figure 9.9. FT-IR spectra of PDMAEMA (black line) and quarternized and ion exchanged PDMAEMA (red line).	370
Figure 9.10. Reaction scheme of click reaction of azide-SN3U with PPMA.	371
Figure 9.11. NMR spectra of propargyl methacrylate before (black line) and after click reaction with azide-SN3U (red line).	372
Figure 9.12. FT-IR spectrum of PPMA before (black line) and after the click reaction with azide-SN3U (red line).	373
Figure 9.13. Formation of free polymer chains (a) and polymer networks (b) and their post-modification to obtain functional copolymers for water purification.	374

Figure 9.14. Possible polymer architectures that can be used to be used with post-modification reactions.....	375
Figure 9.15. Homo-polymer, random copolymer and block copolymer brushes for post-modification reactions.....	376
Figure 9.16. Reaction schemes of SN post modification compounds.	377

CHAPTER 1: INTRODUCTION AND MOTIVATION

1.1. BACKGROUND

Surface characteristics of materials define the physical properties and performance of the final products for many advanced processes and applications involving self-cleaning, antifogging, antifouling, scratch resistance, bio-sensing devices, and improved adhesion. The characteristics of the aforementioned processes and applications can be achieved and optimized by tuning the chemistry, topography, surface modulus, charge density and mobility of the material surfaces employed. Most polymeric materials produced by and used in industry today are non-polar in nature, which renders them inherently hydrophobic. It is therefore challenging to decorate such supports with adhesives, inks, paints, or biological moieties that contain polar groups. Engineering the surface properties of materials can be achieved by introducing functional characteristics to improve performance for a specific application in mind. Therefore, polymer surface modification constitutes an increasingly important scientific and industrial step that must be developed and instituted to create targeted functional materials.

Surface modification techniques used to tune the surface properties of polymers are classified into two major categories: physical treatment and chemical modification. The former utilizes reactive and energetic gases/species that attack and react with the polymer surface, thereby incorporating hydrophilic and reactive moieties on the treated surface.

The most common methods in this genre include treatments with plasma, ultraviolet/ozone (UVO), flame, laser, corona, or ion beam bombardment. Chemical treatment techniques involve the introduction of new functional groups via various chemical reactions. Such methodologies include surface grafting, deposition of self-assembled monolayers (SAMs), or surface polymerization. Since most of these surface modification techniques involve polymer degradation (albeit often more controlled than exposure to physical treatment techniques), careful selection of the proper experimental conditions is imperative to achieve successful modification of the polymer surface without degrading the bulk polymer.

The overarching theme of this study is to engineer surface characteristics of polymeric materials to create novel functional surfaces and use these surfaces in different fashion, including the development of nanocomposites. Another outcome of this work is the synthesis of copolymers containing thioimide functionalities that are capable of water filtration. Recycled poly(ethylene terephthalate) (rPET) and polysiloxane networks are the main substrates utilized for the work presented in this study.

1.2. SURFACE MODIFICATION OF RECYCLED POLY(ETHYLENE TEREPHTHALATE) (rPET) FLAKES

Over the past half a century, the production of polymeric materials has increased approximately a hundred-fold, as documented by the data presented in Figure 1.1.^[1] This

growth has been associated primarily with the highly reduced cost, facile production/manufacture, and beneficial properties of plastics relative to other materials, including metals, ceramics, wood, and others. Currently, synthetic polymers are employed in nearly every commercial product, from cosmetics to computer parts, with the packaging industry becoming a strong leader in polymer consumption, accounting for nearly 30% of all plastics. Utilization of polymeric materials in daily life continues to increase steadily and is expected to reach 365 million tons in 2015 at an annual growth rate of 8.1%.^[2] While the packaging industry is responsible for the largest share of polymer consumption, polymers used in this field are commonly discarded after single use, which promotes growing landfill concerns. The rapid surge of plastic utilization has not proved entirely beneficial, however, due to serious environmental challenges associated with waste (i.e., landfilling and incineration). Environmental considerations, coupled with the limited supply and increasing price of oil, necessitate polymer recycling on a global basis. Polymer recycling is, however, routinely accompanied by nontrivial deterioration of physical properties. Therefore, recycled polymers are frequently used as fillers or other low-value materials for mundane applications.

Since its discovery in the 1940s, poly(ethylene terephthalate) (PET) has become one of the most important and widely-used thermoplastic polymers. Its high tensile and impact strength, adequate CO₂ retention, chemical resistance, clarity, processability, color, and design flexibility have expedited the application of PET in a wide variety of applications, including (but not limited to) textile fibers, soft drink bottles, jars, tire cords, audio tapes, and photographic film. The largest share of PET is used in the manufacture of fibers, whereas the

second largest market is in the production of bottle-grade resin. Of all commercially important thermoplastics and engineering polymers, PET has experienced the largest growth rate with the overall PET consumption in the world reaching 9.1 million tons in 2003^[1] and expected to double by 2010 (data not yet available). Recycling of PET has attracted a lot of attention in the past, primarily because PET can, in principle, be nearly 100% recycled. With the increased production and utilization of PET anticipated in coming years, the interest in and need for efficient PET recycling will most certainly increase. Recycling of PET can be performed in three different ways: primary, secondary, and tertiary recycling.^[3] In primary recycling, the scrap material in a plant is recycled without introducing contaminants and may be processed with virgin material to ensure product quality.^[3] In secondary recycling, post-consumer PET is separated from other polymers or paper via grinding and washing prior to melt-processing. The products of secondary recycling are used mostly in fiber, sheet and film applications. In addition, the properties deteriorate in each stage as the molecular weight is reduced because of residual contaminants. Tertiary recycling involves the depolymerization of PET to its monomeric or oligomeric precursors, depending on the depolymerization route employed. Depolymerization of PET can be conducted via methanolysis, glycolysis, aminolysis, ammonolysis, and hydrolysis.^[3] Repolymerization of oligomers or monomers after suitable purification then allows the use of rPET in food and beverage packaging in conjunction with virgin PET.

The United Resource Recovery Corporation (URRC) is one of the world-leading PET recycling companies that produces food-grade rPET. Its recycling process, UnPET, consists

of a combination of secondary and tertiary recycling methods. The recycling process starts with the acquisition of bales of recycle-designated solid waste from municipalities. Bottles and containers manufactured from PET are separated from other waste in a state-of-the-art process line and then chopped into small flakes. After removal of labels and other polymers, the PET flakes are exposed to caustic solution. Chemical degradation of PET in the caustic solution is restricted to only the outermost surface of the flakes, in marked contrast to thorough degradation of PET in the presence of amines. The flakes are then decontaminated at elevated temperatures, rinsed/neutralized, dried, and packaged. This route allows selective removal of just a thin layer of PET, along with other impurities, from flakes during recycling, instead of depolymerizing entire flakes to recover monomer that can be subsequently repolymerized at a significant energy cost. The UnPET process employs multiple separation and quality-control steps to ensure food-grade rPET and reaps the benefit of high throughput and energy savings while conserving important natural resources, such as water. With this process, approximately 5% of the rPET is depolymerized and the remaining rPET flakes are suitable for producing food-grade packaging. Depolymerization of only 5% of rPET saves the additional depolymerization and separation cost (of the monomers and oligomers) and repolymerization cost.

A large-scale trial study recently performed by the Coca Cola Company in the United Kingdom examined different rPET grades generated from different recycling companies.^[4] In their study, carbonated beverage bottles were fabricated and tested in conventional bottle production. Simultaneously, soft drink-filled bottles were tested by consumers. In Figure

1.2, the average CO₂ retention times are plotted for rPET produced from different manufacturers using different virgin resins at different rPET loading levels. The tests and feedback from the customers demonstrated that the main problem was encountered when rPET was mixed and processed with “virgin” PET (vPET) to yield inferior CO₂ retention.^[4] In this application, an important challenge is the improvement of the barrier properties of rPET, which can be achieved through the development of polymer nanocomposites consisting of nanoscale inorganic species dispersed within a polymer matrix.

It has been repeatedly shown^[5-7] that introducing inorganic fillers into the polymer matrix typically decreases gas permeation by increasing the path length of the diffusing species through the material. Nanoclays as filler materials are ideal for this purpose because of the high aspect ratio of the clay platelets. If they are oriented with their short axis perpendicular to the film surface, they can effectively reduce the diffusion of permeating gas molecules. Polymer-clay nanocomposites (PCNs) are formed when these nanometer-sized clay platelets are dispersed homogeneously throughout polymer matrices so that they strongly influence molecular transport through the polymer. Gas transport in dense polymeric materials typically occurs by the solution-diffusion mechanism. In this case, the permeation of gas molecules is defined as the product of their solubility and diffusivity in the polymer matrix.^[8] The solubility of gas molecules within a polymer depends on the thermodynamic interactions between the penetrant and the matrix, whereas gas diffusion depends on the mobility and size of the gas molecules, as well as the transient voids present in the matrix due to the available free volume in the polymer.

As mentioned earlier, incorporation of impermeable flakes into the polymer matrix generates tortuous diffusion paths that must be traversed by a diffusing species. Nielsen^[8] expressed the tortuosity factor (τ) as the ratio of the actual distance that a permeant travels (d') to the shortest distance that it would travel in the absence of a tortuous path (d), viz.,

$$\tau = \frac{d'}{d} = 1 + \frac{L}{2W} \phi_f \quad (1.1)$$

where L is the flake length, W is the flake thickness and ϕ_f denotes the volume fraction of filler. It can thus be shown that tortuosity affects permeation according to

$$\frac{P_c}{P_p} = \frac{\phi_p}{1 + (L/2W)\phi_f} \quad (1.2)$$

where P_c and P_p represent the permeabilities of the composite and unfilled polymer, respectively, and ϕ_p is the volume fraction of polymer ($= 1 - \phi_f$). Equations (1.1) and (1.2) reveal that the permeation of the gas molecules in a polymer nanocomposite depends on the size, geometry, and spatial orientation of the platelets in the polymer matrix.^[6, 9] Because of the high aspect ratio of clay platelets, only a small amount of clay is required to decrease the permeation through PCNs.^[6, 9-11] Improvement of gas barrier properties of PCNs has been previously investigated through both experiment^[6, 9, 10] and modeling.^[12, 13]

It is important to recognize that PCNs have been studied since the 1960s, and the volume of work conducted in this field has increased dramatically after the first publications in the mid-1980s by Toyota researchers, who reported the preparation of polymer/clay nanocomposites via polymerization of ϵ -caprolactam in the interlayer gallery of

montmorillonite.^[5, 11, 14-16] In general, PCNs possessing only a minute amount of homogeneously distributed clay sheets with high aspect ratios (nanometer in thickness and micrometer in lateral dimension) have been shown to exhibit improved gas barrier properties, mechanical strength, and heat distortion temperature, as well as flame retardancy, without affecting adversely polymer transparency.^[5] Subsequently, other methods of fabricating PCNs have been developed, including solution intercalation and melt compounding.^[5]

Numerous reports in the literature address the preparation of PET/clay nanocomposites and investigate their characteristics. Methods utilized for fabricating PCNs include: 1) in-situ interlayer polymerization^[17-23], 2) solution intercalation^[24-26], and 3) melt intercalation.^[27, 28] The characteristics of PCNs examined include barrier^[18, 21, 29], mechanical^[17-19, 21, 22, 25, 26, 29-32] and thermal properties^[17-21, 23-26, 30, 32, 33], in addition to the effect of added clay on polymer crystallization.^[17, 20, 24, 27] Thus far, PET/clay nanocomposites have been formed by conventional ways (i.e., via in-situ interlayer polymerization, solution and melt intercalation) by using organically-modified clays. This class of clay includes natural clay modified with organic surfactants to improve the compatibility of the clay platelets with nonpolar polymer matrices. We plan to generate rPET/clay nanocomposites by two different protocols in this study: 1) utilizing the functional groups on the surface of rPET for the attachment of dispersed natural clay platelets, and 2) mechanical alloying of rPET flakes with natural clay.

In the first approach, we will take advantage of the surface charges on pristine montmorillonite, a common natural clay, and its ability to be exfoliated in water. First, we intend to modify the rPET surface to increase its surface energy and its interaction with the

clay particles, since increased electrostatic interaction will result in enhanced deposition and stronger attachment of discrete clay platelets to the rPET surface. Through the targeted use of specialty polymers and surface-initiated polymerization methods, the surface of rPET can be rendered hydrophilic, which permits attachment of various inorganic species, such as natural nanoclay (and, for that matter, non-functionalized metal or metal oxide nanoparticles), to functionalize rPET for a wide variety of high-end applications. In addition, the increase in the roughness of the rPET surface due to recycling will increase the number of sites available for clay platelet attachment. In the second approach undertaken, high-energy mechanical alloying performed at ambient temperature will be performed to disperse the clay platelets throughout rPET. In this manner, clay platelets and polymer particles will be repeatedly fractured, elongated and sheared as they collide during vibration.

In Chapters 2-5 of this Dissertation, rPET was utilized as the main polymer matrix, and its surface properties were engineered toward the creation of PCNs. Specifically, Chapter 2 summarizes our efforts to hydrophilize the rPET surface with UVO treatment.^[34] Chapter 3 describes our effort leading to the modification of rPET surfaces with polyelectrolytes, followed by subsequent nanoclay attachment, extrusion and characterization. Chapter 4 illustrates the work conducted on the surface modification of electrospun PET microfiber (generated from rPET flakes) with functional polymer brushes. Finally, Chapter 5 sums up the mechanical alloying of rPET flakes with nanoclay, which was performed via ball milling.

1.3. SURFACE MODIFICATION OF SILICONE ELASTOMER NETWORKS

Silicones, or polysiloxanes, represent heteroatom polymers consisting of an inorganic Si-O backbone of alternating silicon and oxygen atoms with 2 pendant organic groups attached to every silicon atom, as depicted in Figure 1.3. Poly(dimethylsiloxane) (PDMS) is the most commonly used silicone wherein two methyl groups are attached to the silicon atom. The exceptional surface properties of PDMS arise from its high backbone flexibility, which can be attributed to the longer Si-O-Si bond angle, relative to the C-C-C bond, and a correspondingly lower energy barrier for rotation.^[35, 36] This characteristic is responsible for a very low glass transition temperature (T_g) for silicones (≈ 150 K) and high chain flexibility even at ambient temperature. The presence of two stable methyl groups attached to the silicon atom imparts chemical and physical resistance to PDMS.^[36] For instance, due to attractive/repulsive interactions, the methyl groups on the Si-O-Si backbone reside on the surface at an air-interface, but they bury themselves under the polymer backbone at a water-interface to adopt their lowest surface energy configuration. When chemically cross-linked, as portrayed in Figure 1.4, silicones form flexible silicone elastomer networks (SENs) with an elastic modulus of ≈ 1 MPa. The liquid-like nature of the parent polymer between cross-link junctions remains intact, and the high flexibility of the Si-O-Si backbone assures that SENs can readily adopt their lowest surface energy conformations rapidly while responding to environmental changes as mentioned above.

Silicones are employed in numerous applications ranging from the electronics to personal care, automotive, biomedical, and construction industries. Of these application areas, PDMS is especially important in biomedical science since it is biocompatible. For instance, PDMS is used as a material for contact lenses and human implants. These applications demand that the surface of PDMS be hydrophilic to 1) minimize corneal discomfort by enhancing wettability in the presence of tears and 2) reduce platelet adhesion for implant applications. In both cases, the hydrophobic PDMS surface must be altered chemically or physically to increase its surface energy. The inherent inertness of PDMS, however, makes this task challenging. Modification of the surface of PDMS has been realized using various techniques involving: 1) physical treatments, such as plasma, corona, ultraviolet (UV), UV/Ozone (UVO), electron and ion beams, 2) chemical oxidation, or 3) a combination of both physical and chemical means.^[37-44] Among these techniques, oxygen plasma treatment has been widely utilized to make the PDMS surface more hydrophilic via introduction of polar groups. Although it has been shown^[40-42] that plasma treatment propagates several hundred nanometers below the surface of PDMS with irreversible chemical changes at the near-surface region, there is no agreement on the exact nature of the chemical groups formed on the outermost surface. In addition, plasma treatment results in the formation of a brittle, silica-like layer on the surface of PDMS. This layer, which varies in thickness as a function of treatment time, power of the plasma, chamber pressure, and gas composition, alters the mechanical properties of the PDMS surface. Moreover, cracks formed in this silica-like layer

facilitate the diffusion of uncross-linked PDMS oligomers to the surface, which likewise alters the initial hydrophilic state.^[40-44]

In addition to plasma treatment, UVO has also been employed to increase the surface hydrophilicity of PDMS.^[37, 38, 45-47] The UVO treatment involves a photosensitized oxidation process wherein the molecules of a treated material are excited and/or dissociated by the absorption of short-wavelength UV radiation. Atomic oxygen is simultaneously generated when molecular oxygen is dissociated by radiation with a wavelength (λ_1) of 184.9 nm and ozone by radiation at $\lambda_2 = 253.7$ nm.^[48] The radiation at 253.7 nm is absorbed by most hydrocarbons, as well as by ozone. The organic products of this excitation react with atomic oxygen to form simpler, volatile molecules that desorb from the surface. Therefore, when both radiation wavelengths are present, atomic oxygen is continuously generated, and ozone is continually formed and destroyed. Compared to plasma treatment, UVO treatment is a milder type of physical modification that yields similar surface changes but with an approximate order of magnitude increase in processing time. This allows for better control of surface conversion, since different degrees of hydrophilicity will be achieved for different UVO exposure times. Therefore, we intend to utilize UVO to render SENs more hydrophilic.

Even though it is more controlled than plasma modification, UVO treatment of PDMS still causes uncontrollable changes to the surface of SENs. On one hand, at short modification times, a large variety of hydrophilic groups, such as hydroxyls, carboxyls, aldehydes, and peroxides, form on the surface of SENs. Long UVO treatments of PDMS, on the other hand, generate a silica-like surface layer that considerably hardens the originally-

soft SEN surface. While most UVO-modification studies involving SENs have been conducted with PDMS, Efimenko et al.^[37] recently reported results from UVO treatment of poly(vinylmethyloxane) (PVMS), whose higher susceptibility to UVO reduces treatment time and increases chemical tailorability to retain soft, hydrophilic SENs. They have provided experimental evidence that brief UVO treatment times (seconds to a few minutes) are sufficient to form highly hydrophilic PVMS surfaces compared to UVO treatment of PDMS, the surface of which becomes hydrophilic only after prolonged UVO exposure.

Unlike the case of PDMS, which possesses exceptionally high chemical stability due to the presence of two methyl groups, the chemical tailorability of PVMS is made possible due to the vinyl functionality, which can be modified via 1) chemical oxidization to form either alcohol or carboxylic acid moieties capable of subsequent chemical grafting at the newly generated “active” sites, or 2) direct attachment of a desired functionality through addition reactions such as hydrosilation, hydrosulfidation, hydrophosphination, epoxidation, and alkyl halide addition reactions. Therefore, PVMS is a versatile polymer providing multiple functions such as 1) low surface energy due to the methyl group, 2) high flexibility due to the siloxane backbone, and 3) targeted reactivity at the vinyl moiety, which can be used as an attachment point for various chemistries. The ability to tune the chemical nature of PVMS via reactions with vinyls has facilitated the attachment of various reactive groups to the PVMS backbone. In this Dissertation, we outline several such methods. In Chapter 6, for instance, we describe experiments in which trichlorosilane (TCS) molecules are coupled with the vinyl groups in the presence of Pt(0) catalyst via hydrosilylation reaction. Spin-coating

of the synthesized (co-)polymer results in smooth and uniform coatings on a variety of substrates, including, but not limited, PDMS-based SEN, PET, polyethylene, polypropylene, polyamide, polyimide, glass, and silica. The hydrolysis of the TCS groups in the presence of moisture produces cross-linking, which increases the stability of the coatings. The mechanical properties and thickness of such coatings can be altered by tuning the extent of TCS coupling and/or the concentration of copolymer in the spin-coating solution. Chapter 6 summarizes the design, application and characterization of functional coatings based on PVMS layers on various substrates such as PET and PDMS.

1.4. SYNTHESIS OF FUNCTIONAL COPOLYMERS AND POST-POLYMERIZATION MODIFICATION REACTIONS FOR WATER PURIFICATION

Decreasing supplies of fresh water and a continuously increasing human population necessitates the development of efficient water-cleaning technologies to remove heavy metal and cyanide ions and thus provide clean water. Thioimide-based molecules (cf. Figure 1.5) synthesized by the group of Dr. Jiří Šrogl at the Institute of Organic Chemistry and Biochemistry of the Czech Academy of Sciences offer reversible *capture and release* of various metals and cyanide ions from water. In this study, we aimed to synthesize functional macromolecules containing thioimide functionalities to assist water purification. The chemistry of the R₁ and R₂ groups on the thioimide molecule (SN compound) can be optimized to introduce “reactive” functionalities that would allow the synthesis of

copolymers and/or attach SN compounds to already-synthesized “reactive” polymers via post-polymerization modification. Chapter 7 of this Dissertation summarizes copolymerization studies of functional SN monomers, and Chapter 8 extends the work from Chapter 7 by describing attachment of SN-based moieties to neutral polymers by post-post polymerization modification. Preliminary experiments demonstrating the capability of polymer-based SN compounds in removing cyanides from water solutions are also briefly described.

1.5. REFERENCES

- [1] Plastic Business Data and Charts The Association of German Plastics Manufacturers, **2004**.
- [2] F. Pardos, Vol. 2010, http://www.pardos-marketing.com/paper_e03.htm, **2006**.
- [3] G. P. Karayannidis, D. S. Achilias, *Macromolecular Materials and Engineering* **2007**, 292, 128.
- [4] R. Martin, The Water and Resources Action Programme, England **2006**.
- [5] S. S. Ray, M. Okamoto, *Progress in Polymer Science* **2003**, 28, 1539.
- [6] K. Yano, A. Usuki, A. Okada, T. Kurauchi, O. Kamigaito, *Journal of Polymer Science Part A: Polymer Chemistry* **1993**, 31, 2493.
- [7] K. Masaya, *Journal of Polymer Science Part A: Polymer Chemistry* **2004**, 42, 819.
- [8] N. P. Patel, A. C. Miller, R. J. Spontak, *Advanced Materials* **2003**, 15, 729.
- [9] T. Lan, P. D. Kaviratna, T. J. Pinnavaia, *Chemistry of Materials* **1994**, 6, 573.
- [10] K. Yano, A. Usuki, A. Okada, *Journal of Polymer Science Part A: Polymer Chemistry* **1997**, 35, 2289.
- [11] E. P. Giannelis, *Advanced Materials* **1996**, 8, 29.
- [12] R. K. Bharadwaj, *Macromolecules* **2001**, 34, 9189.
- [13] A. A. Gusev, H. R. Lusti, *Advanced Materials* **2001**, 13, 1641.
- [14] C. E. Powell, G. W. Beall, *Current Opinion in Solid State and Materials Science* **2006**, 10, 73.
- [15] A. Okada, A. Usuki, *Macromolecular Materials and Engineering* **2006**, 291, 1449.
- [16] J. W. Gilman, C. L. Jackson, A. B. Morgan, R. Harris, E. Manias, E. P. Giannelis, M. Wuthenow, D. Hilton, S. H. Phillips, *Chemistry of Materials* **2000**, 12, 1866.

- [17] Y. Ke, C. Long, Z. Qi, *Journal of Applied Polymer Science* **1999**, *71*, 1139.
- [18] Z. Ke, B. Yongping, *Materials Letters* **2005**, *59*, 3348.
- [19] J. H. Chang, S. J. Kim, Y. L. Joo, S. Im, *Polymer* **2004**, *45*, 919.
- [20] Y. C. Ke, Z. B. Yang, C. F. Zhu, *Journal of Applied Polymer Science* **2002**, *85*, 2677.
- [21] T. Y. Tsai, C. H. Li, C. H. Chang, W. H. Cheng, C. L. Hwang, R. J. Wu, *Advanced Materials* **2005**, *17*, 1769.
- [22] Y. Imai, S. Nishimura, E. Abe, H. Tateyama, A. Abiko, A. Yamaguchi, T. Aoyama, H. Taguchi, *Chemistry of Materials* **2002**, *14*, 477.
- [23] J. H. Chang, S. J. Kim, *Polymer Bulletin* **2004**, *52*, 289.
- [24] C. F. Ou, M. T. Ho, J. R. Lin, *Journal of Applied Polymer Science* **2004**, *91*, 140.
- [25] J. H. Chang, D. K. Park, *Polymer Bulletin* **2001**, *47*, 191.
- [26] J. H. Chang, D. K. Park, *Journal of Polymer Science Part B: Polymer Physics* **2001**, *39*, 2581.
- [27] I. Y. Phang, K. P. Pramoda, T. Liu, C. He, *Polymer International* **2004**, *53*, 1282.
- [28] A. Sanchez-Solis, I. Romero-Ibarra, M. R. Estrada, F. Calderas, O. Manero.
- [29] D. J. Sekelik, E. V. Stepanov, S. Nazarenko, D. Schiraldi, A. Hiltner, E. Baer, *Journal of Polymer Science Part B: Polymer Physics* **1999**, *37*, 847.
- [30] A. Sanchez-Solis, I. Romero-Ibarra, M. R. Estrada, F. Calderas, O. Manero, *Polymer Engineering and Science* **2004**, *44*, 1094.
- [31] U. Gurmendi, J. I. Eguiazabal, J. Nazabal, *Macromolecular Materials and Engineering* **2007**, *292*, 169.
- [32] M. T. M. Bizarria, A. L. F. D. M. Giraldo, C. M. de Carvalho, J. I. Velasco, M. A. d'Avila, L. H. I. Mei, *Journal of Applied Polymer Science* **2007**, *104*, 1839.
- [33] C. H. Davis, L. J. Mathias, J. W. Gilman, D. A. Schiraldi, J. R. Shields, P. Trulove, T. E. Sutto, H. C. Delong, *Journal of Polymer Science Part B: Polymer Physics* **2002**, *40*, 2661.

- [34] A. E. Ozcam, K. Efimenko, C. Jaye, R. J. Spontak, D. A. Fischer, J. Genzer, *Journal of Electron Spectroscopy and Related Phenomena* **2009**, 172, 95.
- [35] M. J. Owen, *Industrial & Engineering Chemistry Product Research and Development* **1980**, 19, 97.
- [36] S. J. Clarson, J. A. Semlyen, R. G. Jones, W. Andão, J. Chojnowski, - *Prentice Hall polymer science and technology series*.
- [37] K. Efimenko, J. A. Crowe, E. Manias, D. W. Schwark, D. A. Fischer, J. Genzer, *Polymer* **2005**, 46, 9329.
- [38] K. Efimenko, W. E. Wallace, J. Genzer, *Journal of colloid and interface science* **2002**, 254, 306.
- [39] M. H. Jin, X. J. Feng, J. M. Xi, J. Zhai, K. W. Cho, L. Feng, L. Jiang, *Macromolecular Rapid Communications* **2005**, 26, 1805.
- [40] H. Hillborg, J. F. Ankner, U. W. Gedde, G. D. Smith, H. K. Yasuda, K. Wikstrom, *Polymer* **2000**, 41, 6851.
- [41] H. Hillborg, U. W. Gedde, *Polymer* **1998**, 39, 1991.
- [42] H. Hillborg, U. W. Gedde, *Ieee Transactions on Dielectrics and Electrical Insulation* **1999**, 6, 703.
- [43] H. Hillborg, S. Karlsson, U. W. Gedde, *Polymer* **2001**, 42, 8883.
- [44] H. Hillborg, M. Sandelin, U. W. Gedde, *Polymer* **2001**, 42, 7349.
- [45] J. Genzer, K. Efimenko, *Science* **2000**, 290, 2130.
- [46] M. Ouyang, R. J. Muisener, A. Boulares, J. T. Koberstein, *Journal of Membrane Science* **2000**, 177, 177.
- [47] M. Ouyang, C. Yuan, R. J. Muisener, A. Boulares, J. T. Koberstein, *Chemistry of Materials* **2000**, 12, 1591.
- [48] J. R. Vig, *Journal of Vacuum Science & Technology A: Vacuum, Surfaces, and Films* **1985**, 3, 1027.

1.6. FIGURES

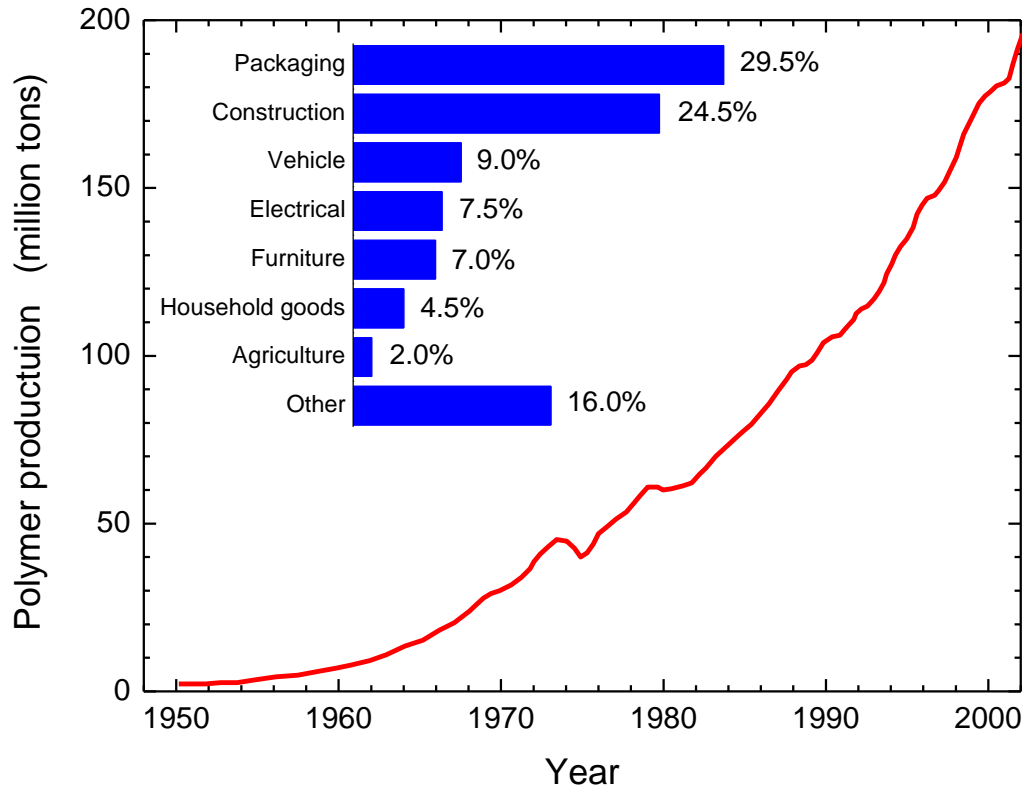


Figure 1.1. Production rate of plastics and distribution of polymer usage areas.^[1]

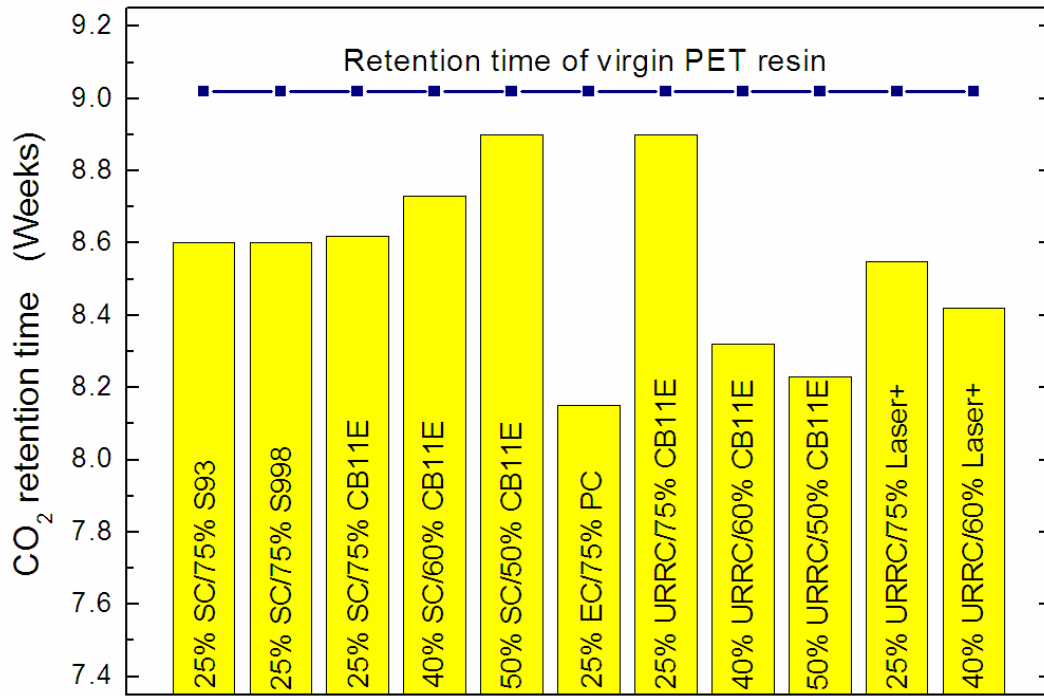


Figure 1.2. CO₂ retention times of the bottles produced from rPET and vPET.^[4]

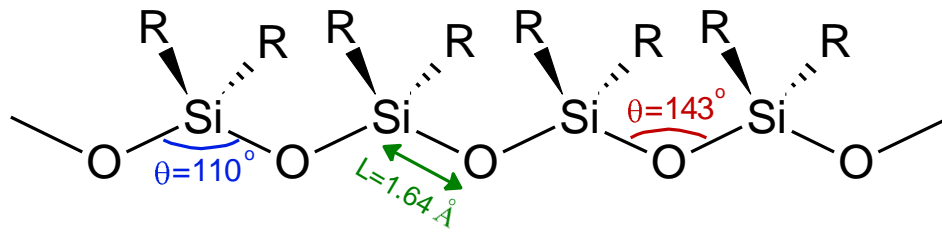


Figure 1.3. The silicone backbone with the bond angles (θ) and the bond length (L) identified. If both R groups are methyl, the polymer is referred to as poly(dimethylsiloxane) (PDMS).

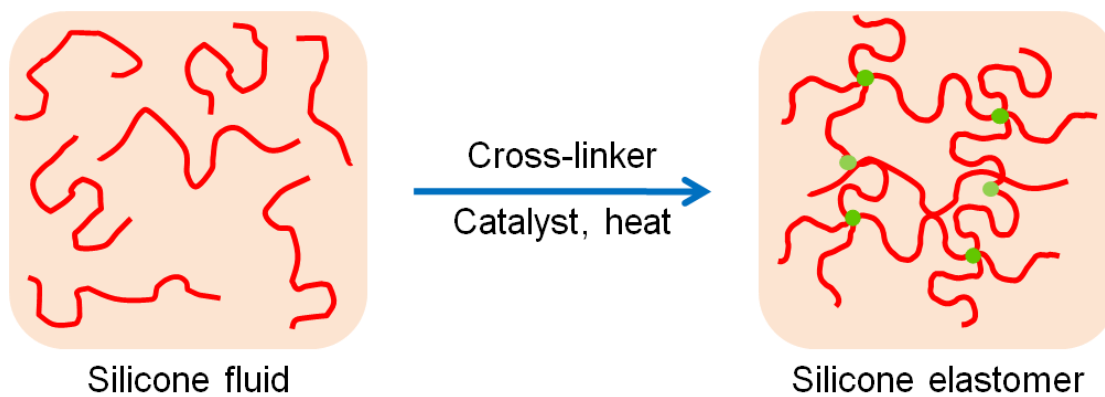


Figure 1.4. Cross-linking of silicone chains to form a silicone elastomer network (SEN).

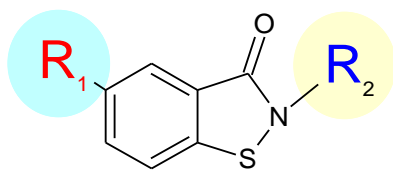


Figure 1.5. Generalized structure of a thioimide compound.

CHAPTER 2: MODIFICATION OF POLY(ETHYLENE TEREPHTHALATE) (PET) SURFACES WITH SELF-ASSEMBLED MONOLAYERS OF ORGANOSILANE PRECURSORS

2.1. INTRODUCTION

Since its discovery in the 1940s, poly(ethylene terephthalate) (PET) has become one of the most important and widely-used thermoplastic polymers.^[1] Its high tensile and impact strength, adequate CO₂ retention, chemical resistance, optical clarity, processability, and design flexibility have expedited commercial use of PET in a wide variety of applications including, but not limited to, high-value/low-cost consumables (*i.e.*, textile fibers, beverage bottles, jars, tire cords, audio tapes, and photographic film). PET is also an ideal candidate for futuristic applications such as a substrate material for flexible electronic circuits. Among all thermoplastics and engineering polymers, PET has experienced the largest growth rate - its overall worldwide consumption reaching 9.1 million tons in 2003 - and is expected to hit nearly double this production level by 2010.^[2]

Like most organic polymers, PET does not possess good adhesion and wetting properties because of its inherently low surface energy. For some applications it is desirable to alter the PET surface character, either chemically or physically, without compromising its bulk properties.^[3] In the past, several efforts have reported on modifying the surface of PET by using chemical treatment (*e.g.*, hydrolysis^[4-7], reduction^[7-9], aminolysis^[5,8-10], and

glycolysis^[7]) and physical modification (e.g., plasma^[11,12], ultraviolet/ozone^[12-16], flame^[12], corona treatments^[12,17,18], electrical discharge^[19], ion beam bombardment^[20], laser treatment^[21], surface physical interpenetrating network formation^[22], and surface graft polymerization after activation of the PET surface).^[3,10] Since most of these surface modification techniques purposefully or inadvertently involve polymer degradation, careful selection of experimental conditions is imperative to the successful surface modification of PET without degrading the bulk polymer and its desirable property attributes.

Ultraviolet/ozone (UVO) treatment has traditionally been used as an expedient technique to remove organic impurities from semiconductor surfaces.^[23] This method of treatment involves a photosensitized oxidation process wherein the molecules of the treated material are excited and/or dissociated by the absorption of short-wavelength UV radiation. The excited molecules then interact with atomic oxygen simultaneously generated as molecular oxygen and ozone are dissociated by UV radiation at wavelengths of 184.9 nm and 253.7 nm, respectively. Therefore, when a specimen is exposed to both wavelengths, molecular oxygen is continuously converted into ozone that subsequently breaks into reactive atomic oxygen. Concurrently, the 253.7 nm radiation is absorbed by most hydrocarbons and the organic products of this excitation react intensely with atomic oxygen to form simpler volatile molecules (*i.e.*, CO₂), which desorb from the surface. Over the past few years, several papers have reported on using UVO treatment to modify the surfaces of polyethylene^[24,25], polypropylene^[13,14,26], PET^[13-16], polystyrene^[15], poly(dimethylsiloxane)^[27] and poly(etherether-ketone).^[25] While the exact surface composition after UVO treatment varies

from polymer to polymer, the concentration of hydrophilic groups, such as –COOH or –OH, at or near the surface generally increases dramatically for all polymers. In addition to these surface-anchored, high-surface-energy moieties and some volatile components (*i.e.*, CO₂), UVO treatment may "leave behind" a residual layer composed of hydrophilic low-molecular-weight organic molecules (LMWOCs). The LMWOCs represent non-volatile components that can be removed by washing the surface with an appropriate solvent, including water.^[13,14]

Modification of PET surfaces by UVO treatment has been investigated previously by Walzak et al.^[12-14] and Bradley et al.^[15,16], who explored the effect of UVO treatment time on PET surface energy^[13-16], chemical composition^[13-16], topography^[15,16], and aging.^[13] They reported an increase in the wettability of PET surfaces that was accompanied by an increase in surface oxygen concentration and roughening with increasing UVO treatment time. In addition, they demonstrated increases in contact angle and carbon concentration after washing the UVO-treated PET specimens with water and/or aging the sample. These increases were attributed to removal of LMWOCs formed during UVO treatment and migration of hydrophilic moieties to the bulk of the sample. In this work, we modify the surface of PET by UVO treatment as a preparatory step that enables more general chemical tailorability of PET surfaces. Specifically, UVO-modified PET surfaces are shown to exhibit a large number of hydrophilic moieties that can serve as attachment points for organosilane molecules (OS). We demonstrate here the applicability of this technique by attaching self-assembled monolayers (SAMs) of semifluorinated OS (SFOS) precursors to UVO-treated

PET substrates and report on the physico-chemical characteristics of SFOS SAMs attached to the surface of PET films.

2.2. EXPERIMENTAL

2.2.1. FILM PREPARATION

Parent PET films were either prepared in house by melt-pressing flakes or kindly donated by DuPont-Teijin Films as untreated Mylar-DL films. The average surface roughness of the films, as measured by atomic force microscopy (AFM), was 2.0 ± 0.2 nm. These films were rinsed with deionized water (DIW) and methanol and then extracted with hexane for at least 8 h. After extraction the films were dried under vacuum and kept in a desiccator under reduced pressure until modification. Thin PET films were prepared by dissolving PET flakes in *o*-chlorophenol at a concentration of 3% (w/w) and subsequently spun-cast onto flat silica substrates that were previously rinsed with methanol and DIW. After deposition, the PET films were exposed to UVO. These films were used to monitor the relative changes in surface properties and the thickness of the film as a function of UVO treatment time.

2.2.2. ULTRAVIOLET/OZONE (UVO) TREATMENT

The UVO treatment of PET surfaces was performed in a commercial UVO chamber (Jelight Company, Inc., model 42). The standard fused quartz lamp, which, according to the manufacturer, emits about 65% of the total radiation at 184.9 nm and has an output of 28 mW/cm² at a distance 6 mm away from the source, was used in this study. The PET films were placed onto glass slides, which were subsequently inserted into the UVO cleaner at a distance of about 5 mm from the UV source and exposed to UVO radiation from one side only for predetermined periods of time.

2.2.3. SEMIFLUORINATED SELF-ASSEMBLED MONOLAYER FORMATION

1H,1H,2H,2H-Perfluorodecyl trichlorosilane (tF8H2), supplied by Alfa-Aesar and used as-received, was employed to form semifluorinated SAMs on the UVO-treated PET films prior to specimen sonication. The tF8H2 and fluorinated oil were mixed in a 1:5 ratio (w/w), and a small amount of this mixture was placed on the bottom of a Petri dish. After virgin and UVO-treated PET and silica substrates were taped to the Petri dish lid, the whole system was enclosed so that the samples hanged face-down on the Petri dish \approx 1 cm away from the tF8H2/oil mixture. Upon exposure for 15 min at ambient conditions, the lid was removed and the samples were first washed thoroughly with absolute ethanol to remove any physisorbed tF8H2 molecules and then dried with nitrogen.

2.2.4. WATER CONTACT ANGLE MEASUREMENTS

Contact angle measurements were performed via the sessile drop technique with DIW (the resistance was $>15 \text{ M}\Omega\text{cm}$) using a Ramé-Hart contact angle goniometer (Model 100-00) equipped with a CCD camera. Images were analyzed with the Ramé-Hart Imaging 2001 software. Static contact angles (S-CAs) were determined upon placement of an 8 μL droplet of DIW on the specimen surface. To measure the advancing and receding contact angles (A-CAs and R-CAs, respectively), a probe droplet was added (2 μL , DIW advancing) or removed (4 μL DIW, receding) and analyzed. Contact angles were measured on 3 to 5 independent spots on each sample and the results were averaged. The corresponding contact angle hysteresis (CAH), defined as the difference between the A-CA and R-CA, was likewise evaluated as a measure of the chemical and structural homogeneity of the surface probed.

2.2.5. ATOMIC FORCE MICROSCOPY

The surface topography of virgin and modified PET samples was examined using an Asylum Research MFP-3D AFM instrument in AC mode using Olympus AC-240 silicon cantilevers. Specimens were mounted with superglue to samples disks to ensure sample immobilization during imaging. Caution was exercised to keep the tip in repulsive mode in the phase channel during imaging. The surface roughness (RMS) was calculated from height images using the MFP-3D software.

2.2.6. ELLIPSOMETRY

The thicknesses of spun-cast PET films were measured with a variable-angle spectroscopic ellipsometer (VASE) manufactured by J.A. Woollam Co. Ellipsometry measures the difference in the polarization state between the light beams incident onto and reflected from the surface thus providing information about the dielectric properties and thickness of the film. The thickness of the films was evaluated using a single layer Cauchy model (Si/SiO_x/PET, index of refraction of PET was $n=1.5751$ at 630 nm) before and after the UVO treatment, as well as after sonication, rinsing with DIW and drying with nitrogen gas, a procedure during which LMWOC debris gets removed from the PET-UVO specimens. Unless otherwise specified, ellipsometric data were collected at an incidence angle of 70° to the surface normal at wavelengths ranging from 400 to 1100 nm in 10 nm increments.

2.2.7. X-RAY PHOTOELECTRON SPECTROSCOPY

The surface chemical composition of UVO-modified PET specimens was determined with a Kratos Axis Ultra DLD x-ray photoelectron spectroscopy (XPS) instrument using monochromated Al K α radiation with charge neutralization. Survey and high-resolution spectra were collected with pass energies of 80 and 20 eV, respectively, by using both electrostatic and magnetic lenses. Elemental chemical compositions were determined from spectral regression using Vision and CasaXPS software.

2.2.8. NEXAFS SPECTROSCOPY

Near-edge x-ray absorption fine structure (NEXAFS) spectroscopy above the carbon, oxygen and fluorine K-edges was also used to examine the composition and molecular orientation of the tF8H2 monolayers and the surface chemistry of the UVO-modified PET samples. The NEXAFS experiments were conducted at the NIST/Dow Soft X-ray Materials Characterization Facility of the National Synchrotron Light Source (NSLS) at Brookhaven National Laboratory. This spectroscopic method involves the resonant soft x-ray excitation of a K shell electron to an unoccupied low-lying antibonding molecular orbital of σ symmetry (σ^*) or π symmetry (π^*).^[28] The initial state K shell excitation endows NEXAFS with its elemental specificity, while the final-state unoccupied molecular orbitals provide NEXAFS with its bonding or chemical selectivity. A measurement of the partial electron yield (PEY) intensity of the NEXAFS spectral features thus allows identification of chemical bonds and determination of their relative population densities on the surface of the samples (the probing depth is \approx 3-4 nm subsurface). In addition, because the incident x-ray is linearly polarized, collection of NEXAFS spectra at various sample/x-ray beam orientations can yield information regarding the molecular orientation of molecules present on the surface. For this purpose, NEXAFS spectra have been collected at $\theta=20, 50$ and 90° , where θ is the angle between the sample normal and the polarization vector of the x-ray beam.

2.3. RESULTS AND DISCUSSION

As mentioned earlier, the atomic oxygen generated during UVO treatment reacts rapidly with various chemical functionalities present on the material surface and breaks polymer chains into smaller molecular fragments. While volatile species (*i.e.*, CO₂) escape readily during this process, the heavier LMWOC fractions remain as deposits on the polymer surface and can be removed by water rinsing or sonication. The sample thickness changes associated with UVO treatment and washing processes are monitored in this study by ellipsometry. In Figure 2.1, the thickness change upon UVO treatment (Figure 2.1a) and the water sonication step (Figure 2.1b) are plotted as functions of UVO treatment time. From these data, it is apparent that the amount of material removed during UVO exposure increases steadily at a rate of ≈ 4.5 nm/min. The quantity of LMWOCs removed by sonication increases with increasing UVO treatment time and saturates at around 12 min, corresponding to a thickness of ≈ 22 nm. These results reveal that the overall rate of PET removal is ≈ 6 nm/min (Figure 2.1c).

The DIW S-CA of the UVO-treated PET surface has also been monitored before and after removal of the water-soluble LMWOCs to discern the effect of residue removal on the surface energy of the film. The data in Figure 2.2a display the S-CA prior to and after sonication as a function of UVO treatment time. In both instances, the S-CA values decrease with increasing UVO treatment time, confirming UVO-induced oxidation of the surface and an increase in the population of hydrophilic groups probed by the DIW droplet. For a given

UVO treatment time, the S-CA values after removal of the LMWOC layer are slightly higher relative to the S-CA prior to the sonication step. It is important to recognize that the S-CA after water sonication appears to reach a plateau around $\approx 40^\circ$ after ≈ 5 min of UVO treatment. The increase in the S-CA, attributed to the removal of a large fraction of residual hydrophilic molecules from the surface by sonication, indicates that the surface functionalities remaining on the surface are not as hydrophilic as the LMWOC debris.

The surface chemical composition evolution of PET films is evident from the XPS measurements presented as a function of UVO treatment time in Figure 2.2. Here, the elemental concentrations of oxygen and carbon are provided in the middle and bottom plots, respectively. The removal of LMWOCs promotes a decrease in the concentration of atomic oxygen and a corresponding increase in the atomic carbon concentration relative to values measured on PET-UVO surfaces. The concentrations of atomic oxygen and carbon increase and decrease, respectively, with increasing UVO treatment time, and they both reach a plateau after ≈ 4 -5 min. Note that this time agrees favorably with the onset of the plateau in the S-CA data (*cf.* Figure 2.2 top). It is not surprising that the XPS and S-CA data exhibit similar trends, since both techniques probe the upper-most regions of a sample: ≈ 10 nm (XPS) and ≈ 0.5 nm (S-CA). In addition to the S-CA and XPS measurements, we have also monitored the variation in surface chemical composition in PET-UVO samples by NEXAFS spectroscopy. Though not shown, the NEXAFS K-edge jump results also agree qualitatively with the XPS and S-CA trends presented in Figure 2.2.

Chemical changes due to oxidation of the PET surface are elucidated by analyzing high-resolution XPS 1s scans for carbon and oxygen. Figure 2.3 shows the relative intensities of the major component peaks in both the O1s (525-540 eV) and C1s (275-294 eV) regions. Visual inspection of the XPS spectra reveals that an increase in UVO exposure time causes the peaks to broaden and the peak intensities in the O1s region to increase, while those in the C1s region to decrease. These results indicate that the oxygen content in the sample increases while that of carbon decreases (on a relative basis). The component peaks located at 285.0, 286.6, 287.9, and 289.0 eV correspond to the C-C/C-H, C-O/C-O-C, O-C-O/C=O, and O=C-O signals, respectively.^[29-32] Intensity variations in these characteristic "XPS fingerprints" with increasing UVO treatment time are displayed in Figure 2.4 for samples before and after sonication. For example, the peak located at 289.0 eV, the characteristic binding energy for carbon in carboxyl groups, increases in intensity relative to the peak located at 285.0 eV, assigned to C-C/C-H groups. This observation establishes that the percentage of lower binding energy component from high-resolution oxygen spectra (data not shown for C=O : 532.8 eV and C-O : 533.6-544.3 eV) increases. The binding energy of carbon in acid and ester functionalities is slightly different.^[29,31,32] From the data presented in Figure 2.4, the percentage of C-C/C-H bonds decreases initially from $\approx 50\%$ down to $\approx 40\%$ and does not change further during the course of longer UVO treatment. However, removal of the LMWOC layer via sonication increases the amount of C-C/C-H bonds compared to those in the samples prior to sonication. The population of O=C-O bonds increases and reaches a plateau region after ≈ 4 min of UVO exposure for both sonicated and un-sonicated specimens.

Conversely, the opposite trend is evident for the O=C-O bonds relative to C-C/C-H bonds, *i.e.*, after washing off the LMWOC layer, the amount of O=C-O bonds decreases in comparison to samples before sonication. The amount of C-O bonds increases for the first 2 min and then levels off. Washing-off the LMWOC layer has the same effect on the concentration of the C-O bonds. According to the data provided in Figure 2.4, UVO treatment of PET introduces carboxylic acids and hydroxyl groups onto the PET surface. Surface-bound -OH groups are crucial to the success of this study, since they will serve as attachments points for organosilane precursors, as described below.

The surface morphology of PET after UVO treatment for 0, 2, 8 and 30 min has been examined by AFM. Figure 2.5 shows representative AFM images acquired from samples before (left) and after (right) washing the UVO-treated PET films. For comparison, an AFM image of the parent PET substrate is included in Figure 2.5a. From images such as these, it is evident that the surface topography of the films does not change significantly in the first ≈ 2 min of UVO treatment. After ≈ 8 min, however, UVO treatment appreciably alters the surface topography. Specifically, discrete, spheroidal grains measuring $\approx 82 \pm 4$ nm in diameter become apparent. The size of these grains increases with increasing UVO exposure time, reaching $\approx 113 \pm 7$ nm in diameter after 30 min. After removing the LMWOC layer, the size of the grains decreases to $\approx 66 \pm 2$ nm and $\approx 81 \pm 6$ nm at 8 and 30 min, respectively. We note that similar results are obtained by scanning electron microscopy (images not shown here).

The presence of surface-bound hydrophilic functionalities introduced during the UVO treatment of PET can be utilized to attach reactive OS precursors, which are known to chemisorb to (predominantly) –OH groups on the surface.^[33,34] As a proof of concept, we use SFOS, which is based on a trichlorosilane head group, as molecules that react rapidly with surface-bound –OH groups even at ambient temperatures.^[35] The SFOS SAMs have been deposited from vapor on top of the PET-UVO samples, as detailed in the Experimental section. The properties of the PET-UVO/tF8H2 samples have been characterized by a variety of analytical methods, as described in detail below. As mentioned earlier, the removal of physisorbed tF8H2 molecules is performed using absolute ethanol to be more efficient and likewise prevent hydrolysis of unreacted OS from the surface. Independent ellipsometry experiments have been conducted to compare the removal efficacy of the LMWOC layer from UVO-treated PET after washing with ethanol and sonicating in DIW. This comparative study has verified that absolute ethanol constitutes a better solvent for removing LMWOCs from the PET-UVO surfaces than DIW.

In Figure 2.6 the S-CA of PET-UVO/tF8H2 samples after sonication is presented as a function of UVO treatment time. For comparison we also provide data from tF8H2 SAMs formed on top of a silicon wafer covered with a thin layer of silica (SiO_x/tF8H2). Whereas the S-CA for the SiO_x/tF8H2 samples remains at ≈115° for all UVO times and agrees well with previously reported results^[35], the S-CA values of tF8H2-treated PET are consistently lower than those measured on SiO_x/tF8H2. Furthermore, excluding the datum point for untreated PET, the S-CA values generally decrease with increasing UVO treatment time.

This reduction is due to the removal of LMWOC components that have reacted with tF8H2 during the ethanol rinsing step. By comparing the S-CA values of PET-UVO (*cf.* Figure 2.2) and PET-UVO/tF8H2 (*cf.* Figure 2.6) samples at long UVO treatment times, it is apparent that some tF8H2 SAMs remain on the PET-UVO surface even after washing. The CAH for the PET-UVO/tF8H2 samples ranges between 10° and 15°, which are not very different from the CAH measured in regard to SiO_x/tF8H2 SAMs (7°-11°). This finding is interesting and somehow uneasy to reconcile, since it implies that the surfaces of the PET-UVO/tF8H2 specimens remain relatively uniform. This implication and other issues related to the effect of LMWOC layer removal on SFOS SAMs are currently being investigated and will be reported in the future.

The population and molecular orientation of the tF8H2 molecules comprising the SAMs on top of the PET-UVO substrates have been interrogated by NEXAFS spectroscopy. In Figure 2.7, PEY NEXAFS spectra collected from PET-UVO/tF8H2 samples at the fluorine K-edge at $\theta=50^\circ$ are shown. At this geometry, representing the so-called “magic angle,” the PEY NEXAFS intensities are independent of molecular orientation and hence provide a convenient measure of molecular concentration in the specimens.^[28] These and subsequent PEY NEXAFS spectra have been normalized so that the intensity in the “pre-edge” region (photon energies < 685 eV) is set equal to zero. The value of the so-called “edge-jump,” defined as the difference between the “post-edge” (photon energies > 700 eV) and the “pre-edge,” represents a convenient relative measure of the concentration of fluorine in the sample. From the data displayed in Figure 2.7, the highest fluorine content measured is

present in the PET-UVO/tF8H2 sample prepared by exposing PET films to UVO for 2 min. The fluorine level decreases with increasing UVO treatment time due to the removal of the LMWOC layer, along with the tF8H2 SAM attached to it. This result agrees well with the trend in the CA data discussed previously (*cf.* Figure 2.6). The density of the tF8H2 molecules comprising the surface SAM constitutes another important parameter to consider because it determines the stability of the SAMs on top of the LMWOC layers. That is, the presence of hydrophobic tF8H2 SAMs protects the LMWOC layer by preventing/delaying the rinsing liquid from reaching the LMWOC layer and removing it. Upon UVO treatment, the PET surface roughens and, as a result, the quality of the SAM deteriorates. Recall that we have earlier demonstrated that the thickness of LMWOC layer increases with increasing UVO treatment time. Thicker LMWOC layers are easier to remove as the rinsing liquid can penetrate through defects present in the SAM. The highest quality SAM is obtained at very short UVO times presumably because of the interplay between the optimum hydrophilicity and thickness of the LMWOC layer and a sufficient density of tF8H2 in the SAM. In our previous work, we have established that dense tF8H2 SAMs form on substrates possessing only a moderate degree of hydrophilicity.^[27] Because of the trichlorosilane functionality, the tF8H2 molecules form in-plane linkages via condensation between neighboring –OH groups (formed by hydrolysis of the chlorine atom). Interestingly, the entire sheet of cross-linked tF8H2 SAM is anchored firmly to the underlying substrate at only a few points of attachment. Presumably the same situation exists here, where only a relatively small number

of $-OH$ groups generated on PET after ≈ 2 min of UVO treatment is sufficient to anchor the SAM to a relatively thin LMWOC layer (*cf.* Figure 2.1).

To provide an independent measure of this “optimal” UVO treatment time, we explore the trends present in the carbon K-edge NEXAFS spectra. Figure 2.8 shows the carbon K-edge PEY NEXAFS spectra acquired at $\theta=50^\circ$ from PET-UVO/tF8H2 samples prepared by treating PET substrates for various UVO times followed by tF8H2 SAM deposition and washing. In all the spectra, the peak at 292 eV, which corresponds to the $1s \rightarrow \sigma^*$ transition of the C-F bond, is readily detected. While the spectra corresponding to UVO times ≤ 4 min appear qualitatively similar to those measured from $SiO_x/tF8H2$ SAMs (data not shown), a new spectral feature appears at 285 eV in samples treated for UVO times in excess of 4 min. This peak, composed of two smaller peaks located at 284.8 and 285.3 eV, identifies the $1s \rightarrow \pi^*$ transition in the C=C signal from PET. Detection of this peak requires that PET must be present within the first $\approx 3-4$ nm of the sample surface, a typical probing depth for the PEY NEXAFS signal, and that, by inference, an incomplete SAM is present on the sample surface. Along with the appearance of the $1s \rightarrow \pi^*_{C=C}$ signal, the intensity of the $1s \rightarrow \sigma^*_{C-F}$ peak decreases, indicating a reduced concentration of fluorine in the specimen. Quantitative comparison of the spectra shown in Figure 2.8 in conjunction with the corresponding NEXAFS spectrum collected from the PET-UVO sample treated for the same UVO exposure time can yield the amount of tF8H2 present in the sample. In Figure 2.9a we replot the carbon K-edge PEY NEXAFS spectrum from the PET-UVO/tF8H2 sample treated for 6 min and superimpose the spectrum measured from the PET-UVO sample treated for the same

exposure time. The latter spectrum was multiplied by a scaling coefficient (K) to match the intensity of the $1s \rightarrow \pi^*_{C-C}$ peak (from 283 to 288 eV) in the PET-UVO/tF8H2 sample. Subsequent subtraction of the two spectra yields a spectrum that corresponds closely to that of a pure tF8H2 SAM, as shown in Figure 2.9b. The PEY NEXAFS carbon K-edge jump intensities obtained from such difference spectra as the one shown in Figure 2.9b are plotted on the left ordinate in Figure 2.10. Included for completeness in Figure 2.10 are the corresponding K values on the right ordinate. The edge-jump values exhibit a maximum at 2 min of UVO treatment, in agreement with our previous observations, after which time they start to decrease with increasing UVO time, eventually leveling off at ≈ 8 -10 min. The magnitude of K can be considered as a measure of the fraction of tF8H2 SAMs removed together with the LMWOC layer upon rinsing. The K values are small at short UVO times, but increase sharply with increasing UVO treatment time after about 4 min and ultimately reach a plateau (between 0.23 and 0.29) for times longer than ≈ 8 -10 min. We recognize that, in this analysis, we have neglected small differences in the x-ray absorption cross section between PET-UVO and PET-UVO/tF8H2. While approximate, the values of K displayed in Figure 2.10 provide valuable information about the coverage of the PET-UVO substrate by the SFOS SAM.

The concentration of tF8H2 molecules on the UVO-modified PET surface determines the number of generated Auger electrons, which contribute to the PEY signal. In addition, the orientation of the anti-bonding orbitals relative to the electric vector of the polarized x-ray beam also affects the intensity of the $1s \rightarrow \sigma^*$ transition signals. To extract information

regarding the molecular concentration and orientation of SFOS molecules from NEXAFS spectroscopy, PEY NEXAFS spectra have been collected from PET-UVO/tF8H2 samples at various orientations of the samples with respect to the incident x-ray beam. In Figure 2.11, normalized PEY NEXAFS spectra are presented as a function of photon energy around the carbon K-edge at $\theta=20^\circ$ and 90° for different UVO treatment times. The most important peaks in these spectra appear at 292 and 295 eV, corresponding to the $1s \rightarrow \sigma^*_{C-F}$ and $1s \rightarrow \sigma^*_{C-C}$ signals, respectively. By comparing the relative intensities of these two peaks at various orientations, we can infer that the tF8H2 chains are oriented nearly perpendicularly to the substrates (the peak at 292 eV is higher and that at 295 eV is lower at $\theta=90^\circ$ relative to the intensities collected $\theta=20^\circ$).^[36,37] While a quantitative measure of molecular orientation is not provided here, it suffices to say that a reasonable measure of the degree of perpendicular orientation is the difference between the spectra collected at $\theta=20^\circ$ and 90° . The largest difference between these peak intensities in the spectra shown in Figure 2.11 is evident for the PET-UVO/tF8H2 sample treated for 3 min. At long UVO times, the NEXAFS spectra do not exhibit any discernible tF8H2 orientation, even though the SFOS SAMs remain attached to the underlying substrate, as evidenced by the presence of the fluorine signal. The absence of orientation detected in the specimens does not, however, necessarily mean that the tF8H2 chains are not oriented in the SAMs. Due to surface roughening of the substrate, portions of the SAM may still be oriented but point in different directions. Since these regions are expectedly much smaller than the size of the probe (≈ 0.25

mm²), NEXAFS, in its current configuration, is not capable of measuring the molecular orientation on such rough samples.

2.4. CONCLUSIONS

The surface of PET has been modified by using UVO, followed by subsequent attachment of a semifluorinated organosilane (SFOS) SAM to the underlying oxidized PET substrate. We observe that UVO modification increases the surface energy of PET by degrading some of the PET chains present on the surface. Such UVO-mediated degradation leads to the formation of small volatile species and larger organic aggregates, the latter of which remain on the PET surface in the form of a LMWOC layer. The surface energy and atomic oxygen concentration of the PET-UVO samples increases with increasing UVO treatment time up to 4-5 min, as evidenced from CA, XPS and NEXAFS measurements. Removal of the highly hydrophilic LMWOC layer causes small, but noticeable, increases in the S-CA and surface carbon content. In addition, an increase in UVO treatment time is accompanied by surface roughening, as discerned by AFM. The oxidized PET surface can be used as a substrate for depositing a hydrophobic organosilane SAM layer. The quality of the SAMs generated for different UVO treatment times has been monitored with CA and NEXAFS. The S-CA of PET-UVO/tF8H2 samples reveals that some tF8H2 SAMs are removed from the substrate along with the underlying LMWOC layer during sample wash. Complementary NEXAFS measurements confirm these observations. Specifically, the

concentration of fluorine ascertained from the edge-jump in the fluorine K-edge NEXAFS spectra exhibits a maximum at a UVO exposure time of 2 min, in favorable quantitative agreement with CA results. Our data confirm that the 2 min UVO treatment time represents an optimum condition for creating stable PET-UVO/tF8H2 samples. During this brief UVO exposure, oxidation of PET is sufficiently mild so that the LMWOC layer thickness does not increase substantially. Yet, it appears to be long enough so that an adequate concentration of surface-bound -OH groups, which serve as attachment points for the SFOS SAMs, is created on top of the PET-UVO surfaces. Detailed analysis of the PEY NEXAFS spectra in samples prepared by long UVO treatment times shows that <80% of the tF8H2 SAM remains attached to the substrate after sonication, which removes the LMWOC layer and a portion of the SFOS SAM attached to it. Since the bulk properties of PET remain unaffected during UVO surface treatment and subsequent SFOS SAM attachment, the results presented here provide an enticing avenue to tough materials with patternable and functionalized surfaces that can be used in 3D device fabrication or as responsive sensors.

2.5. REFERENCES

- [1] Scheirs, J.; Long, T. E. Modern polyesters : chemistry and technology of polyesters and copolyesters; John Wiley & Sons: Hoboken, NJ, **2003**; , pp 750.
- [2]. Plastic Business Data and Charts The Association of German Plastics Manufacturers <http://www.vke.de> **2004**.
- [3] Roux, S.; Demoustier-Champagne, S. Journal of Polymer Science Part A: Polymer Chemistry **2003**, 9, 1347-1359.
- [4] Dave, J.; Kumar, R.; Srivastava, H. C. Journal of Applied Polymer Science **1987**, 2, 455-477.
- [5] Ellison, M. S.; Fisher, L. D.; Alger, K. W.; Zeronian, S. H. Journal of Applied Polymer Science **1982**, 1, 247-257.
- [6] Saunders, E. M.; Zeronian, S. H. Journal of Applied Polymer Science **1982**, 11, 4477-4491.
- [7] Chen, W.; McCarthy, T. J. Macromolecules **1998**, 11, 3648-3655.
- [8] Bui, L. N.; Thompson, M.; McKeown, N. B.; Romaschin, A. D.; Kalman, P. G. Analyst **1993**, 5, 463-474.
- [9] Avny, Y.; Rebenfeld, L. Journal of Applied Polymer Science **1986**, 3, 4009-4025.
- [10] Fukai, R.; Dakwa, P. H. R.; Chen, W. Journal of Polymer Science Part A: Polymer Chemistry **2004**, 21, 5389-5400.
- [11] Hsieh, Y. L.; Chen, E. Y. Industrial & Engineering Chemistry Product Research and Development **1985**, 2, 246-252.
- [12] Strobel, M.; Walzak, M. J.; Hill, J. M.; Lin, A.; Karbasheski, E.; Lyons, C. S. Journal of Adhesion Science and Technology **1995**, 3, 365-383.
- [13] Hill, J. M.; Karbasheski, E.; Lin, A.; Strobel, M.; Walzak, M. J. Journal of Adhesion Science and Technology **1995**, 12, 1575-1591.

- [14] Walzak, M. J.; Flynn, S.; Foerch, R.; Hill, J. M.; Karbaszewski, E.; Lin, A.; Strobel, M. *Journal of Adhesion Science and Technology* **1995**, 9, 1229-1248.
- [15] Teare, D. O. H.; Ton-That, C.; Bradley, R. H. *Surface and Interface Analysis* **2000**, 4, 276-283.
- [16] Ton-That, C.; Teare, D. O. H.; Campbell, P. A.; Bradley, R. H. *Surf Sci* **1999**, 278-282.
- [17] Pochan, J. M.; Gerenser, L. J.; Elman, J. F. *Polymer* **1986**, 7, 1058-1062.
- [18] Strobel, M.; Lyons, C. S.; Strobel, J. M.; Kapaun, R. S. J. *Adhes. Sci. Technol.* **1992**, 4, 429-443.
- [19] Briggs, D.; Rance, D. G.; Kendall, C. R.; Blythe, A. R. *Polymer* **1980**, 8, 895-900.
- [20] Bertrand, P.; Depuydt, Y.; Beuken, J. M.; Lutgen, P.; Feyder, G. *Nucl. Instrum. Methods Phys. Res. Sect. B-Beam Interact. Mater. Atoms* **1987**, 887-890.
- [21] Arenholz, E.; Heitz, J.; Wagner, M.; Bauerle, D.; Hibst, H.; Hagemeyer, A. *Appl. Surf. Sci.* **1993**, 1-4, 16-19.
- [22] Desai, N. P.; Hubbell, J. A. *Biomaterials* **1991**, 2, 144-153.
- [23] Vig, J. R. *Journal of Vacuum Science & Technology A: Vacuum, Surfaces, and Films* **1985**, 3, 1027-1034.
- [24] Peeling, J.; Clark, D. T. J. *Polym. Sci. Pol. Chem.* **1983**, 7, 2047-2055.
- [25] Mathieson, I.; Bradley, R. H. *Int J Adhes* **1996**, 1, 29-31.
- [26] MacManus, L. F.; Walzak, M. J.; McIntyre, N. S. *Journal of Polymer Science Part A: Polymer Chemistry* **1999**, 14, 2489-2501.
- [27] Efimenko, K.; Crowe, J. A.; Manias, E.; Schwark, D. W.; Fischer, D. A.; Genzer, J. *Polymer* **2005**, 22, 9329-9341.
- [28] Stöhr, J. *NEXAFS spectroscopy*; Springer-Verlag: Berlin ; New York, **1992**; Vol. 25, pp 403.
- [29] Peeling, J.; Courval, G.; Jazzar, M. S. *Journal of Polymer Science: Polymer Chemistry Edition* **1984**, 419-428.

- [30] Briggs, D. J. Surface analysis of polymers by XPS and static SIMS; Cambridge University Press: Cambridge, U.K. ; New York, **1998**; , pp 198.
- [31] Windawi, H.; Ho, F. F. Applied electron spectroscopy for chemical analysis; Wiley: New York, **1982**; Vol. 64, pp 213.
- [32] Dwight, D. W.; Fabish, T. J.; Thomas, H. R.; American Chemical Society. Division of Organic Coatings and Plastics Chemistry; American Chemical Society. Division of Polymer Chemistry Photon, electron, and ion probes of polymer structure and properties; American Chemical Society: Washington, D.C., **1981**; Vol. 162, pp 442.
- [33] Ulman, A. Chem. Rev. **1996**, 4, 1533-1554.
- [34] Schreiber, F. Prog Surf Sci **2000**, 5-8, 151-256.
- [35] Genzer, J.; Efimenko, K.; Fischer, D. A. Langmuir **2002**, 24, 9307-9311.
- [36] Genzer, J.; Sivaniah, E.; Kramer, E. J.; Wang, J. G.; Korner, H.; Xiang, M. L.; Char, K.; Ober, C. K.; DeKoven, B. M.; Bubeck, R. A.; Chaudhury, M. K.; Sambasivan, S.; Fischer, D. A. Macromolecules **2000**, 5, 1882-1887.
- [37] Genzer, J.; Efimenko, K. Science **2000**, 5499, 2130-2133.

2.6. FIGURES

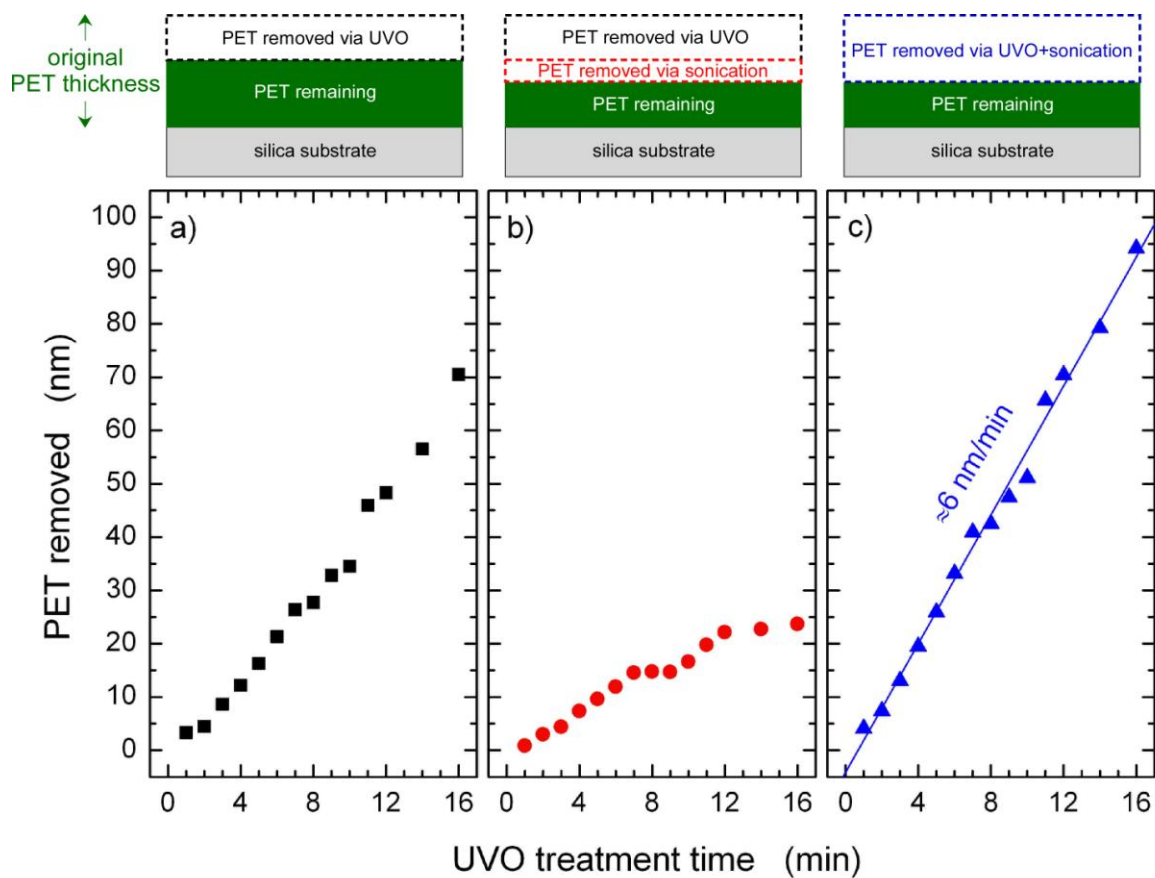


Figure 2.1. Thickness of PET at various stages of surface treatment. The original thickness decreases with increasing UVO treatment time (a) and decreases further after subsequent sonication (b). The total amount of PET removed from the sample is shown in (c).

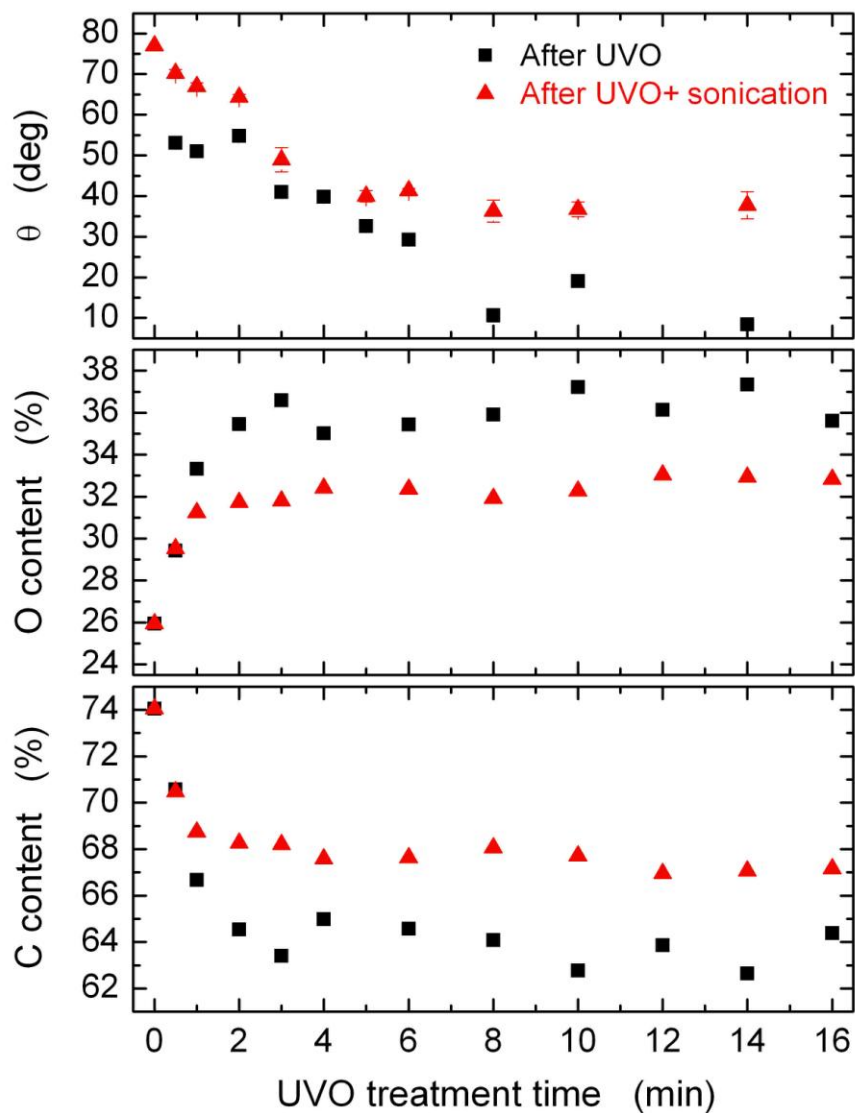


Figure 2.2. Static water contact angle (top), oxygen content (middle), and carbon content (bottom) as functions of UVO treatment time immediately after UVO treatment (black squares) and after UVO followed by sonication (red triangles). The contact angle was measured by the contact angle goniometer and the elemental compositions were determined by XPS.

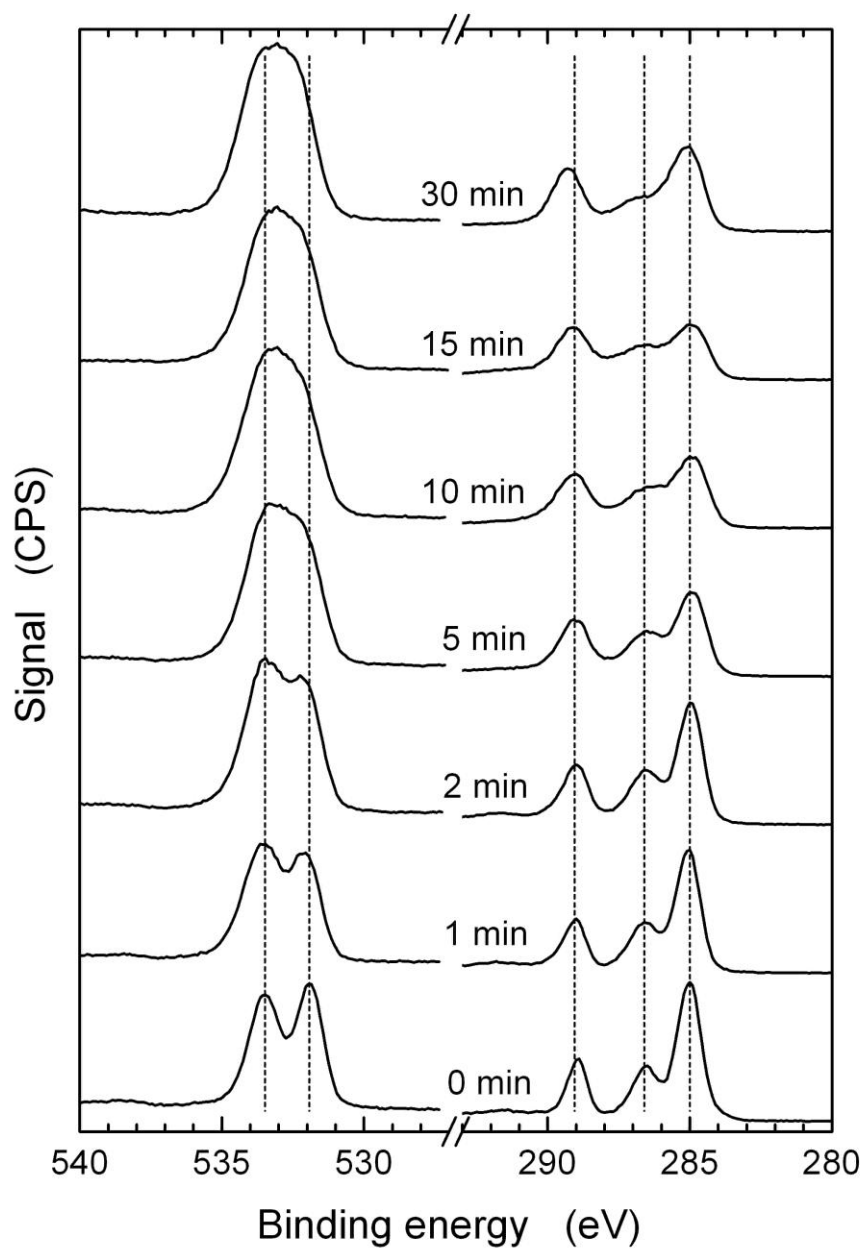


Figure 2.3. High resolution XPS spectra of PET samples in the oxygen (before break) and carbon (after break) treated with UVO for various times.

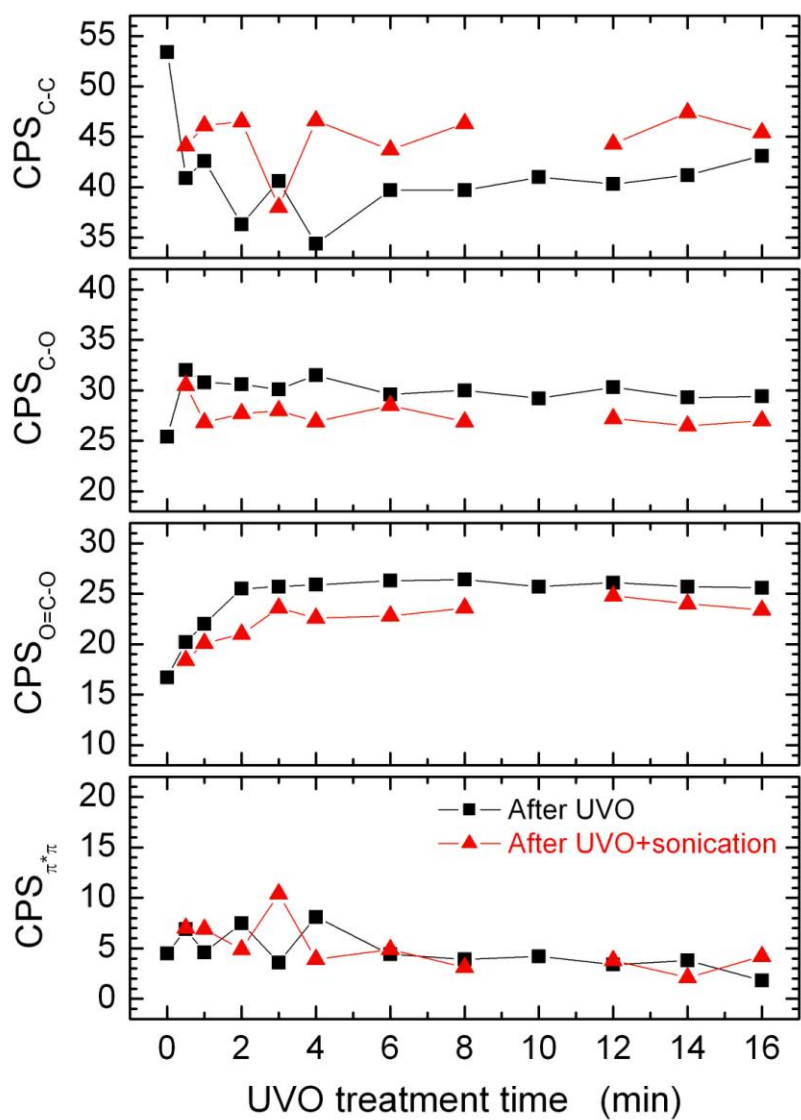


Figure 2. 4. Atomic percentages of various chemical functionalities present in the PET-UVO specimens, determined by XPS, as a function of the UVO treatment time before (black squares) and after (red triangles) sonication. The lines are meant to guide the eye.

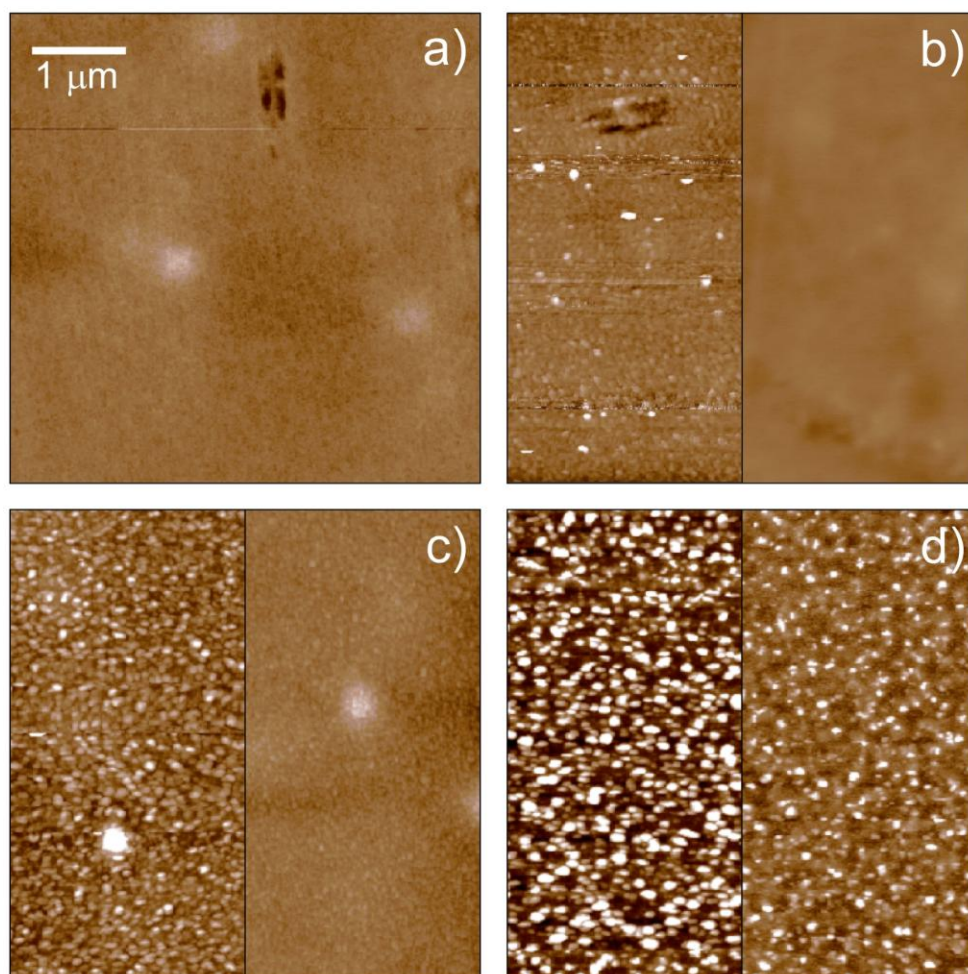


Figure 2.5. AFM images of PET surfaces treated with UVO for various times (in min): a) 0, b) 2, c) 8, and d) 30. The left and right panels in parts (b)-(d) correspond to the image taken from samples before and after sonication, respectively. The height scale z ranges from 0 (dark brown) to 30 nm (white).

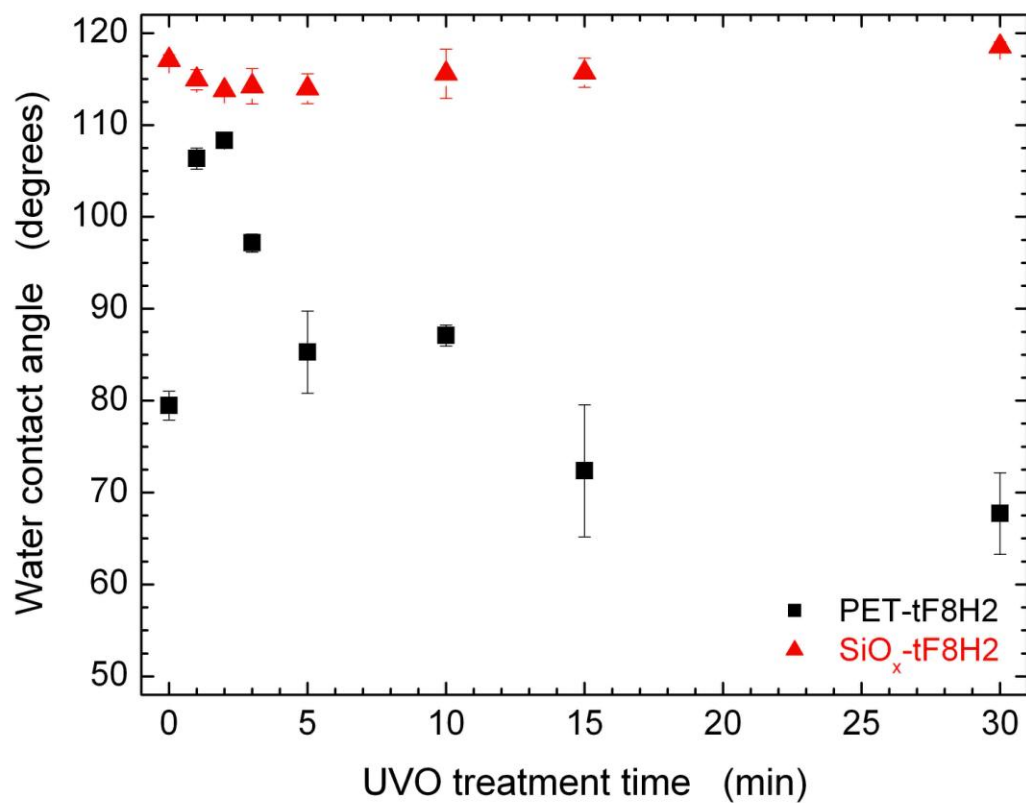


Figure 2.6. Water contact angles of PET-UVO/tF8H2 (squares) and SiO_x/tF8H2 (triangles) samples as function of UVO treatment time.

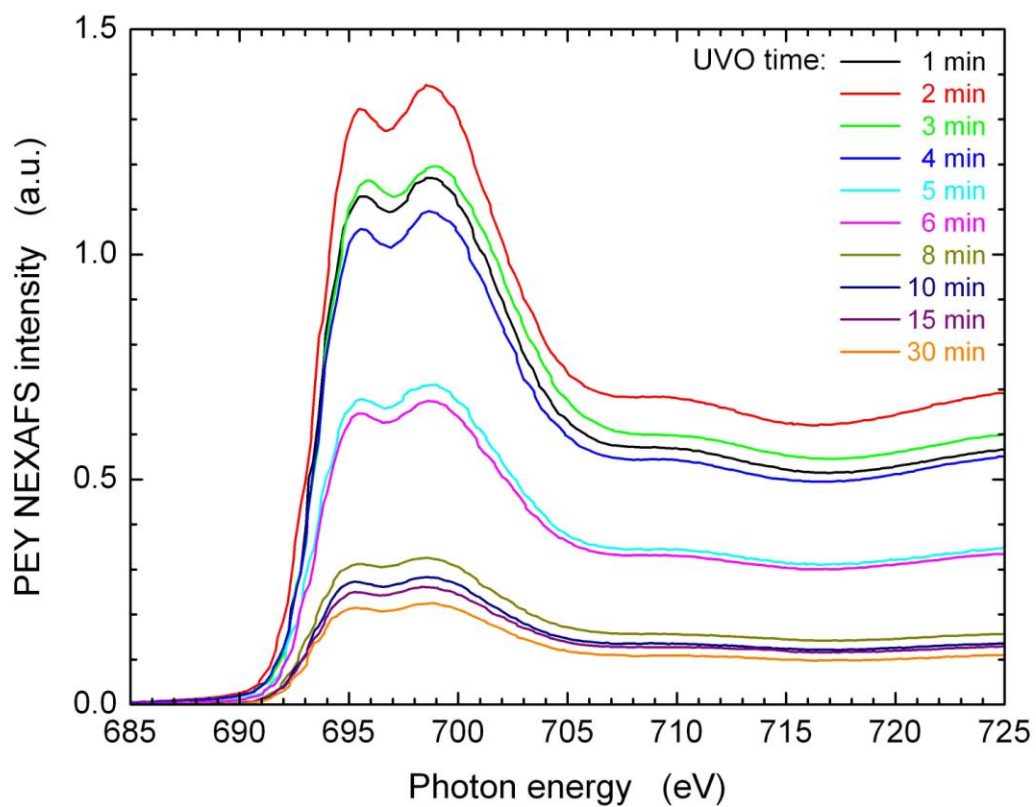


Figure 2.7. Fluorine K-edge PEY NEXAFS spectra collected from PET modified with UVO for various times ranging from 1 to 30 min and covered with tF8H2 SAM.

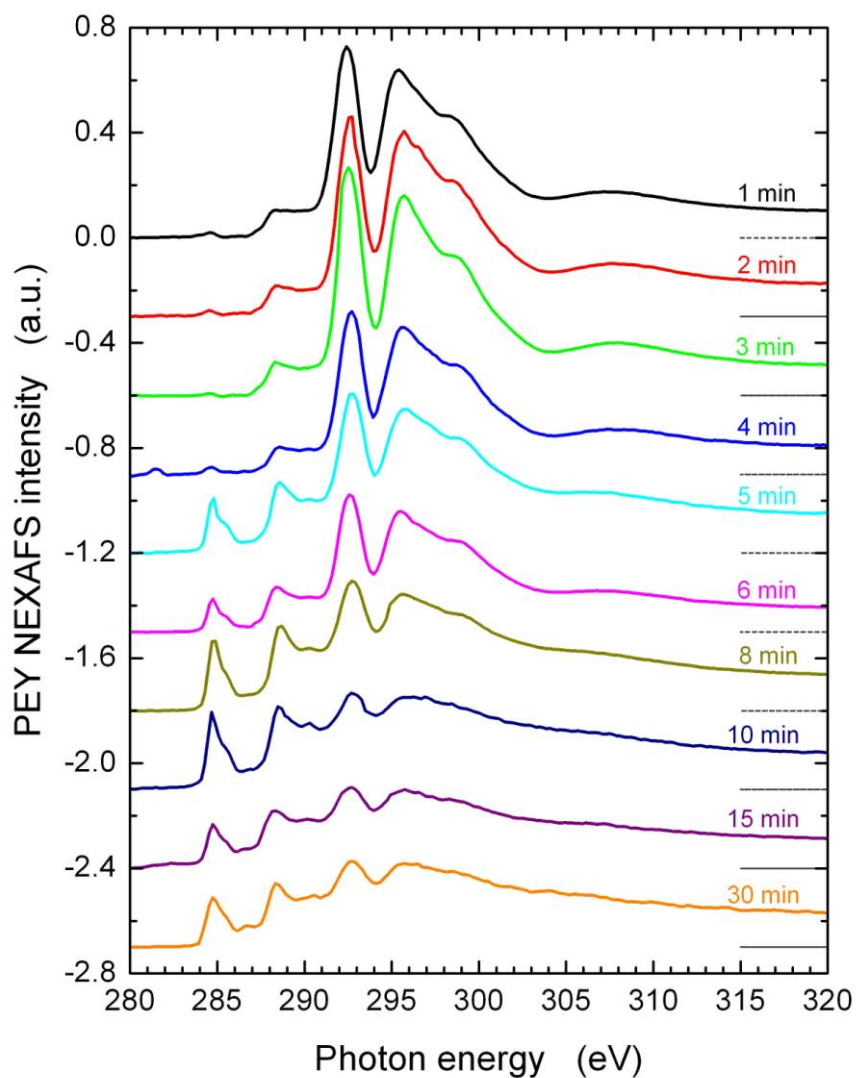


Figure 2.8. Carbon K-edge PEY NEXAFS spectra collected from PET modified with UVO for various times ranging from 1 to 30 min and covered with tF8H2 SAM. The PEY NEXAFS spectra for samples treated for UVO times longer than 1 min have been shifted vertically by 0.3 (with respect to the preceding spectrum) on a relative intensity scale. The dotted lines below each spectrum denote the PEY NEXAFS intensity corresponding to the pre-edge intensity signal for that spectrum.

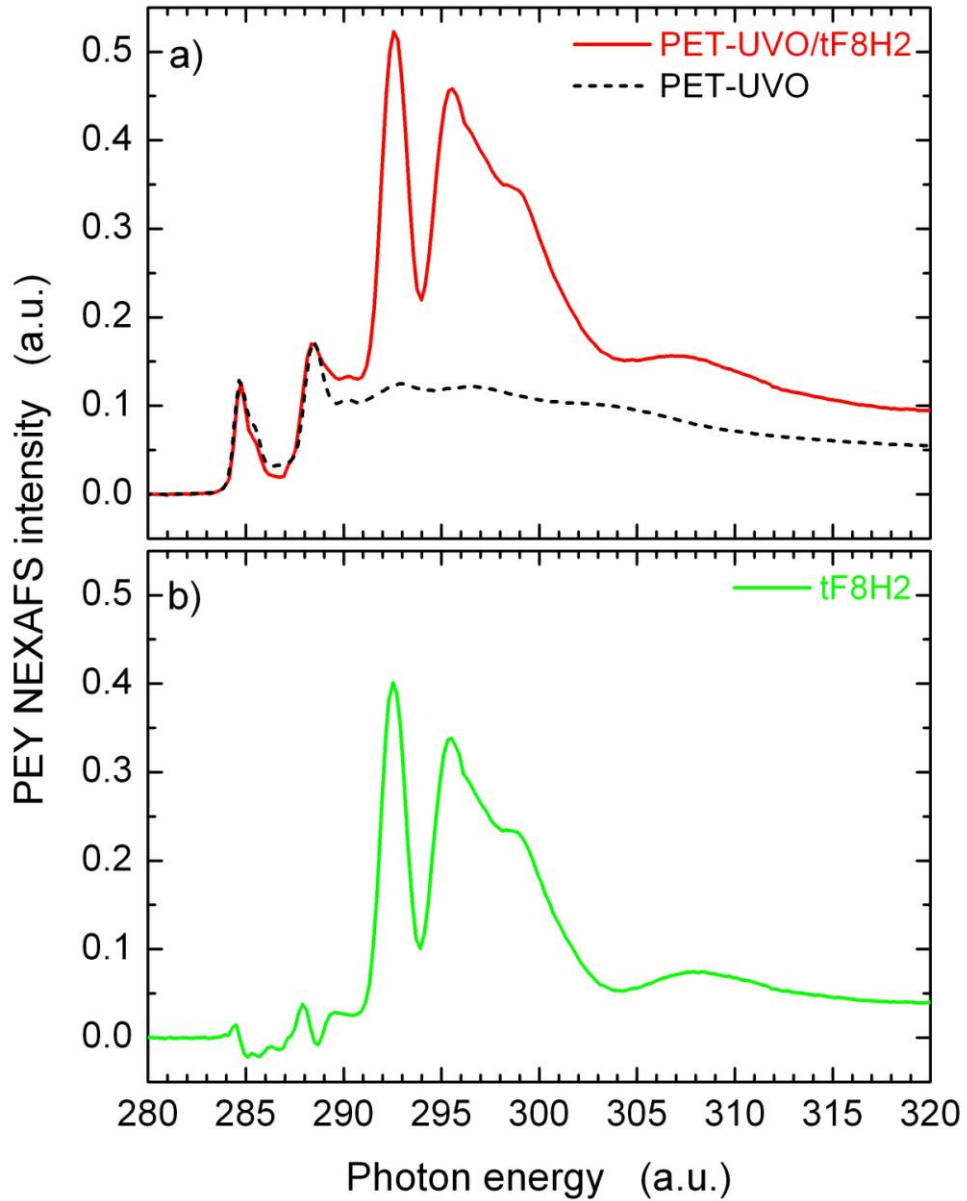


Figure 2.9. a) PEY NEXAFS spectrum from PET-UVO (black dashed line) and PET-UVO covered with tF8H2 SAM (red solid line). In both cases the UVO time was 6 min. b) Difference PEY NEXAFS intensity obtained by subtracting the PET-UVO spectrum (dashed line in part a) from the PET-UVO/tF8H2 spectrum (solid line in part a).

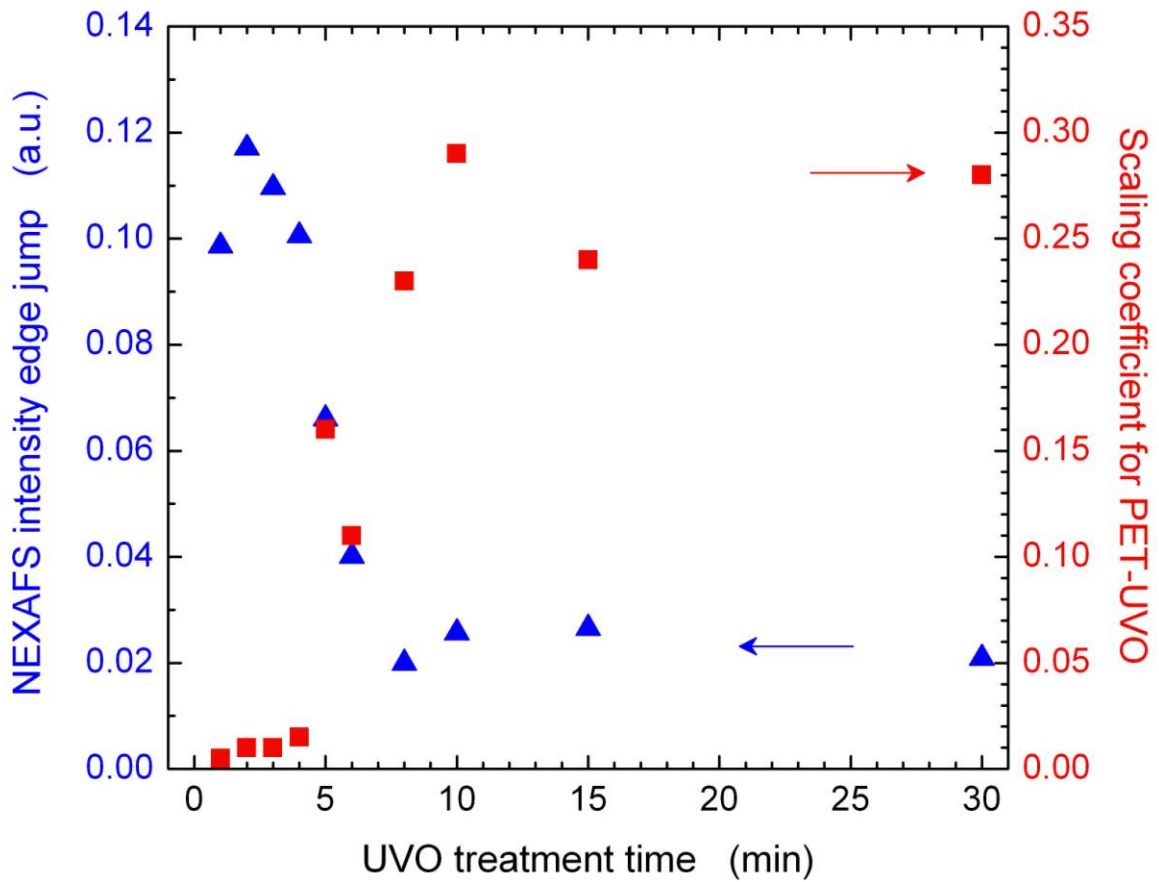


Figure 2.10. Edge-jump in PEY NEXAFS intensity from difference spectra (cf. Figure 9) determined at 320 eV as a function of UVO treatment time (blue triangles). Scaling coefficient (K) values as defined in the text as a function of UVO treatment time (red squares).

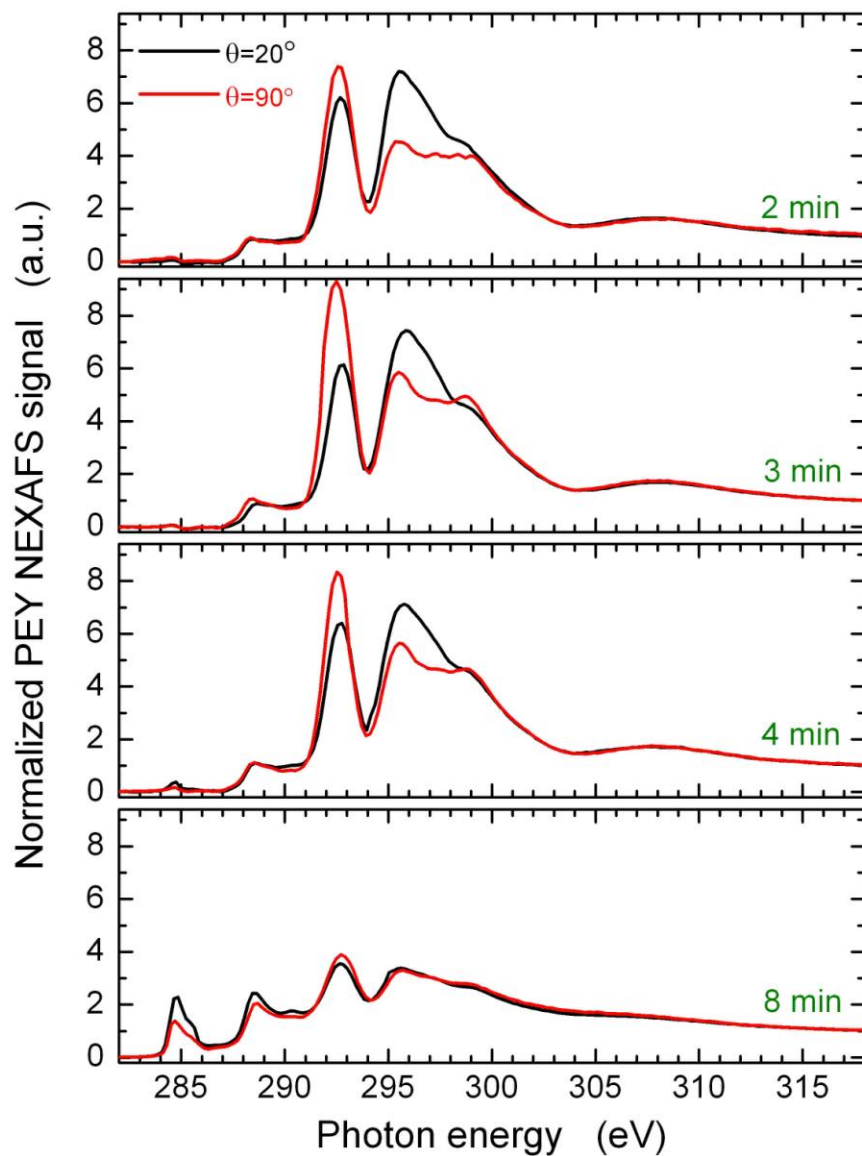


Figure 2.11. Normalized PEY NEXAFS spectra collected from PET-UVO/tF8H2 specimens at the carbon K-edge in two different sample orientations θ (defined as the angle between the surface normal and the electric vector of the incident x-ray beam): 20° (black) and 90° (red). The PET was treated with UVO for various times ranging from 2 (top) to 8 (bottom) min.

CHAPTER 3: MODIFICATION OF RECYCLED POLY(ETHYLENE TEREPHTHALATE) (RPET) FLAKES WITH POLYELECTROLYTES

3.1. INTRODUCTION

The chief aim of this study is to reduce the permeability of light gases, such as O₂ and CO₂, through recycled poly(ethylene terephthalate) (rPET) by incorporating nanoclay sheets in the rPET matrix. In the past, it has been shown^[1, 2] that the incorporation of inorganic fillers in a polymer matrix promotes a decrease of the permeability due to the tortuous path and solubility reduction introduced by the impermeable fillers. High-aspect-ratio layered silicates, such as nanoclays, constitute excellent candidates as nanoscale fillers because they measure a nanometer or so in thickness and micrometers in lateral dimensions. The tortuosity factor and, by inference, the barrier properties of a membrane increase when clay platelets in the polymer matrix are oriented with their short axis perpendicular to the film surface.^[2-6] The higher aspect ratio and “parallel” orientation of layered silicates increase the tortuosity factor as depicted schematically in Figure 3.1. In this simplistic representation, the extended residence time of a penetrating gas molecules spends within a region (due to boundary constraints^[1]) is not considered. Homogenous dispersion of nanometer-sized layered silicates within a polymer matrix results in formation of polymer-clay nanocomposites (PCNs), which tend to exhibit improved gas barrier properties, mechanical strength and heat distortion

temperature, as well as flame retardancy, without adversely affecting polymer transparency at small loading levels.^[7]

Layered silicates can be classified into 3 categories on the basis of their lamellar crystal structure: 1:1, 1:2 and 2:2 type. Type 1:1 has a crystal structure composed of one crystal sheet of silica tetrahedra combined with one crystal sheet of alumina octahedra. Type 2:1 possesses a crystal structure composed of 1 sheet of alumina octahedra sandwiched between 2 sheets of silica tetrahedras. Finally, type 2:2 adopts a crystal structure consisting of alternating crystal sheets of 2 silica tetrahedra and 2 alumina or 2 magnesium octahedra.^[8] Selected examples of these clay families are listed in Table 3.1. The 2:1 layered silicates (or phyllosilicates) are commonly used in the production of PCNs, and montmorillonite belongs to this family of materials.^[7] In this case, clay platelets measuring *ca.* 1 nm thick consist of 2 silica tetrahedron lattices and 1 alumina octahedron lattice, as schematically depicted in Figure 3.2.^[8-11] The lateral dimensions of montmorillonite sheets range from 30 nm to several microns,^[7] and platelets are held together by weak intermolecular forces.^[8-12] Isomorphic substitution can occur in both the silica tetrahedral and alumina octahedral lattices. In the octahedral lattices, Al^{3+} can be substituted with Mg^{2+} , Fe^{2+} or Zn^{2+} , whereas Si^{4+} can be substituted with Al^{3+} in the tetrahedral lattices. These substitutions result in negative charges on the clay surface, which are counterbalanced by alkali or alkaline earth cations in the interlayer space. In addition to negative charges on the clay surfaces, the clay edges are positively charged ($< \text{pH } 9$) due to broken bonds in the alumina octahedral and silica tetrahedral lattices. Clay edges resembles aluminum bauxite ($[\text{Al}(\text{OH})_3]$), which is

positively charged when the pH of the medium is below 9 and negatively charged when the pH is above 9.^[8] The cations originally residing between the clay platelets can be replaced by alkyl ammonium, phosphonium or imidazolium salts, which effectively act as surfactants and facilitate the mixing of clay platelets in a nonpolar polymer. Organic modification plays two major roles in the mixing process: 1) it increases the gallery spacing, which reduces the intermolecular forces between clay platelets; and 2) it increases the interactions between polymer molecules and organic modifiers, thereby facilitating dispersion.^[13]

Three different spatial arrangements of the silicate layers in the polymer matrix develop after processing,^[8] as portrayed in Figure 3.3. A phase-separated morphology or conventional (macro-)composite is obtained if the distance between silicate layers is unaffected by compounding. In this case, the properties of the final product may, in fact, be worse than the original resin.^[8] An intercalated morphology is obtained if individual extended polymer chains diffuse through the silicate layers and increase the interlayer distance without destroying the order of the silicate layers. Finally, the highly sought exfoliated morphology is achieved only when ordering of the silicate layers is largely eliminated, resulting in silicate layers that are individually and homogeneously dispersed within the polymer matrix.^[9, 10, 14] Improvements in barrier and mechanical properties are generally maximized with the latter level of dispersion. Dispersion of clays in a hydrophobic polymer matrix, such as PET, is problematic, however, due to unfavorable interactions between natural clay and the polymer matrix. The inherently hydrophobic nature of PET impedes the dispersion of clay when mixed together.

Early commercial efforts, such as the pioneering work conducted at Toyota, have relied on the organic modification of natural clays with quaternary alkyl ammonium salts to assist clay dispersion in polymer matrices.^[7, 9, 14-16] This option is not necessarily a viable solution in the case of PET because of the high processing temperature required for PET and the relatively low thermal stability of clay modifiers. In particular, the low thermal stability of organically-modified clays at the processing temperatures of PET accelerate PET degradation, which consequently prohibits the use of rPET/clay nanocomposites in "clean" applications, such as food packaging. The degradation of organically-modified clays, especially alkyl ammonium-modified clays, during melt compounding has been extensively studied.^[11, 13, 14, 17-23] The data provided in Figure 3.4 illustrates the thermal degradation behavior of three organically-modified clays, as well as natural montmorillonite, in an oxidative environment. Degradation of the organic modifiers will reduce, if not entirely preclude, interactions between the matrix and silicate layers and, in so doing, deteriorate the properties of the resultant composite.^[24] In addition, the degradation products of alkyl ammonium salts accelerate the degradation of some polymers, including PET,^[21, 22] polystyrene,^[14, 18-20] nylon-6,^[11, 13, 18, 23] and polypropylene.^[14] Since, the degradation products of alkyl ammonium groups may introduce serious health concerns (and thus may not warrant approval from the Food and Drug Administration for food applications), we intend to use Na⁺ montmorillonite (Na⁺ MMT) in this study.

To avoid the high-temperature problems associated with organically-modified clays, we have developed an alternative strategy that utilizes the surface chemical functionalities and

roughness created during caustic recycling as a platform onto which inexpensive, natural clay platelets dispersed in water can be attached to the rPET surface. The surface of the rPET is modified either through water-mediated adsorption of a polyelectrolyte or surface growth of a polymer brush, both of which serve to enhance attachment of natural clay platelets, as well as water-dispersed nanoparticles, to the altered rPET surface. We refer to this mechanism as a "molecular Lego[®]" approach: it uses the idea of connecting blocks by combining the surface properties and topology (i.e., increased hydrophilicity and area) of "sticky" rPET so as to attach inorganic species to the surface of rPET, which can subsequently be melt-processed into nanocomposites (illustrated in Figure 3.5). Because the inorganic species are dispersed and attached to rPET flakes in water, this step can be added as a unit operation into an existing process line. After the attachment of virtually single clay platelets to the rPET surface, drying and extrusion of the mixture is expected to yield exfoliated and oriented rPET/clay nanocomposites.

Specifically, we plan to attach the clay platelets onto "rough" rPET surfaces prior to extrusion. Success requires an understanding and control of the interactions between the polymer and clay platelets. Negative charges present on the surface of Na⁺ MMT platelets and positive charges along clay edges^[25] can be exploited to serve this binding purpose. Following the procedure of Pinnavaia^[26] and Kleinfeld^[27] (later verified by Hanley et al.^[28] using small-angle neutron scattering), we have endeavored to disperse smectic-type layered silicates as single platelets in water and utilize them in producing well-dispersed rPET/clay nanocomposites. Controlling the adhesion of clay on rPET surfaces is critical as it fixes the

number of adsorbed clay platelets and the interaction needed to securely bind individual clay platelets, which will further assist in delamination of clay stacks that may not be completely exfoliated during extrusion.

Most of the physical treatment methods currently employed to modify polymer surfaces (i.e., corona, ultraviolet/ozone and plasma treatment^[29]) are not well-suited to modify the irregular and topologically complex shapes of rPET flakes. Therefore, chemical modification techniques are utilized to achieve homogenous surface modification. As mentioned in Chapter 2, chemical surface modification can be performed via hydrolysis^[30-32], aminolysis^[33-35], reduction^[30, 35] and glycolysis.^[30] We intend to increase the electrostatic interactions between the rPET and clay surfaces by introducing positive charges on the surface of rPET. In this spirit, aminolysis seems to be the best route for solution-based modification of rPET surfaces. Since amine groups react readily with the ester functionality present on PET to yield amide groups, decorating PET with multifunctional amines may offer a simple, yet powerful, means of introducing free amine groups that can be positively charged in aqueous solutions with $\text{pH} < 7$. In addition, multifunctional and high-molecular-weight amines lower the extent of polymer degradation during aminolysis.^[33] Therefore, amine-containing polyelectrolytes are used as “macromolecular glue” for binding PET and negatively charged clay platelets. Kleinfeld et al.^[27] have been among the first groups to report the use of polydimethyldiallyl dimethylammonium chloride (PDDA) to prepare well-organized alternating layers comprising clay/polyelectrolyte stacks on a silicon wafer. Later, other efforts^[36-38] have employed the same approach to prepare polyelectrolyte/clay

multilayered composites. Successful adsorption of polyethyleneimine (PEI) on PET was demonstrated by Fukai and co-workers,^[34] who used the free amines introduced by the adsorption of PEI to graft aldehyde-terminated polyethylene oxide chains.

Two different routes have been investigated here to determine the effect of clay particles on the barrier properties of polymer membranes. For proof-of-concept purposes, high melting and low permeable PET has been substituted with a poly(dimethylsiloxane) (PDMS) elastomer and a linear low-density poly(ethylene-*co*-octene) (LLDPE) thermoplastic to demonstrate barrier property enhancement due to the incorporation of clay platelets. The PDMS elastomer possesses a high gas permeability, but its chemically cross-linked nature does not allow melt-processing of surface-modified films. Therefore, the low melting LLDPE copolymer is selected to permit multiple melt-processing steps without significant polymer degradation.

3.2. EXPERIMENTAL

3.2.1. MATERIALS

The rPET employed in this study was generously donated by the United Resource Recovery Corporation (Spartanburg, SC). Two grades of PEI with different molecular weights (25 and 60 kDa, denoted PEI25 and PEI60, respectively) were obtained from Scientific Polymer Products (Ontario, NY) and Sigma-Aldrich. *o*-Chlorophenol and a second

polyelectrolyte, poly(allylamine hydrochloride) (PAH) with a molecular weight of ≈ 15 kDa, were acquired from Sigma-Aldrich. Natural clay (Na^+ MMT) was supplied by Southern Clay Products (Gonzales, Texas). The LLDPE copolymer (EXACTTM 5062) with a melt flow index of 0.5 g per 10 min was kindly provided by ExxonMobil (Houston, TX), whereas the PDMS elastomer was generated from vinyl terminated PDMS chains (Gelest, Morrisville, PA) with a molecular weight of 49 kDa and cross-linked with tetrakis(dimethylsiloxy)silane at room temperature for 24 h and subsequent annealing at 70°C for 48 h for complete cross-linking.

3.2.2. THIN PET FILM PREPARATION

Thin rPET films were prepared by spin-coating rPET/*o*-chlorophenol solutions on silicon wafers. Specifically, rPET flakes were dissolved in *o*-chlorophenol at 80°C and a concentration of 1 wt% and subsequently spun-cast onto flat silica substrates that were previously rinsed with methanol and cleaned by exposure to ultraviolet/ozone (UVO). These films were used to monitor relative changes in film thickness and wettability after polyelectrolyte and clay adsorption as a function of polyelectrolyte adsorption time.

3.2.3. POLYELECTROLYTE AND CLAY ADSORPTION ON PET SURFACE

The two polyelectrolytes (PEI and PAH) were used to study the effect of polycation structure on wettability and clay adsorption as a function of polyelectrolyte adsorption time.

Polyelectrolyte solutions were prepared in deionized water at a concentration of 1% (w/v). Thin rPET films spun-cast on silicon wafers were immersed in each polyelectrolyte solution for predetermined periods of time. At the end of the deposition interval, the substrates were washed with copious amounts of deionized water and dried under nitrogen flow. Substrates modified with a polyelectrolyte were exposed to a suspension of 1 wt% Na⁺ MMT in deionized water for 1 h and then washed with deionized water to remove loosely adhered clay platelets prior to drying under nitrogen. Variations in layer thickness and wettability were determined by ellipsometry and water contact angle measurements, respectively, after both polyelectrolyte and clay adsorption. In addition, rPET flakes were soaked in a solution of PEI60 at a concentration of 1 wt% in deionized water for 2 h, followed by an agitated wash in deionized water to remove loosely adsorbed PEI chains. These PEI-modified rPET flakes were then exposed to a 1 wt% Na⁺ MMT suspension in deionized water for 1 h and repeatedly washed as above. The resultant MMT-modified rPET/PEI flakes (designated rPET/PEI/MMT) were dried under vacuum at 70°C. As a control, rPET flakes were immersed in a 1 wt% Na⁺ MMT suspension for 1 h, followed by washing, to determine the extent of clay adsorption in the absence of PEI (designated as rPET/MMT).

3.2.4. POLYELECTROLYTE AND CLAY ADSORPTION ON PDMS NETWORK AND POLY(ETHYLENE-OCTENE) SURFACE

The LLDPE and PDMS membranes were exposed to brief UVO treatment to increase surface wettability and introduce functional groups prior to polyelectrolyte deposition, thereby increasing the affinity between the polyelectrolyte and membrane surface. The

membranes were exposed to 3 and 10 min of UVO, respectively, at ambient temperature. At the end of UVO treatment, the membranes were immersed in an aqueous solution of PEI60 (1% wt in deionized water) for 15 min, washed with deionized water, immersed in a 1 wt % Na⁺ MMT suspension for 15 min, washed with deionized water, and finally dried at ambient temperature. The modified LLDPE membranes were cut into pieces and melt-pressed at 100°C. This process was repeated several times to form PCNs with clay platelets dispersed throughout the LLDPE matrix. The combined effects of clay modification and melt pressing on thermal stability and barrier properties were decoupled by adsorbing only PEI on LLDPE, followed by melt pressing. In addition, polyelectrolyte chains and clay platelets were sequentially adsorbed on the PDMS elastomer to form polyelectrolyte-mortared “nano-bricks” on the surface of the elastomer prior to permeability measurements.

3.2.5. ELLIPSOMETRY

The thickness of various films and layers deposited on silicon substrates was determined by variable-angle spectroscopic ellipsometry (VASE, J.A. Woollam Co.). Ellipsometry measures the difference in polarization state between incident light and light reflected from a surface, thereby providing information about the thickness and dielectric properties of thin films. Ellipsometric data were collected from at least three points on each substrate at an incidence angle of 70° with respect to the surface normal and at wavelengths ranging from 400 to 1100 nm in 10 nm increments.

3.2.6. WATER CONTACT-ANGLE MEASUREMENTS

Water contact-angle (WCA) experiments were performed via the sessile drop technique with deionized water (possessing a resistance of $>15 \text{ M}\Omega\text{-cm}$) using a Ramé-Hart contact-angle goniometer (Model 100-00) equipped with a CCD camera. Resultant data were analyzed with the Ramé-Hart Imaging 2001 software. The WCAs were determined after releasing an 8 mL droplet of deionized water on the surface. At least 4 different measurements were performed across the sample surface, and average WCA values were calculated with corresponding standard errors.

3.2.7. X-RAY PHOTOELECTRON SPECTROSCOPY

The surface chemical compositions of rPET flakes after polyelectrolyte and clay adsorption were determined by x-ray photoelectron spectroscopy (XPS) performed on a Kratos Axis Ultra DLD instrument with monochromated Al $K\alpha$ radiation with charge neutralization. Survey and high-resolution spectra were collected with pass energies of 80 and 20 eV, respectively, by using both electrostatic and magnetic lenses. Elemental chemical compositions were calculated from spectral regression using the Vision software.

3.2.8. MELT PROCESSING OF RPET FLAKES

The rPET, rPET/PEI, rPET/PEI/MMT and rPET/MMT flakes were dried under vacuum at 70°C for more than 24 h prior to extrusion. The 19 mm single-screw extruder (Wayne

Machine & Die Co.) with a length:diameter ratio of 30:1 was equipped with a Saxton mixing section at its end. Samples were extruded at 30 and 75 rpm through the bore maintained at a temperature profile (in °C) of 265/270/275/280 and 275/280/285/290. The adapter and die temperatures were held constant at 280 and 290°C, respectively.

3.2.9. MELT RHEOLOGY

Discs for rheology were melt-pressed at 275°C in circular molds with a diameter and thickness of 25 and 1 mm, respectively. Once pressed, the molds were quenched between large aluminum blocks. Steady shear experiments using parallel plates were conducted on an Advanced Rheometric Expansion System (ARES) from TA Instruments. Tests were performed in strain-controlled mode at strain rates ranging from 2 to 50 s⁻¹ at 280 °C in air.

3.2.10. FOURIER TRANSFORM INFRARED SPECTROSCOPY

Fourier-transform infrared (FTIR) spectroscopy was conducted in attenuated total reflection (ATR) mode to monitor the chemical changes that took place in the polymer after extrusion of the rPET flakes. Spectra were recorded on a Nicolet 6700 spectrometer equipped with a Ge crystal, and the data were analyzed by the Omnic software suite. For each sample, 256 scans were acquired after collection of the background at a resolution of 4 cm⁻¹.

3.2.11. ATOMIC FORCE MICROSCOPY

The surface topography of rPET flakes was examined using a Digital Instruments Nanoscope-4 atomic force microscope (AFM) operated in non-contact mode. Specimens were mounted to sample disks to ensure immobilization during imaging. The root-mean-square (rms) surface roughness was calculated from height images.

3.2.12. GAS PERMEATION

Nielsen^[39] expressed the tortuosity factor (τ) as the ratio of the actual distance that a permeant travels (d') to the shortest distance that it would travel in the absence of a tortuous path (d), viz.,

$$\tau = \frac{d'}{d} = 1 + \frac{L}{2W}\phi_f \quad (3.1)$$

where L is the flake length, W is the flake thickness and ϕ_f denotes the volume fraction of filler. It can thus be shown that tortuosity affects permeation according to

$$\frac{P_c}{P_p} = \frac{\phi_p}{1 + (L/2W)\phi_f} \quad (3.2)$$

where P_c and P_p represent the permeabilities of the composite and unfilled polymer, respectively, and ϕ_p is the volume fraction of polymer ($= 1 - \phi_f$). Equations (1.1) and (1.2) reveal that the permeation of the gas molecules in a polymer nanocomposite depends on the size, geometry, and spatial orientation of the platelets in the polymer matrix.^[2, 40]

Gas permeation measurements were performed using the constant-volume/variable-pressure technique.^[39, 41] Polymeric membranes of thickness l were sandwiched between 2 pieces of Al tape that have openings of known area (A) for gas to undergo transport through the membrane. After pulling vacuum on both sides of the membrane, gas was introduced at a predetermined pressure from the upstream side of the membrane. Gas permeated through the membrane and into the vessel of known volume (V) on the downstream side. The downstream pressure was recorded and the permeability (P) was calculated from

$$P = \frac{Vl}{ART\Delta p} \left(\frac{dp}{dt} \right) \quad (3.3)$$

where R is the universal gas constant, T denotes absolute temperature, Δp is the difference between upstream and downstream pressures, and dp/dt is the steady rate at which the pressure increases on the downstream side. The permeabilities of O_2 and CO_2 were measured at $23^\circ C$ and an upstream pressure of 2 atm.

3.2.12. THERMOGRAVIMETRIC ANALYSIS

Thermogravimetric analysis (TGA) was performed using a TA Instruments Q500 unit operated under an air atmosphere. Samples were heated from 25 to $900^\circ C$ in Pt pans at a heating rate of $10^\circ C/min$. The amount of clay in a given clay-modified LLDPE membrane was determined after complete thermo-oxidative degradation of the organic matrix. In addition, the onset degradation temperature corresponding to the temperature where the sample reached 95 wt% of its initial weight was also ascertained.

3.3. RESULTS AND DISCUSSION

Caustic recycling results in a significant increase in the surface area/roughness of rPET due to the difference in etching (degradation) rates of crystalline and amorphous regions of PET flakes. The effect of this recycling process on the surface roughness of rPET is readily shown by AFM. To discern a relative change in roughness, AFM height scans have been collected from a single rPET flake, as well as the inner side of a soft drink bottle, which is the precursor to rPET. Although the roughness of rPET flakes is expected to vary due to the stochastic nature of chemical etching, the rms roughness of PET increases substantially (from ≈ 10 to ≈ 170 nm) upon recycling, as seen in the images provided in Figure 3.6. It is evident from these images that the roughness of the rPET surface has increased markedly due to recycling. This increase in surface roughness provides a larger surface area available for clay platelet attachment, which, in turn, permits control over the clay loading via the clay coverage on the rPET surface before extrusion. In addition, caustic recycling introduces functional groups, such as $-\text{COOH}$ and $-\text{OH}$, on the surface of rPET flakes.^[30, 31, 42] The presence of these polar groups serves to enhance the attraction of polyelectrolyte chains to the rPET surface, which facilitates subsequent attachment of clay platelets.

Polyelectrolyte adsorption has been performed with two amine-containing polycations: PEI and PAH. The former is a highly branched polymer that contains 25% primary, 50% secondary and 25% tertiary amine moieties,^[43] whereas the latter is a linear polymer that consists exclusively of pendant primary amine groups. Since the addition of PEI or PAH into a clay suspension may result in gel formation,^[44] we first adsorb the polycation chains

directly onto rPET, rinse away excess polycation and then attach the clay particles from a water suspension in a subsequent step. The second step eliminates deposition of multilayered clay platelets and excess polycation on the rPET surface, which may be problematic during extrusion since free amines may degrade or react further with the ester bonds of PET. Thin rPET films spun-cast on silicon wafer are used as model substrates to monitor changes in wettability and thickness after polycation and clay platelet adsorption, as depicted in Figure 3.7. The WCA value of bare rPET on silicon wafer is measured as $71.6 \pm 0.4^\circ$ in Figure 3.8a, which is in good agreement with reported values.^[29] The wettability of the rPET/PAH film does not change significantly as a result of polycation adsorption, as its WCA is $\approx 66^\circ$ independent of deposition time. However, the WCA values of rPET/PEI25 and rPET/PEI60 are observed to level off at $\approx 50^\circ$ after 2 h of adsorption (and do not change appreciably up to 14 h). Although clay platelet adsorption on bare rPET does not profoundly affect the WCA value measured as $67.2 \pm 0.6^\circ$ in Figure 3.8b, adsorption of clay platelets on polycation-treated rPET suppresses the WCA to 28.7 ± 0.6 , 30.2 ± 1.4 and $40.9 \pm 0.9^\circ$ for rPET/PEI60/MMT, rPET/PEI25/MMT and rPET/PAH/MMT substrates, respectively. It is interesting to recognize here that the polycation adsorption time does not play an important role on the measured WCA.

The thickness of adsorbed polycation chains and clay platelets on thin rPET films has been measured by VASE, and the results are summarized in Figure 3.9. The polyelectrolyte layers consistently measure below 1 nm for all the polycations studied in Figure 3.9a, and this thickness does not change noticeably with adsorption time over the time interval

examined (14 h). In Figure 3.9b, the thickness of the adsorbed clay layer on PEI-modified rPET is likewise seen to be almost constant, within experimental uncertainty, at ≈ 3 nm for both grades of PEI. This effectively corresponds to two Na^+ MMT platelets stacked together. In the case of the rPET/PAH film, the thickness of the clay layer is closer to ≈ 2 nm, which amounts to 1-2 Na^+ MMT platelets. This slight, but apparent, difference in clay adsorption is attributed to the linear nature of the PAH chains: the more hydrophilic primary amine groups orient towards the rPET surface, thereby leaving a more hydrophobic PAH backbone exposed at the film/air interface and limiting the attachment of clay platelets on PAH-modified rPET flakes. Since the highly branched PEI chains have unbound primary, secondary and tertiary amines oriented towards the film/air interface, these moieties are able to interact more extensively with clay platelets in aqueous suspension and bind them more effectively to the PEI-modified rPET surface. The results displayed in Figure 3.9b are consistent with those presented in Figure 3.8b in that the wettability of PEI/MMT-adsorbed rPET thin films is greater than that of PAH/MMT-adsorbed rPET films. For this reason, only PEI60 is considered further as the preferred means by which to modify the surface of rPET.

The surface chemical composition of rPET, rPET/MMT, rPET/PEI60 and rPET/PEI60/MMT has been measured by XPS. The rPET flakes analyzed 1 month after recycling possess a surface oxygen concentration of $22.9 \pm 1.7\%$ (cf. Figure 3.10a), which is lower than the theoretical value of PET (28.6%).^[29] Plausible reasons for this mismatch may be due to carbon contamination of the rPET surface or surface segregation of lower surface energy carbonaceous species within rPET. To discern the origin of this difference, virgin

Mylar is selected for comparison, since it is known to possess oxygen-rich species on its surface. The surface oxygen concentration of 22.5% is in excellent agreement with that of rPET, suggesting that the two materials may have comparable surface chemistries. It immediately follows that the surface oxygen concentration and, by inference, hydrophilicity of PET increase after recycling. Adsorption of PEI60 on rPET flakes introduces a small nitrogen peak corresponding to $5.4 \pm 0.5\%$ located at ≈ 400 eV. In addition, the surface oxygen concentration decreases further to $18.4 \pm 0.7\%$ (cf. Figure 3.10b) after PEI60 attachment due to the ≈ 1 nm polyelectrolyte layer adsorbed on rPET. Recall that PEI60 does not possess oxygen in its chemical structure.

Immersion of unmodified rPET flakes into a Na^+ MMT suspension results in adsorption of clay platelets, but the net population of attached platelets is low, as evidenced from the surface silicon concentration measured by XPS. According to Figure 3.11a, the concentration of silicon that originates from clay is $1.1 \pm 0.2\%$, thereby confirming almost negligible adsorption of clay platelets on the unmodified rPET surface. The population of attached platelets increases by an order of magnitude after introducing “sticky” PEI60 groups on the surface of rPET. As alluded to earlier, the adsorbed PEI60 layer acts as a “molecular adhesive” for the clay platelets, in which case the atomic concentration of silicon on the rPET/PEI60 surface reaches $12.1 \pm 0.8\%$. The accompanying increase in surface oxygen concentration to $51.0 \pm 3.0\%$ relative to rPET/PEI60 also confirms the presence of inorganic silicates on the surface. Lastly, the existence of a small, yet discernible, sodium peak located at 1070 eV reflects the presence of sodium atoms in the interlayer spacing of stacked Na^+

MMT clay sheets. The thickness of these clay stacks on rPET/PEI60 can be presumed to be less than ≈ 10 nm, in agreement with results from VASE (cf. Figure 3.9b) due to detection of attenuated carbon ($32.4 \pm 3.9\%$) and nitrogen ($3.0 \pm 0.4\%$) peaks that originate from the underlying rPET/PEI60 substrate.

The rPET, rPET/PEI60, rPET/MMT, and rPET/PEI60/MMT flakes have all been melt-processed using a single-screw extruder operated at die temperatures of 280 and 290°C at 30 rpm. Circular discs of non-extruded materials and extrudates have been prepared for analysis by melt rheology to determine the zero-shear viscosity (η_0), which provides a relative measure of polymer molecular weight. Viscosities measured up to shear rates of 50 s^{-1} show little, if any, dependence on shear rate and thus exhibit the Newtonian behavior required for evaluation of η_0 . Values of η_0 for rPET are $\approx 43.7 \text{ Pa}\cdot\text{s}$ before extrusion and $\approx 20.4 \text{ Pa}\cdot\text{s}$ after extrusion, yielding a 50% decrease in η_0 that translates into a reduction in rPET molecular weight due to degradation during extrusion. For comparison, values of η_0 measured from virgin PET decrease from 24.1 to 15.3 Pa·s (a 37% reduction) under identical extrusion conditions. The more pronounced change in η_0 for rPET is attributed to its recycling-induced functionalized surface, which can help to promote molecular degradation at elevated temperatures. Attachment of Na^+ MMT clay platelets on rPET flakes results in an increase in η_0 to $\approx 56.4 \text{ Pa}\cdot\text{s}$ although corresponding XPS spectra indicate relatively small amounts of adsorbed clay. The value of η_0 for PEI60-modified rPET flakes is $\approx 32.8 \text{ Pa}\cdot\text{s}$, which increases to $\approx 37.6 \text{ Pa}\cdot\text{s}$ after Na^+ MMT adsorption. These modest increases in η_0 upon incorporation of clay platelets are expected on the basis of reports from previous studies.^[45]

Representative FTIR spectra of virgin PET and rPET prior to surface modification and extrusion are shown in Figure 3.12 and appear indistinguishable. The peaks located at 1270, 1120 and 1100 cm^{-1} correspond to the ether groups of PET, whereas the peak at 745 cm^{-1} corresponds to main-chain phenyl ring. Degradation of PET during extrusion will most likely occur at the ether linkages, in which case a reduction in the intensity of the ether peak can be sensibly expected. The integrated area under the peaks at 1270 and 745 cm^{-1} have been calculated and their ratios are included in the inset of Figure 3.12 for rPET, rPET/PEI60 and rPET/PEI60/MMT flakes before and after extrusion. On the basis of these FTIR peak ratios, we can conclude that the presence of either PEI60 or Na^+ MMT does not contribute to the thermal degradation of rPET during extrusion.

The high melting temperature of PET causes catastrophic degradation of many other, especially highly functional, polymers, including the PEI60 polyelectrolyte employed here. For this reason, we have substituted a PDMS elastomer and LLDPE thermoplastic for PET to ascertain the effect of adsorbed clay platelets on gas barrier properties. In the former case, a highly permeable PDMS elastomer film serves as the substrate for a surface wall composed of Na^+ MMT clay platelets held together with PEI60 as “nano-bricks.” This surface structure remains intact during analysis due to the non-processable nature of chemically cross-linked PDMS. The corresponding O_2 and CO_2 permeabilities measured through specimens with different numbers of sequential PEI60/MMT surface layers decreases by ≈ 86 and $\approx 89\%$ after 17 such layers, as evidenced in Figure 3.13. In the latter case with LLDPE, PCNs have been prepared by first modifying the surface with PEI60, followed by Na^+ MMT platelet

adsorption. In stark contrast to the PDMS specimens, these surface-modified materials have been melt-pressed multiple times to disperse the nearly exfoliated clay throughout the polymer matrix. On one hand, the clay loading within the LLDPE matrix increases with an increase in the number of PEI60/MMT adsorption cycles, as determined by TGA analysis. The concentration of clay increases steadily to $\approx 1.6\%$ after 25 cycles, according to Figure 3.14. On the other hand, the inorganic residue from control LLDPE membranes treated only with PEI does not differ appreciably from 0.1 wt%, which corresponds to the carbonaceous ash remaining after pyrolysis.

The O_2 and CO_2 permeabilities measured through LLDPE PCNs prepared via our “molecular Lego[®]” approach are provided in Figure 3.15. The O_2 permeability of the LLDPE systems decreases from 19.9 to 16.4 Barrers after clay platelet adsorption and melt pressing 25 times. Likewise, the CO_2 permeability drops from 42.2 to 30.9 Barrers under identical fabrication conditions. These results can be compared with permeabilities calculated from the Nielsen model (Equation 3.2) for clay platelets varying in length from 50 to 200 nm (cf. Figure 3.16). The trends of the measured permeabilities agree reasonably well with model calculations for 50 and 100 nm platelets, but significant discrepancy exists between the experimental values and model calculations for platelets with a length of 200 nm. This disagreement may be due to the orientation of the clay platelets and/or the presence of clay stacks in the polymer matrix. As discussed earlier in this chapter, the thickness of clay layers adsorbed on the surface of PEI60-treated rPET is $\approx 3\text{-}4$ nm, which corresponds to ≈ 2 stacked platelets.

In the case of PEI60-modified LLDPE, Figure 3.15 reveals that the presence of the polyelectrolyte has little influence on gas permeability at low cycle numbers. At high cycle numbers, the presence of PEI promotes increases in both O₂ and CO₂ permeability, possibly due to degradation. Evidence of such degradation cannot, however, be gleaned from the FTIR spectrum displayed in Figure 3.17 nor the onset degradation temperature determined from TGA in Figure 3.18. In contrast, the presence of clay platelets in the LLDPE matrix promotes a clearly discernible increase in the heat stability of this PCN. In this case, the onset degradation temperatures increase from ca. 335 to 355°C, which can be explained by an increasingly more uniform dispersion of clay platelets throughout the polymer matrix.

3.4. CONCLUSIONS

The high aspect ratio and nanoscale thickness of clay platelets make these materials ideal candidates by which to improve the barrier properties of polymeric membranes. Absorption of water in the interlayer of stacked layers of natural clay exerts hydrostatic pressure that causes an increase in the interlayer spacing and subsequent exfoliation of clay platelets. Due to the hydrophobic nature of most polymers, such clays are routinely modified to promote hydrophobicity and facilitate dispersion of clay platelets within a polymer matrix. Since the organic species used to modify clay possess a low thermal stability at the high processing temperature required for PET, an alternative route has been developed to prepare rPET/clay nanocomposites wherein exfoliated clay platelets are attached to the surface of rPET via a

molecular Lego[®] approach. Un-PET recycling increases the surface roughness of PET due to processing in caustic solution. The increase in surface roughness increases the available surface area for clay platelet attachment and introduces functional groups on the surface of rPET. Adsorption experiments reveal that thin layers of linear and branched polycations adsorb on rPET and promote subsequent adsorption of Na⁺ MMT clay platelets in 1-2 stacks. The efficacy of the polycation in this regard depends on its ability to interact with rPET and maintain the accessibility of hydrophilic groups at the film/air. Surface concentrations measured by XPS are consistent with results obtained by ellipsometry and water contact-angle analysis. Specifically, decoration of the modified rPET surface with clay platelets results in the appearance of silicon and sodium peaks, which correspond to Na⁺ MMT layers. Extrusion of these materials yields nanocomposites with fully exfoliated clay platelets, but the molecular weight of the extruded rPET decreases slightly due to degradation. Due to the inherently low permeability of PET, substitution of rPET with more highly permeable PDMS and LLDPE facilitates examination of corresponding O₂ and CO₂ permeability upon surface modification. The barrier performance of PDMS elastomers improves considerably after sequentially building an impermeable clay/polyelectrolyte surface layer on the surface of PDMS. In addition, the formation of PCNs by modifying the surface of LLDPE, followed by progressive melt-mixing, likewise demonstrate a reduction in gas permeability, in favorable agreement with predictions from the Nielsen model. The presence of clay platelets in LLDPE furthermore serves to improve the thermal stability of LLDPE, as determined by TGA experiments.

3.5. REFERENCES

- [1] M. A. Osman, V. Mittal, H. R. Lusti, *Macromolecular Rapid Communications* **2004**, 25, 1145.
- [2] K. Yano, A. Usuki, A. Okada, T. Kurauchi, O. Kamigaito, *Journal of Polymer Science Part A: Polymer Chemistry* **1993**, 31, 2493.
- [3] J.-H. Lee, D. Jung, C.-E. Hong, K. Y. Rhee, S. G. Advani, *Composites Science and Technology* **2005**, 65, 1996.
- [4] Z. Ke, B. Yongping, *Materials Letters* **2005**, 59, 3348.
- [5] D. J. Sekelick, E. V. Stepanov, S. Nazarenko, D. Schiraldi, A. Hiltner, E. Baer, *Journal of Polymer Science Part B: Polymer Physics* **1999**, 37, 847.
- [6] B. Xu, Q. Zheng, Y. H. Song, Y. Shanguan, *Polymer* **2006**, 47, 2904.
- [7] S. S. Ray, M. Okamoto, *Progress in Polymer Science* **2003**, 28, 1539.
- [8] Y. C. Ke, P. Stroeve, *Polymer-Layered Silicate and Silica Nanocomposites*, Elsevier, Amsterdam **2005**.
- [9] E. P. Giannelis, *Advanced Materials* **1996**, 8, 29.
- [10] E. P. Giannelis, R. Krishnamoorti, E. Manias, *Polymer-Silicate Nanocomposites: Model Systems for Confined Polymers and Polymer Brushes*, **1999**.
- [11] D. L. VanderHart, A. Asano, J. W. Gilman, *Macromolecules* **2001**, 34, 3819.
- [12] R. A. Vaia, H. Ishii, E. P. Giannelis, *Chemistry of Materials* **1993**, 5, 1694.
- [13] D. L. VanderHart, A. Asano, J. W. Gilman, *Chemistry of Materials* **2001**, 13, 3796.
- [14] J. W. Gilman, C. L. Jackson, A. B. Morgan, R. Harris, E. Manias, E. P. Giannelis, M. Wuthenow, D. Hilton, S. H. Phillips, *Chemistry of Materials* **2000**, 12, 1866.
- [15] A. Okada, A. Usuki, *Macromolecular Materials and Engineering* **2006**, 291, 1449.

- [16] C. E. Powell, G. W. Beall, *Current Opinion in Solid State and Materials Science* **2006**, *10*, 73.
- [17] W. Xie, Z. Gao, W. P. Pan, D. Hunter, A. Singh, R. A. Vaia, *Chemistry of Materials* **2001**, *13*, 2979.
- [18] J. W. Gilman, W. H. Awad, R. D. Davis, J. Shields, R. H. Harris, C. Davis, A. B. Morgan, T. E. Sutto, J. Callahan, P. C. Trulove, H. C. DeLong, *Chemistry of Materials* **2002**, *14*, 3776.
- [19] J. Zhu, F. M. Uhl, A. B. Morgan, C. A. Wilkie, *Chemistry of Materials* **2001**, *13*, 4649.
- [20] J. Zhu, A. B. Morgan, F. J. Lamelas, C. A. Wilkie, *Chemistry of Materials* **2001**, *13*, 3774.
- [21] J. H. Chang, S. J. Kim, *Polymer Bulletin* **2004**, *52*, 289.
- [22] C. H. Davis, L. J. Mathias, J. W. Gilman, D. A. Schiraldi, J. R. Shields, P. Trulove, T. E. Sutto, H. C. DeLong, *Journal of Polymer Science Part B: Polymer Physics* **2002**, *40*, 2661.
- [23] R. D. Davis, J. W. Gilman, D. L. VanderHart, *Polymer Degradation and Stability* **2003**, *79*, 111.
- [24] J. H. Chang, S. J. Kim, Y. L. Joo, S. Im, *Polymer* **2004**, *45*, 919.
- [25] Y. Ke, C. Long, Z. Qi, *Journal of Applied Polymer Science* **1999**, *71*, 1139.
- [26] T. J. Pinnavaia, *Science* **1983**, *220*, 365.
- [27] E. R. Kleinfeld, G. S. Ferguson, *Science* **1994**, *265*, 370.
- [28] H. J. M. Hanley, C. D. Muzny, D. L. Ho, C. J. Glinka, E. Manias, *International Journal of Thermophysics* **2001**, *22*, 1435.
- [29] A. E. Ozcam, K. Efimenko, C. Jaye, R. J. Spontak, D. A. Fischer, J. Genzer, *Journal of Electron Spectroscopy and Related Phenomena* **2009**, *172*, 95.
- [30] W. Chen, T. J. McCarthy, *Macromolecules* **1998**, *31*, 3648.
- [31] M. S. Ellison, L. D. Fisher, K. W. Alger, S. H. Zeronian, *Journal of Applied Polymer Science* **1982**, *27*, 247.

- [32] J. Dave, R. Kumar, H. C. Srivastava, *Journal of Applied Polymer Science* **1987**, *33*, 455.
- [33] Y. Avny, L. Rebenfeld, *Journal of Applied Polymer Science* **1986**, *32*, 4009.
- [34] R. Fukai, P. H. R. Dakwa, W. Chen, *Journal of Polymer Science Part A: Polymer Chemistry* **2004**, *42*, 5389.
- [35] L. N. Bui, M. Thompson, N. B. McKeown, A. D. Romaschin, P. G. Kalman, *The Analyst* **1993**, *118*, 463.
- [36] W. S. Jang, I. Rawson, J. C. Grunlan, *Thin Solid Films* **2008**, *516*, 4819.
- [37] Y. C. Li, J. Schulz, J. C. Grunlan, *Acs Applied Materials & Interfaces* **2009**, *1*, 2338.
- [38] Y. C. Li, J. Schulz, S. Mannen, C. Delhom, B. Condon, S. Chang, M. Zammarano, J. C. Grunlan, *Acs Nano* **2010**, *4*, 3325.
- [39] N. P. Patel, A. C. Miller, R. J. Spontak, *Advanced Materials* **2003**, *15*, 729.
- [40] T. Lan, P. D. Kaviratna, T. J. Pinnavaia, *Chemistry of Materials* **1994**, *6*, 573.
- [41] N. P. Patel, C. M. Aberg, A. M. Sanchez, M. D. Capracotta, J. D. Martin, R. J. Spontak, *Polymer* **2004**, *45*, 5941.
- [42] S. Roux, S. Demoustier-Champagne, *Journal of Polymer Science Part A: Polymer Chemistry* **2003**, *41*, 1347.
- [43] D. M. Hubbe, Vol. 2010, Poly(ethylene imine) (PEI), <http://www4.ncsu.edu/~hubbe/PEI.htm>.
- [44] Y. Lvov, K. Ariga, I. Ichinose, T. Kunitake, *Langmuir* **1996**, *12*, 3038.
- [45] D. J. Frankowski, S. A. Khan, R. J. Spontak, *Advanced Materials* **2007**, *19*, 1286.

3.6. TABLES AND FIGURES

Table 3.1. Classifications of layered silicate crystals

Unit crystal lamellae type	Family of clay	Examples of clay
1:1	Family of kaolinite	Kaolinite, perlite clay, etc.
	Family of illite	Illite, etc.
2:1	Family of saponite	Montmorillonite , saponite, vermiculite
	Family of hydromica	Illite, glauconite
2:2	Family of chlorite and others	Chlorite

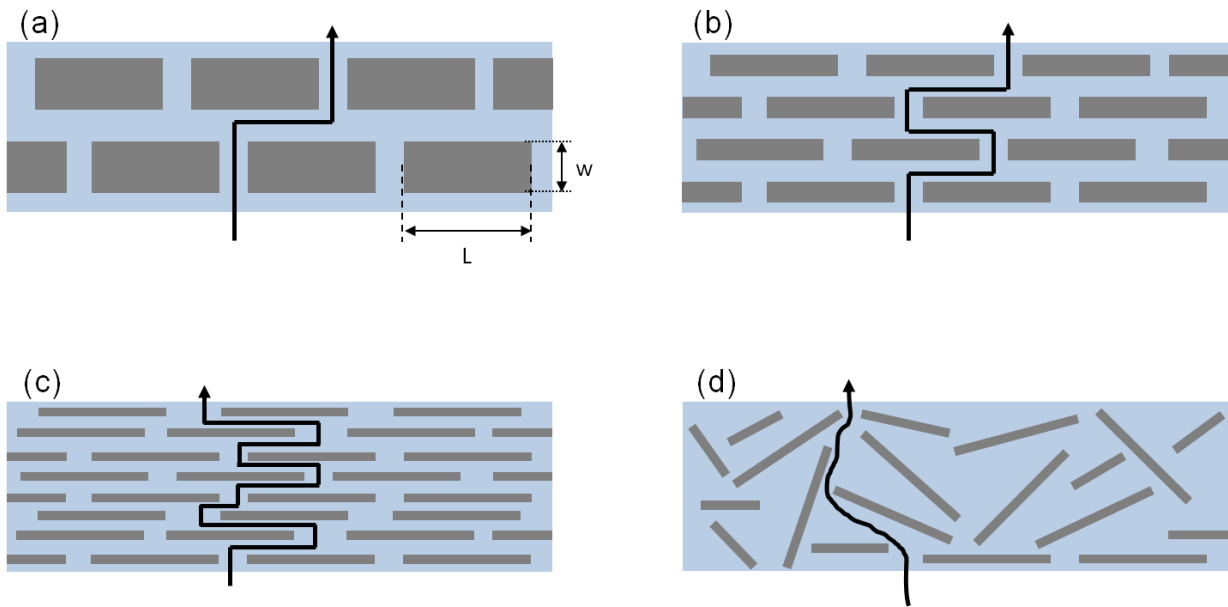


Figure 3.1. The effect aspect ratio (a, b and c) and orientation (d) on the tortuosity factor.

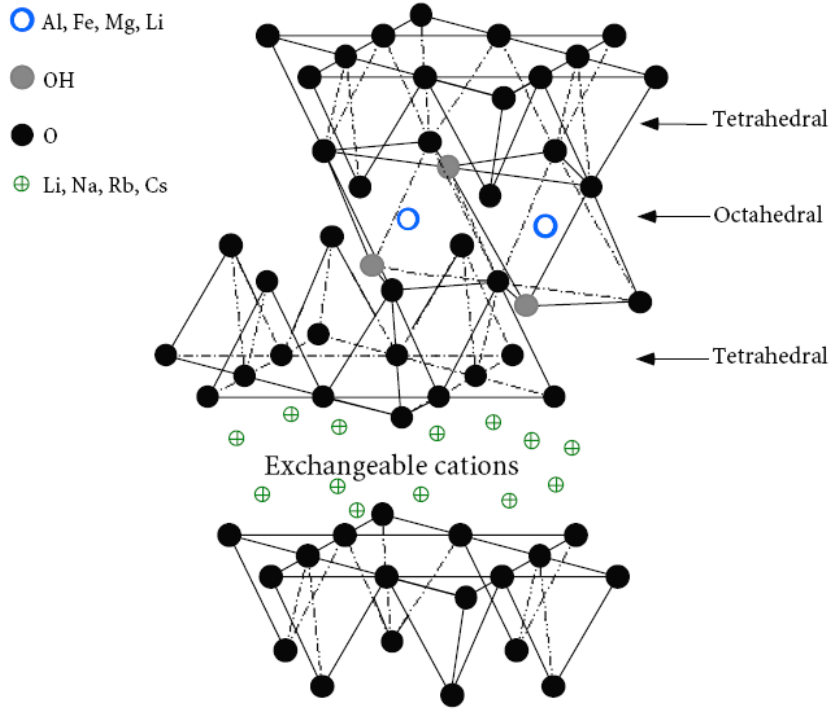


Figure 3.2. Chemical structure of 2:1 layered silicates.^[10]

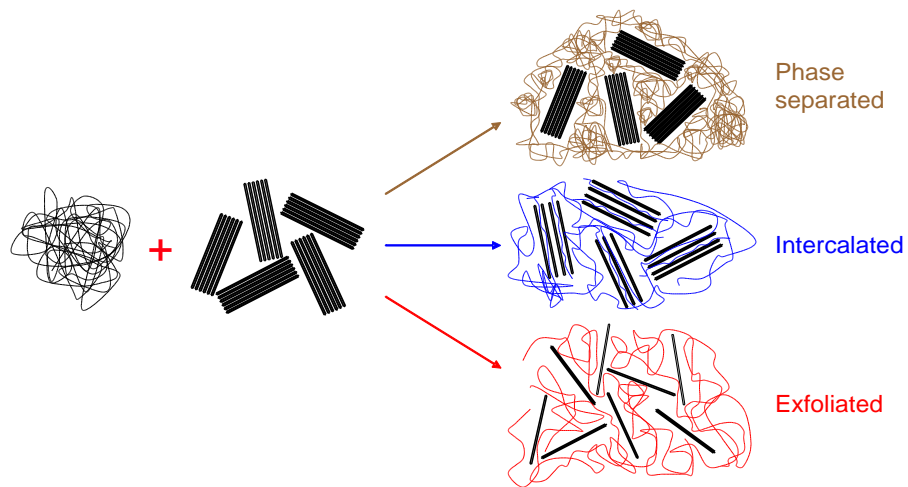


Figure 3.3. Different morphologies of polymer/clay composites.^[10]

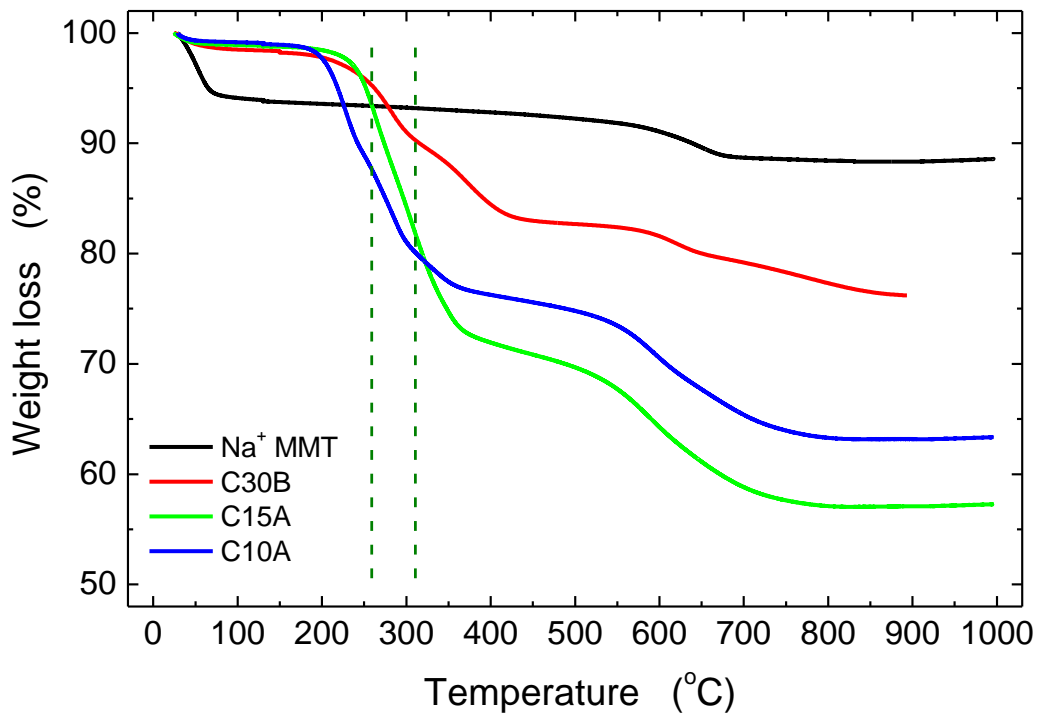


Figure 3.4. Degradation behavior of various clays in air atmosphere (C30B, C15A and C10A are the organically modified clays of Southern Clay Products. C30B is natural montmorillonite modified with methyl, tallow, bis-2-hydroxyethyl quaternary ammonium, C15A is natural montmorillonite modified with dimethyl, dehydrogenated tallow quaternary ammonium, C10A is natural montmorillonite modified with dimethyl, benzyl, hydrogenated tallow quaternary ammonium). The dashed line represent the range of melt processing temperature of PET.

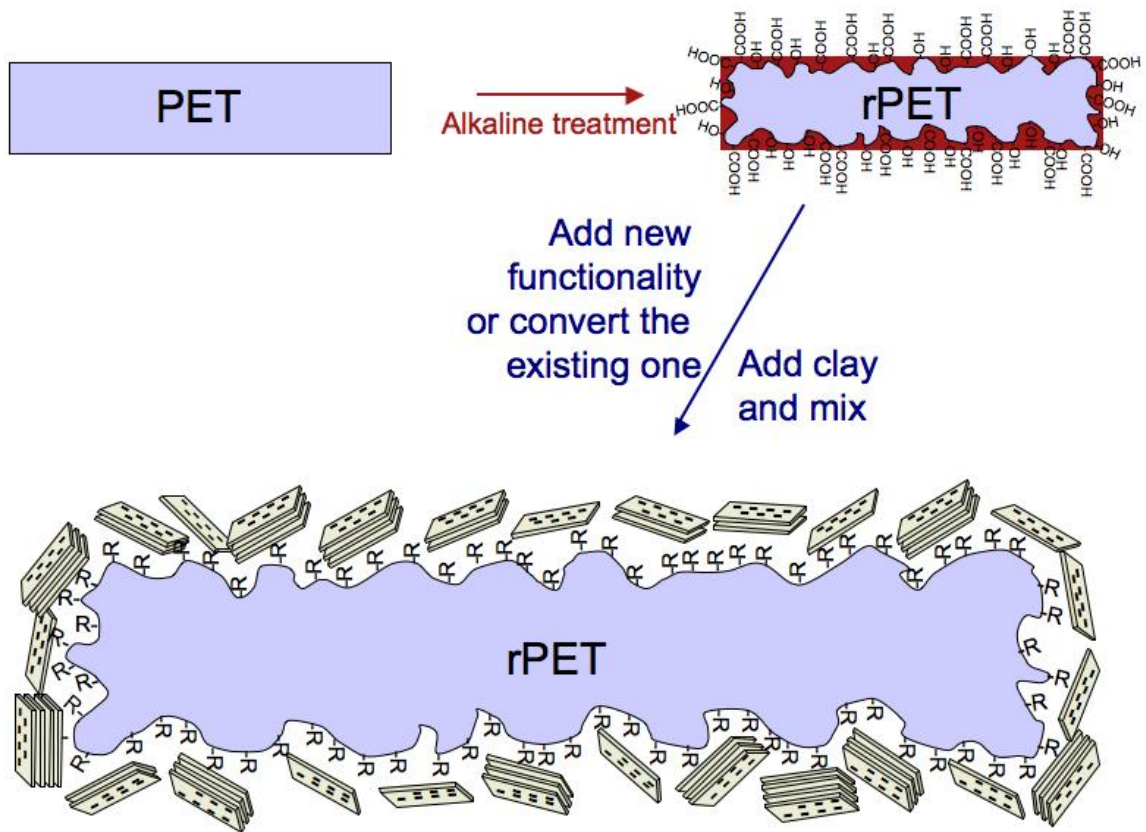


Figure 3.5. The proposed starting point for rPET/clay nanocomposite formation.

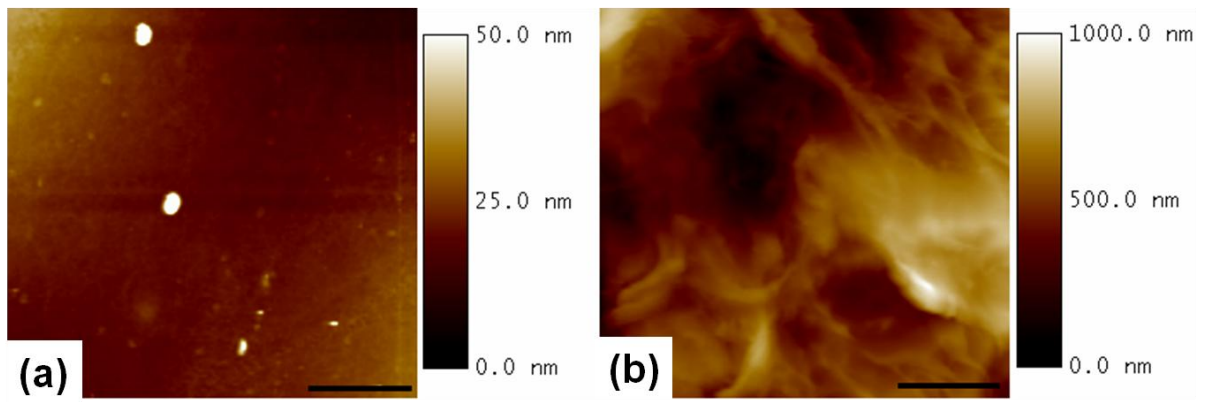


Figure 3.6. Surface topography of PET soft drink bottle (a) and rPET flake (b). The scale bar is 2 μm for both images.

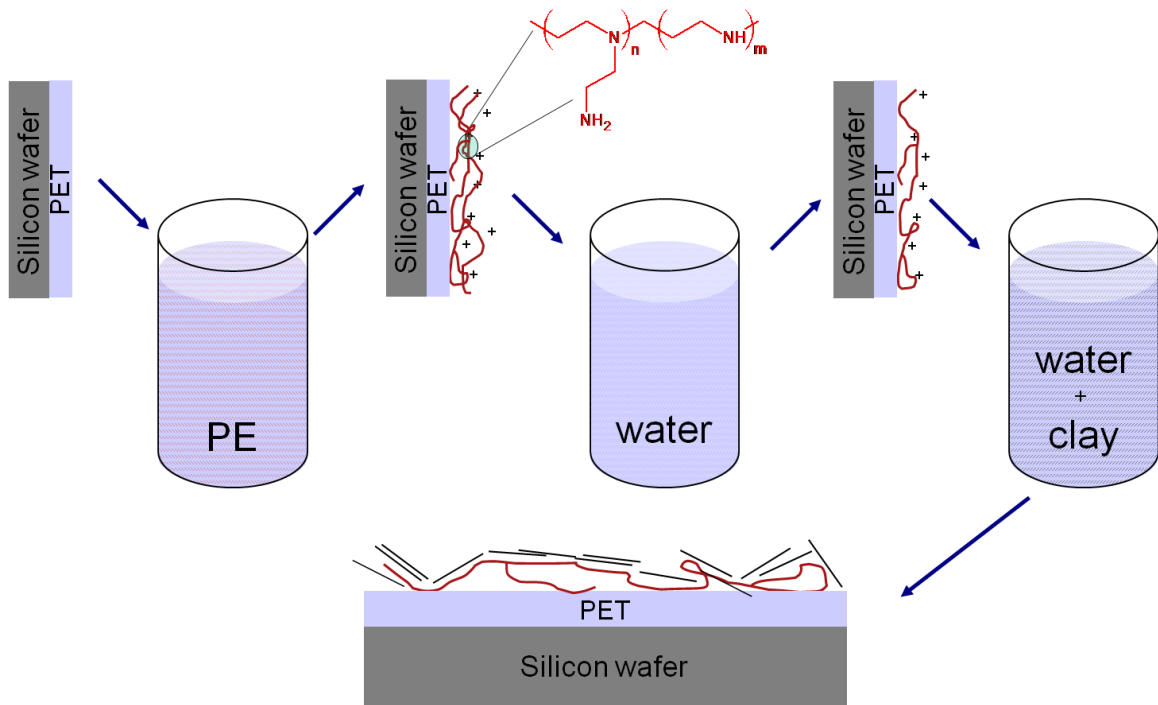


Figure 3.7. Schematic representation of polyelectrolyte adsorption on PET flake surface with subsequent clay platelet adsorption.

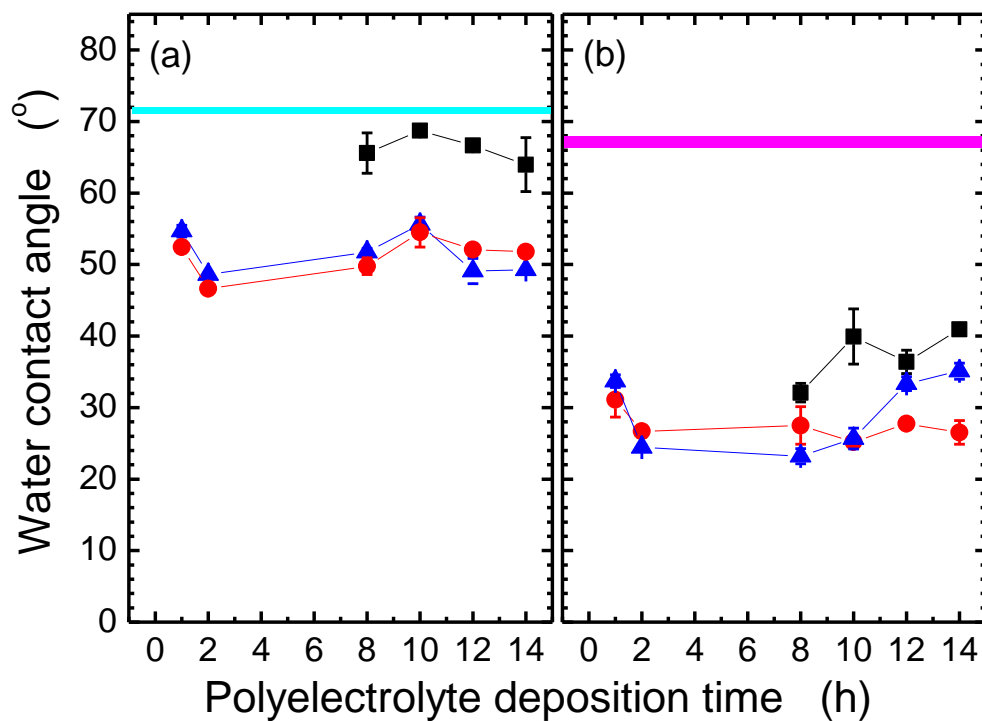


Figure 3.8. Water contact angle of PET surface after polyelectrolyte (a) and subsequent clay (b) adsorption as a function of polyelectrolyte deposition time for PAH (■), PEI25 (●) and PEI60 (▲). Green and pink lines represent the water contact angle values of bare PET thin film and PET thin film exposed to clay suspension in DI water, respectively.

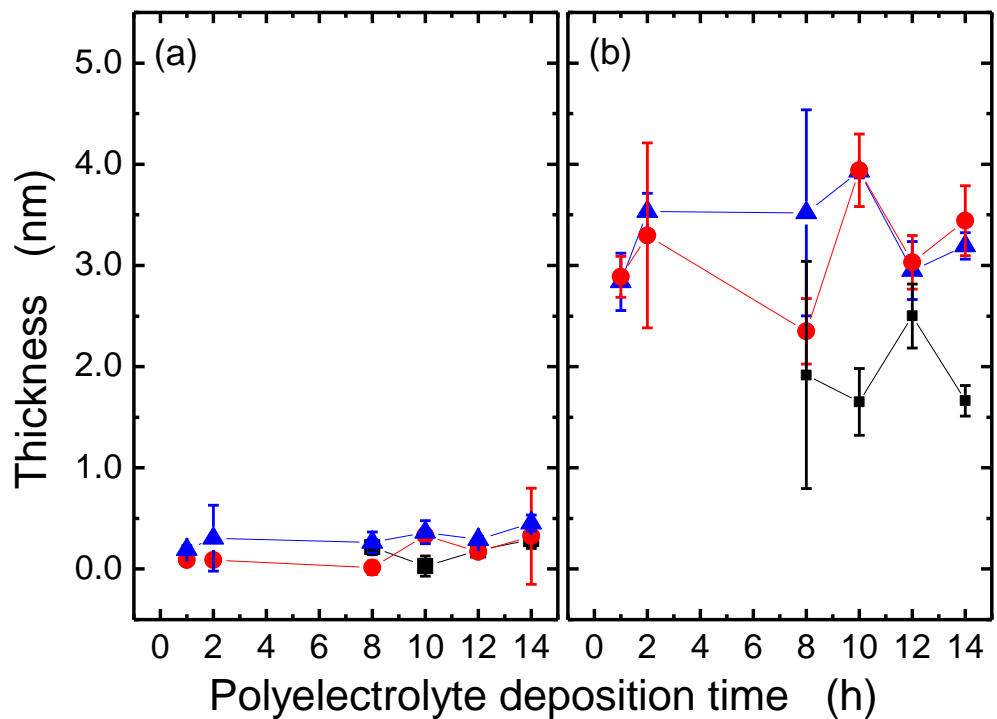


Figure 3.9. Thickness of the polyelectrolyte (a) and clay (b) layers after polyelectrolyte and subsequent clay adsorption as a function of polyelectrolyte deposition time for PAH (■), PEI25 (●) and PEI60 (▲).

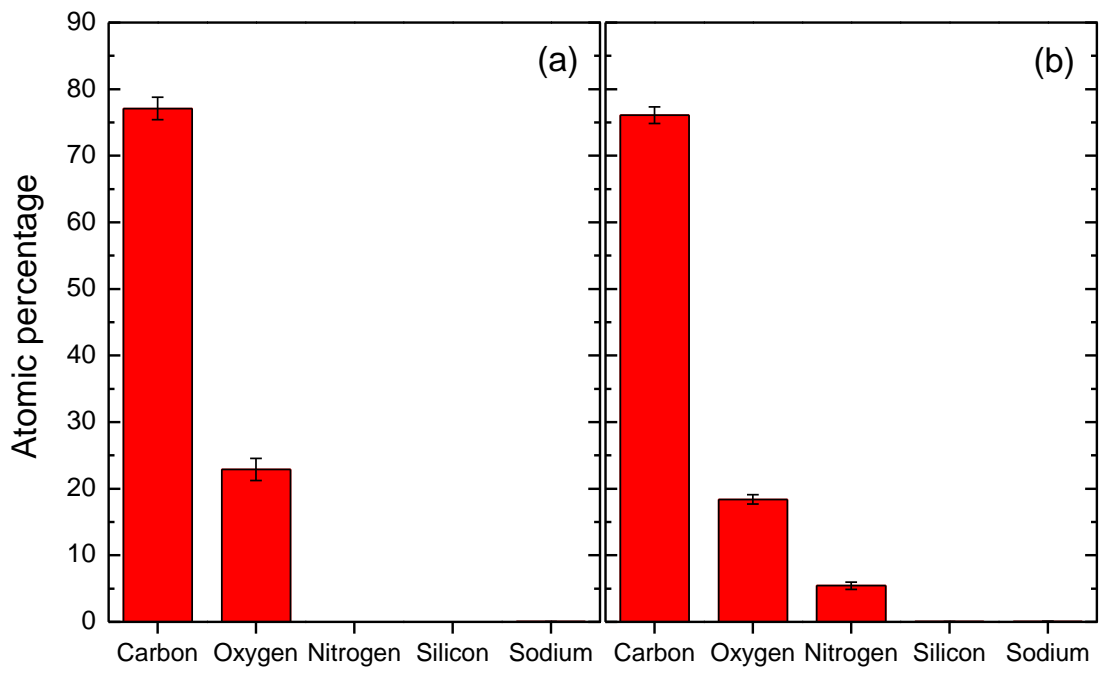


Figure 3.10. Surface composition of rPET (a) and PEI treated rPET surface (b).

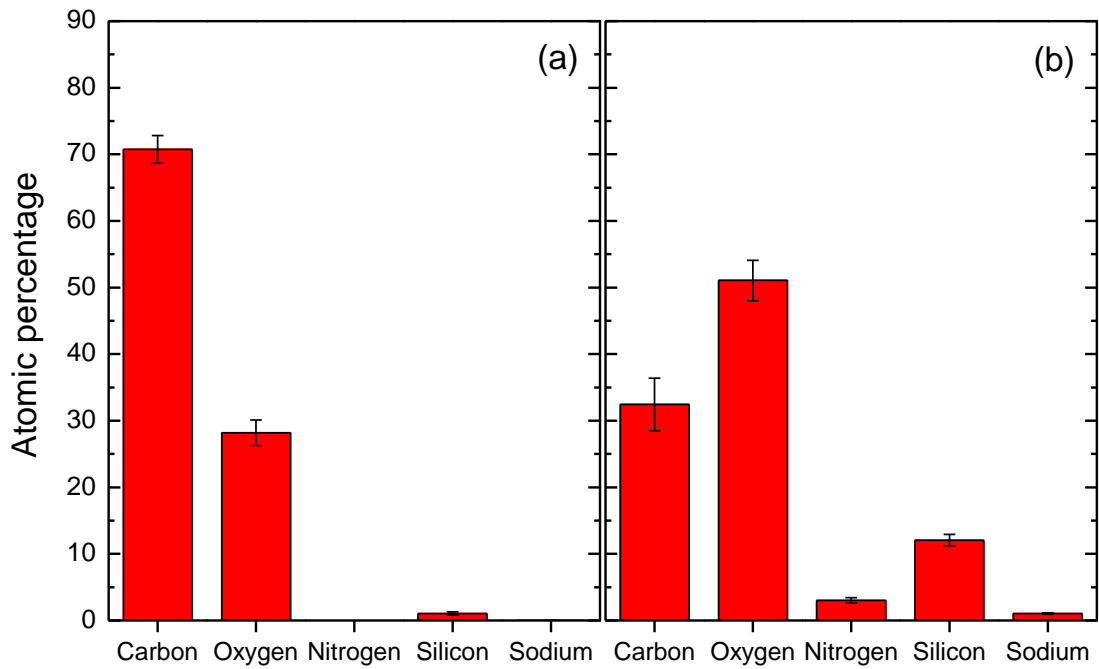


Figure 3.11. Surface composition of rPET surface exposed to clay suspension (a) and PEI60 treated rPET surface exposed to clay suspension (b).

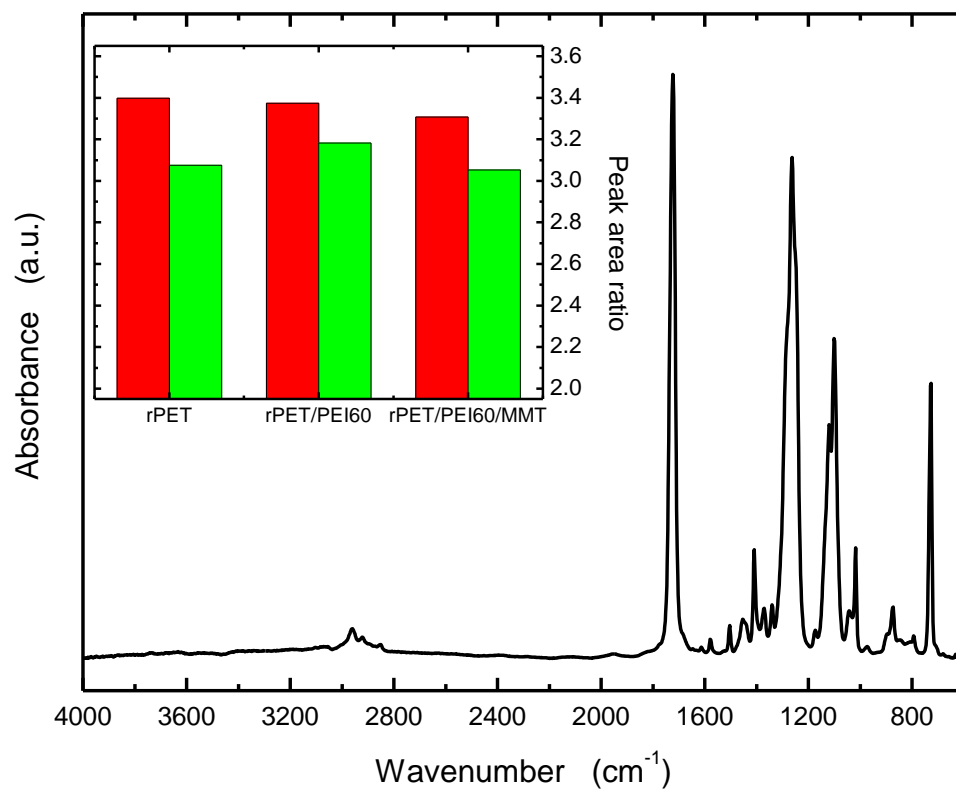


Figure 3.12. FT-IR spectra collected on a rPET flake and the inset shows the ratio of FT-IR peak areas located at 1200 and 750 cm⁻¹ before (red columns) and after extrusion (green columns) for rPET, rPET/PEI60 and rPET/PEI60/MMT flakes.

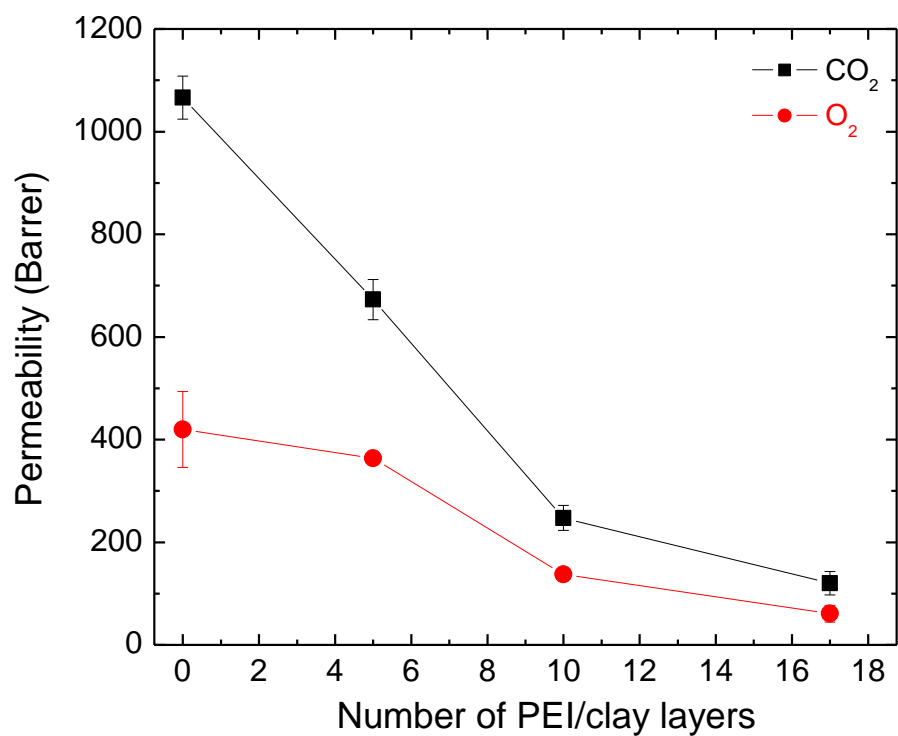


Figure 3. 13. Carbon dioxide (■) and oxygen (●) permeability through PDMS network as a function of PEI60/clay layers.

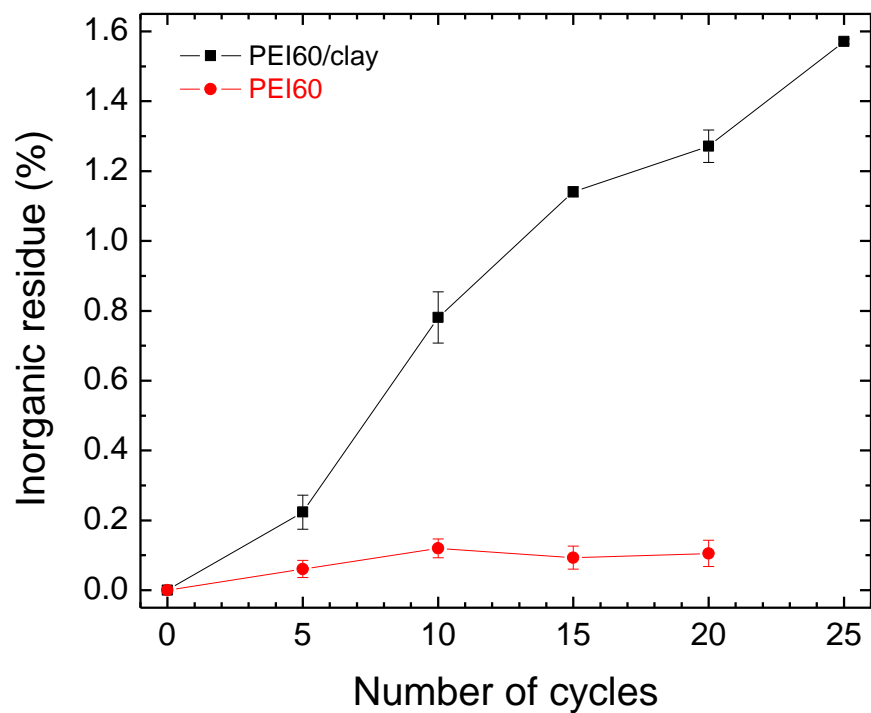


Figure 3. 14. Percentage of remaining inorganic residue after pyrolysis modified LLDPE as a function of processing cycles for PEI60/clay (■) and PEI60 (●).

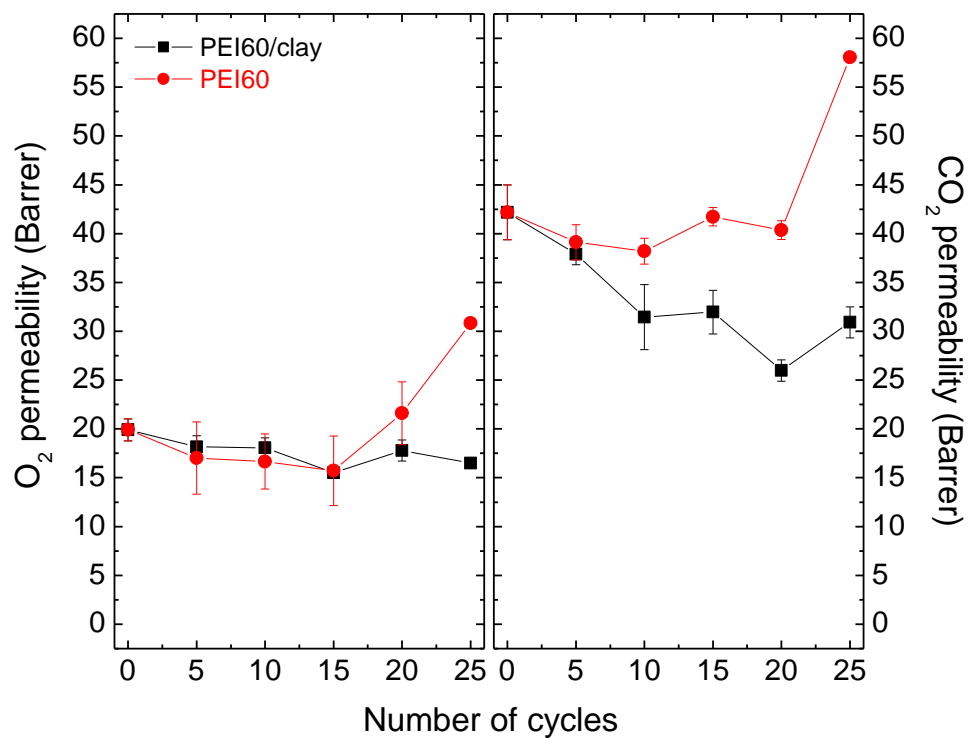


Figure 3. 15. Oxygen (left) and carbon dioxide (right) permeabilities through LLDPE as a function of processing cycles for PEI60/clay (■) and PEI60 (●).

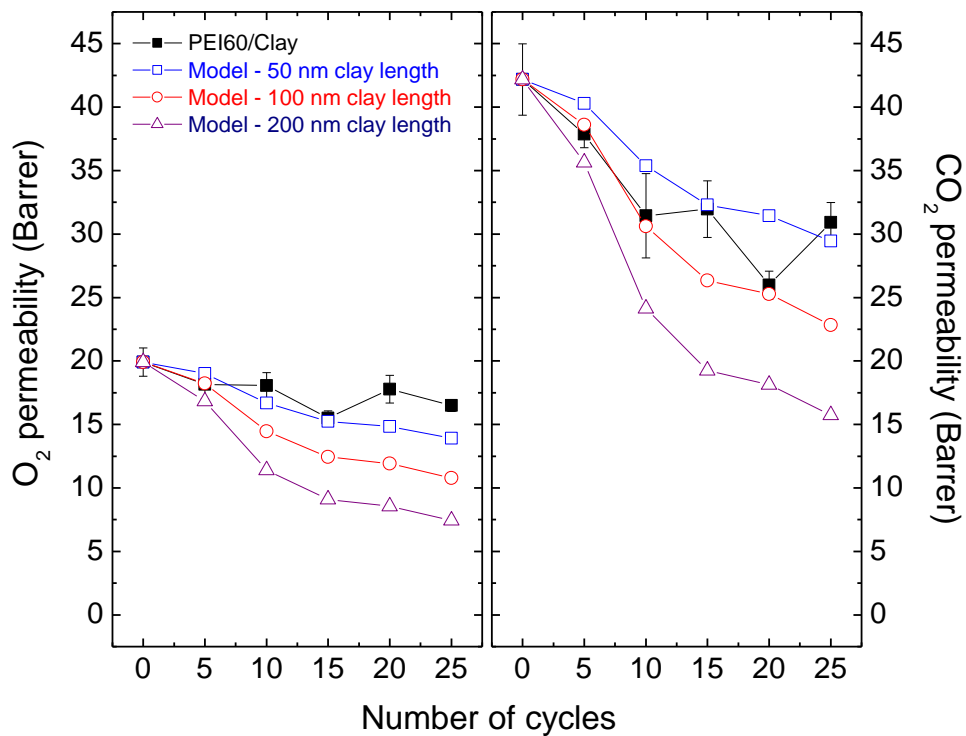


Figure 3. 16. The comparison of experimentally obtained permeabilities (■) of oxygen and carbon dioxide with calculated with Nielsen model based on the inorganic residue concentration determined from TGA for the clay aspect ratios of 50 (□), 100 (○) and 200 (△).

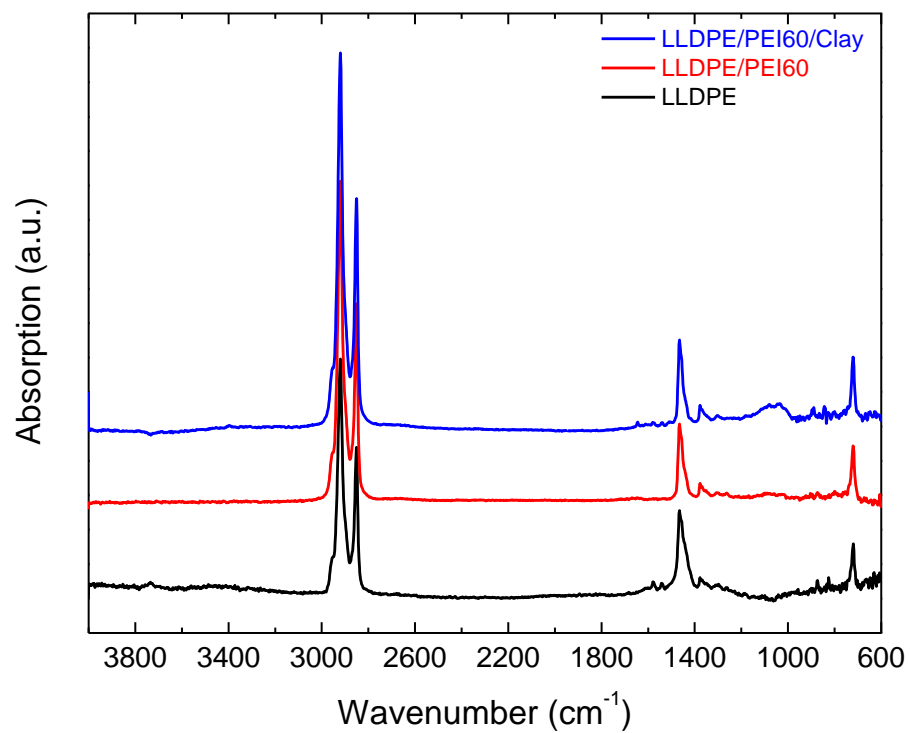


Figure 3. 17. FT-IR spectra of virgin LLDPE (black line), PEI60 (red line) and PEI60/clay (blue line) treated and melt processed LLDPE films.

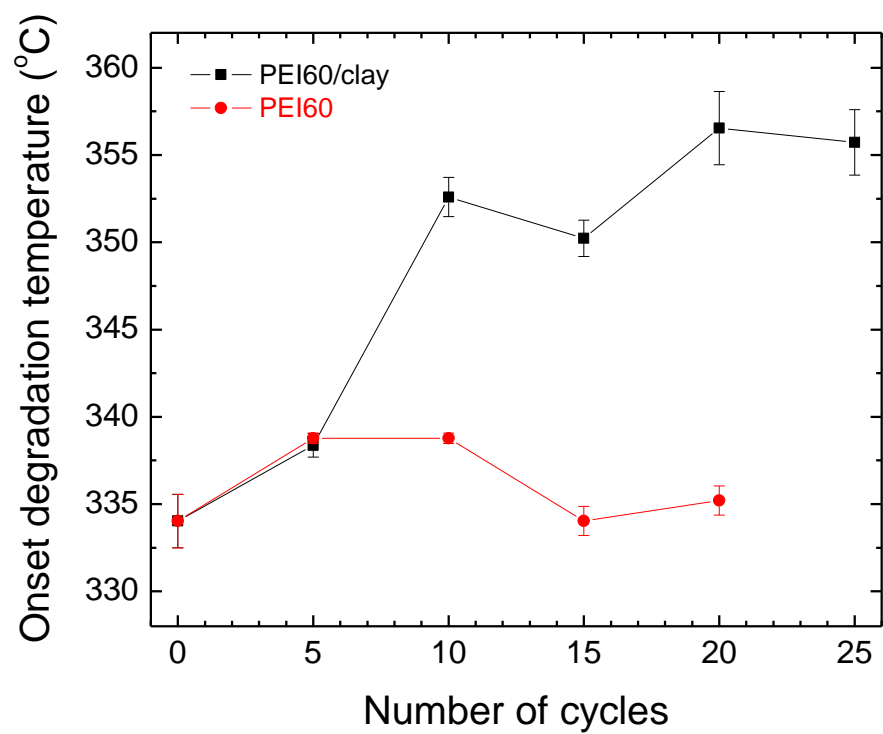


Figure 3. 18. Onset degradation temperature measured by TGA experiments for LLDPE membrane treated with PEI60/clay (■) and PEI60 (●).

CHAPTER 4: RESPONSIVE PET NANO/MICROFIBERS VIA SURFACE-INITIATED POLYMERIZATION

4.1. INTRODUCTION

Electrospinning is an emerging fabrication technique capable of generating solid polymer fibers that range from tens of nanometers to several microns in diameter. Such nano/microfibers are of fundamental and technological interest due to their high surface-to-volume ratio. During wet electrospinning, a polymer solution of sufficiently high viscosity and conductivity is subjected to an electric field. When the electrostatic forces overcome surface tension, a charged jet emitted from the tip of a Taylor cone^[1] undergoes a whipping action^[2] wherein the solvent evaporates, and is subsequently collected as a dry, randomly oriented fiber mat on a grounded collector plate. This process strategy is appealing due to the simple setup required and the ability to tailor fiber characteristics with relative ease.^[3] Although the morphology of electrospun nano/ microfibers is desirable, they tend to lack the functionality that is sought in contemporary applications. One way to overcome this deficiency is by developing multicomponent nano/ microfibers, in which the fiber-forming polymer is modified with one or more species designed to enhance targeted properties.^[4-6] Surface-active compounds added to the polymer solution prior to electrospinning may, however, remain trapped within the resultant fiber upon solidification and thus exhibit substantially reduced activity.^[7] While antibacterial biocides incorporated in this fashion lose

much of their efficacy,^[8] quaternary ammonium species covalently bonded to as-spun fibers can create a permanent antibacterial surface.^[9] Alternatively, polarizable antibacterial copolymers co-dissolved with the fiber-forming polymer can be brought to the fiber surface, where they remain anchored in place, by the electric field during electrospinning.^[10,11]

Polymers such as poly(ethylene terephthalate) (PET), which is widely known for its mechanical strength, transparency, and solvent resistance, tend to possess a hydrophobic surface and a low surface energy,^[12] in which case electrospun nano/microfibers require post-treatment so that chemically-active species are positioned on the fiber surface. Methods by which to achieve such surface functionalization include UV treatment,^[8] mineralization,^[13] core-shell formation,^[14] chemical vapor deposition,^[15] or inclusion of reactive compounds.^[16, 17] Once these chemically-active groups are available, covalent bonding,^[18] immobilization^[19] or electrostatic interactions^[20] can be used to introduce functional moieties to the fiber surface without adversely affecting the bulk fiber properties. While surface modification could permit the use of electrospun PET^[21] nano/microfibers in filtration media,^[22] protective textiles,^[23] tissue scaffolds,^[24] and drug-delivery vehicles,^[25] most of the modification approaches listed above purposefully or inadvertently promote PET degradation. Thus, the conditions by which surface modification is conducted must be monitored carefully to avoid compromising the bulk properties of PET.

Grafting polymer brushes represents an alternative approach by which to modify and control the surface properties of materials.^[26] Numerous studies have reported on surface-initiated grafting on surfaces of various geometries with a plethora of different monomers by

employing numerous polymerization routes. Poly(*N*-isopropylacrylamide) (PNIPAAm) is solely considered here because of its thermoresponsive nature^[27] (it possesses a lower critical solution temperature, T_c , in water at $\approx 32^\circ\text{C}$). Prior efforts to polymerize styrene^[28, 29] and NIPAAm^[30] on flat PET surfaces have relied on different means of activating the PET surface (e.g., saponification, plasma treatment and aminolysis) for the purpose of attaching initiators. The major drawback of such treatments, however, is that they may increase surface roughness by degrading PET, which is of concern with regard to electrospun PET nano/microfibers. Independent studies^[31] have confirmed that 3-aminopropyltriethoxysilane (APTES) can be used to functionalize the surface of PET via amidation with negligible degradation of the parent PET material. Unlike short alkyl amines (which can diffuse into and react throughout, and thus weaken, PET^[32,33]), the bulky triethoxysilane group on APTES hinders diffusion, changes its chemical nature upon amidation and creates a barrier by restricting the diffusion of other APTES molecules. Moreover, since the ethoxysilane groups of APTES are exposed at the polymer/air interface, hydrolysis of triethoxysilane yields silanol groups that facilitate initiator attachment.

In this work, we modify electrospun PET microfibers with APTES to create surface-bound hydroxyl groups for the attachment of [11-(2-bromo-2-methyl)propionyloxy]undecyltrichlorosilane (BMPUS), which serves as an ATRP initiator for the polymerization of NIPAAm. Several analytical techniques are employed to (i) characterize the properties of as-spun and post-modified PET microfibers and (ii) follow the polymerization of NIPAAm via ATRP. In addition, we investigate the thermoresponsive nature of PNIPAAm-decorated

PET microfibers by attaching Au nanoparticles at temperatures above and below the T_c of PNIPAAm.

4.2. EXPERIMENTAL

Food-grade recycled PET flakes were kindly supplied by the United Resource Recovery Corp. (Spartanburg, SC). Hexafluoroisopropanol (HFIP) was obtained from Oakwood Products Inc. (Estill, SC), and anhydrous toluene, 2-chlorophenol, APTES, NIPAAm, copper I bromide (CuBr), and N,N,N',N',N''-pentamethyldiethylenetriamine (PMDETA) were all purchased from Sigma-Aldrich and used as-received. Citrate-stabilized Au nanoparticles^[34] (diameter = 16.9 ± 1.8 nm) and BMPUS initiator^[35] were prepared as described earlier. The PET flakes were dissolved in HFIP at different concentrations and electrospun at ambient temperature and 10 kV to generate microfibers varying in diameter. Thin films of PET measuring 12 and 180 nm thick, as discerned by ellipsometry (v.i.), were spun-cast at 25°C on silicon wafers from 0.5 and 3.0% (w/w) solutions, respectively, in 2-chlorophenol. Microfiber mats and thin films were stored under vacuum for at least 48 h prior to use to remove entrapped solvent.

The APTES was deposited on the PET microfibers and thin films by exposing the samples to 1% (v/v) APTES/anhydrous toluene solutions for 24 h at ambient temperature, followed by sonication in toluene to remove loosely adsorbed APTES molecules. The ethoxysilane groups of the surface-anchored APTES molecules were hydrolyzed in acidic

water (pH \approx 4.5-5.0). After drying the samples under reduced pressure, BMPUS was deposited on the PET-SiOH surfaces by established protocols.^[36,37] The PNIPAAm brushes were subsequently grown from PET-SiOH surfaces by ATRP of NIPAAm, as described elsewhere.^[34] Briefly, 6.30 g NIPAAm was dissolved in a mixture of 4.86 g methanol and 6.30 g water in an argon-purged Schlenk flask, and oxygen was removed via three freeze-thaw cycles. After removal of oxygen, PMDETA (0.56 g) and CuBr (0.16 g) were added to the solution prior to an additional freeze-thaw cycle. The Schlenk flask was sealed and transferred to an argon-purged glove box. Microfiber mats and thin films of PET were submersed in the solution for specific time intervals, after which they were removed, promptly rinsed with methanol and deionized water, and sonicated in deionized water.

The thickness of the thin PET films was measured by variable-angle spectroscopic ellipsometry (J.A. Woollam) at a 70° incidence angle before and after each modification step to discern the PNIPAAm brush height. Surface chemical composition was monitored by XPS performed on a Kratos Analytical AXIS ULTRA spectrometer at a take-off angle of 90°. The FTIR analysis of the PET microfibers was conducted in transmission mode on a Nicolet 6700 spectrometer after embedding the microfiber mats in KBr pellets. For each sample, 1024 scans were acquired after background correction at a resolution of 4 cm⁻¹. Resultant XPS and FTIR spectra were analyzed using the Vision and Omnic Spectra software suites, respectively. The thermoresponsive behavior of PET and PET-PNIPAAm microfibers was interrogated by measuring the WCA at different temperatures via the sessile drop technique on a Ramé-Hart Model 100-00 instrument. As-spun and modified PET microfibers were

coated with ≈ 16 nm of Au, and their diameter and surface morphology were examined by field-emission scanning electron microscopy (SEM) performed on a JEOL 6400F electron microscope operated at 5 kV.

4.3. RESULTS AND DISCUSSION

The diameters of electrospun PET microfibers, prepared according to the protocol provided above and measured by SEM, are 450 ± 100 , 800 ± 200 and 1200 ± 300 nm for 6, 8 and 10% (w/w) solutions, respectively, of PET in HFIP. The surfaces of unmodified PET microfibers consistently appear smooth (cf. Figure 4.1) with some slight dimpling observed occasionally along the fiber axis. Microfibers modified with thermoresponsive PNIPAAm brushes have been generated in a sequence of four steps, which are depicted schematically in Figure 4.1. Briefly, APTES molecules are attached to the PET surface via aminolysis between PET and the primary amine of APTES. Next, the ethoxysilane groups on APTES are hydrolyzed to generate silanol groups for BMPUS attachment. Finally, PNIPAAm brushes are grown directly from the PET microfiber surface. A second SEM image displaying PET microfibers modified with PNIPAAm brushes is included for comparison in Figure 4.1 to demonstrate that these microfibers appear marginally rougher than the as-spun microfibers at the end of the modification and brush growth process. The difference in microfiber morphology is almost indiscernible and the PNIPAAm brushes on spin-coated PET films on silicon wafers appears smooth, combination of these verifies that the brush is uniformly

distributed on the surface of the microfibers. Below, we provide a detailed assessment of each of the steps in this polymerization sequence.

In Figure 4.2, Fourier-transform infrared (FTIR) spectra are presented for three materials: (a) as-spun microfibers (PET), (b) APTES-modified PET microfibers following hydrolysis (PET-SiOH) and (c) PET microfibers with PNIPAAm brushes (PET-PNIPAAm). The appearance of new peaks located at 1650 cm^{-1} (amide I band) 1550 cm^{-1} (amide II band), 1470 cm^{-1} , and 3300 cm^{-1} in Figure 4.2b is due to the formation of secondary amide groups, thereby confirming the grafting of APTES to the PET microfiber surface. Detection of these groups by FTIR is attributed to the large surface area afforded by the microfibers. Successful attachment of APTES can also be inferred from the surface properties of modified microfibers upon exposure to acidic water, which promotes hydrolysis of the ethoxysilane groups to silanol groups. Resulting changes in static water contact angle (WCA) and specimen thickness are measured on flat PET films spun-cast on silicon wafer. Values of WCA for films of PET-SiOH and PET after hydrolysis are $50\pm 0.8^\circ$ and $71\pm 0.8^\circ$, respectively, whereas that for untreated PET is $75\pm 0.2^\circ$. In addition, the results of X-ray photoelectron spectroscopy (XPS) measurements provided in Figure 4.3a reveal the existence of a small N_{1s} peak at 400 eV, which corresponds to 0.6 atom% N from hydrolyzed APTES on the PET-SiOH surface. In the next step, BMPUS molecules are attached to the PET-SiOH surface (cf. Figure 4.1) to serve as initiator centers for the "grafting from" polymerization of NIPAAm.

Subsequent growth of PNIPAAm brushes from the initiator centers at the fiber surface is verified by the FTIR and XPS spectra presented in Figures 4.2c and 4.3b, respectively. The characteristic secondary amide IR vibrations located at 1650 cm^{-1} , 1550 cm^{-1} , 1470 cm^{-1} , and 3300 cm^{-1} are the most pronounced for PET-PNIPAAm microfibers. In addition, the appearance of a relatively intense N_{1s} peak at 400 eV in Figure 4.3b indicates an elevated concentration of N, which is consistent with the presence of PNIPAAm brushes. Quantitation of this spectrum yields the following atomic concentrations: $76.8\pm 0.4\%$ C, $11.6\pm 0.5\%$ N and $11.6\pm 0.3\%$ O. These values agree favorably with theoretical concentrations (75.0% C, 12.5% N and 12.5% O) obtained from the chemical structure of PNIPAAm. The high-resolution C_{1s} spectra included in the insets of Figures 4.3a and 4.3b likewise demonstrate that the PNIPAAm brushes cover the PET film surface. In Figure 4.3a, the spectrum displays peaks at 289.0 and 286.6 eV corresponding to O-C=O and C-O functionalities, respectively. These signature peaks for PET disappear upon growth of the PNIPAAm brushes, which are responsible for a new peak at 287.8 eV (N-C=O groups) and a shoulder at 286.1 eV (C-N bonds).^[38] Since the XPS fingerprint for PET is lost upon PNIPAAm brush growth, it can be inferred that the thickness of the dry brushes is at least the probe depth of XPS ($\sim 10\text{ nm}$). According to ellipsometry measurements of PET-PNIPAAm films on silicon wafer, the dry thickness of the PNIPAAm brush after a polymerization time of 30 min is $\approx 40\text{ nm}$, which, assuming an average grafting density of 0.45 chains/nm^2 ,^[39] corresponds to a molecular weight of $\approx 48\text{ kDa}$. Although the microfibers possess a curved surface, we contend that, on the basis of the brush gyration diameter ($\approx 40\text{ nm}$) relative to the microfiber diameter (600-

1200 nm), the thickness of the PNIPAAm brush does not differ substantially from that produced on a flat film.

The thermoresponsiveness of the PNIPAAm brushes grown on PET microfibers is first evaluated with WCA experiments performed successively above and below the T_c of PNIPAAm, as shown in Figure 4.4. The WCA of unmodified PET microfibers at 25°C (Figure 4.4a) is $\approx 125^\circ$, which is higher than that of a flat PET film (75°) because of the "rough" nature of the microfiber mat. Despite this increase in surface roughness, the size of the water droplet on the surface of unmodified PET microfibers does not change during the course of the measurement, and the measured WCA remains constant. This result also verifies that no significant evaporation of water takes place during the course of the WCA measurement (liquid evaporation during WCA measurement may sometimes reduce the apparent contact angle values due to pinning of the contact line). In Figure 4.4b, the WCA of the unmodified PET microfibers at 60°C is $\approx 124^\circ$ and likewise does not change, which suggests that water evaporation is again negligible. Cycling the specimen between these two temperatures in Figures 4.4c and 4.4d yields comparable results, confirming that the PET surface stays hydrophobic. Measured WCA values of PET-PNIPAAm microfibers, on the other hand, display significantly different behavior. At 25°C (Figure 4.4a), the WCA is also $\approx 125^\circ$ when the water droplet is initially placed on the microfiber surface, but quickly decreases to 0° in just over 40 s as the water is wicked by the hydrophilic PNIPAAm brushes on the surface of the microfibers. When the temperature is increased beyond T_c of PNIPAAm to 60°C (Figure 4.4b), the water droplet is not strongly affected by the microfiber due to the

increased hydrophobicity of the PNIPAAm chains, and the WCA is $\approx 124^\circ$. Repetition of these measurements upon thermal cycling in Figures 4.4c and 4.4d confirm that the thermoresponsiveness of PNIPAAm brushes on PET microfibers is reversible with no evidence of hysteresis.

A second probe of the thermoresponsive nature of PNIPAAm brushes on PET microfibers employs Au nanoparticles as tracers. Previous studies^[34,40] have established that Au nanoparticles attach to PNIPAAm chains via hydrogen bonding between the citrate groups present on the nanoparticle surface and the amide groups on PNIPAAm. To discern the extent to which the PNIPAAm brushes could bind Au nanoparticles, electrospun PET microfibers have been submerged in a 0.05 mg/ml suspension of Au nanoparticles in deionized water for 24 h at the same two temperatures examined in Figure 4.4, i.e., 25 and 60°C. Images acquired by SEM after drying the fibers reveal that the nanoparticle loading on the surface of PET-PNIPAAm microfibers is significantly higher at 25°C (Figure 4.5a) than at 60°C (Figure 4.5b). This difference is attributed to the thermoresponsiveness of the PNIPAAm chains, which are hydrophilic and swell in water at temperatures below T_c , but become hydrophobic and collapse in water at temperatures above T_c . As a result of such temperature-driven swelling or contracting of the brush, the number of NIPAAm units available for attachment of the Au particles increases or decrease, respectively, which, in turn, governs the concentration of Au nanoparticles bound to PNIPAAm.

4.4. CONCLUSIONS

In this study, we have demonstrated that the surface of electrospun PET microfibers can be modified via amidation of the amine group on APTES with the ester group on PET to permit further chemical modification ultimately resulting in the growth of polymer brushes by ATRP. Step-by-step examination of the PET surface during the modification sequence, along with quantitative analysis whenever possible, verifies expectations, and establishes the sequence as a straightforward and viable route for PET microfiber functionalization. The thermoresponsive behavior of the PNIPAAm brushes on PET microfibers has been investigated using both contact angle measurements to determine the nature of the modified PET surface and Au nanoparticle tracers to determine the extent of brush swelling at temperatures below and above the lower critical solution temperature of PNIPAAm in water. Surface functionalization of electrospun PET microfibers using this approach and PNIPAAm in particular yields mechanically robust and highly porous mats that are temperature-sensitive, which means that they are suitable candidates for diverse technologies as responsive filters, scaffolds, delivery vehicles, and sensors.

The effect of fiber diameter affecting the curvature of the fiber surface on polymerization rate and polydispersity of polymer brushes should be studied by carrying out “grafting from” polymerization from PET fibers having various diameters ranging from nanometers to micrometers. In addition, the attachment of metal nanoparticles to PNIPAAm chains can be

repeated with different fiber diameters to determine the effect of convex-ness of the surface on nanoparticle uptake.

4.5. REFERENCES

- [1] G. Taylor, *Proc. Royal Soc. A (London)* **1969**, 313, 453.
- [2] Y. M. Shin, M. M. Hohman, M. P. Brenner, G. C. Rutledge, *Appl. Phys. Lett.* **2001**, 78, 1149.
- [3] S. V. Fridrikh, J. H. Yu, M. P. Brenner, G. C. Rutledge, *Phys. Rev. Lett.* **2003**, 90.
- [4] S. K. Chae, H. Park, J. Yoon, C. H. Lee, D. J. Ahn, J. M. Kim, *Adv. Mater.* **2007**, 19, 521.
- [5] W. K. Son, J. H. Youk, T. S. Lee, W. H. Park, *Macromol. Rapid Commun.* **2004**, 25, 1632.
- [6] Y. Dzenis, *Science* **2004**, 304, 1917.
- [7] S. Sundarrajan, S. Ramakrishna, *J. Mater. Sci.* **2007**, 42, 8400.
- [8] C. Yao, X. S. Li, K. G. Neoh, Z. L. Shi, E. T. Kang, *Appl. Surf. Sci.* **2009**, 255, 3854.
- [9] J. Lin, S. Y. Qiu, K. Lewis, A. M. Klibanov, *Biotechnol. Bioeng.* **2003**, 83, 168.
- [10] X. Y. Sun, R. Shankar, H. G. Börner, T. K. Ghosh, R. J. Spontak, *Adv. Mater.* **2007**, 19, 87.
- [11] X. Y. Sun, L. R. Nobles, H. G. Börner, R. J. Spontak, *Macromol. Rapid Commun.* **2008**, 29, 1455.
- [12] J. R. Dann, *J. Colloid Interface Sci.* **1970**, 32, 302.
- [13] J. L. Chen, B. Chu, B. S. Hsiao, *J. Biomed. Mater. Res. A* **2006**, 79A, 307.
- [14] K. Muller, J. F. Quinn, A. P. R. Johnston, M. Becker, A. Greiner, F. Caruso, *Chem. Mater.* **2006**, 18, 2397.
- [15] C. C. Ho, W. S. Chen, T. Y. Shie, J. N. Lin, C. Kuo, *Langmuir* **2008**, 24, 5663.

- [16] N. D. Luong, I. S. Moon, D. S. Lee, Y. K. Lee, J. D. Nam, *Mater. Sci. Eng. C* **2008**, *28*, 1242.
- [17] F. X. Dong, Z. Y. Li, H. M. Huang, F. Yang, W. Zheng, C. Wang, *Mater. Lett.* **2007**, *61*, 2556.
- [18] P. Ye, Z. K. Xu, J. Wu, C. Innocent, P. Seta, *Biomaterials* **2006**, *27*, 4169.
- [19] Z. G. Wang, L. S. Wan, Z. K. Xu, *Soft Matter* **2009**, *5*, 4161.
- [20] N. D. Winblade, I. D. Nikolic, A. S. Hoffman, J. A. Hubbell, *Biomacromolecules* **2000**, *1*, 523.
- [21] I. S. Chronakis, B. Milosevic, A. Frenot, L. Ye, *Macromolecules* **2006**, *39*, 357.
- [22] S. Kaur, Z. Ma, R. Gopal, G. Singh, S. Ramakrishna, T. Matsuura, *Langmuir* **2007**, *23*, 13085.
- [23] S. Lee, S. K. Obendorf, *Textile Res. J.* **2007**, *77*, 696.
- [24] S. Liao, R. Murugan, C. K. Chan, S. Ramakrishna, *J. Mech. Behavior Biomed. Mater.* **2008**, *1*, 252.
- [25] J. Zeng, A. Aigner, F. Czubayko, T. Kissel, J. H. Wendorff, A. Greiner, *Biomacromolecules* **2005**, *6*, 1484.
- [26] Advincula, R., Brittain, W. J., Caster, K., Rühle, J. Eds.; *Polymer Brushes: Synthesis, Characterization, Applications*, Wiley-VCH Verlag: Weinheim, **2004**.
- [27] S. Kidoaki, S. Ohya, Y. Nakayama, T. Matsuda, *Langmuir* **2001**, *17*, 2402.
- [28] S. Roux, S. Demoustier-Champagne, *J. Polym. Sci. A: Polym. Chem.* **2003**, *41*, 1347.
- [29] L. Bech, T. Elzein, T. Meylheuc, A. Ponche, M. Brogly, B. Lepoittevin, P. Roger, *Eur. Polym. J.* **2009**, *45*, 246.
- [30] T. Farhan, W. T. S. Huck, *Eur. Polym. J.* **2004**, *40*, 1599.
- [31] A. Y. Fadeev, T. J. McCarthy, *Langmuir* **1998**, *14*, 5586.
- [32] M. S. Ellison, L. D. Fisher, K. W. Alger, S. H. Zeronian, *J. Appl. Polym. Sci.* **1982**, *27*, 247.

- [33] Y. Avny, L. Rebenfeld, *J. Appl. Polym. Sci.* **1986**, 32, 4009.
- [34] R. R. Bhat, J. Genzer, *Appl. Surf. Sci.* **2006**, 252, 2549.
- [35] K. Matyjaszewski, P. J. Miller, N. Shukla, B. Immaraporn, A. Gelman, B. B. Luokala, T. M. Siclovan, G. Kickelbick, T. Vallant, H. Hoffmann, T. Pakula, *Macromolecules* **1999**, 32, 8716.
- [36] M. R. Tomlinson, K. Efimenko, J. Genzer, *Macromolecules* **2006**, 39, 9049.
- [37] R. R. Bhat, M. R. Tomlinson, J. Genzer, *Macromol. Rapid Commun.* **2004**, 25, 270.
- [38] G. Beamson, D. J. Briggs, *High Resolution XPS of Organic Polymers: The Scienta ESCA300 Database*, Wiley: Chichester, **1992**.
- [39] M. R. Tomlinson, J. Genzer, *Langmuir* **2005**, 21, 11552.
- [40] S. Gupta, M. Agrawal, P. Uhlmann, F. Simon, M. Stamm, *Chem. Mater.*, 22, 504.

4.6. FIGURES

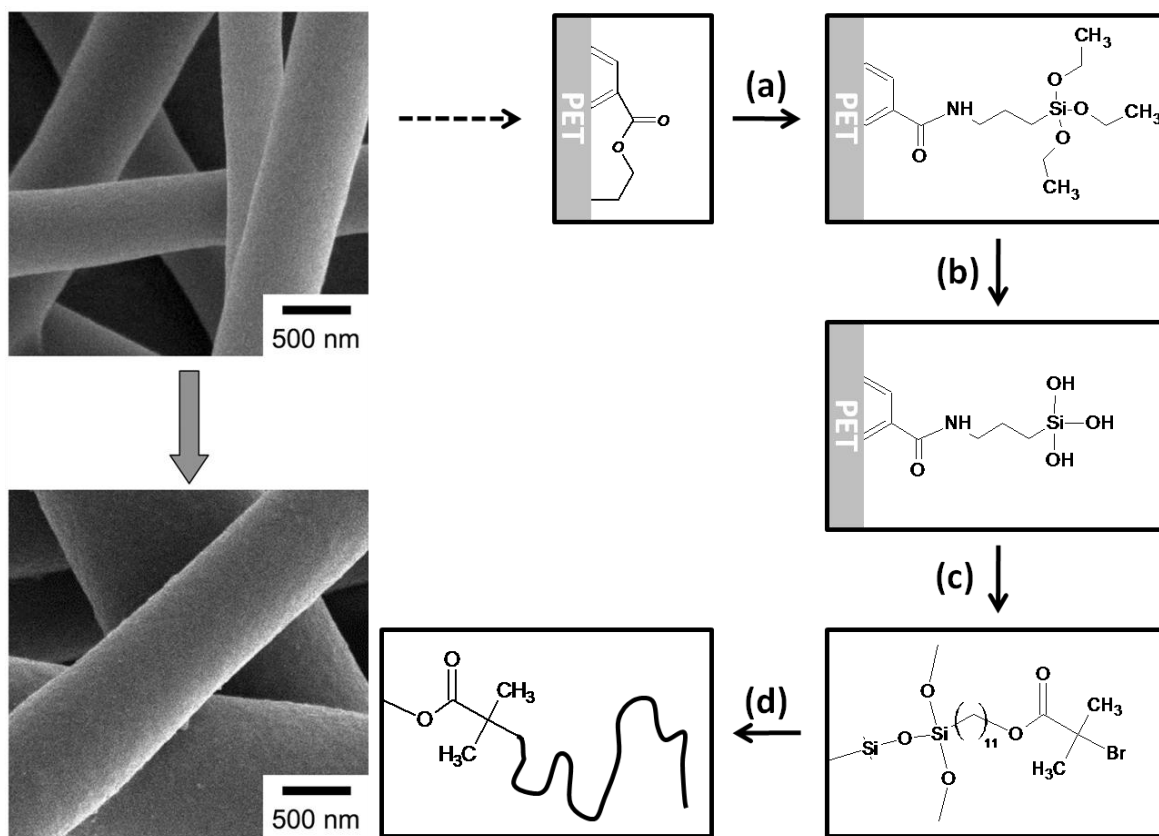


Figure 4.1. Sequence of surface modification steps employed in this study to functionalize electrospun PET microfibers with thermoresponsive PNIPAAm brushes. The steps require deposition and amidation of APTES (a), followed by hydrolysis of the ethoxysilane groups on APTES to form silanol groups (b), which permit attachment of BMPUS (c) and subsequent ATRP of NIPAAm to yield PNIPAAm brushes (d). The top and bottom SEM images display PET and PET-PNIPAAm microfibers, respectively.

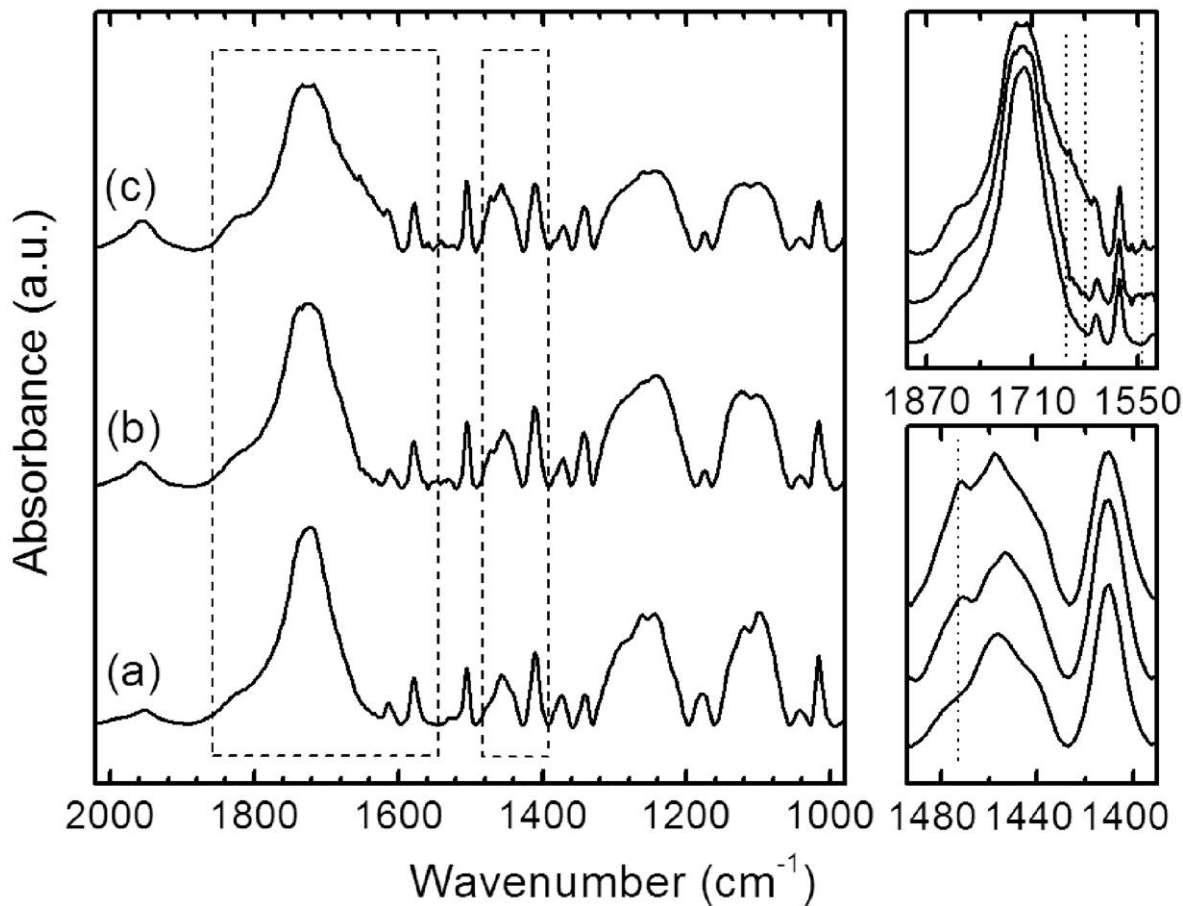


Figure 4.2. FTIR spectra of (a) as-spun PET, (b) PET-SiOH and (c) PET-PNIPAAm microfibers. Spectra arranged in the same order in the expanded views reveal the appearance of peaks associated with the formation of secondary amide moieties (dotted lines; see text for assignments).

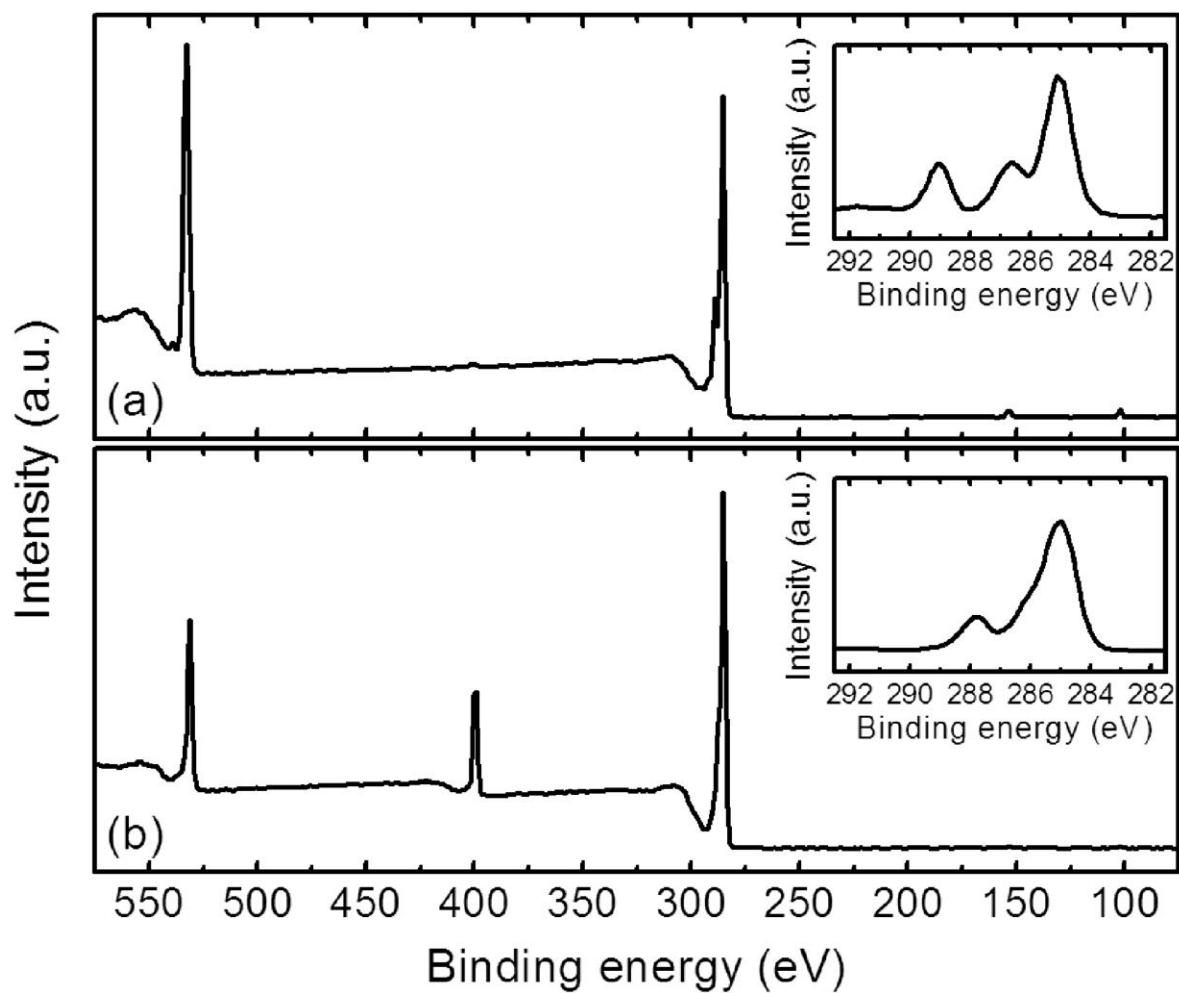


Figure 4.3. XPS spectra of (a) PET-SiOH microfibers and (b) PET-PNIPAAm microfibers. The survey scans confirm the presence of N upon amidation of PET by APTES in (a) and PNIPAAm brush formation in (b). The high-resolution insets show the C_{1s} peak (≈ 285 eV) before (a) and after (b) PNIPAAm brush growth.

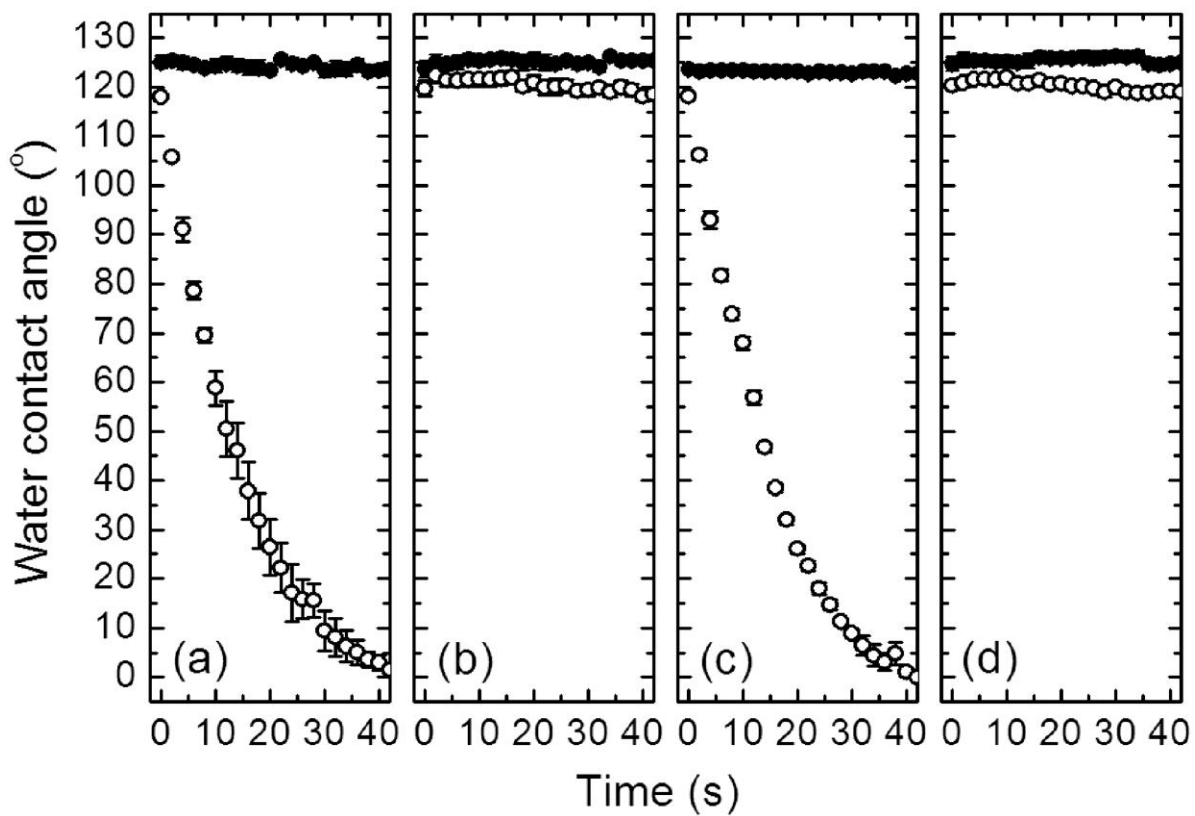


Figure 4.4. Cyclic WCA measurements of as-spun PET (●) and PET-PNIPAAm (○) microfibers at temperatures (in °C) below and above the T_c of PNIPAAm in water: (a) 25, (b) 60, (c) 25, and (d) 60. The error bars correspond to one standard deviation in the data.

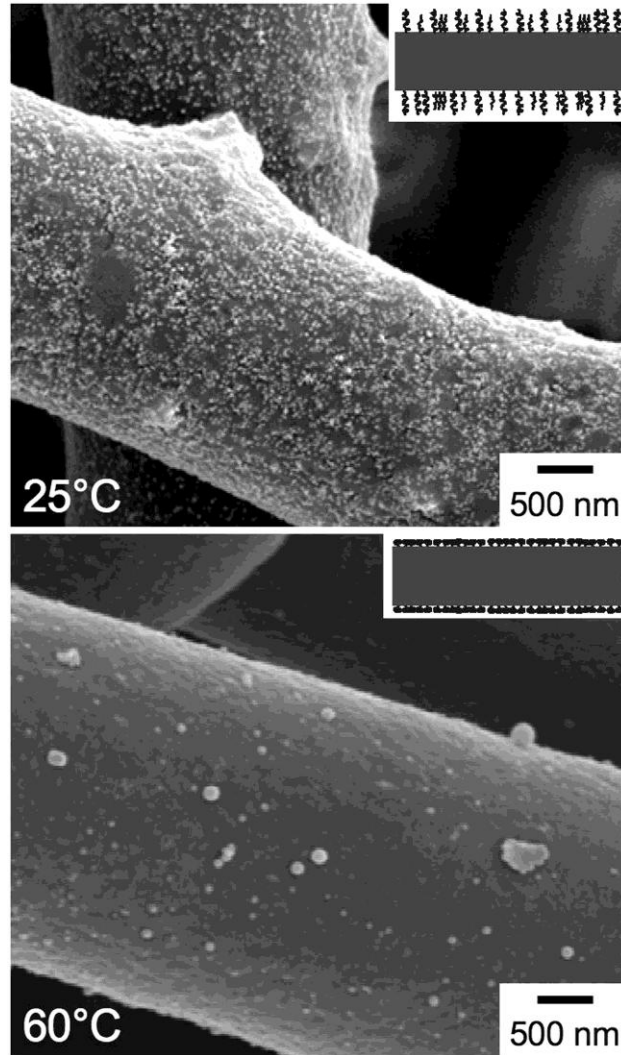


Figure 4.5. SEM images acquired from PET-PNIPAAm microfibers exposed to aqueous suspensions of Au nanoparticles at temperatures (labeled) below and above the T_c of PNIPAAm. The illustrations in the insets (not drawn to scale) portray the conformation of the PNIPAAm brush at each temperature.

CHAPTER 5: GENERATION OF FUNCTIONAL NANO/MICRO FIBERS THROUGH SURFACE-INITIATED POLYMERIZATION

5.1. INTRODUCTION

Electrospinning produces solid fibers with diameters ranging from several tens of nanometers up to several microns; these fibers possess a high surface area to volume ratio and are organized in high porosity mats. These fibers are utilized in a broad range of applications involving (but not limited to) filters^[1], sensors^[2], composite materials, scaffolds in tissue engineering, drug delivery, protective clothing and energy storage applications.^[3, 4] During electrospinning a polymer solution or melt with a sufficiently high viscosity is subjected to an electric field acting between the needle and a collector plate. When the electrostatic forces overcome the surface tension a charged polymer solution/melt jet is emitted from the tip of a conical structure known as the 'Taylor Cone'.^[5] The jet undergoes a whipping process during which any solvent present evaporates and the polymer is collected as a dry, randomly oriented fiber mat on a grounded collector plate.^[6] Electrospinning represents an appealing means of nano/microfiber production due to the relatively simple setup and the ability to tune independent fiber properties on the basis of both processing and solution characteristics.

Although the structural characteristics of electrospun fibers are advantageous, the bulk properties tend to lack functionality that is desired for more multifunctional applications.

One way of overcoming this problem is to create composite nanofibers, allowing the incorporation of two chemically and physically different components which can enhance the mechanical^[7], conductive^[8], and magnetic^[9] properties, just to name a few. However, encapsulated molecules often show reduced activity when constrained in a polymer matrix and may not always exist at the surface.^[10] For example, when antibacterial biocides are blended with a polymer prior to electrospinning their efficacy is limited and leave no potential to attack airborne pathogens.^[11] In contrast, surface modification through the covalent bonding of poly(quarternary ammonium) can create a permanent antibacterial surface on a fiber.^[12]

Because polymer surfaces exhibit typically low surface energy, they need to be treated chemically or physically.^[13] Physical treatment techniques include plasma^[14], the formation of 'layers'^[15], UV treatment^[11], mineralization^[14], etching^[16], or the inclusion of a composite material that is reactive.^[17, 18] Once there are chemically-active groups present on the surface, covalent bonding^[19], immobilization^[20], and electrostatic interactions^[21] can be used to stabilize reactive groups to the surface of the fiber. Modification of just the surface of polymer fibers, not the bulk, can open these materials up for multifunctional applications where the fibers can interact with their environment such as filtering of target molecules^[22], protective textiles^[23], tissue scaffolds^[24], and drug delivery.^[25]

To-date a wide variety of synthetic and natural polymers have been electrospun from pure or blended solutions; including poly(ethylene terephthalate) (PET) fibers. Electrospun PET fibers have been used in several applications that benefited from PET's structural and

mechanical strength, transparency, and resistance to many solvents.^[26] However, like most organic polymers, PET does not possess good adhesion and wetting properties because of its inherently low surface energy (42 mJ/m²). For application of PET fibers, it is desirable to alter the surface properties of PET fibers without compromising their bulk characteristics. In the past, modification of PET surfaces was carried out via various methods, including, chemical treatment (i.e., hydrolysis^[27-30], reduction^[30-32], aminolysis^[28, 31-33], glycolysis^[30], polyelectrolyte deposition^[34], surface graft polymerization after activation of PET surface^[33, 35]) and physical modification (i.e., plasma^[36, 37], ultraviolet/ozone^[37-42], flame^[37], corona treatment^[37, 43, 44], electrical discharge^[45], ion beam bombardment^[46] and laser treatment^[47]). Since most of these surface modification techniques involve, purposefully or inadvertently, polymer degradation, careful selection of experimental conditions is imperative to the successful surface modification of PET without degrading the bulk polymer and its desirable properties.

Grafting polymer brushes on the surfaces represents an attractive approach to modify and control surface properties of materials. Surface-initiated graft polymerization on flat surfaces has been performed successfully with a variety of monomers and polymerization methods.^[48] Numerous studies employed controlled radical polymerization based on atom transfer radical polymerization (ATRP);^[49, 50] ATRP is appealing to material scientists because of its controlled nature and implementation that does not necessitate drastic purification of the chemicals used and can be used to polymerize numerous functional monomers, such as N-

isopropylacrylamide (NIPAAm)^[51], 2-(dimethylamino)ethyl methacrylate (DMAEMA)^[52] and 2-hydroxyethyl methacrylate (HEMA).^[53]

In the past, graft polymerization on PET surfaces was carried out and reported by Roux et al (for styrene)^[35], Farhan et al (for NIPAAm)^[54] and Bech et al^[55] (for styrene). Previous reports utilized various means of attaching the polymerization initiators for “grafting from” polymerization. For instance, Roux et al. attached free radical polymerization initiators via electrostatic interactions and covalent bonding after activation PET surface by saponification and oxidation of PET surface. Farhan et al. and Bech et al. attached ATRP initiators after activating PET surface via plasma treatment and aminolysis, respectively. The major drawback of saponification, aminolysis and plasma treatment is that these methods of activating PET surfaces result in rough topography and severe degradation of the parent material. Because of the micro/nano meter dimensions of electrospun PET fibers keeping materials degradation and surface roughness at a minimum is paramount. In our work, we selected to functionalize PET fiber surfaces by means of 3-aminopropyltriethoxysilane (APTES). Bui et al.^[31], Fadeev et al.^[56], and Xiang et al.^[57] have shown previously that the primary amine group in APTES gets inserted into the PET chain via amidation reaction with negligible degradation of PET. With this reaction mechanism the triethoxysilane groups of APTES are exposed to air interface and hydrolysis of ethoxysilane yields silanol groups on the PET surface that can be used as facile attachment points for the polymerization initiator.

One of the potential applications of PDMAEMA is the generation of functional materials that kill bacteria upon contact after quarternization of pendent dimethylamino groups of

DMAEMA repeat units. PDMAEMA chains quarternized with alkyl halogens possess positive charges and hydrophobic alkyl chains which induce cation exchange and penetration through the cell membrane, respectively. These result in disruption of the membrane integrity and death of bacterial cells.^[58] Antibacterial properties of quarternary ammonium compounds (QAC) were shown earlier both in solution^[59] and on solid surfaces.^[60-63] The latter has an important advantage over the free QACs because they are covalently attached to the substrates, which in turn permits their repeated usability. In addition, it limits uncontrolled biocidal release to the environment.^[64] Quarternization of PDMAEMA on PET fibers with alkyl bromides with different methylene lengths resulted in polycationic brushes on PET fiber surface that has antibacterial properties.

PHEMA brushes on solid surfaces can be used to design new functional objects that resist protein adsorption.^[65] Prevention of protein adsorption is one of the main challenges for certain applications such as artificial implants. Adsorption of biomass on functional material surfaces causes the decay of functionality over time. The biomass starts accumulating starting with protein adsorption and protein denaturation; it takes place on any surface proteins come in contact with. Protein adsorption on various surfaces has been studied extensively over the past several decades; it was shown that that polymeric coatings containing ethylene glycol units resist biomass adhesion due to the presence of a hydration layer.^[65-67] The presence of the hydration layer between the surface and protein molecules forms a surface barrier for proteins to adsorb on the surface.

In this work, we employ the aforementioned modification of PET fibers with APTES in order to create surface-bound hydroxyl groups needed for the attachment of [11-(2-bromo-2-methyl)propionyloxy] undecyltrichlorosilane (BMPUS), which acts as an initiator for ATRP polymerization of polymer brushes. A palette of analytical techniques, including scanning electron microscopy (SEM), x-ray photoelectron spectroscopy (XPS), water contact angle measurements, and Fourier transform infrared (FT-IR) spectroscopy is employed to characterize the properties of the bare PET fibers and to follow the polymerization of DMAEMA and HEMA via ATRP. We also demonstrate the post-polymerization modifications of the PDMAEMA and PHEMA brush-decorated PET fibers via quarternization and fluorination. In addition, antibacterial and protein resistance properties of post-modified PDMAEMA and PHEMA brushes on PET fibers are shown.

5.2. EXPERIMENTAL

5.2.1. MATERIALS

Food-grade recycled PET flakes were kindly supplied by United Resource Recovery Corporation (Spartanburg, SC). Anhydrous toluene, 2-chlorophenol, methanol, iodomethane, iodopropane, iodobutane, bromoethane, bromopropane, bromobutane, trifluoroacetic anhydride (TFAA), fibrinogen from human plasma, 1X-PBS buffer (composition: 0.137M NaCl, 0.0027M KCl, and 0.0119M phosphates), 3-aminopropyltriethoxysilane (APTES), 2-

(dimethylamino)ethyl methacrylate (DMAEMA), 2-hydroxyethyl methacrylate (HEMA), Cu I bromide (CuBr), Cu I chloride (CuCl), bipyridine and N,N,N',N',N''-pentamethyldiethylenetriamine (PMDETA) were purchased from Sigma-Aldrich and used as received. Hexafluoroisopropanol (HFIP) was purchased from Oakwood Products Inc. (Estill, SC). The initiator for atom-transfer radical polymerization, (11-(2-bromo-2-methyl)propionyloxy)-undecyl trichlorosilane (BMPUS) was synthesized as described earlier.^[50]

5.2.2. INSTRUMENTATION

The thicknesses of thin PET films on silicon wafers were measured with variable angle spectroscopic ellipsometer, VASE, (J.A. Woollam) at 70° incidence angle (between the beam and the surface normal) before and after each modification step to determine the approximate PDMAEMA and PHEMA brush thicknesses on the PET fibers. In addition, the thickness polymer brushes grown on silicon wafers were also measured with VASE to determine the extent of modification after quarternization, fluorination, and protein adsorption steps. The surface chemical composition of modified fibers after each modification step was measured with X-ray photoelectron spectroscopy (XPS) at a take-off angle of 90°; under these conditions the probing depth of XPS is \approx 9-10 nm.^[68] Fourier transform infrared (FT-IR) spectroscopy was utilized to monitor chemical changes that took place on the fiber surface after surface modification. The spectra were recorded on a Nicolet 6700 spectrometer after embedding fiber mats into potassium bromide (KBr) pellets in transmission mode and the

data were analyzed by Omnic Spectra software. For each sample 1024 scans were collected after collection of background with a resolution of 4 cm^{-1} . As-spun and modified PET microfibers were coated with $\approx 8 \text{ nm}$ of Au, and their diameter and surface morphology were examined by field-emission scanning electron microscopy (SEM) performed on a JEOL 6400F electron microscope operated at 5 kV.

5.2.3. PET SURFACE MODIFICATION AND POLYMER BRUSH GROWTH

PET flakes were dissolved in hexafluoroisopropanol (HFIP) at different polymer concentrations and electrospun at 10 kV to generate fibers possessing different diameters. PET fiber diameter increased from 450 to 1200 nm, by varying the concentration of the PET in HFIP solution between 6 and 10% (w/w), respectively, as measured by SEM. Thin films of PET on silicon wafers (12 and 180 nm) were prepared via spin-coating from PET solutions in 2-chlorophenol (0.5% and 3% w/w, respectively). The latter set of specimens was employed to follow each modification step by measuring film thickness increments associated with the various chemical modification steps and protein adsorption. The fiber mats and thin films were kept under vacuum at least 48 hrs prior their use in order to remove entrapped solvent.

Surface initiated polymerization initiator, BMPUS, was deposited on PET fiber surface after activation of PET fiber surface with APTES as reported earlier.^[69] Subsequently, functional polymer brushes of PDMAEMA and PHEMA were grown from initiator

decorated PET surfaces by ATRP by following established protocols.^[52] Specifically, 10.09 g HEMA was mixed with 6.81 g of methanol, 1.88 g of water and 0.63 g of bipyridine in an argon purged Schlenk flask and oxygen was removed via three freeze-thaw cycles. After removal of oxygen, CuCl (0.18 g) was added to the solution and 1 more freeze-thaw cycle was carried out. The Schlenk flask with polymerization solution was tightly sealed and transferred to an argon-purged glove box. Fiber mats and silicon substrate-containing ATRP initiators were submerged in the solutions for specific amounts of time. After removal from the polymerization solution, the samples were removed from the polymerization medium, promptly rinsed with methanol, DI water, and sonicated in DI water for 10 minutes.

PDMAEMA brushes on PET fibers and silicon wafers were quarternized with iodomethane, iodopropane, iodobutane, bromoethane, bromopropane and bromobutane in acetonitrile at 60 °C for ≈20 hours. Excess amount of quarternization agents was added to the glass vial containing modified PET fiber mats and acetonitrile to quarternize fully the PDMAEMA brushes. Likewise, PHEMA brushes on PET fibers and silicon wafers were fluorinated with TFAA to study the effect of fluorinated PHEMA (fPHEMA) on protein adsorption. Specifically, TFAA was used to couple fluorinated moieties to the hydroxyl terminus of the pendent group in HEMA. All reactions were carried out at room temperature in the gas phase and the samples were washed with copious amounts of ethanol and water and dried under reduced pressure before protein adsorption experiments. In both post-polymerization modification processes listed above, virgin/unmodified PET fibers were kept in post-polymerization modification reaction mixtures as controls.

5.2.4. TESTING ANTIBACTERIAL BEHAVIOR OF PET FIBERS WITH GRAFTED PDMAEMA BRUSHES

qPDMAEMA decorated PET fibers were subjected to antibacterial testing using a modified ASTM standard (E2149-01 *Standard Test Method for Determining the Antimicrobial Activity of Immobilized Antimicrobial Agents under Dynamic Contact Conditions*). *E. coli* was used as model gram-negative bacteria to test its activity against PET fiber mats modified with quarternized PDMAEMA. *E. coli* bacteria were grown in Lauria-Bertani (LB) medium overnight and the number of bacteria was determined as 0.5×10^9 via UV-Vis spectrometer (optical density 1×10^{-9} cells). After serial dilutions the modified PET fiber mates ($\approx 1 \text{ cm}^2$) were incubated in a bacterial suspension containing 3×10^5 *E. coli* cells in sterile conical tubes at 37 °C while being shaken at 300 rpm for 1 hr. The resultant suspension containing cells was then diluted with LB medium to the desired concentration and plated on L-agar plates. The L-agar plates were then incubated at 37 C for 18 hours, where each surviving cell develops into a distinct colony and thus provides information that governs the bacterial activity. The number of viable cells was determined as colony forming units (CFU) on each L-agar plate.

5.2.5. TESTING PROTEIN RESISTANCE OF PET FIBERS WITH GRAFTED PHEMA BRUSHES

Dry fibrinogen (FIB) from human plasma contains 60% protein, 15% sodium citrate, and 25% sodium chloride. A solution of 0.1 mg/ml solution was prepared at isoelectric point of

FIB (pH=5.5) by dissolving the FIB in 1X-PBS buffer solution. NaN_3 was added to the buffer at a concentration of 0.2% to prevent any bacterial growth during the experiment. Finally, the solution was filtered through a 0.2 μm filter and adsorption studies of FIB were accomplished by incubating substrates in protein solution for 16 hrs at room temperature. Both modified and unmodified PHEMA brushes on PET fibers and silicon wafers were tested along with PET fibers and spin-coated PET on silicon wafers. After incubation, the samples were washed thoroughly with DI water, dried under reduced pressure and stored in glass vials for further characterization. The thickness of the adsorbed FIB layer was measured by ellipsometry on flat samples (silicon wafers) and the nitrogen concentration on all the samples was measured by XPS to determine the amount of adsorbed protein.

5.3. RESULTS AND DISCUSSION

The diameters of electrospun PET microfibers, prepared according to the protocol provided in the Experimental section and measured by SEM, are 450 ± 100 , 800 ± 200 and 1200 ± 300 nm for 6, 8 and 10% (w/w) solutions, respectively, of PET in hexafluoroisopropanol (HFIP). The surfaces of unmodified PET microfibers appear consistently smooth as shown in Figure 5.1. Functional PDMAEMA and PHEMA brushes have been grown on PET microfibers in a sequence of four steps as reported earlier for PNIPAAm brushes.^[69] Briefly, APTES molecules were attached to the PET surface via aminolysis between PET and the primary amine of APTES. Then, the ethoxysilane groups

on APTES were hydrolyzed to generate silanol groups for BMPUS attachment. Finally, PDMAEMA and PHEMA brushes were grown directly from the PET fiber surface via ATRP.

As previously reported by Bui^[31] and Fadeev^[56] the primary amine group in APTES reacts with the ester functionality in PET by forming an amide bond via aminolysis (cf. Figure 5.1). Bui^[31] and Fadeev^[56] claim that the aminolysis of PET with APTES does not degrade the bulk PET as opposed to aminolysis of PET with short alkyl amines. Short alkyl amines can diffuse into the PET fibers and react all the way through the fiber resulting in weaker fibers.^[28, 32] The presence of bulky triethoxysilane group on APTES molecules can hinder the diffusion of APTES into PET by increasing the size of the molecule, changing the solubility parameter of alkyl amine it is attached to and creating a protective layer on PET surface by reducing the diffusion of other APTES molecules through this protective layer. Fadeev^[56] and Youngblood^[70] could not detect the formation of amide groups on PET surface due to the small amount of amide groups in their flat PET samples; the presence of amide groups on the PET-SiOH fiber surfaces was confirmed earlier via FT-IR by Spontak et al. (cite) as a result of increased surface area due to the high surface area to volume ratio of PET fibers. Spontak et al., claimed that the appearance of new peaks located at 1650 cm^{-1} (amide I band) 1550 cm^{-1} (amide II band), 3300 cm^{-1} , 1470 cm^{-1} and 3300 cm^{-1} are due to the formation of secondary amide groups on PET fiber surface. In addition, attachment of APTES and hydrolysis of the exposed triethoxysilane groups by acidic water yielded reactive silanol groups, as confirmed by both the decrease in the water contact angle and thickness

measurements; the quantities were measured on flat spin-coated PET films on silicon wafers. For instance, the water contact angles of APTES modified PET and PET substrate were measured as $50^{\circ}\pm 0.8^{\circ}$ and $71^{\circ}\pm 0.8^{\circ}$, respectively, after hydrolysis in acidic water as opposed to water contact angle of PET substrate that is $75^{\circ}\pm 0.2^{\circ}$. XPS spectra collected on PET-SiOH fibers also revealed a small nitrogen 1s peak located around 400 eV which corresponds to 0.6% nitrogen atom present on PET-SiOH surface.

The BMPUS molecules were attached to the PET-SiOH surface and acted as initiator centers for “grafting from” polymerization of DMAEMA and HEMA. ATRP of DMAEMA and HEMA resulted in dry thicknesses of ≈ 50 and ≈ 45 nm, respectively as determined by ellipsometry from spin-coated thin PET films on silicon wafer. Here we assumed that the thickness of polymer brushes grown on a flat substrate was the same as that produced on the fiber; given the relatively large diameter of the fiber, the curvature of the convex surface is not substantial.

The FT-IR spectra of polymer brushes grown on PET fibers are shown in Figure 5.3 along with spectra of electrospun PET fiber, PDMAEMA and PHEMA brushes on silicon wafers. The IR spectra of PDMAEMA and PHEMA brushes on silicon wafers are shown to point out the chemical changes that took place on the PET fibers. A comparison of FT-IR spectra of PET fibers (dashed lines) with grafted PDMAEMA (blue line on graph a) and PHEMA (blue line on graph b) brushes to PET fiber verify that the brushes grew from the PET fiber surface. For instance, the appearance of new stretching vibrations located at 2770 and 2820 cm^{-1} for PDMAEMA brush on PET fiber (blue line in Figure 5.1a) is due to the C-

H bond of the $-N(CH_3)_2$ group of PDMAEMA. Likewise, the increase in the intensity of the peak located at $\approx 3400\text{ cm}^{-1}$ for PHEMA brush on PET fiber (blue line in Figure 5.1b) is due to the broad $-OH$ peak originating from PHEMA brushes.

The chemical composition of PDMAEMA and PHEMA grafted to PET fiber surface was assessed by XPS; these values are tabulated in Table 5.1. The theoretical values of these parameters were calculated based on the number of atoms present on each repeat unit of both polymers with the assumption that the thickness of the polymer brush is higher than the probing depth of the XPS ($\approx 10\text{ nm}$). The XPS spectra of PET fibers with grafted PDMAEMA and PHEMA brushes are plotted in Figure 5.4. Bare PET fiber exhibits 2 peaks for carbon (285 eV) and oxygen (536 eV). The atomic percentages, calculated based on the area under these curves by utilizing the sensitivity factors, are 73.2 ± 0.4 and 26.8 ± 0.4 for carbon and oxygen, respectively. The growth of PDMAEMA on PET fiber surface resulted in the appearance of the nitrogen peak at 400 eV (cf. Figure 5.4b); this confirms the presence of PDMAEMA brushes on PET fibers. Quantification of XPS spectra results in atomic concentrations of 73.6 ± 0.5 , 7.6 ± 0.1 and 18.8 ± 0.5 for carbon, nitrogen and oxygen, respectively. Introduction of PHEMA brushes on PET fibers did not change the number and position of the peaks located in the XPS spectra, instead, it changed the relative peak areas. The atomic concentration of PHEMA on PET fibers was measured as 70.3 ± 0.5 and 29.7 ± 0.5 for carbon and oxygen, respectively. All these values determined experimentally are in a good agreement with theoretical values calculated via the structural formula of PET, PDMAEMA and PHEMA as tabulated in Table 5.1.

Ellipsometry measurements conducted on flat silicon wafers, as well as independent XPS measurements on fiber surfaces, suggest that the polymer brushes cover the PET surfaces, as the dry thickness of the brush exceeds the probing depth of XPS (≈ 10 nm). The characteristic “XPS fingerprints” of PET fibers disappeared after grafting PDMAEMA and PHEMA brushes from the high resolution XPS spectra of as shown in Figure 5.4 insets. The introduction of the peak for C-N bond located at 286.1 eV resulted in broadening of the peaks corresponding to the C-C (at 285.0 eV) and C-O (at 286.6 eV) bonds for PDMAEMA brushes on PET fiber. For PHEMA brushes on PET fiber, the intensity of the peak located at 286.6 corresponding to C-O bond increased relative to C-C bond at 285.0 eV compared to the XPS spectra of bare PET fiber. Besides, the peak located at 290.0 eV corresponding to O-C=O groups of acrylates were still present for both PDMAEMA and PHEMA brushes on PET fibers.^[71]

Post-polymerization modification reactions were carried out on polymer brushes grafted to PET fibers to further functionalize the PET fibers to introduce antibacterial and protein resistance properties. Several quarternization agents with different alkyl lengths, including, iodomethane, iodopropane, iodobutane, bromoethane, bromopropane and bromobutane, were used to introduce positive charges on the qPDMAEMA pendent groups, which causes death of gram negative bacteria. Similarly, TFAA was used to fluorinate the -OH groups of PHEMA brushes and thus investigate the effect of fPHEMA on protein resistance. The morphology of PET fibers after post-polymerization modification reactions are shown in Figure 5.5. From that data it is clear that the samples conserved the fibrous structure.

Chemical modification of PDMAEMA and PHEMA brushes on silicon wafers with quarternization and fluorination agents results in multiple changes in the IR spectra of the samples. For example, the stretching vibrations located at 2770 and 2820 cm^{-1} for PDMAEMA brush on silicon wafer (black line in Figure 5.6a) is due to the C-H bond of the $-\text{N}(\text{CH}_3)_2$ group of PDMAEMA; these peaks disappear after quarternization reaction (red line in Figure 5.6a). In addition, water adsorbed by the more hydrophilic qPDMAEMA brushes gave rise to the peak located at $\approx 3400 \text{ cm}^{-1}$. Similarly, new peaks for carbonyl groups of C-CO-CF (at 1789 cm^{-1}) bond and C-F bonds (at 1224 and 1157 cm^{-1}) appear after conversion of PHEMA to fPHEMA (red line in Figure 5.6b). In addition, the $-\text{OH}$ groups of PHEMA are consumed during the fluorination reaction with TFAA and the peak for the $-\text{OH}$ group located at ≈ 3400 disappears. Examination of FT-IR spectra of PDMAEMA and PHEMA brushes grafted on the PET fibers reveals the aforementioned characteristic peaks in their spectra both before and after quarternization and fluorination as shown in Figure 5.6 (blue and olive lines). All of these characteristics serve as a proof of the presence of functional polymer brushes on PET fibers.

The chemical compositions of polymer brushes on PET fibers and silicon wafers were determined with XPS after quarternization and fluorination reactions. Examination of the XPS spectra reveals the appearance of new peaks for iodine or bromine and fluorine after quarternization of PDMAEMA and fluorination of PHEMA. Quantification of the XPS spectra yields the atomic concentrations tabulated in Table 5.2 for qPDMAEMA (with alkyl bromides) and Table 5.3 for fPHEMA. Interestingly, the concentration of bromine in the

qPDMAEMA brushes on PET fiber is $\approx 50\%$ greater than that in the qPDMAEMA brushes on silicon wafers. Initially, it was thought that alkyl bromides were adsorbed on and/or absorbed by the PET fibers. However, the examination of the XPS spectra of control PET fibers kept in the quarternization reaction medium revealed that no adsorption of alkyl bromides on the PET fibers took place during the course of the quarternization reaction. Therefore, we claim that the extent of quarternization is greater for the PDMAEMA brushes on PET fibers because of the convex nature of the PET fibers, which results in lower steric hindrance for the quarternization reaction as compared to flat surfaces. The same behavior is also valid for quarternization reaction of PDMAEMA brushes on PET fibers and silicon wafers with alkyl iodides (data not shown).

The extent of fluorination of PHEMA brushes on PET fibers and silicon wafers is similar and these values are in agreement as reported earlier for TFAA modified PHEMA brushes.^[65] This behavior differs from the aforementioned results obtained for qPDMAEMA brushes, but this may be due to the smaller size of TFAA compared to quarternization agents and the quantitative gas phase reaction of TFAA, where it can diffuse through the brush and react with the $-\text{OH}$ groups of PHEMA without any restriction. Arifuzzaman et al.,^[65] reported that the surface concentration of TFAA modified PHEMA brushes on silicon wafer does not change as a function of XPS take-off angle, which suggests that the PHEMA brushes were modified homogeneously throughout the XPS probing depth. This behavior implies that the gas phase reaction of TFAA is quantitative with PHEMA brushes on silicon wafer and supports the similar surface composition obtained for fPHEMA brushes on PET

fibers and silicon wafers. In addition, fluorination with TFAA did not affect the surface composition of the bare PET fibers kept in fluorination medium as evidenced from the XPS data.

The presence of quarternary ammonium compounds endows the surfaces with antibacterial character due to the existence of cationic groups which disrupt the cell membrane and cause lysis of bacterial cells.^[72] For instance, for gram negative bacteria, the phosphate groups of the lipopolysaccharide molecules of the bacterial outer membrane are stabilized with divalent cations via bridging and neutralizing, which would otherwise strongly repel each other. Bacteria lose their natural counterions and its outer membrane is de-stabilized upon interacting with QACs due to the electrostatic compensation of these charges with cationic charges of the QACs. Therefore, it is claimed that the release of counterions from bacteria's cell wall initiates the death of the bacteria as illustrated in Figure 5.7a.^[64,72,73] Quarternization of PDMAEMA on PET fibers with alkyl bromides with different methylene lengths resulted in string (quenched) polycationic brushes on PET fiber surface. As reported earlier, the antibacterial efficacy of a quarternary ammonium compound depends on the type of the extent of quarternization and the length of the alkyl chain in the quarternization agent. The extent of quarternization regulates the number of positive charges available that interact with the cell wall of the bacteria while the length of the alkyl chain in the quarternization agent affects the efficacy by perturbing the cell membrane by penetrating through the cell wall. Bacteria killing efficiency increases generally with increasing the length of alkyl spacer but it deteriorates after 6 methylene units.^[61] The presence of

polycationic qPDMAEMA brushes on PET fibers provides antibacterial properties against *E. coli* as shown in Figure 5.7b as the number of CFUs on the agar plates are lower in qPDMAEMA than those which belong to PDMAEMA brushes grafted to PET fibers. In addition, the antibacterial efficiency of qPDMAEMA brushes grafted to PET fibers increases with increasing alkyl lengths of the quarternization agent from bromoethane to bromobutane as shown in Figure 5.7c.

The resistance of PHEMA and fPHEMA to protein adsorption on flat surfaces has been studied in recent years; it is shown that the presence of PHEMA^[53] and fPHEMA^[65] brushes reduces protein adsorption as a function of grafting density and molecular weight. Here we study the protein resistance on the PHEMA brushes on PET fibers before and after fluorination with TFAA. A series of samples including PHEMA brushes on PET fibers, fPHEMA brushes on PET fibers, PHEMA brushes on silicon wafer, fPHEMA brushes on silicon wafer, bare PET fibers and bare PET fibers exposed to TFAA were incubated in FIB solution for 16 hours. The adsorption of fibrinogen on flat substrates was monitored with ellipsometer by measuring the thickness of the brushes (on silicon wafers) and monitoring the concentration of nitrogen with XPS (on fibers and silicon wafers) which originates only from the FIB layer. A comparison of the thickness values of FIB layer on flat surfaces indicates that the presence of PHEMA brushes minimizes protein adsorption dramatically. As shown in Figure 5.8, the thickness of FIB falls down from ≈ 4 nm to almost 0 nm after grafting PHEMA brushes on silicon wafer. The reduction in FIB layer thickness is further evidenced by the XPS data that reveal nitrogen concentration decrease from 15.1 % down to

0.6%. The amount of FIB adsorbed on spin-coated PET on silicon wafer was comparable to the amount adsorbed on bare silica wafer, but the concentration of adsorbed FIB on PET fiber was lower than the spin-coated PET on silicon wafer based on the surface nitrogen concentration. This may be due to the presence of small number of pin-holes on the spin-coated PET film, where the FIB may have sensed silicon substrate underneath the PET film (even the film was smooth and uniform based on visual inspection and optical constants obtained from ellipsometry model calculations). The introduction of PHEMA brushes on PET fibers prevents the absorption of FIB according to surface nitrogen concentration. In addition, the fluorination of PHEMA brushes on silicon wafer improves slightly the protein resistance based on both thickness and XPS data. However, the concentration of nitrogen increases slightly due to fluorination of PHEMA brushes on PET fibers. The nitrogen content of the TFAA exposed PET fiber does not change because TFAA did not cause any changes to the PET fibers according to surface nitrogen concentration determined from XPS spectra.

5.4. CONCLUSIONS AND FUTURE WORK

In this work, we demonstrated that PET fiber surfaces can be modified via the amidation reaction of the amine group on APTES with the ester group of PET and subsequent growth of functional polymer brushes (PDMAEMA and PHEMA) via ATRP. Post-polymerization modification of these functional polymer brushes was carried out by quarternization and

fluorination reactions for PDMAEMA and PHEMA, respectively. Protein resistance of PHEMA and anti-bacterial properties of quarternized PDMAEMA brushes on electrospun PET fibers are discussed. These functional fibers can be used as advanced materials such as affinity filters, antibacterial clothing and sensors. We aim to use the modified PET fiber mats as multi-use filters for water purification applications. Therefore, the stability of polymer brushes on PET fiber will be tested as a function of pH and temperature of the surrounding water.

5.5. REFERENCES

- [1] R. Gopal, S. Kaur, C. Y. Feng, C. Chan, S. Ramakrishna, S. Tabe, T. Matsuura, *Journal of Membrane Science* **2007**, 289, 210.
- [2] S. K. Chae, H. Park, J. Yoon, C. H. Lee, D. J. Ahn, J.-M. Kim, *Advanced Materials* **2007**, 19, 521.
- [3] Y. Dzenis, *Science* **2004**, 304, 1917.
- [4] L. Chen, L. Bromberg, J. A. Lee, H. Zhang, H. Schreuder-Gibson, P. Gibson, J. Walker, P. T. Hammond, T. A. Hatton, G. C. Rutledge, *Chemistry of Materials*, 22, 1429.
- [5] G. Taylor, *Proceedings of the Royal Society of London Series a-Mathematical and Physical Sciences* **1969**, 313, 453.
- [6] Y. M. Shin, M. M. Hohman, M. P. Brenner, G. C. Rutledge, *Applied Physics Letters* **2001**, 78, 1149.
- [7] F. Ko, Y. Gogotsi, A. Ali, N. Naguib, H. H. Ye, G. L. Yang, C. Li, P. Willis, *Advanced Materials* **2003**, 15, 1161.
- [8] E. J. Ra, K. H. An, K. K. Kim, S. Y. Jeong, Y. H. Lee, *Chem. Phys. Lett.* **2005**, 413, 188.
- [9] A. Wang, H. Singh, T. A. Hatton, G. C. Rutledge, *Polymer* **2004**, 45, 5505.
- [10] K. M. Sawicka, P. Gouma, *Journal of Nanoparticle Research* **2006**, 8, 769.
- [11] C. Yao, X. S. Li, K. G. Neoh, Z. L. Shi, E. T. Kang, *Applied Surface Science* **2009**, 255, 3854.
- [12] J. Lin, S. Y. Qiu, K. Lewis, A. M. Klibanov, *Biotechnology and Bioengineering* **2003**, 83, 168.
- [13] J. P. Deng, L. F. Wang, L. Y. Liu, W. T. Yang, *Progress in Polymer Science* **2009**, 34, 156.

- [14] J. L. Chen, B. Chu, B. S. Hsiao, *Journal of Biomedical Materials Research Part A* **2006**, 79A, 307.
- [15] K. Muller, J. F. Quinn, A. P. R. Johnston, M. Becker, A. Greiner, F. Caruso, *Chemistry of Materials* **2006**, 18, 2397.
- [16] C. C. Ho, W. S. Chen, T. Y. Shie, J. N. Lin, C. Kuo, *Langmuir* **2008**, 24, 5663.
- [17] N. D. Luong, I. S. Moon, D. S. Lee, Y. K. Lee, J. D. Nam, *Materials Science & Engineering C-Biomimetic and Supramolecular Systems* **2008**, 28, 1242.
- [18] F. X. Dong, Z. Y. Li, H. M. Huang, F. Yang, W. Zheng, C. Wang, *Materials Letters* **2007**, 61, 2556.
- [19] P. Ye, Z. K. Xu, J. Wu, C. Innocent, P. Seta, *Biomaterials* **2006**, 27, 4169.
- [20] Z. G. Wang, L. S. Wan, Z. K. Xu, *Soft Matter* **2009**, 5, 4161.
- [21] N. D. Winblade, I. D. Nikolic, A. S. Hoffman, J. A. Hubbell, *Biomacromolecules* **2000**, 1, 523.
- [22] S. Kaur, Z. Ma, R. Gopal, G. Singh, S. Ramakrishna, T. Matsuura, *Langmuir* **2007**, 23, 13085.
- [23] S. Lee, S. K. Obendorf, *Textile Research Journal* **2007**, 77, 696.
- [24] S. Liao, R. Murugan, C. K. Chan, S. Ramakrishna, *Journal of the Mechanical Behavior of Biomedical Materials* **2008**, 1, 252.
- [25] J. Zeng, A. Aigner, F. Czubyko, T. Kissel, J. H. Wendorff, A. Greiner, *Biomacromolecules* **2005**, 6, 1484.
- [26] I. S. Chronakis, B. Milosevic, A. Frenot, L. Ye, *Macromolecules* **2006**, 39, 357.
- [27] J. Dave, R. Kumar, H. C. Srivastava, *Journal of Applied Polymer Science* **1987**, 33, 455.
- [28] M. S. Ellison, L. D. Fisher, K. W. Alger, S. H. Zeronian, *Journal of Applied Polymer Science* **1982**, 27, 247.
- [29] E. M. Saunders, S. H. Zeronian, *Journal of Applied Polymer Science* **1982**, 27, 4477.

- [30] W. Chen, T. J. McCarthy, *Macromolecules* **1998**, *31*, 3648.
- [31] L. N. Bui, M. Thompson, N. B. McKeown, A. D. Romaschin, P. G. Kalman, *The Analyst* **1993**, *118*, 463.
- [32] Y. Avny, L. Rebenfeld, *Journal of Applied Polymer Science* **1986**, *32*, 4009.
- [33] R. Fukai, P. H. R. Dakwa, W. Chen, *Journal of Polymer Science Part A: Polymer Chemistry* **2004**, *42*, 5389.
- [34] L. Dauginet, A. S. Duwez, R. Legras, S. Demoustier-Champagne, *Langmuir* **2001**, *17*, 3952.
- [35] S. Roux, S. Demoustier-Champagne, *Journal of Polymer Science Part A: Polymer Chemistry* **2003**, *41*, 1347.
- [36] Y. L. Hsieh, E. Y. Chen, *Industrial & Engineering Chemistry Product Research and Development* **1985**, *24*, 246.
- [37] M. Strobel, M. J. Walzak, J. M. Hill, A. Lin, E. Karbasheski, C. S. Lyons, *Journal of Adhesion Science and Technology* **1995**, *9*, 365.
- [38] J. M. Hill, E. Karbasheski, A. Lin, M. Strobel, M. J. Walzak, *Journal of Adhesion Science and Technology* **1995**, *9*, 1575.
- [39] M. J. Walzak, S. Flynn, R. Foerch, J. M. Hill, E. Karbasheski, A. Lin, M. Strobel, *Journal of Adhesion Science and Technology* **1995**, *9*, 1229.
- [40] D. O. H. Teare, C. Ton-That, R. H. Bradley, *Surface and Interface Analysis* **2000**, *29*, 276.
- [41] C. Ton-That, D. O. H. Teare, P. A. Campbell, R. H. Bradley, *Surface Science* **1999**, *435*, 278.
- [42] A. E. Ozcam, K. Efimenko, C. Jaye, R. J. Spontak, D. A. Fischer, J. Genzer, *Journal of Electron Spectroscopy and Related Phenomena* **2009**, *172*, 95.
- [43] M. Strobel, C. S. Lyons, J. M. Strobel, R. S. Kapaun, *Journal of Adhesion Science and Technology* **1992**, *6*, 429.
- [44] J. M. Pochan, L. J. Gerenser, J. F. Elman, *Polymer* **1986**, *27*, 1058.
- [45] D. Briggs, D. G. Rance, C. R. Kendall, A. R. Blythe, *Polymer* **1980**, *21*, 895.

- [46] P. Bertrand, Y. Depuydt, J. M. Beuken, P. Lutgen, G. Feyder, *Nuclear Instruments & Methods in Physics Research Section B-Beam Interactions with Materials and Atoms* **1987**, 19-2, 887.
- [47] E. Arenholz, J. Heitz, M. Wagner, D. Bauerle, H. Hibst, A. Hagemeyer, *Applied Surface Science* **1993**, 69, 16.
- [48] R. Barbey, L. Lavanant, D. Paripovic, N. Schuwer, C. Sugnaux, S. Tugulu, H. A. Klok, *Chemical Reviews* **2009**, 109, 5437.
- [49] K. Matyjaszewski, H. Dong, W. Jakubowski, J. Pietrasik, A. Kusumo, *Langmuir* **2007**, 23, 4528.
- [50] K. Matyjaszewski, P. J. Miller, N. Shukla, B. Immaraporn, A. Gelman, B. B. Luokala, T. M. Siclovan, G. Kickelbick, T. Vallant, H. Hoffmann, T. Pakula, *Macromolecules* **1999**, 32, 8716.
- [51] Y. K. Jhon, R. R. Bhat, C. Jeong, O. J. Rojas, I. Szleifer, J. Genzer, *Macromolecular Rapid Communications* **2006**, 27, 697.
- [52] R. R. Bhat, J. Genzer, *Applied Surface Science* **2006**, 252, 2549.
- [53] R. R. Bhat, B. N. Chaney, J. Rowley, A. Liebmann-Vinson, J. Genzer, *Advanced Materials* **2005**, 17, 2802.
- [54] T. Farhan, W. T. S. Huck, *European Polymer Journal* **2004**, 40, 1599.
- [55] L. Bech, T. Elzein, T. Meylheuc, A. Ponche, M. Brogly, B. Lepoittevin, P. Roger, *European Polymer Journal* **2009**, 45, 246.
- [56] A. Y. Fadeev, T. J. McCarthy, *Langmuir* **1998**, 14, 5586.
- [57] J. H. Xiang, P. X. Zhu, Y. Masuda, K. Koumoto, *Langmuir* **2004**, 20, 3278.
- [58] K. Lewis, A. M. Klibanov, *Trends in biotechnology* **2005**, 23, 343.
- [59] S. Lenoir, C. Pagnouille, C. Detrembleur, M. Galleni, R. Jerome, *Journal of Polymer Science Part A-Polymer Chemistry* **2006**, 44, 1214.
- [60] J. Huang, R. R. Koepsel, H. Murata, W. Wu, S. B. Lee, T. Kowalewski, A. J. Russell, K. Matyjaszewski, *Langmuir* **2008**, 24, 6785.

- [61] J. Lin, S. Y. Qiu, K. Lewis, A. M. Klibanov, *Biotechnology progress* **2002**, *18*, 1082.
- [62] H. Murata, R. R. Koepsel, K. Matyjaszewski, A. J. Russell, *Biomaterials* **2007**, *28*, 4870.
- [63] J. Y. Huang, H. Murata, R. R. Koepsel, A. J. Russell, K. Matyjaszewski, *Biomacromolecules* **2007**, *8*, 1396.
- [64] R. Kugler, O. Bouloussa, F. Rondelez, *Microbiology-Sgm* **2005**, *151*, 1341.
- [65] S. Arifuzzaman, A. E. Ozcam, K. Efimenko, D. A. Fischer, J. Genzer, *Biointerphases* **2009**, *4*, FA33.
- [66] S. Herrwerth, W. Eck, S. Reinhardt, M. Grunze, *Journal of the American Chemical Society* **2003**, *125*, 9359.
- [67] M. Mrksich, G. M. Whitesides, *Annual Review of Biophysics and Biomolecular Structure* **1996**, *25*, 55.
- [68] J. C. Vickerman, I. Gilmore, *Surface Analysis: the principal techniques*, John Wiley & Sons, Ltd., Chichester **2009**.
- [69] A. E. Ozcam, K. E. Roskov, J. Genzer, R. J. Spontak, *Submitted*.
- [70] J. A. Howarter, J. P. Youngblood, *Macromolecules* **2007**, *40*, 1128.
- [71] G. Beamson, D. J. Briggs, *High resolution XPS of organic polymers : the Scienta ESCA300 database*, Wiley, Chichester England ; New York **1992**.
- [72] P. Gilbert, L. E. Moore, *Journal of applied microbiology* **2005**, *99*, 703.
- [73] Y. Endo, T. Tani, M. Kodama, *Applied and Environmental Microbiology* **1987**, *53*, 2050.

5.6 TABLES AND FIGURES

Table 5.1. Atomic concentration of PET fiber surface with grafted PDMAEMA and PHEMA brushes

Polymer brush on PET fiber		Atomic concentration on PET fiber surface (%)		
		Carbon	Nitrogen	Oxygen
PET fiber	Theoretical	71.4	—	28.6
	Experimental	73.2±0.4	—	26.8±0.4
PDMAEMA	Theoretical	72.7	9.1	18.2
	Experimental	73.6±0.5	7.6±0.1	18.8±0.5
PHEMA	Theoretical	66.7	—	33.3
	Experimental	70.3±0.5	—	29.7±0.5

Table 5.2. Atomic concentration of PET fiber surface with grafted PDMAEMA brushes after quarternization post-polymerization modification reactions

Sample name	Atomic concentration on PET fiber surface (%)			
	Carbon	Nitrogen	Oxygen	Bromine
qPDMAEMA on PET fiber with bromoethane	73.9	5.3	17.3	3.5
qPDMAEMA on SiOx wafer with bromoethane	71.2	7.2	19.2	2.4
Bromoethane on PET fiber (control)	71.6	—	28.4	—
qPDMAEMA on PET fiber with bromopropane	74.6	5.7	16.5	3.2
qPDMAEMA on SiOx wafer with bromopropane	72.4	6.7	18.2	2.7
Bromopropane on PET fiber (control)	73.7	—	26.3	—
qPDMAEMA on PET fiber with bromobutane	74.0	5.2	17.3	3.5
qPDMAEMA on SiOx wafer with bromobutane	73.5	6.4	17.8	2.3
Bromobutane on PET fiber (control)	72.6	—	27.4	—

Table 5.3. Atomic concentration of PET fiber surface with grafted PHEMA brushes after fluorination post-polymerization modification reactions

Sample name	Atomic concentration on PET fiber surface (%)		
	Carbon	Oxygen	Fluorine
fPHEMA on PET fiber	54.4±0.2	25.0±0.2	20.6±0.1
fPHEMA on silicon wafer	53.2	24.6	22.2
TFAA treated PET fiber (control)	74.2	25.3	0.5

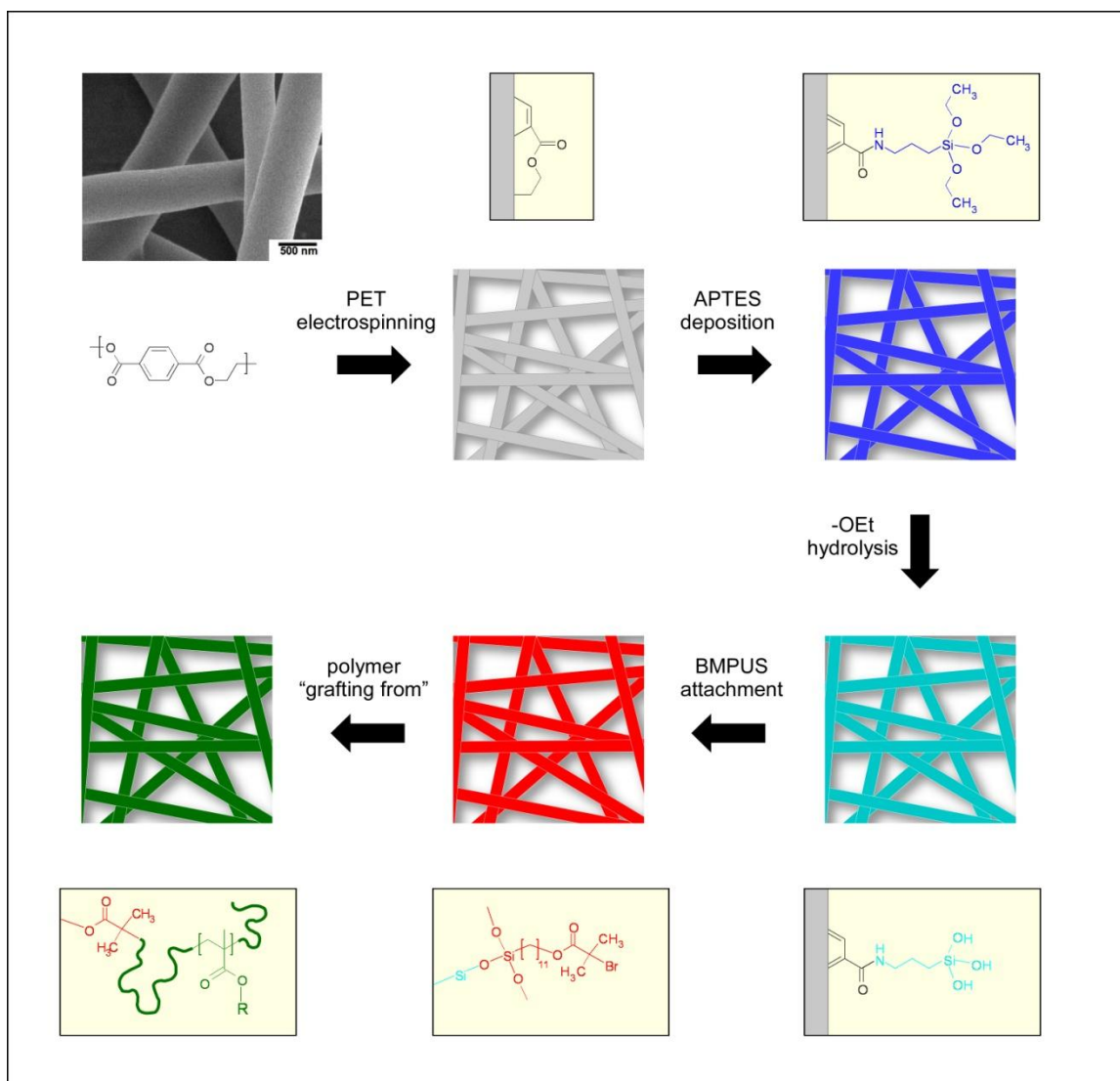


Figure 5.1. Surface modification and polymer brush growth steps on PET fibers. Two polymers were grafted to the PET surface: PHEMA ($\text{R}=(\text{CH}_2)_2\text{OH}$) and PDMAEMA ($\text{R}=(\text{CH}_2)_2\text{N}(\text{CH}_3)_2$).

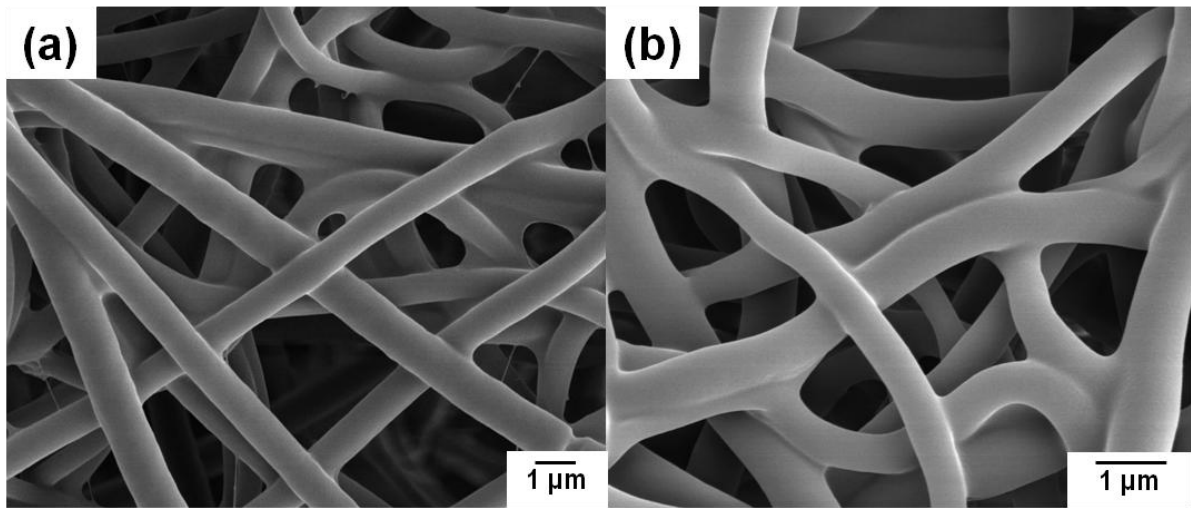


Figure 5.2. Morphology of PET fibers after PDMAEMA (a) and PHEMA (b) brush growth.

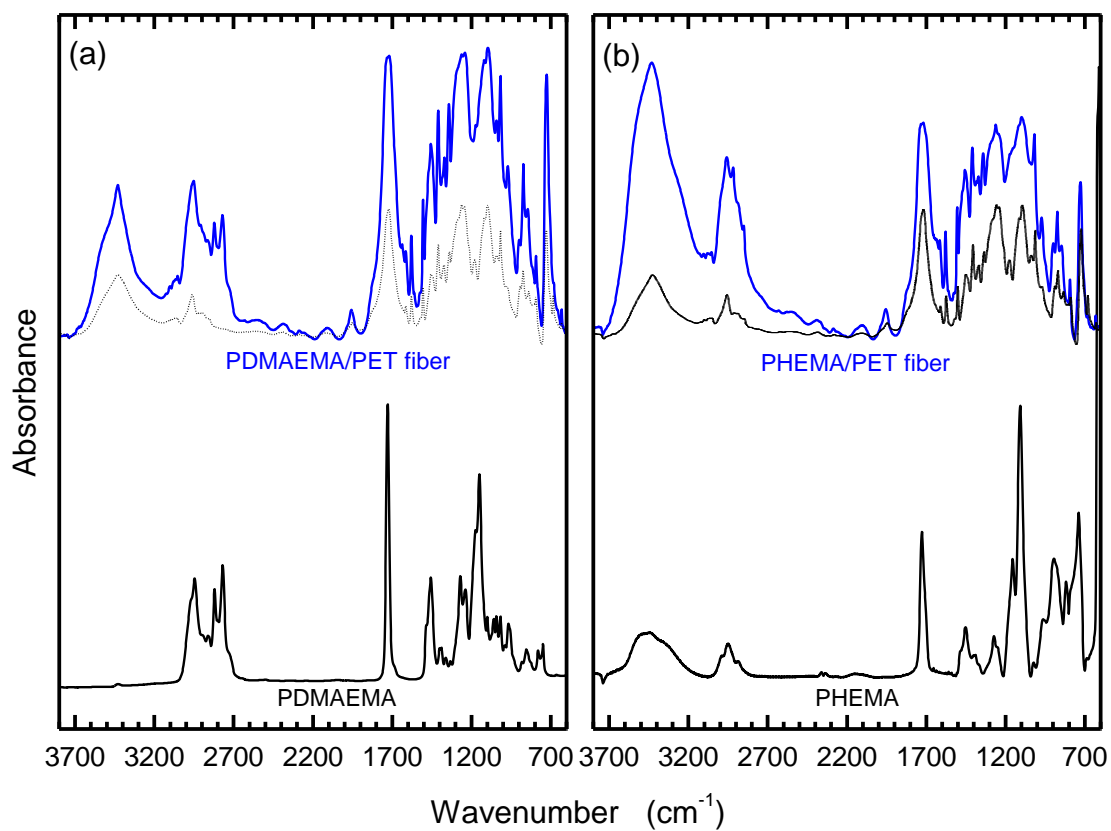


Figure 5.3. FT-IR spectra of PDMAEMA (a) and PHEMA (b) brushes on PET fibers (solid blue line) along with PDMAEMA and PHEMA homopolymers (solid black line) and PET fiber (dotted black line).

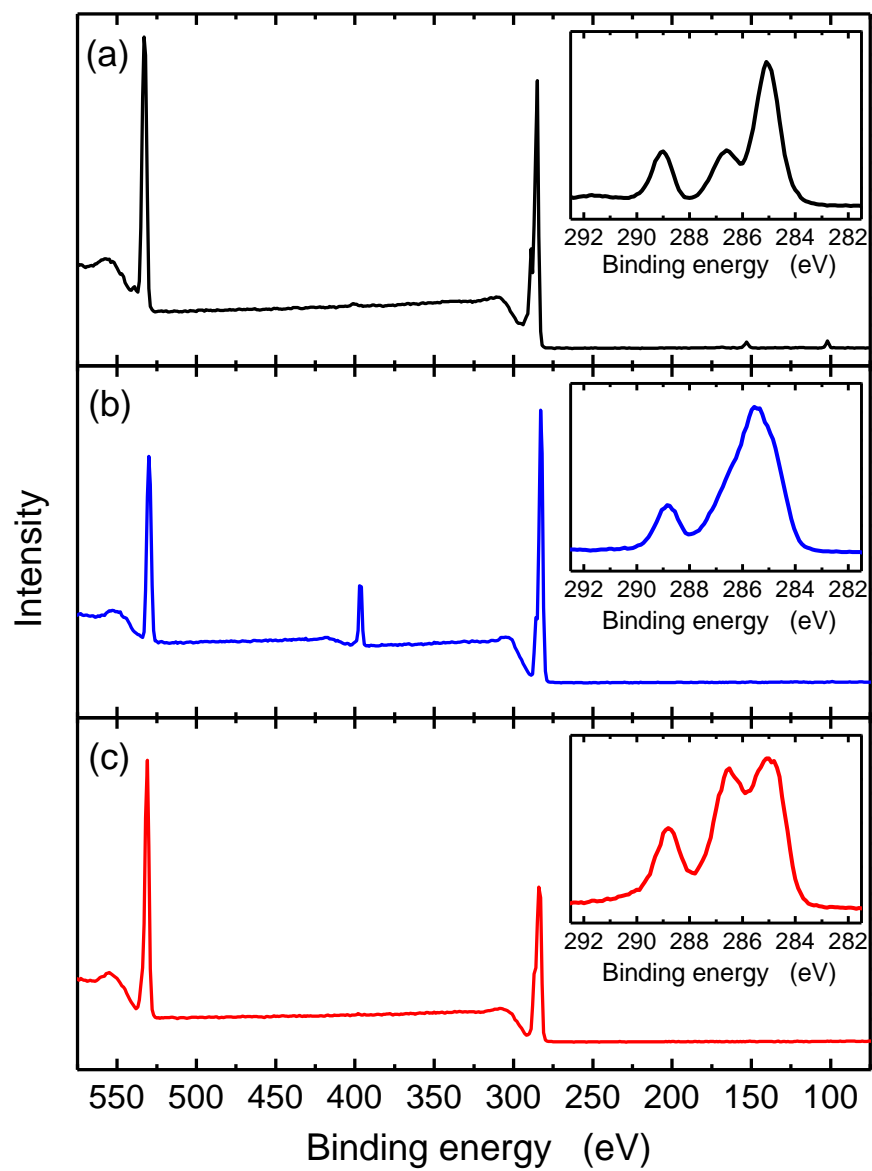


Figure 5.4. PET fiber (a), PDMAEMA brush attached to PET fiber (b) and PHEMA brush attached to PET fiber (c).

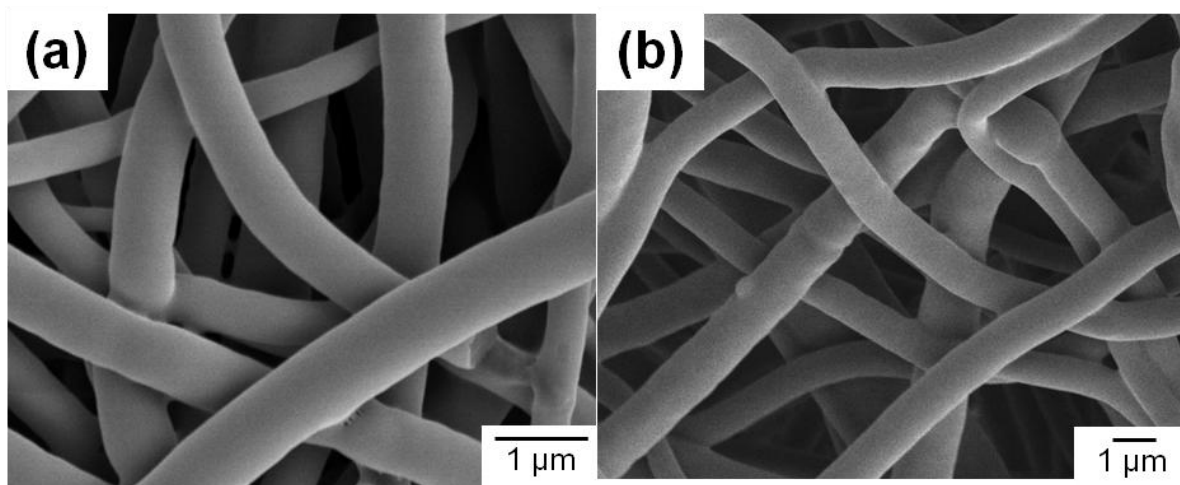


Figure 5.5. Morphology PDMAEMA (a) and PHEMA (a) brushes on PET fibers after quaternization and fluorination reactions, respectively.

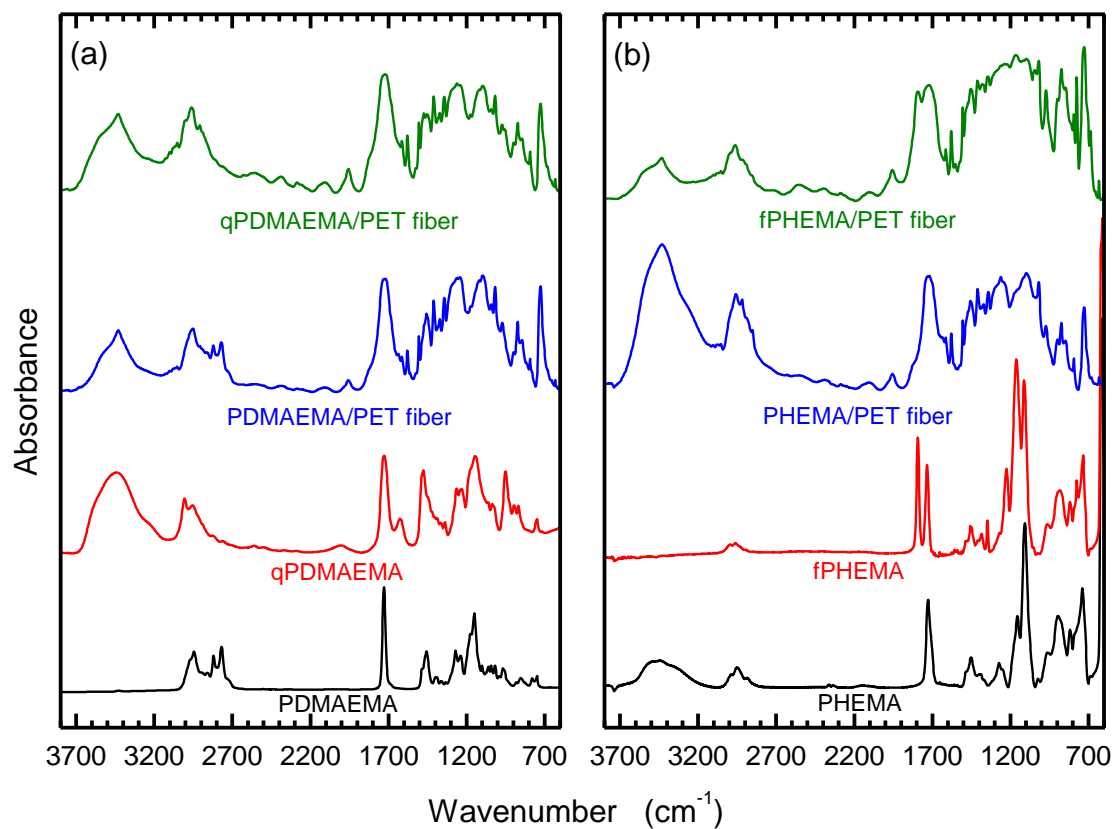


Figure 5.6. FT-IR spectra of PDMAEMA (a) and PHEMA (b) brushes on PET fibers along with PDMAEMA and PHEMA homo-polymers and PET fiber before and after quaternization and fluorination reactions.

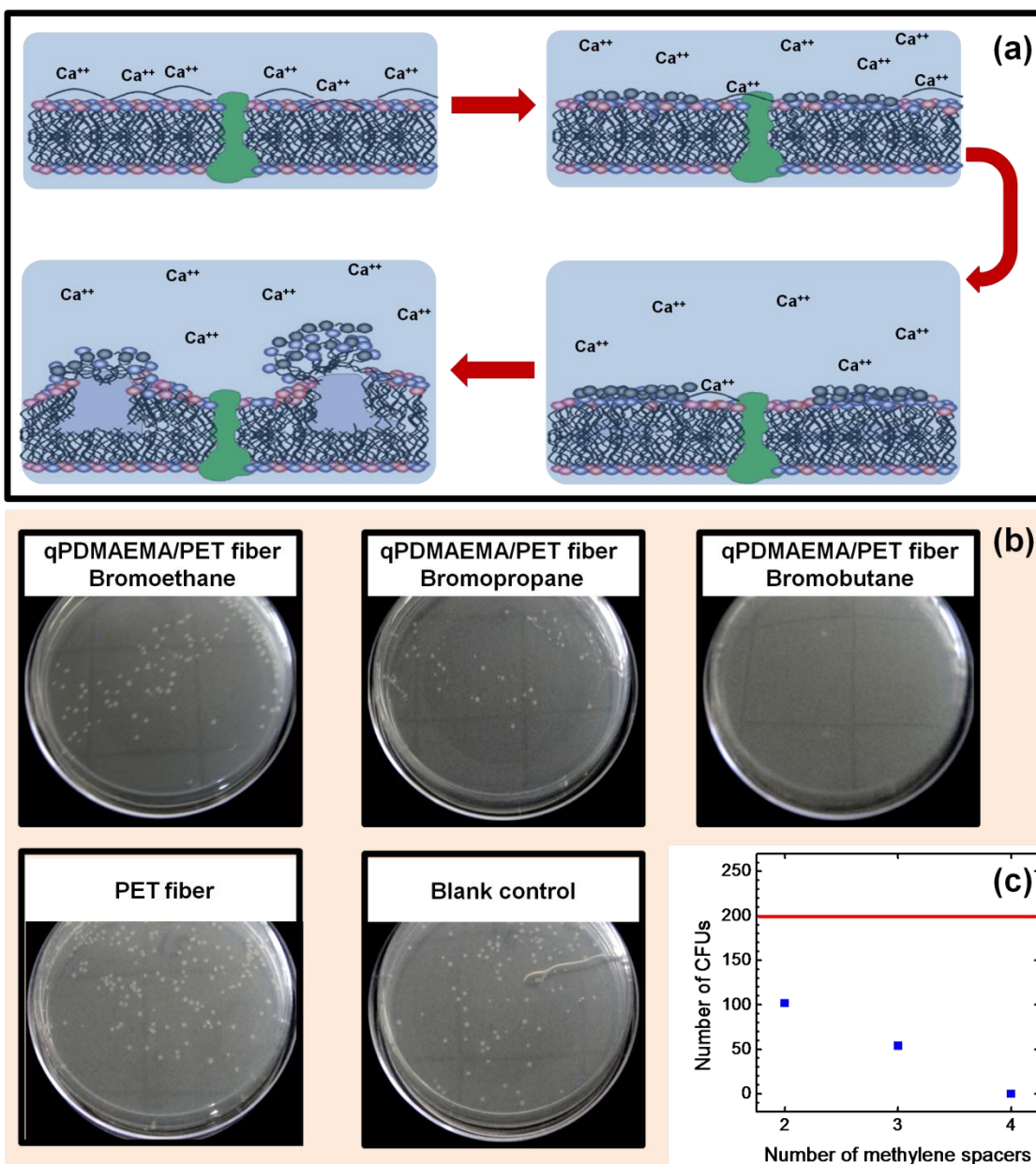


Figure 5.7. Mechanism of bacterial lysis upon interaction with quarternized PDMAEMA (a), photos of agar plates those shows the number of colony forming units after incubation at 37 C for 18 hours (b) and number of CFUs on agar plates after exposing the bacteria to qPDMAEMA brushes on PET fibers. The red line is the initial number of *E. coli* exposed to qPDMAEMA brushes on PET fibers (c) (Scheme in Figure 7.a was obtained from ref. 72).

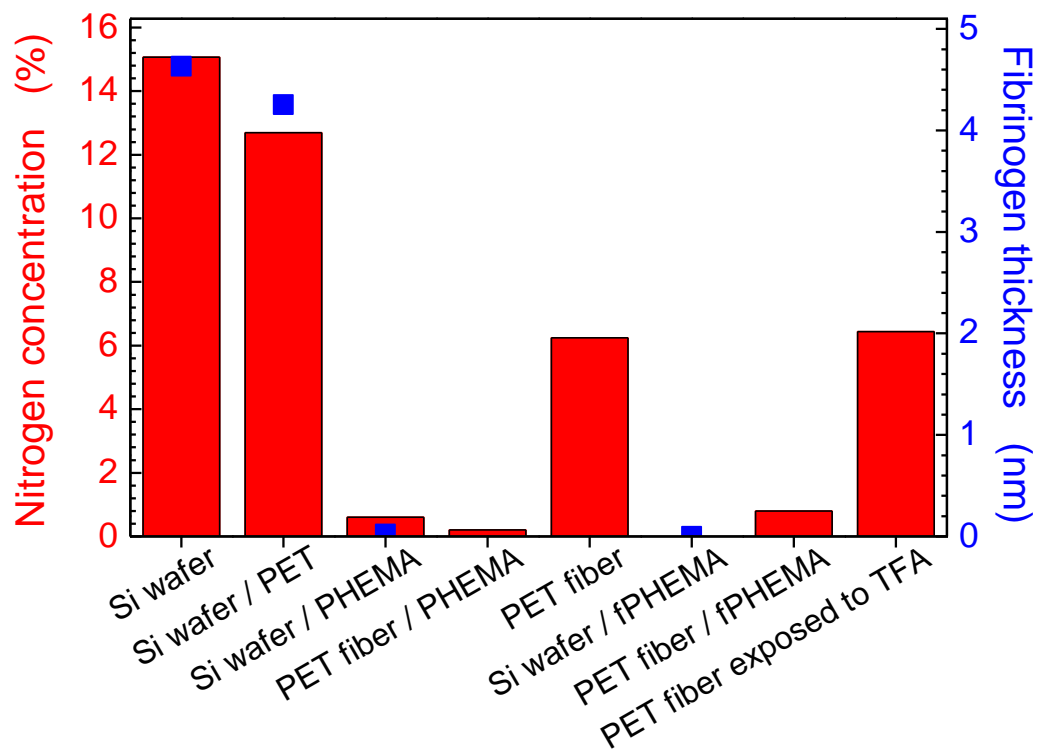


Figure 5.8. Surface nitrogen concentration on modified PET fibers and flat substrates and corresponding thickness after fibrinogen adsorption experiments.

CHAPTER 6: MECHANICAL ALLOYING OF POLY(ETHYLENE TEREPHTHALATE) (PET) WITH LAYERED SILICATES

6.1. INTRODUCTION

In the past decade, hybrid organic-inorganic nanocomposites have attracted great attention,^[1-5] especially those derived from polymers modified with layered silicates (e.g., nanoclays). Nanocomposites are hybrid materials wherein at least one of the components possesses a characteristic nanoscale dimension. Layered silicates constitute excellent candidates in this regard since they tend to measure a nanometer or so in thickness and up to micrometers in their lateral dimensions. Homogeneous dispersion of such high-aspect-ratio platelets in a polymer matrix yields polymer-clay nanocomposites (PCNs).^[6, 7] Incorporation of a small amount of such nanoclay platelets to a polymer matrix can promote significant enhancement in several properties, including mechanical, thermal and barrier properties, solvent resistance and flame retardancy. Three different morphologies of PCNs can develop after processing, depending on the degree of platelet dispersion.^[1, 8, 9] 1) A phase-separated morphology, or conventional composite, is obtained if the distance between silicate layers is not affected by compounding. 2) An intercalated morphology results if individual polymer chains diffuse through silicate layers and increase the interlayer distance without destroying the order of the silicate layers. 3) An exfoliated morphology, which is highly sought, is

achieved only when the ordering of the silicate layers is destroyed and the silicate layers are individually and homogeneously dispersed within a polymer matrix. In this case, improvements in barrier, thermal and mechanical properties are maximized.^[10-12]

Three different routes have been traditionally utilized to generate PCNs: in-situ polymerization^[3, 13], solution intercalation^[14] and melt compounding.^[15, 16] Of these, melt intercalation is preferable because it is environmentally benign (by avoiding the use of volatile organic compounds, VOCs), successful for more polymer-clay combinations than other intercalation routes and scalable to meet industrial needs.^[1, 5] However, the inherent hydrophilic nature of layered silicates necessitates modification of the platelet surfaces to render them organophilic through cationic exchange of the Na⁺ ions in the interlayer spacing. The ion exchange reaction also provides a decrease in silicate-silicate interactions that, in turn, favors platelet separation. Conventional routes by which to form organic/inorganic nanocomposites require surface modification of constituent substances, high extrusion temperatures or high concentrations of solvent, as previously mentioned in Chapter 3. All these requirements could, in principle, be avoided by mechanically alloying the nanoclay platelets with dry polymer powder in the solid state. Mechanical alloying could disperse layered silicates homogeneously in a polymer matrix due to continuous fracture and welding of polymer powders, as displayed schematically in Figure 6.1. For these reasons, we explore the viability of forming PCNs derived from poly(ethylene terephthalate) (PET) in the solid state without any surface modification or melt extrusion.

High-energy ball-milling is a material modification process that relies on mechanical forces such as impacting and shearing generated by steel ball bearings upon rapid vibration. Ball-milling is performed in the solid state (although liquids, gases or supercritical fluids could be added as desired) and constitutes a highly nonequilibrium processing route to create metastable materials by physical means.^[17] It was first introduced by Benjamin and co-workers^[18] in the late 1960s to produce complex oxide dispersion-strengthened alloys. Mechanical milling and mechanical alloying are subcategories of high-energy ball-milling and have been used to refine the nano/microstructure of materials, extend solid solubility, homogenize the composition of mixtures, and create metastable crystalline phases and amorphous glasses.^[17] While mechanical milling refers to the processing of a single species to change its nano/microstructure, mechanical alloying involves the compounding of different materials at atomic or molecular levels.^[19] During milling, two competing processes, namely, fracturing and cold-welding, occur in which solid particles fracture, weld and continuously re-fracture and re-weld, as illustrated in Figure 3.1.

Mechanical milling of organic materials was first reported by Abagyan et al.,^[20] who investigated the formation of radicals upon mechanical attrition. However, studies regarding the mechanical milling of polymers were not performed systematically until Shaw et al.^[21, 22] investigated the effect of mechanical attrition on a variety of polymers in the 1990s. Their seminal work was followed and largely broadened by several independent studies aimed at examining the mechanical milling of polymers,^[19, 23-25] the mechanical alloying of polymer blends^[26-30] and the mechanical alloying of polymers and fillers.^[31-34] The history of ball-

milling natural and organically-modified layered silicates (kaolinite,^[35, 36] montmorillonite^[37-40], ripidolite and beidellite^[41]) dates back to the late 1990s and were performed to determine the restructuring of platelets after high-energy processing. Frost et al.^[35, 36], Hrachova et al.^[42], Perrin-Sarazin et al.^[39], Dellisanti et al.^[40] and Sonni et al.,^[41] all claimed that the structure of layered silicates changed and clay stacks delaminated during high-energy ball-milling. That is, increasing milling time causes delamination and fracture of clay particles, followed by a continued loss of crystallinity and finally amorphization of the clay structure. On the other hand, Ramadan et al.^[38] studied the effect of high-energy ball-milling on the restructuring of natural montmorillonite (Na⁺ MMT), as well as an organically-modified montmorillonite (Cloisite 30B, which consists of MMT with a quaternary ammonium salt (methyl, tallow, bis-2-hydroxyethyl, quaternary ammonium) as a surfactant). They reported a decrease in the intensity of the basal reflections by x-ray diffractometry (XRD), which signifies loss of clay stacking and ordering. In addition, they claimed that the crystal structures of the both natural and organically-modified clays did not deteriorate due to high-energy milling on the basis of XRD patterns at high scattering angles (θ). According to transmission electron microscopy (TEM), fragmentation of clay platelets occurred, resulting in platelets measuring ≈ 50 nm.

Thus far, mechanical alloying of layered silicates with polymers has been conducted in the presence of solvent^[43, 44] and in the solid state.^[34, 45, 46] Lu et al.^[44] have facilitated exfoliation of organically-modified montmorillonite platelets in an epoxy matrix by ball milling in ketone. They confirmed the formation of epoxy/MMT nanocomposites by XRD

and TEM and reported improved mechanical properties. Likewise, Koo et al.^[43] prepared polyvinylpyrrolidone/montmorillonite nanocomposites by ball milling via a solution intercalation route in the presence water. They reported PCNs that were optically transparent and exhibited improved thermal resistance. Shao et al. have likewise investigated the preparation of polypropylene/vermiculite^[46] and nylon-6/natural clay^[45] nanocomposites via high-energy milling in the solid state. According to their findings, exfoliation of the layered silicates resulted in improved thermal and mechanical properties. Mangiacapra et al.^[34] have demonstrated that pectin/montmorillonite nanocomposites can be prepared via high-energy ball milling and yield PCNs with improved mechanical, thermal and barrier properties. Lastly, Perrin-Sarazin et al.^[39] have explored the preparation of polypropylene/montmorillonite nanocomposites in the solid state via high-energy ball milling with improved thermomechanical properties.

6.2. EXPERIMENTAL

6.2.1. MATERIALS

Recycled PET flakes generated by the Un-PET caustic solution process were kindly supplied by the United Resource Recovery Corporation (URRC) (Spartanburg, SC). Virgin PET (vPET) pellets, obtained from Voridian as bottle-grade (CB12) resin with a molecular weight of 30 kDa, were also milled in a separate steel vials. *O*-chlorophenol and acetone

were purchased from Sigma (St. Louis, MO). Natural montmorillonite (Na⁺ MMT) was obtained from Southern Clay Products (Gonzales, Texas).

6.2.2. BALL MILLING

Mechanical milling and alloying were performed using a Spex 8000 shaker mill at ambient temperature. Hardened steel vials were loaded with 3 g of polymer for mechanical milling and 3 g of 5% (w/w) clay/polymer mixture for mechanical alloying with 30 g of steel balls (10 balls with 7.9 mm and 9 balls with 6.4 mm in diameter). Samples were loaded in a glove box under argon to reduce the extent of oxidative degradation during milling. While the temperature inside the vial cannot be measured during milling, Balik et al.^[19] have speculated that the local temperature of the polymer during milling may be slightly above the glass transition temperature (75°C) of PET.

6.2.3. SOLUTION VISCOSITY

The molecular weight of milled PET was determined from intrinsic viscosity (IV) measurements performed on dilute solutions of PET in *o*-chlorophenol in a Rheotek RPV-1 automated Ubbelohde viscometer operated at 25°C. Mark-Houwink constants are reported as $K = (3.0 \times 10^{-4} \text{ dL/g})(\text{g/mol})^{-a}$ with $a = 0.77$ under the present experimental conditions.

6.2.4. DIFFERENTIAL SCANNING CALORIMETRY

Differential scanning calorimetry (DSC) experiments were conducted using a TA Instruments Q1000 calorimeter equipped with a refrigerated cooling system. Experiments were performed in a 4-part cycle: heating from 40 to 280°C at 10°C/min, held at 280°C for 3 min and cooled to 40°C at 10°C/min, held at 40°C for 3 min and repeated. The glass transition temperatures (T_g s) and crystallinities were determined from inflection points and areas under the melting/crystallization peaks, respectively.

6.2.5. THERMOGRAVIMETRIC ANALYSIS

Thermo gravimetric analysis (TGA) experiments were performed using a TA Instruments Q500 unit operated under air and nitrogen atmosphere. The samples were heated from 25 to 900°C in platinum pans at a heating rate of 10°C/min.

6.2.6. X-RAY DIFFRACTION

X-ray diffractometry was performed on powder specimens using a Rigaku Smartlab diffractometer and Cu K α radiation ($\lambda=0.1541\text{nm}$). The generator was operated at 40 kV and 44 mA. Samples were scanned from 2.0° to 10.0° 2 θ at a scan rate of 1°C/min.

6.2.7. ELECTRON MICROSCOPY

The morphology of ball-milled rPET and rPET/clay samples was examined by scanning electron microscopy (SEM). Prior to surface imaging the milled powders were sputter-coated with ~8 nm gold. Surface images were acquired on a JEOL 6400F field-emission electron microscope operated at an accelerating voltage of 5 kV. The morphology of clay platelets in the rPET matrix after ball milling was examined by TEM. Ball-milled rPET/clay powders were melt-pressed to obtain specimens measuring ≈ 1 mm thick for ultramicrotomy, which was conducted at ambient temperature on a Leica Ultracut 7 and yielded sections approximately 120 nm thick. Images were collected on a field-emission Hitachi HF2000 electron microscope operated at an accelerating voltage of 200 kV.

6.3. RESULTS AND DISCUSSION

The molecular weights of the rPET and vPET grades were investigated as a function of milling time from IV measurements at 25 °C in *o*-chlorophenol, and they were found to decrease with increasing milling time, as shown in Figure 6.2. The initial molecular weights of rPET and vPET were approximately 25.9 and 29.0 kDa, respectively. After milling for 16 h, the reduction in molecular weight is slightly more pronounced for vPET than rPET (57.8% vs. 53.4%). This finding is in agreement with prior observations of Smith et al.,^[47] who reported a faster and greater decrease in molecular weight for higher molecular weight

poly(methyl methacrylate) milled at cryogenic temperatures. In contrast, Bai et al.^[19] observed a lower 46.7% decrease in the molecular weight of vPET milled for 16 h at ambient temperature. According to Bai et al.,^[19] the shape of the molecular weight distribution curve does not change as a result of milling. While we have not measured the molecular weight of alloyed PET/clay samples, Zhu et al.^[32] have demonstrated that the degradation of PET is more extensive after alloying PET with silica particles at cryogenic temperatures. We therefore expect to see a similar trend with alloyed PET/clay mixtures. Although the properties of milled PET generally deteriorate as the molecular weight decreases, the decrease in molecular weight in the presence of clay may conversely improve the properties of the resultant PCNs, as shown by Frankowski et al.^[15], who demonstrated an increase in modulus upon degradation of polystyrene chains in the presence of organically-modified clay. The reason for this observation was attributed to enhanced intercalation of the clay platelets in the presence of shorter polymer chains. In our case the increased population of endgroups that develop upon milling may interact more favorably with clay surfaces and edges, thereby promoting a net improvement in several properties.

The degree of crystallinity was calculated by integrating the melting or crystallization peaks and dividing by the heat of fusion for 100% crystalline PET (160 J/g).^[19] The crystallization of milled polymers and alloyed polymer/clay mixtures reveals an interesting trend, as is evident in Figure 6.3. During the 1st heating cycle the apparent crystallinity is considerably higher than the subsequent heating and cooling cycles, presumably because of a locally oriented but rotationally disordered morphology, which is a result of mechanical

milling/alloying. These oriented and possibly extended chains form crystals measured during the first heating, which serves to increase the apparent crystallinity. After melting, the thermal history of the polymers is largely erased and the specimens resemble unmilled polymers.^[19, 25] Since we are mostly interested in assessing the effect of clay on crystallization, we do not correct the 1st heat of melting by subtracting the heat of crystallization. In experiments with mechanically milled polymers, the degree of crystallinity is observed to increase with increasing milling time, which agrees with the molecular weight results provided earlier. In contrast, milling experiments with PET/clay mixtures reveal that the crystallinity does not change appreciably with milling time. This is contrary to what we expect on the basis of experiments involving the milling of pure PET. Since Zhu et al.^[32] have found that PET degrades faster after alloying with silica particles, one might expect that the shorter PET chains would crystallize more readily, although no measurements were conducted to discern if this was indeed the case. While we cannot offer a conclusive explanation for this behavior at the present time, we hypothesize that the trend may be due to a confining effect of clay platelets or the formation of a very large number of microcrystallites because of the large number of nucleation sites. Clearly more work is required to elucidate this unexpected behavior.

In general, PET exhibits a 2-step degradation mechanism when heated in an oxidative environment: the 1st and 2nd degradation temperatures correspond to the first and second peaks evident in the derivative weight loss curve for thermal and thermoxidative degradation, respectively (cf. Figure 6.4). The thermal degradation behavior of mechanically milled PET

and mechanically alloyed PET/clay samples is summarized in Figure 6.5. In Figure 6.5a the mass of residue remaining after full pyrolysis is presented. Onset degradation temperatures measured for milled and alloyed samples are comparable at each milling time, as evidenced by the data provided in Figures 5.5b and 5.5c. An interesting feature of Figure 6.5b is the presence of an initial reduction in the onset degradation temperature up to 6 h of milling, followed by a gradual increase with increasing milling time. While the onset peak degradation temperatures of these samples are similar (data not shown), the 2nd peak degradation temperatures for alloyed PET/clay samples are far below those of milled PET. It cannot simply reflect a decrease in molecular weight, because a 57% reduction in molecular weight (16 h of milling) results in a difference in 2nd peak degradation temperature of 30-50 °C. However, the difference of the 2nd peak degradation temperature between milled and alloyed samples after only 4 h of treatment ranges from 40 to 60 °C (which would be anticipated to indicate a substantially greater reduction in molecular weight).

The crystalline order of the clay platelets before and after milling alone and with PET was assessed by XRD and corresponding patterns are displayed in Figure 6.6. The natural Na⁺ montmorillonite has a clearly delineated peak centered at 7.5°, which corresponds to an interlayer spacing of 1.17 nm. This is in agreement with previous studies^[34, 43] of this nanoclay. For comparison, a physical mixture of Na⁺ MMT with ball-milled rPET powder was prepared at a concentration of 5 wt%. The XRD pattern of this mixture exhibits a less pronounced peak still centered at 7.5°, as expected. As shown in this figure, mechanical-alloying 5 wt% Na⁺ MMT with rPET results in the complete disappearance of the (001) basal

peak for Na⁺ MMT after 2, 5, 8 and 16 h. Disappearance of the (001) reflex has been previously observed^[34, 39, 43] in polymer/clay specimens subjected to ball milling and is attributed to homogenous dispersion and exfoliation of clays. An interesting and unexpected observation in Figure 6.6 is the development of a new peak centered at 4.1°, which corresponds to 2.2 nm, after 16 h of alloying. This feature is larger than any of the nanoclay characteristics over the range of 2θ examined and therefore is most likely not indicative of the nanoclay. If this is the case, it may reflect milling-induced orientation of the PET chains, which agree with the extended chain model proposed by Bai et al.^[19]

A series of TEM images acquired from microtomed thin sections of specimens composed of 5 wt% Na⁺ MMT in rPET after 2 and 16 h of mechanical alloying are presented in Figure 6.7 and are consistent with the XRD patterns displayed in Figure 6.6. Dispersion of clay platelets in the rPET matrix occurs as a result of solid-state deformation, and the presence of both exfoliated and intercalated clay platelets are visible in these micrographs. The average length of the Na⁺ MMT platelets is ≈100 and ≈70 nm after 2 and 16 h, respectively, whereas the corresponding platelet thickness at the low end is about 3-4 nm, which corresponds to a stack of 2-3 platelets.

6.4. CONCLUSION AND FUTURE WORK

We plan to continue our work on milling PET/clay mixtures in order to elucidate the mechanism of composite formation. We already milled rPET, PET, rPET+5%Na⁺ MMT and

vPET+5%Na⁺ MMT to compare the effect of milling time on rPET and vPET and to compare the effect of clay addition and milling time on thermal degradation, crystallization, gas barrier and mechanical properties. Our preliminary results reveal an interesting crystallization behavior for milled polymers with and without clay. Our results also revealed that the extent of crystallization of the mechanically milled PET samples increases with increasing milling time. We tentatively attribute this to the decrease in molecular weight of the PET samples, which facilitates the formation of crystals due to easier packing of polymer chains. The extent of crystallization of alloyed PET/clay mixture does not seem to change with increasing milling time. We detect “double melting peaks” for both PET+clay and PET only samples, a phenomenon that we do not completely comprehend at this time. The distribution of clay platelets in the PET matrix was determined by using x-ray diffraction (XRD) and transmission electron microscopy (TEM). The (001) basal peak for Na⁺ MMT located at 7.5° disappeared after mechanical alloying with rPET for all mechanical alloying periods studied. In addition, TEM micrographs showed exfoliated individual clay platelets along with intercalated platelets. We appreciate that an understanding the morphology of such composites by TEM is paramount because the size of the inorganic clay platelets were reduced during milling, which led to a corresponding decrease in the original high aspect ratio of the clay platelets in the PET matrix. We also measured the sorption behavior of CO₂ through films prepared from PET/clay composites prepared by mechanical alloying. However, no effect of clay platelets was seen and this may be due to the reduced aspect ratio of the clay platelets as a result of mechanical alloying.

So far we have shown exfoliation, intercalation and dispersion of Na⁺ MMT platelets in rPET matrix that took place in solid state at a concentration of 5% (w/w) with no organic-modification of the montmorillonite. This process may be feasible on large scale to prepare rPET/clay nanocomposites to improve barrier and mechanical properties of rPET. Mechanical alloying of rPET and Na⁺ MMT can be carried out in large scales and higher clay loadings to prepare masterbatches, which can be compounded with rPET flakes during melt processing to prepare rPET/clay nanocomposites.

The melt rheology studies of mechanically milled rPET and vPET and mechanically alloyed rPET/Na⁺ MMT and vPET/Na⁺ MMT did not result in substantial conclusions due to the degradation problems of the polymers. In addition, relatively small amounts of mechanically alloyed/milled samples (≈ 3 gr) did not allow repetition of these experiments. Working in larger scales would allow preparation of larger and multiple specimen discs for rheology studies which would allow substantial understanding of the effect of clay platelets on melt flow of the mechanically alloyed samples.

6.5. REFERENCES

- [1] Y. C. Ke, P. Stroeve, *Polymer-Layered Silicate and Silica Nanocomposites*, Elsevier, Amsterdam **2005**.
- [2] E. P. Giannelis, *Advanced Materials* **1996**, *8*, 29.
- [3] K. Yano, A. Usuki, A. Okada, *Journal of Polymer Science Part A: Polymer Chemistry* **1997**, *35*, 2289.
- [4] A. Usuki, N. Hasegawa, M. Kato, S. E. R. Kobayashi, *Polymer-Clay Nanocomposites*, **2005**.
- [5] A. Okada, A. Usuki, *Macromolecular Materials and Engineering* **2006**, *291*, 1449.
- [6] P. C. LeBaron, Z. Wang, T. J. Pinnavaia, *Applied Clay Science* **1999**, *15*, 11.
- [7] E. Manias, A. Touny, L. Wu, K. Strawhecker, B. Lu, T. C. Chung, *Chemistry of Materials* **2001**, *13*, 3516.
- [8] H. Ishida, S. Campbell, J. Blackwell, *Chemistry of Materials* **2000**, *12*, 1260.
- [9] K. A. Carrado, *Applied Clay Science* **2000**, *17*, 1.
- [10] R. A. Vaia, H. Ishii, E. P. Giannelis, *Chemistry of Materials* **1993**, *5*, 1694.
- [11] D. L. VanderHart, A. Asano, J. W. Gilman, *Chemistry of Materials* **2001**, *13*, 3796.
- [12] T. J. Pinnavaia, *Science* **1983**, *220*, 365.
- [13] K. Yano, A. Usuki, A. Okada, T. Kurauchi, O. Kamigaito, *Journal of Polymer Science Part A: Polymer Chemistry* **1993**, *31*, 2493.
- [14] Z. Shen, G. P. Simon, Y.-B. Cheng, *Polymer* **2002**, *43*, 4251.
- [15] D. J. Frankowski, S. A. Khan, R. J. Spontak, *Advanced Materials* **2007**, *19*, 1286.
- [16] A. G.-R. O. M. A. Sanchez-Solis, *Macromolecular Symposia* **2003**, *192*, 281.

- [17] C. C. Koch, in *Materials science and technology : a comprehensive treatment - 1991*, (Eds: R. W. Cahn, P. Haasen, E. J. Kramer).
- [18] J. S. Benjamin, *Metallurgical Transactions* **1970**, *1*, 2943.
- [19] C. Bai, R. J. Spontak, C. C. Koch, C. K. Saw, C. M. Balik, *Polymer* **2000**, *41*, 7147.
- [20] G. V. Abagyan, P. Y. Butyagin, *Doklady Akademii Nauk Sssr* **1964**, *154*, 1444.
- [21] J. Pan, W. J. D. Shaw, *Journal of Applied Polymer Science* **1994**, *52*, 507.
- [22] J. Pan, W. J. D. Shaw, *Journal of Applied Polymer Science* **1995**, *56*, 557.
- [23] J. Font, J. Muntasell, E. Cesari, *Materials Research Bulletin* **1997**, *32*, 1691.
- [24] Y. G. Zhu, Z. Q. Li, D. Zhang, T. Tanimoto, *Journal of Polymer Science Part B-Polymer Physics* **2006**, *44*, 986.
- [25] Y. G. Zhu, Z. Q. Li, D. Zhang, T. Tanimoto, *Journal of Applied Polymer Science* **2006**, *99*, 2868.
- [26] J. Font, J. Muntasell, E. Cesari, *Materials Research Bulletin* **1999**, *34*, 157.
- [27] A. P. Smith, C. Bai, H. Ade, R. J. Spontak, C. M. Balik, C. C. Koch, *Macromolecular Rapid Communications* **1998**, *19*, 557.
- [28] A. P. Smith, R. J. Spontak, H. Ade, S. D. Smith, C. C. Koch, *Advanced Materials* **1999**, *11*, 1277.
- [29] A. P. Smith, H. Ade, C. C. Koch, S. D. Smith, R. J. Spontak, *Macromolecules* **2000**, *33*, 1163.
- [30] A. P. Smith, H. Ade, C. C. Koch, R. J. Spontak, *Polymer* **2001**, *42*, 4453.
- [31] Y. G. Zhu, Z. Q. Li, D. Zhang, T. Tanimoto, *Journal of Polymer Science Part B-Polymer Physics* **2006**, *44*, 1161.
- [32] Y. G. Zhu, Z. Q. Li, D. Zhang, T. Tanimoto, *Journal of Polymer Science Part B-Polymer Physics* **2006**, *44*, 1351.
- [33] G. Gorrasi, M. Sarno, A. Di Bartolomeo, D. Sannino, P. Ciambelli, V. Vittoria, *Journal of Polymer Science Part B-Polymer Physics* **2007**, *45*, 597.

- [34] P. Mangiacapra, G. Gorrasi, A. Sorrentino, V. Vittoria, *Carbohydrate Polymers* **2006**, *64*, 516.
- [35] R. L. Frost, E. Mako, J. Kristof, E. Horvath, J. T. Klopogge, *Langmuir* **2001**, *17*, 4731.
- [36] R. L. Frost, E. Mako, J. Kristof, E. Horvath, J. T. Klopogge, *Journal of colloid and interface science* **2001**, *239*, 458.
- [37] Y. C. Lee, C. L. Kuo, S. B. Wen, C. P. Lin, *Applied Clay Science* **2007**, *36*, 265.
- [38] A. R. Ramadan, A. M. K. Esawi, A. A. Gawad, *Applied Clay Science*, *47*, 196.
- [39] F. Perrin-Sarazin, M. Sepehr, S. Bouaricha, J. Denault, *Polymer Engineering and Science* **2009**, *49*, 651.
- [40] F. Dellisanti, V. Minguzzi, G. Valdre, *Applied Clay Science* **2006**, *31*, 282.
- [41] I. Sondi, M. Stubicar, V. Pravdic, *Colloids and Surfaces a-Physicochemical and Engineering Aspects* **1997**, *127*, 141.
- [42] J. Hrachova, J. Madejova, P. Billik, P. Komadel, V. S. Fajnor, *Journal of colloid and interface science* **2007**, *316*, 589.
- [43] C. M. Koo, H. T. Ham, M. H. Choi, S. O. Kim, I. J. Chung, *Polymer* **2003**, *44*, 681.
- [44] H. J. Lu, G. Z. Liang, X. Y. Ma, B. Y. Zhang, X. B. Chen, *Polymer International* **2004**, *53*, 1545.
- [45] W. G. Shao, Q. Wang, F. Wang, Y. H. Chen, *Journal of Polymer Science Part B-Polymer Physics* **2006**, *44*, 249.
- [46] W. G. Shao, Q. Wang, Y. H. Chen, Y. Gu, *Materials and Manufacturing Processes* **2006**, *21*, 173.
- [47] A. P. Smith, R. J. Spontak, H. Ade, *Polymer Degradation and Stability* **2001**, *72*, 519.

6.6. FIGURES

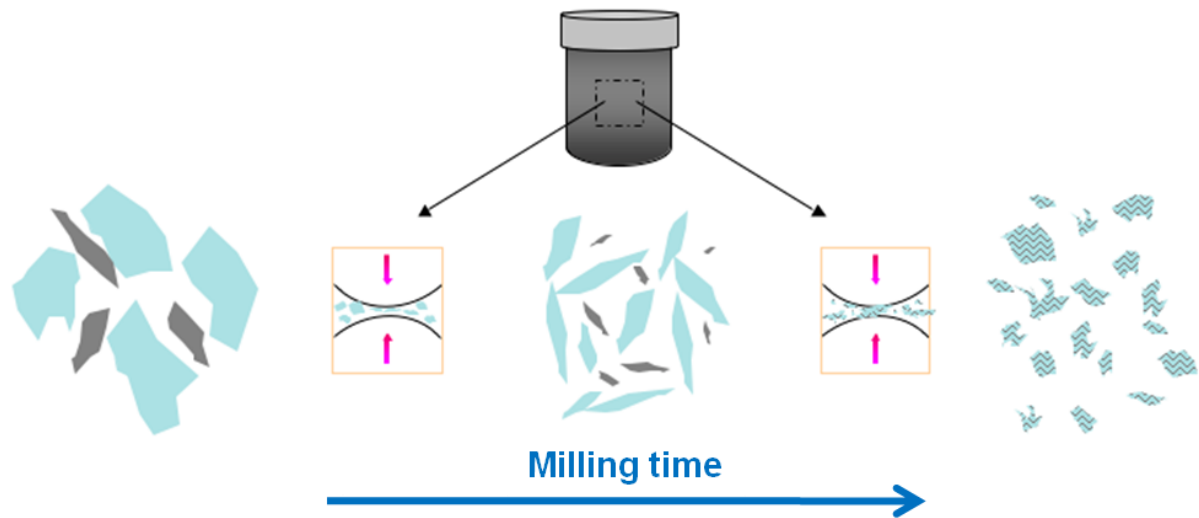


Figure 6.1. Fundamental principle of high-energy-mechanical-milling.

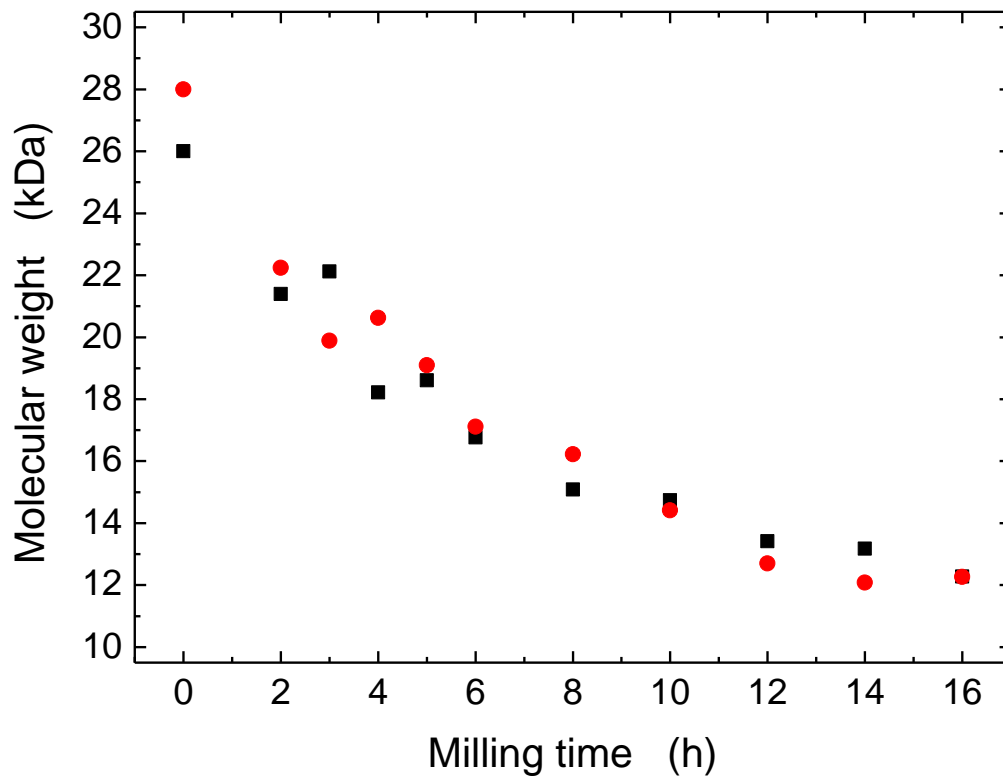


Figure 6.2. Change in molecular weight of rPET (■) and vPET (●) as a function of milling time.

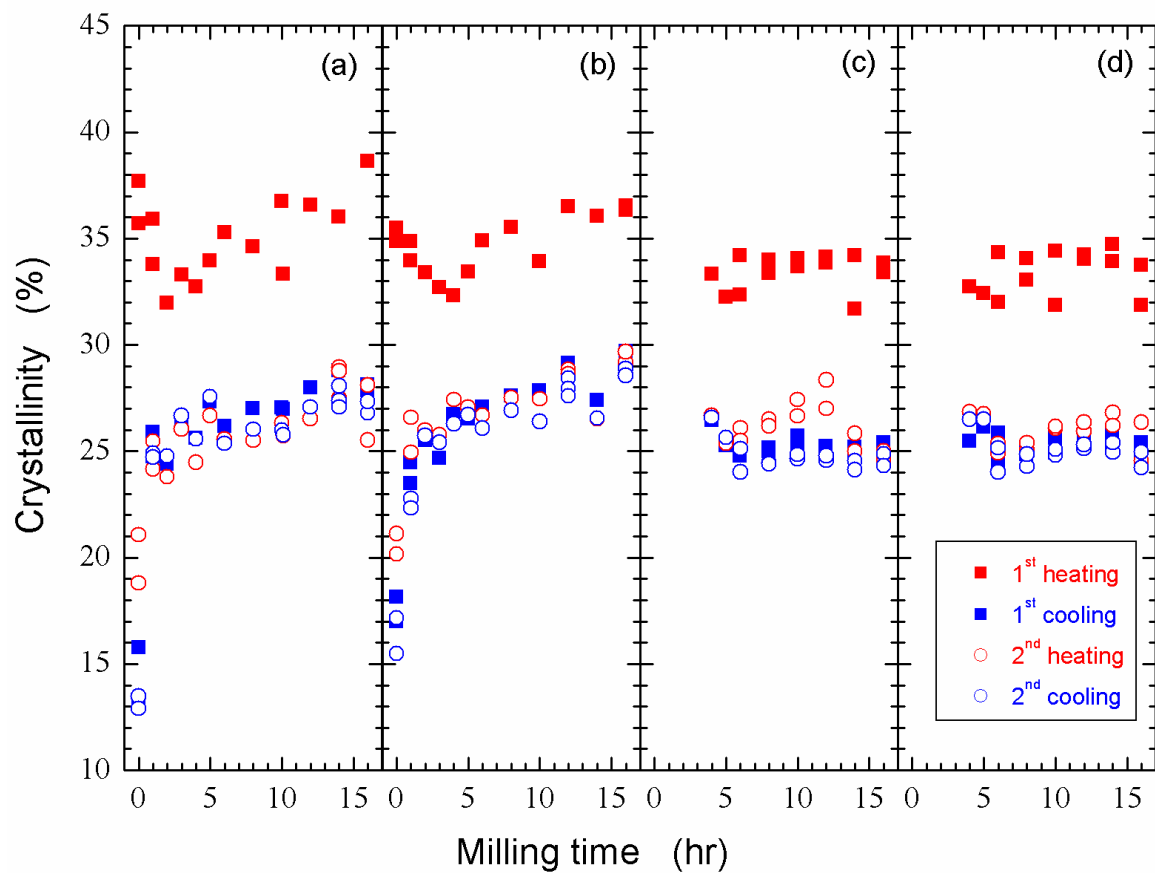


Figure 6.3. Crystallinity of (a) vPET, (b) rPET, (c) vPET+5%Na⁺MMT and (d) rPET+5%Na⁺MMT as a function of milling time.

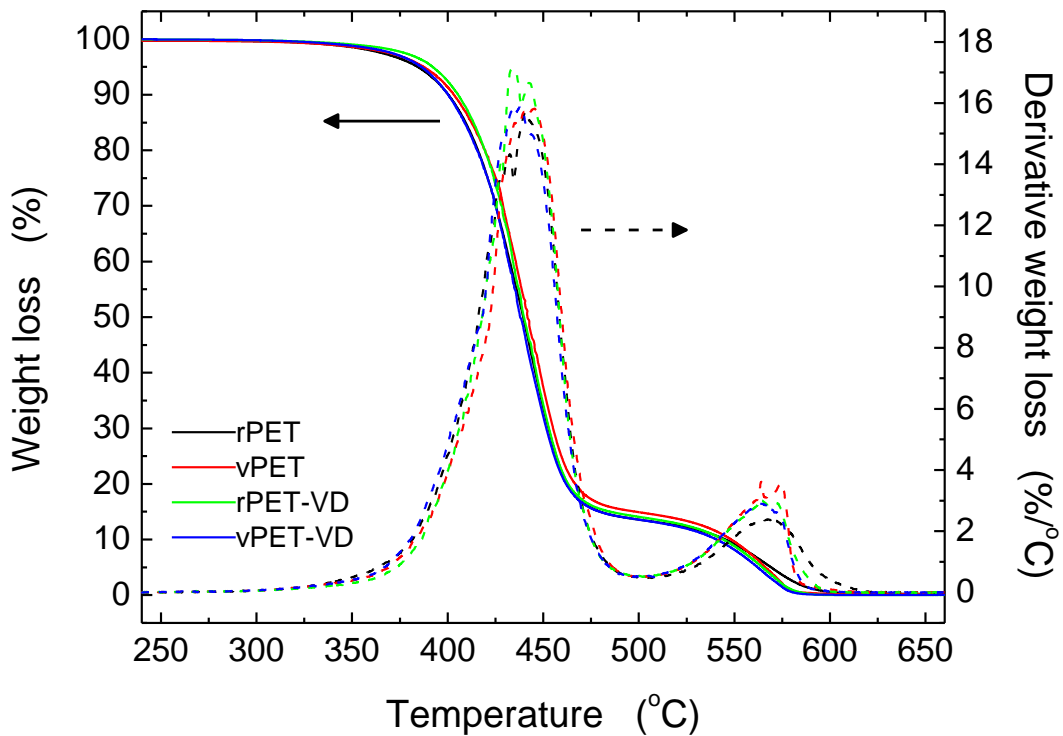


Figure 6.4. Weight-loss of rPET and vPET, as well as vacuum-oven dried rPET and vPET (see legend). The solid and dashed lines represent the weight loss and the derivative of the weight loss, respectively.

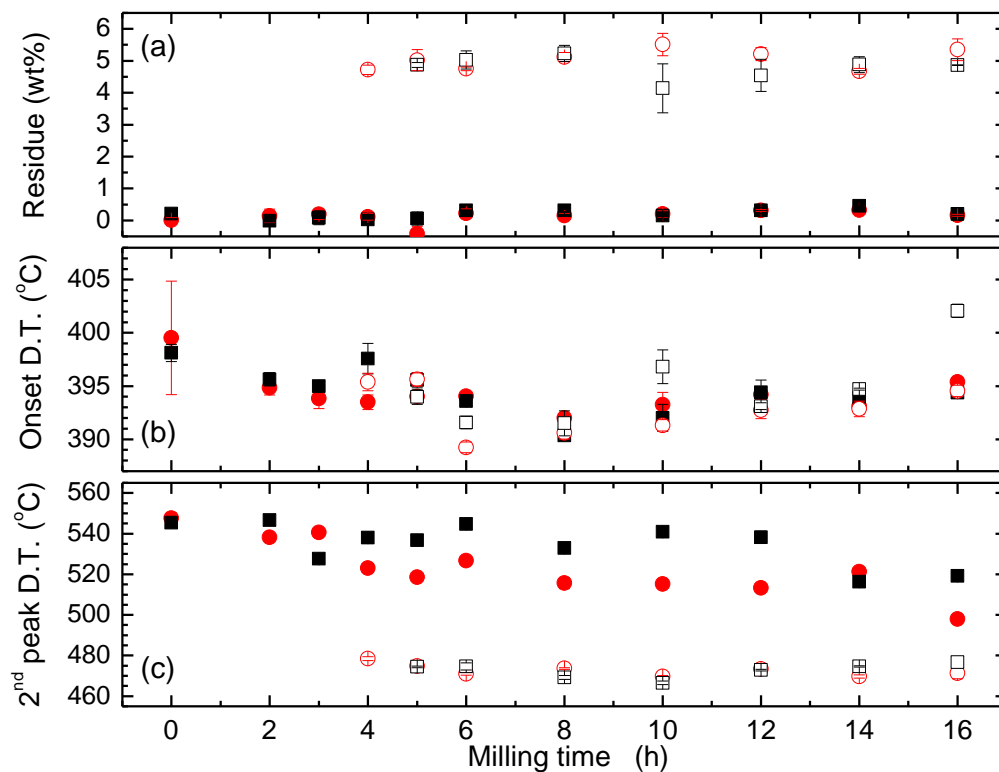


Figure 6.5. Summary of thermal degradation behavior of mechanically milled rPET (■) and vPET (●) mechanically alloyed rPET/clay (□) and vPET/clay (○) samples: (a) residue after complete pyrolyzing all organics (b) onset degradation temperatures and (c) 2nd peak degradation temperatures.

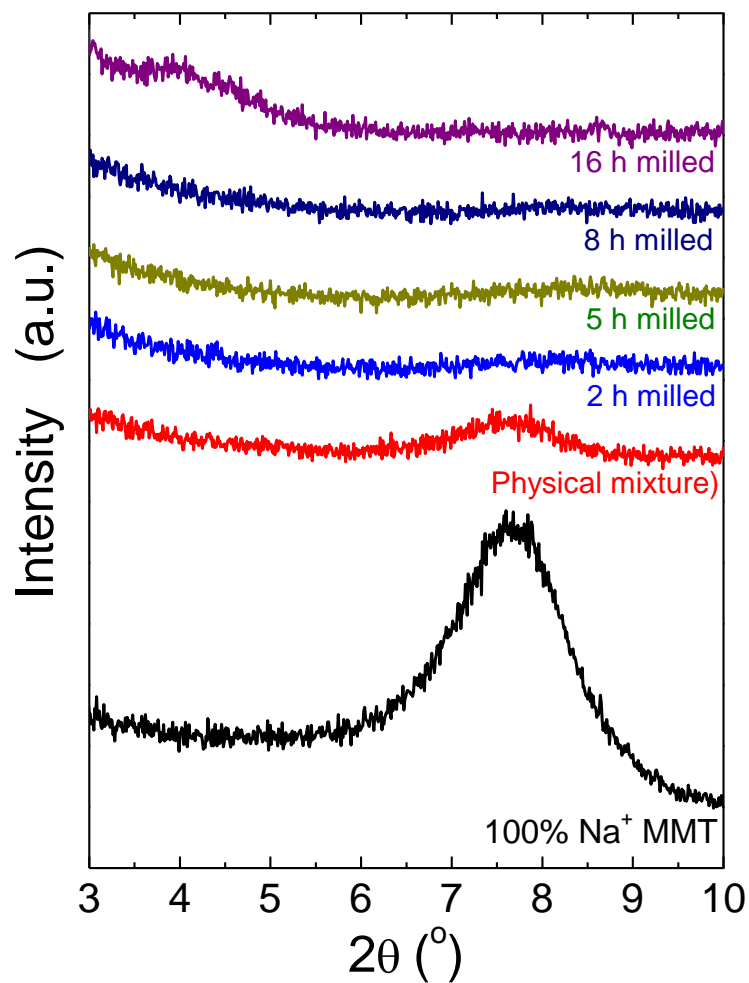


Figure 6.6. XRD patterns of as received Na⁺ MMT, 5% (w/w) physical mixture of Na⁺ MMT and 2 hr milled rPET, 2, 5, 8 and 16 h mechanically alloyed 5% Na⁺ MMT and rPET mixture.

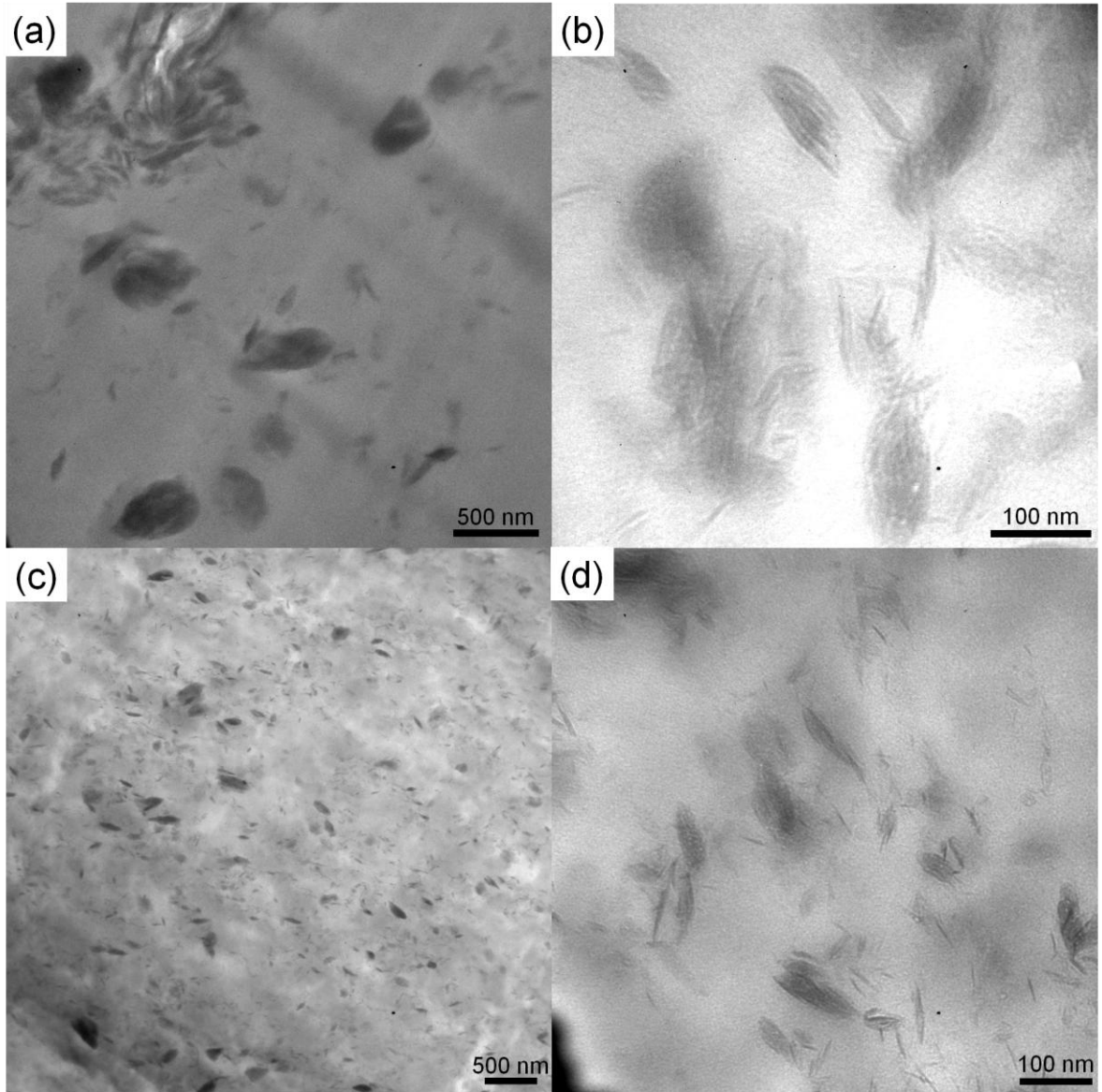


Figure 6.7. TEM micrographs of mechanically alloyed 5% (w/w) Na⁺ MMT and rPET for 2 hours (a) and (b) and 16 hours (c) and (d).

CHAPTER 7: UNIVERSAL COATINGS BASED ON FUNCTIONAL SILICONES

7.1. INTRODUCTION

Silicones or polysiloxanes, are hybrid materials comprising an inorganic Si-O backbone of alternating silicon and oxygen atoms with 2 pendant organic groups attached to every silicon atom as shown in Figure 7.1. Silicones are employed in numerous applications ranging from electronics to personal care, automotive, biomedical and construction industry. Poly(dimethylsiloxane) (PDMS) is the most commonly used silicone which has two methyl groups attached to silicon atom. PDMS is especially important for biomedical science among these application areas since PDMS is being biocompatible.

The exceptional surface properties of PDMS arise from the high backbone flexibility, the larger Si-O-Si bond angle, the longer bond length relative to the C-C-C bond and low energy barriers for rotation. All aforementioned properties lead to a very low glass transition temperature (T_g) for silicones (≈ 150 K) and this low T_g results in high chain flexibility even at room temperature.^[1] In addition, the presence of two stable methyl groups attached to the silicon atom gives chemical and physical resistance to PDMS. For instance, due to attractive/repulsive interactions, the methyl groups on the Si-O-Si backbone will orient themselves to the surface at an air-interface, but they will bury themselves under the polymer backbone at a water-interface to adopt their lowest surface energy configuration. On the

other hand, the pendent methyl groups on hydrocarbon backbones with fixed bond angles with steric hindrances.^[1-3] The backbone flexibility also results in a difference in the rotational potential energies in the siloxane bond (3 kJ/mol) and hydrocarbon bond (14 kJ/mol for polyethylene).

As mentioned above, the silicones have low T_g s and therefore they are fluids at room temperature and they flow. When chemically cross-linked (cf. Figure 7.2), silicones form flexible silicone elastomer networks (SEN) with an elastic modulus of ≈ 1 MPa, but its liquid-like nature between cross-link junctions would remain intact. The high flexibility of the Si–O backbone assures that SEN can readily adopt the lowest surface energy conformations while responding to changes of the environment as mentioned above. SENs have been applied actively in various technological applications for the past 50 years, ranging from insulation to advanced medical screening devices. PDMS networks have been employed as a major material in those applications due to its wide availability, low cost and chemical inertness. For instance, PDMS is used as a material for contact lenses and human implants. These applications demand that the surface of PDMS be hydrophilic to minimize the discomfort of cornea by enhancing wettability of lens by tears and to reduce the platelet adhesion for implant applications. Therefore, the hydrophobic PDMS surface has to be chemically or physically altered to increase the surface energy. However, overcoming the chemical stability of PDMS is a challenging task.

Over the past years, modification of PDMS surface was carried out using various techniques involving: 1) physical treatments such as plasma, corona, ultraviolet (UV),

UV/Ozone (UVO), electron and ion beams, 2) chemical oxidation or 3) a combination of both physical and chemical means.^[4-7] While various chemical routes are often employed to alter the chemical nature of materials, modifying the surfaces of PDMS by chemistry alone is limited to strong base or acid exposures that lead to uncontrollable and non-uniform surface modification. Additional difficulty arises from the fact that the PDMS surface gets contaminated with modifier and often cannot be easily cleaned. Finally, exposing the SEN to solutions of extreme pH causes network breakdown.

Physical surface modification techniques allow relatively controlled modification and in-plane uniformity of the surface. Among these techniques, plasma treatment has been widely utilized to impart the PDMS surface more hydrophilic by introducing polar groups. Plasma treatment involves a mixed state of ionized gases, which consist of electrons, ions, gas atoms and molecules in their ground or excited states.^[8, 9] Exposing the gas to a high electric field between two electrodes generates the plasma. Prior studies have shown that the exposure of SEN surfaces to plasma of various gases (N₂, O₂, Ar, He, NH₃) leads to rapid conversion of the methyl groups on the PDMS backbone to various hydrophilic moieties and the type of plasma gas affects greatly the chemical composition of the interface.^[10] However, there is no agreement on the exact nature of chemical groups formed on the outermost surface. The oxygen plasma is the most commonly used plasma treatment and it renders the PDMS surfaces highly hydrophilic as evidenced by corresponding changes in the water contact angle. It was shown by several researchers that plasma treatment propagates several hundred nanometers below the surface with irreversible chemical changes at the near-surface region

of PDMS.^[8, 11, 12] It is rather difficult to control the extent of physical modification with plasma since the reaction is happening quickly (a few seconds, depending on the dose). During plasma treatment, a brittle silica-like layer is formed on top of PDMS surface that alters the mechanical properties of PDMS surface. The main effects responsible for increases in the Young's modulus of the plasma-modified PDMS surfaces are backbone degradation and depolymerization/repolymerization of the parent chains leading to the formation of a very brittle silica-like layer.^[13] In addition, the thickness of the silica layer is a function of treatment time, power of the plasma, chamber pressure and gas composition. This undesirable effect is accompanied by instantaneous formation of small cracks in the silica like layer due to the mismatch between the mechanical properties of the top hardened layer and elastic bulk PDMS. Numerous researchers reported that the chemical composition of the plasma-treated PDMS surfaces changes over time due to uncontrollable diffusion of short silicone oligomers through the surface cracks, so-called hydrophobic recovery.^[8, 9, 11, 12, 14]

Alternatively, the oxygen plasma technique can be substituted successfully by the UVO treatment that produces polar functionalities on the surfaces of PDMS that are of similar nature but are present predominantly in only a thin layer of the base material. The UVO treatment is a photosensitized oxidation process in which the molecules of the treated material are excited and/or dissociated by the absorption of short-wavelength UV radiation. Atomic oxygen is simultaneously generated when molecular oxygen is dissociated by $\lambda_1=184.9$ nm and ozone by $\lambda_1=253.7$ nm. The 253.7 nm radiation is absorbed by most hydrocarbons and also by ozone.^[15, 16] The organic products of this excitation react with

atomic oxygen to form simpler, volatile molecules, which desorb from the surface. Therefore, when both wavelengths are present, atomic oxygen is continuously generated, and ozone is continually formed and destroyed. Compared to plasma treatment, UVO treatment is recognized as a milder type of physical modification to polymer surfaces with similar surface changes but with approximately an order of magnitude increase in processing time.^[17]
^{18]} This allows for better control of the surface conversion, as different degrees of hydrophilicity will be obtained for different treatment times. Therefore, in our work we utilize UVO treatment in order to render SENSs more hydrophilic.

Even UVO treatment of SENSs is more controlled than the plasma treatment; the UVO modification of PDMS still causes uncontrollable changes to the SENSs surface, which prevents formation of a soft hydrophilic surface on SENSs. Previous work by our group has shown that extended UVO treatment times (60 mins and longer) results in the formation of a 5 nm thick silica-like layer whose density is only 50% of that of pure silica.^[16]

Replacing one of the methyl groups of PDMS with a vinyl functionality increases the chemical tailorability of the polysiloxane and results in formation of poly(vinylmethylsiloxane) (PVMS). PVMS possesses properties similar to PDMS, yet it offers the flexibility with regard to the number of alternative chemical pathways leading to the modification of pendent vinyl groups. PVMS is a unique polymer providing multiple functions: 1) the low surface energy methyl group, 2) the highly flexible siloxane backbone, and 3) the vinyl moiety that can be used as an attachment point for various chemistries. Earlier, Efimenko and coworkers used PVMS and shortened the UVO treatment time due to

the higher susceptibility of vinyl groups to UVO treatment than the more stable methyl groups.^[19] They provided experimental evidence that only brief UVO treatment times (seconds to a few minutes) are sufficient to form highly hydrophilic SEN surfaces compared to the UVO treatment of PDMS, which render the PDMS surface hydrophilic only after prolonged UVO treatment.

Novel applications drive constantly the need for developing new types of surface coatings or surface-modification processes that lead to the fabrication of functional structures on flexible and transparent substrates. Flexible electronics, including the manufacture of displays, novel platforms for sensory detection, and more efficient and reliable contact lenses are just a few examples. Many of these applications employ relatively inert polymeric substrates that are not readily chemically modifiable. While modification of these surfaces by physical means is possible, the methods commonly employed involve plasma or corona treatments that degrade gradually the surfaces, which may compromise the mechanical, optical or electrical characteristic of the substrates.^[20, 21] There is therefore need for designing alternative modification routes that would involve less harsh and yet versatile means of altering the surface properties of flexible polymeric supports.

Due to biocompatibility and high permeability for gases, SENs have been employed successfully in a new generation of contact lenses. However, in order for this application to be successful, both the interior and the surface of each contact lens have to be rendered hydrophilic, in order to: 1) allow for steady permeation of oxygen and water vapor through the network and 2) improve the lubrication of lens surfaces (thereby reducing the friction

between the contact lens and the eye lid) and minimize undesirable biofouling, such as protein adsorption from the tear fluid. Surface modification of contact lenses is currently accomplished by grafting protein-repellent groups, such as poly(ethylene glycol) (PEG). Most manufacturers of soft contact lenses use PDMS as one of the base components, due to its low price and high gas permeability, and modify the surfaces of PDMS-based contact lenses by first exposing them to cold oxygen plasma, which activates the surfaces, and then chemisorbing the PEG chains. While this method leads to hydrophilic protein-repellent surfaces, the lens durability is not typically very high because the surface coating is rather thin and it gets compromised with time due to hydrophobic recovery from the base PDMS as well as failure of the PEG layer itself. While increasing the thickness of the hydrophilic top layer would lead to improvements in the lifetime of the device, this task is not straightforward to carry out.

Changing the base material is not an option because it would increase the cost of the device and (very likely) decrease gas permeability. One way to proceed then would be to increase the extent of modification due to the physical treatment of the base PDMS material. However, even relatively mild UVO treatment that has been used in the past to modify the surfaces of SENs eventually produces hard skin on top of the base PDMS as pointed out earlier.^[13, 16] In addition, the gas permeability through these thicker and dense oxide-like layers decreases dramatically.^[22] An alternative method of creating thick hydrophilic coatings may involve forming a laminate system comprising the base PDMS coated with a functional layer made of a more hydrophilic silicone film, such as PVMS.

Various attempts to build bi-layered PVMS/PDMS laminates are summarized in Figure 7.3. Initial efforts leading to the formation of sandwich layers of PVMS and PDMS networks failed due to the migration of low-molecular weight cross-linking agents in PDMS matrix, which hindered network formation. Spincoating PVMS on top of PDMS networks did not result in stable coatings because of thermodynamic incompatibility between PDMS and PVMS and subsequent dewetting of the PVMS films from the PDMS network substrate regardless of the molecular weight and the concentration of the PVMS in the spin-coating solution. For these reasons, coupling cross-linkable groups to PVMS was performed in order to stabilize the PVMS layers and prevent their dewetting from the PDMS network surfaces.

The presence of the vinyl group allows for relatively simple chemical modifications of the parent PVMS material. In this work we couple trichlorosilane (TCS) to the PVMS backbone via hydrosilylation reaction in the presence of a platinum catalyst, as shown in Figure 7.4. The coupling reaction results in the formation of silicone random copolymers comprising the parent (VMS) and modified (VMS-TCS) units. Importantly, the chlorosilane groups get converted quickly and quantitatively into silanols (Si-OH) with a minute amount of moisture. The silanol groups in PVMS-TCS can then either condense with each other (resulting in a relative stable network) or attach to hydrophilic functionalities on surfaces. In this work, we benefit from both functions of the Si-OH groups and stabilize the thin PVMS-TCS layers on solid surfaces via cross-linking during the spin-coating process and attachment to the underlying substrate. In this Chapter we will show that the PVMS-TCS platform offers unique opportunities for tailoring both physical and chemical characteristics of the

coating. The chemical composition of the copolymer, reflecting the extent of coupling between PVMS and TCS, can be tuned by varying the concentration of TCS. Further chemical modification can be achieved by thiol-ene coupling onto the remaining unreacted vinyl groups of the PVMS-TCS copolymer; this additional chemical modification results in functional coatings that can provide protein resistant, self-cleaning, scratch resistant, and other characteristics. In addition, mechanical properties of the functional coating, such as the Young's modulus, can be tailored by varying the chemical composition and/or the thickness of the coating; the latter can be adjusted conveniently by varying the concentration of the copolymer in the spin-coating solution.

The primary focus of this Chapter is to describe our efforts to study the properties of the PVMS-TCS coatings on top of PDMS networks, poly(ethylene terephthalate) (PET) films. We note, however, that PVMS-TCS copolymer produces stable layers on a variety of other surfaces, including (but not limited to): polyethylene, polypropylene, nylons, polyimide (Kapton®) and others.

7.2. EXPERIMENTAL

7.2.1. MATERIALS

PVMS fluid was synthesized as described in the Appendix of this chapter. 1H,1H,2H,2H-perfluorodecyl trichlorosilane (t-F8H2) and 1H,1H,2H,2H-perfluorinated

decanethiol (F8-SH) were supplied by Alfa-Aesar and Oakwood Chemical, respectively, and used as received. ω -thiol terminated poly(ethylene glycol) methyl ether (PEG-SH) with a molecular weight of 5 kDa was purchased from Polymer Source (Quebec, Canada). The Darocur® 1173 was kindly donated by Ciba Specialty Chemicals. A custom-designed peptide, CGRGDSY (RGD) used in this study was obtained from Peptide 2.0, Inc. (Chantilly, VA). Free radical polymerization (FRP) initiator, 2,2'-Azobis[2-methyl-N-(2-hydroxyethyl)propionamide], was purchased from Wako Specialty Chemicals (Richmond, VA). Trichlorosilane (TCS), methyl methacrylate (MMA), anhydrous toluene, anhydrous tetrahydrofuran (THF), chloroform, acetone, methanol and ethanol were purchased from Sigma-Aldrich. α - ω -vinly-terminated PDMS (62 kDa), tetrakis (dimethylsiloxy) silane (TDSS) and Pt(0)-1,3-divinyl-1,1,3,3-tetramethyldisiloxane complex were purchased from Gelest (Morrisville, PA). Polypropylene (PP), polyethylene (PE) and nylon-6 (PA) pellets were kindly donated by Sunoco (product CP360H), BASF (product Ultramid B27 02) and DOW (6850 LLDDe), respectively. PET (Mylar-DL) and polyimide (Kapton®) films were kindly supplied by DuPont-Teijin and DuPont, respectively.

7.2.2. FILM PREPARATION

Mylar-DL films were untreated on both sides to avoid the effect of surface treatment on the adhesion of functional silicone coatings on PET. PE, PP and PA were melt-pressed from PP, PE and PA pellets between two flat Kapton films. The melt-pressed films were washed

with copious amounts of deionized (DI) water and methanol, dried under vacuum and kept in a desiccator under reduced pressure until utilization. PDMS and PVMS network films with a thickness of ≈ 600 μm were prepared as summarized in Appendix of in this Chapter. Shortly, polysiloxane base, cross-linker and the catalyst were mixed in predetermined amounts, the mixture was stirred vigorously and degassed under reduced pressure to remove trapped air bubbles. It was then cast into square Petri dishes and cured at room temperature for 24 hours followed by a 72 hour cure at 70 °C

7.2.3. PVMS-TCS COUPLING REACTIONS AND MODIFICATIONS

The hydrosilylation reaction coupling of TCS to PVMS was performed in the presence Pt(0)-1,3-divinyl-1,1,3,3-tetramethyldisiloxane complex in anhydrous toluene (or THF). The PVMS fluid was dissolved in anhydrous toluene at a specific concentration in a glass vial and a corresponding amount of TCS was added to the PVMS solution. The Pt(0) complex was added to the mixture and the vial was capped under nitrogen. The reaction mixture was stirred with a magnetic stir bar for $\approx 1-2$ hours at room temperature.

Additional chemical modification of PVMS was carried out to further functionalize the coating. First, a fraction of the pendent vinyl groups of PVMS chains was modified in solution via thiol-ene addition reaction involving a functional thiol (specified below). Subsequently, a portion of the remaining vinyl groups was coupled with TCS molecules to introduce cross-linkable groups on the PVMS-thiol-TCS fluid. Two different thiol

molecules, F8-SH and PEG-SH, were utilized to prepare PVMS-thiol-TCS coating; the reactions were carried out in dry THF in quartz vessels under UV light ($\lambda = 254$ nm) for 12 hours at room temperature. TCS molecules and the Pt(0) catalyst were subsequently added to the vessel and the reaction mixture was stirred for $\approx 1-2$ hours at room temperature.

In addition, azo-based FRP (2,2'-Azobis[2-methyl-N-(2-hydroxyethyl)propionamide]) initiator was coupled to chlorosilane groups of PVMS-TCS in THF at room temperature. The FRP initiator was first dissolved in dry THF and then mixed with THF solution of PVMS-TCS. The reaction mixture was stirred at room temperature for $\approx 1-2$ hours and applied onto the PET, PP and SiO_x substrates. PVMS-TCS-azo coated substrates were immersed in methyl methacrylate (MMA) solution, de-oxygenated and heated to 90 °C for 2 hours. At the end of polymerization, the substrates were rinsed, sonicated, and rinsed again with THF, in order to remove any physisorbed PMMA chains, and dried with a stream of nitrogen gas.

The remaining vinyl groups of spin-coated PVMS-TCS coating on PDMS network were utilized to introduce additional functionality via thiol-ene addition reaction. The photoinitiator, Darocur® 1173, was dissolved in DIW at a concentration of 0.5% (w/w) and was mixed with peptide solution at a concentration of 0.5 mg/ml (1:1 ratio). The mixture of peptide and photoinitiator was then placed onto PVMS and PVMS-TCS coated PDMS networks and was covered with a glass cover-slip; ≈ 100 μm spacers were used to keep the constant distance between the glass cover and the substrate. The samples were exposed to UV light ($\lambda = 365$ nm) for different periods of time. At the end of the reaction the substrates

were washed with copious amounts of water and dried under reduced pressure. XPS and nanoindentation experiments were performed to determine the concentration of surface nitrogen and the modulus of the modified substrates.

7.2.4. PVMS-TCS THIN FILM FORMATION

The PVMS-TCS solution was spin-coated on the substrate (i.e., PDMS network, PET, PA, PE, PP, Kapton®, glass, or silicon wafer) by using a Headway Research PWM-32 spin-coater at a speed and acceleration of 2000 rpm and 1000 rpm/sec respectively for 60 seconds. The adhesion of spin-coated PVMS-TCS layer to the aforementioned polymer substrates was determined qualitatively by using a Scotch Tape Adhesion Test. A piece of Scotch tape was pressed gently on the PVMS-TCS coating and peeled off at angle of 90°. The presence of the PVMS-TCS coating (thickness \approx 200 nm) on the substrate was checked at a grazing angle with naked eye. Coatings having a thickness \approx 200 nm film possess a yellowish tint on the substrate surface.

7.2.5. WATER CONTACT ANGLE MEASUREMENTS

Water contact angle experiments were performed via the sessile drop technique with DI water ($R > 15 \text{ M}\Omega\text{cm}$) using the Ramé-Hart contact angle goniometer (model 100-00) equipped with a CCD camera, and analyzed with the Ramé-Hart Imaging 2001 software. Water contact angles (WCA) were determined after releasing a 8 μL droplet of DI water on

the surface. At least 4 different measurements were carried out across the sample surface and the average values of WCA were reported with corresponding standard error values.

7.2.6. X-RAY PHOTOELECTRON SPECTROSCOPY

The surface chemical composition of freshly prepared samples was determined by using a Kratos Axis Ultra DLD x-ray photoelectron spectroscopy (XPS) using monochromated Al K α radiation with charge neutralization. Survey and high-resolution spectra were collected with pass energies of 80 and 20 eV, respectively, by using both electrostatic and magnetic lenses. Elemental chemical compositions were calculated from spectral regression using the Vision software.

7.2.7. FOURIER TRANSFORM INFRARED SPECTROSCOPY

Fourier transform infrared spectroscopy (FT-IR) spectra were recorded on a Nicolet 6700 spectrometer and the data were analyzed by means of the Omnic software. Transmission-mode FT-IR was used to monitor the extent coupling reaction. The attenuated total reflection geometry (ATR) FTIR was employed to monitor chemical changes that took place on the polymer surfaces after surface modification. A drop of PVMS-TCS copolymer solution at the end of the coupling reaction was spread on a KBr crystal, and the IR spectra were collected after all solvent evaporated to determine the extent of coupling. The IR spectra of

surface-modified films were collected in the ATR mode with a Ge crystal. For each sample 256 scans were collected after recording the background with a resolution of 4 cm^{-1} .

7.2.8. ULTRAVIOLET/OZONE TREATMENT

The UVO treatment of all substrates was carried out in a commercial UVO chamber (Jelight Company, Inc., model 42). We used the standard Fused Quartz lamp that emits about 65% of its total radiation at 184.9 nm and has an output of 6.2 mW/cm^2 at a distance 6 mm away from the source, as measured by a UV light detector (International Light Technologies, Peabody, MA). The substrates were placed onto glass slides and put into the UVO-cleaner at a distance of ≈ 5 mm from the mercury lamp and exposed to the radiation from one side only for controlled periods of time.

7.2.9. FORMATION OF SEMIFLUORINATED SELF-ASSEMBLED MONOLAYERS

Semifluorinated self-assembled monolayers (SAMs) on the UVO-treated substrates were prepared from 1H,1H,2H,2H-Perfluorodecyl trichlorosilane (tF8H2). tF8H2 and a fluorinated oil were mixed in a 1:5 ratio (w/w), and a small drop of this mixture was placed on the bottom of a Petri dish. The substrates (i.e., UVO treated PVMS-TCS coated substrates, PET films, UVO-treated PET films, or silica) were taped to the lid of the Petri dish; the lids were placed back on the Petri dishes so that the samples hanged face-down in

the Petri dish ≈ 1 cm away from the tF8H2/oil mixture. After exposure for 15 min at ambient conditions, the lid was removed and the samples were washed thoroughly with absolute ethanol to remove any physisorbed tF8H2 molecules and subsequently blow dried with a stream of nitrogen gas.

7.2.10. SCANNING ELECTRON MICROSCOPY

The surface morphology of UVO-modified samples was examined with a Hitachi S-3200 scanning electron microscope. The films were coated with a 8 nm thick layer of gold and representative images were collected at 1000x and 10000x magnification.

7.2.11. SPECTROSCOPIC ELLIPSOMETRY

The thicknesses of films on non-transparent substrates were determined with a variable angle spectroscopic ellipsometer (VASE) (J.A. Woollam Co.). Ellipsometry measures the difference in the polarization state between the light beams incident onto and reflected from the surface; providing information about the thickness and dielectric properties of the film. All ellipsometric data were collected at an incidence angle of 70° with respect to the surface normal and at wavelengths ranging from 400 to 1100 nm in 10 nm increments.

7.2.12. NEAR-EDGE X-RAY ABSORPTION FINE STRUCTURE

Near-edge x-ray absorption fine structure (NEXAFS) spectroscopy at the carbon, oxygen and fluorine K-edges was utilized to examine the composition and molecular orientation of the tF8H2 SAMs and the surface chemistry of the UVO-modified PVMS-TCS coated PET samples. The NEXAFS experiments were conducted at the NIST/Dow Soft X-ray Materials Characterization Facility of the National Synchrotron Light Source (NSLS) at Brookhaven National Laboratory. NEXAFS involves the resonant soft x-ray excitation of a K shell electron to an unoccupied low-lying antibonding molecular orbital of σ symmetry (σ^*) or π symmetry (π^*).^[23] The initial state K shell excitation endows NEXAFS with its elemental specificity, while the final-state unoccupied molecular orbitals provide NEXAFS with its bonding or chemical selectivity. A measurement of the partial electron yield (PEY) intensity of the NEXAFS spectral features thus allows for identification of chemical bonds and determination of their relative population densities on the sample surface (the probing depth is \approx 1-2 nm into the film). Because the incident x-ray is polarized, collecting the NEXAFS spectra at various sample/x-ray beam geometries yields information about the molecular orientation of adsorbates (the tF8H2 molecules in our case) present on the surface. For this purpose, the NEXAFS spectra were collected at $\theta = 20, 50$ and 90° , where θ is the angle between the sample normal and the electric vector of the x-ray beam.

7.2.13. NANOINDENTATION

The mechanical properties of PVMS-TCS coating on self-standing PET films, PDMS networks, and silicon wafers were tested by using Hysitron Triboindenter. The instrument operating either in quasi-static or dynamic modes, was equipped, force and displacement controlled (feedback) and an integrated AFM head. Indentations were performed at room temperature in the acoustic enclosure of the Triboindenter. A 46 μm conical diamond tip was used to perform indentations after calibration of the diamond tip on standard fused quartz. Force-displacements curves of the indents were analyzed by the Oliver-Pharr method by using the software TriboScan supplied by Hysitron. Only the results of displacement-controlled quasi-static indentations are reported. The reduced modulus is calculated using equation (7.1):

$$E_r = \frac{S\sqrt{\pi}}{2\sqrt{A}} \quad (7.1)$$

$$\frac{1}{E_r} = \left(\frac{1-\nu^2}{E} \right)_{\text{sample}} + \left(\frac{1-\nu^2}{E} \right)_{\text{indenter}} \quad (7.2)$$

where (S) is the stiffness of the unloading curve, (A) is the projected contact area, and ν is Poisson's ratio (taken to be ≈ 0.5 , a typical value for silicone elastomer networks). The initial unloading contact stiffness (the slope of the initial portion of the unloading curve) is defined as:

$$S = \frac{dP}{dh} \quad (7.3)$$

For a standard diamond indenter probe, E_{indenter} is 1140 GPa and ν_{indenter} is 0.07.

7.3. RESULTS AND DISCUSSION

The coupling of trichlorosilane (TCS) molecules to the pendent vinyl groups of PVMS was performed via the hydrosilylation reaction in the presence of Pt(0) catalyst at room temperature, as shown schematically in Figure 7.4. This reaction resulted in random copolymers comprising the VMS and VMS-TCS units (cf. Figure 7.5.a).

After spin-coating the PVMS-TCS copolymer onto the substrate, cross-linking among neighboring Si-OH groups takes place that leads to the formation of a stable and robust coating layer. The stability of the spin-coated PVMS-TCS films on PET-coated silicon wafers (PET/SiO_x) and bare silicon wafers (SiO_x) was investigated via ellipsometry before and after sonicating the samples in good solvents (toluene, THF and chloroform) along with more polar solvents (acetone, methanol, ethanol and water). The thickness of the PVMS-TCS layer on PET/SiO_x and planar silica substrates did not change as a function of prolonged sonication time (>30 minutes) thus verifying the stability of the PVMS-TCS coating. In addition, the same stability test was applied to UVO-treated PVMS-TCS layers on SiO_x for different UVO exposures, which rendered the coating more hydrophilic. No material removal was observed after sonication in toluene and ethanol, suggesting that the coating was stable even under rather harsh environmental conditions. Because ellipsometry cannot be

performed readily on transparent substrates to verify the presence of the PVMS-TCS layers, the stability of the coatings on PET, PP, PE, PDMS, PA and Kapton® was verified qualitatively by using the adhesion Scotch Tape Adhesion Test, described in the experimental section. Adhesion of PVMS-TCS coatings to the substrates such as PP and PE, increased with a brief UVO treatment ($\approx 2\text{-}3$ minutes of UVO and subsequent ethanol washing to remove low-molecular organic compounds formed during UVO treatment) of the parent polymeric substrates, which introduced -OH functional groups as anchoring points for the PVMS-TCS coating. The chemical composition of the PVMS-TCS copolymer films was determined by monitoring the number of vinyl groups coupled with the TCS molecules. The extent of coupling is tunable and can be altered by changing the ratio of the vinyl to TCS in the reaction medium. For instance, the vinyl:TCS ratio was varied in the reaction solution and the extent of coupling was determined with FT-IR by monitoring the area under the vinyl peaks of PVMS: $\text{C}=\text{C}$ twist/ $=\text{CH}_2$ wagging ($\approx 960\text{ cm}^{-1}$), $=\text{CH}_2$ scissors ($\approx 1407\text{ cm}^{-1}$) and $\text{C}=\text{C}$ stretch ($\approx 1587\text{ cm}^{-1}$).^[24] In Figure 7.5b we plot the percentage of the coupled vinyl groups as a function of the vinyl:TCS ratio along with the theoretical values (black line) calculated based on complete coupling (quantitative reaction) of TCS to vinyl groups of PVMS. The experimental extents of reaction were in accord with the theoretical values, as shown in Figure 7.5b. This agreement confirms the quantitative nature of TCS coupling to the vinyl groups of PVMS.

7.3.1. PVMS-TCS COATING ON PDMS NETWORK SUBSTRATES

As stated earlier, PDMS networks are inherently hydrophobic. Hydrophilization of PDMS requires typically harsh physical treatments that increase the film wettability. However, it is challenging to prepare hydrophilic PDMS surfaces without compromising their mechanical and permeation characteristics using plasma or UVO treatment techniques. We first attempted to avoid the physical hydrophilization process of the PDMS network by spin-coating a thin layer of PVMS fluid directly onto the PDMS network substrate (PVMS/PDMS). However, the PVMS coatings deposited on the PDMS network substrates were unstable and dewetted after spin-coating a solution of PVMS fluid from toluene, as shown in Figure 7.5c. The dewetting was driven by both the thermodynamic incompatibility between PVMS and PDMS and autophobicity due to the presence of the PDMS network. The latter effect was established by spin-coating PDMS fluids with various molecular weights on PDMS networks; they all resulted in dewetted top PDMS films on the PDMS networks. Spin-coating PVMS-TCS copolymers onto PDMS network substrates (PVMS-TCS/PDMS) revealed that the stability of top PVMS-TCS layer increased with increasing the extent of TCS coupling to the vinyl groups of PVMS. Optical micrographs of spin-coated layers of PVMS/PDMS and PVMS-TCS/PDMS along with the representative cartoons are depicted in Figure 7.5c. The thicknesses of the spin-coated PVMS-TCS layers were below ≈ 50 nm, as measured via ellipsometry for films deposited onto silicon wafers. Relative to pure PVMS, that exhibited islands on the substrates, the dewetted patterns comprised holes when PVMS-TCS with 25% of TCS coupling was deposited via spin-coating on top of

PDMS network substrates. The sizes of the holes decreased with increasing the extent of TCS coupling. The spin-coated layers become completely defect free and stable when all the vinyl groups in PVMS were consumed for the coupling reaction. We propose that a stable PVMS-TCS copolymer layer is formed when the rate of cross-linking exceeds the rate of dewetting during spin-coating process. Cross-linking (even partial) of the PVMS-TCS stabilizes the film by decreasing chain mobility, which in turn diminishes the tendency of films to dewet from the PDMS support.

Increasing the thickness of polymer layers generally improves their stability on substrates. More stable and smoother PVMS-TCS coatings on PDMS networks were obtained when the thickness of the layer was increased above ≈ 50 nm. The thickness of the PVMS-TCS layer is tunable as documented by the data in Figure 7.6, that depicts the thickness of PVMS-TCS on silicon wafers (PVMS-TCS/SiO_x) as a function of the vinyl:TCS ratio and the PVMS-TCS copolymer concentration in the spin-coating solution. The thickness of the layer increases with increasing PVMS-TCS copolymer concentration in the spin-coating solution. In addition, increasing the extent of TCS coupling also leads to thicker layers due to the higher number of available cross-linkable TCS groups, although this effect is not as pronounced as increasing copolymer concentration in the spin-coating solution.

By increasing the number of cross-linkable TCS groups in the PVMS-TCS copolymer the density of the cross-links increases (effectively increasing the density of the network by decreasing the molecular weight between the cross-link points). This improves the stability of the top PVMS-TCS layer on the substrate (cf. Figure 7.7) and results in concurrent

increases in the modulus of the top PVMS-TCS layer. The relative modulus of PVMS-TCS layer was measured on PDMS networks and the data are plotted in Figure 7.8 as a function of the vinyl:TCS ratio and the PVMS-TCS copolymer concentration in the spin-coating solution. As evidenced from the data, the thickness of the PVMS-TCS layer does not have a large impact on the modulus except for low vinyl:TCS ratios. First, the modulus of the PVMS-TCS layer matches the modulus of the substrate (PDMS-62 kDa \approx 1.4 MPa). Second, the thickness of the PVMS-TCS layer is lower than the penetration depth of the indenter tip; therefore the modulus measured represents a composite modulus for the PVMS-TCS layer and the PDMS substrate. Nevertheless, the effect of the vinyl:TCS ratio on Young's modulus is visible for films prepared from PVMS-TCS coatings with the lowest vinyl:TCS ratio where the thickness of the film does not change dramatically for constant copolymer concentration and slightly-varying vinyl:TCS ratio.

Varying the cross-linking density and thickness of the PVMS-TCS layer both affect gas permeation through this film. One would expect that the permeability would be high for thin PVMS-TCS films with a relatively low cross-linking density. Increasing the density and/or thickness of PVMS-TCS would reduce gas permeability. These trends are supported by the data presented in Figure 7.9, where we plot the permeability of oxygen through PVMS, PDMS and PVMS-TCS/PDMS. The important finding here is that the presence of a relatively thin (thickness \approx 150 nm) layer of PVMS-TCS on top of PDMS does not change the permeability of oxygen.

The chemical composition and wettability of the PVMS-TCS/PDMS network laminates were monitored with FT-IR and water contact angle (WCA) measurements, respectively, for the aforementioned vinyl:TCS ratios and copolymer concentration in spin-coating solution and for films exposed to UVO treatment. The UVO exposure time was set to 10 minutes based on the WCA contact angle data obtained on UVO treated PDMS and PVMS networks, where both PDMS and PVMS network surfaces became more hydrophilic.

The WCA values for the of PVMS-TCS/PDMS samples are plotted in Figure 7.10a as a function of the copolymer concentration in solution and the vinyl:TCS ratio. The WCA benchmark values for bare PDMS and PVMS networks were measured as $106.3 \pm 2.3^\circ$ and $96.7 \pm 2.7^\circ$, respectively. A comparison of the WCA values for PVMS-TCS/PDMS with the WCA on bare PDMS and PVMS surfaces reveals that the wettability of coated PVMS-TCS/PDMS increases slightly and it approaches the wettability of the bare PVMS network. The WCA of the PDMS networks coated with 0.5% copolymer solution possess relatively high WCA values due to dewetted PVMS-TCS coating (cf Figure 7.5c); here both the PVMS-TCS and PDMS substrate are in contact with the probing liquid. After the UVO treatment the WCA of PDMS and PVMS networks reached $76.4 \pm 2.2^\circ$ and $29.1 \pm 3.8^\circ$, respectively. The contact angle data reveal that the wettability of the UVO-treated PVMS-TCS/PDMS composite resembles that of the PVMS network if the concentration of the PVMS-TCS in the spin-coating solution is above 1% wt (cf. Figure 7.10b). In contrast, the WCA values of PVMS-TCS layers obtained from 0.5% PVMS-TCS copolymers in the spin-

coating solution lie between the PDMS and PVMS samples treated with UVO for 10 minutes due to the incomplete coverage of the PVMS-TCS coating.

The FT-IR spectra of the PVMS-TCS/PDMS laminates were collected in the ATR mode; the data are summarized in Figure 7.11a for bare PDMS (black line), PVMS-TCS/PDMS (from 0.5 (red line), 1 (blue line), 3 (dark yellow line) and 5% (purple line) PVMS-TCS copolymer in spin-coating solution) and PVMS network (olive line). An increase in the PVMS-TCS copolymer layer thickness on the PDMS network substrate resulted in an increase in the intensity of the vinyl peaks located at 960, 1407 and 1600 cm^{-1} ; the spectra resembled that of the bare PVMS network. This effect was expected since the probing depth of ATR (Ge crystal) is $\approx 1 \mu\text{m}$ and increased PVMS-TCS thickness resulted in an increase in the signal originating from the PVMS-TCS. The FT-IR spectra of these samples after 10 minutes of UVO treatment are plotted in Figure 7.11b. New peaks appeared after the UVO treatment that correspond to hydroxyl (3300 and 940 cm^{-1}) and carboxyl (1725 cm^{-1}) groups.^[24] The intensity of these peaks increased with increasing thickness of the PVMS-TCS layer on the PDMS network substrate; the PVMS-TCS layer on PDMS spin-coated from 5% copolymer solution had an identical spectrum with the UVO-treated PVMS network. Therefore, the chemical composition of the PVMS-TCS/PDMS after 10 minutes of UVO treatment resembles closely that of the UVO-modified PVMS network.

The functionality of the PVMS-TCS/PDMS surfaces was tested by post-modification reaction with unreacted vinyls in the PVMS-TCS coating by means of a thiol-ene addition reaction. A thiol-terminated peptide, specified in the Experimental section, was attached to

the remaining vinyl groups of PVMS-TCS/PDMS and PVMS networks in the presence of a photoinitiator (Darocur® 1173) under UV light ($\lambda = 365$ nm). The peptide-functionalized surfaces were characterized with XPS and nanoindentation to determine the surface nitrogen concentration and modulus, respectively. Monitoring the concentration of nitrogen allowed for the determination of a relative amount of peptide attachment to the vinyl groups, since the nitrogen signal originates only from the peptide. The concentration of nitrogen increased with increasing UV exposure time for both PVMS and PVMS-TCS/PDMS, as shown in Figure 7.12a. The modulus of the PVMS network increased 3 fold after 10 minutes of UV exposure, because the photoinitiator molecules diffused through PVMS network, activated by the UV light and caused a secondary network formation, which increased the modulus dramatically. In contrast, the modulus of the PVMS-TCS/PDMS networks did not get affected as a result of the post-modification for 3 reasons: 1) a fraction of the vinyl groups was already consumed for the TCS coupling, 2) a portion of the remaining vinyl groups was consumed by the thiol-ene addition reaction and therefore less vinyl groups were left for cross-linking; 3), the inert nature of the PDMS substrate underneath the PVMS-TCS coating did not allow for the alteration of its modulus with the photoinitiator molecules. In addition, the thickness of the PVMS-TCS layer was small (≈ 200 nm) and therefore the change in the modulus of the PVMS-TCS layer did not contribute substantially to the measured composite modulus (The penetration depth of the indenter tip was 1000 nm into the sample).

Other chemical modification routes were also explored. Here the PVMS chains were modified initially via thiol-ene addition reaction and then the TCS molecules were coupled to

the remaining vinyl groups to introduce cross-linkable groups, as represented in Figure 7.13. Two different thiol molecules, fluorinated thiol (F8-SH) and thiol-terminated PEG (PEG-SH), were utilized for these reactions to generate hydrophobic and hydrophilic, respectively, surfaces. The chemical structures and the WCAs of the functional copolymer layers spin-coated onto silicon wafers are shown in Figure 7.14. The F8 fluorinated mesogens attached to the coating rendered the surface hydrophobic with a WCA of $112.3 \pm 0.8^\circ$. The PEG oligomers rendered the surface hydrophilic with a WCA of $55.1 \pm 3.1^\circ$. Chemical changes occurring on the surface of the coating were confirmed with FT-IR.

7.3.2. PVMS-TCS COATING ON PET SUBSTRATES

In addition to the PDMS network substrates, the PVMS-TCS coating was applied to PET (Mylar DL) films. The surface properties of these bilayer films were studied before and after the UVO treatment and after subsequent deposition of semifluorinated t-F8H2 SAMs.

PVMS-TCS copolymer solutions with different concentration were spin-coated onto Mylar films (PVMS-TCS/PET) and silicon wafers (PVMS-TCS/SiO_x). The thicknesses of the PVMS-TCS/SiO_x measured with ellipsometry were 102.1 ± 1.7 , 204.8 ± 2.7 nm and ≈ 1 μ m for samples spin-coated from 1.5, 3.3 and 10% (w/w) PVMS-TCS solutions in toluene, respectively. We assumed that the thicknesses of PVMS-TCS on PET were similar to the thickness of PVMS-TCS measured on SiO_x.

The FT-IR spectra of PET, PVMS-TCS/PET (PVMS-TCS with thicknesses of $\approx 1 \mu\text{m}$ and $\approx 200 \text{ nm}$), and the PVMS network are shown in Figure 7.15. After the TCS coupling to PVMS, the intensity of the C=C stretch ($\approx 1587 \text{ cm}^{-1}$) signal disappeared and the intensities of the bands corresponding to C=C twist/ $=\text{CH}_2$ wagging ($\approx 960 \text{ cm}^{-1}$) and $=\text{CH}_2$ scissors ($\approx 1407 \text{ cm}^{-1}$) decreased. The FT-IR spectra thus indicate that the coupling of TCS to the vinyl group of PVMS was efficient and close to quantitative. Further examination of the FT-IR spectra revealed that the amount of Si-O-Si bonds and -OH groups increased compared to the PVMS fluid. Simultaneous formation of -OH groups took place ($\approx 3300 \text{ cm}^{-1}$), which can be used for further modification of the surface with organosilane or acid chlorides. PVMS-TCS/PET and PVMS-TCS/SiO_x obtained from 1.5 and 3.3% (w/w) PVMS-TCS copolymer solution were utilized for further characterization and modification. Similar results were obtained for all thicknesses; therefore only the results for $\approx 200 \text{ nm}$ thick PVMS-TCS coating are summarized here.

The wettability of PET (PET-UVO), PVMS-TCS/PET (PVMS-TCS/PET-UVO) and PVMS-TCS/SiO_x (PVMS-TCS/SiO_x-UVO) was measured as a function of the UVO treatment time and the WCA data are plotted in Figure 7.16. As discussed in Chapter 2 of this Thesis, the UVO treatment causes chain scission and introduces hydrophilic moieties into the PET surface. As a result, the wettability of PET increases with increasing UVO exposure dose and the WCA decreases and reaches a plateau at $\approx 40^\circ$ after ≈ 5 minutes of the UVO treatment. In contrast, the WCA of PVMS-TCS/PET-UVO (\blacktriangle , Figure 7.16b) and PVMS-TCS/SiO_x-UVO (\blacksquare , Figure 7.16b) reach complete wettability in only 6 minutes. The

WCA of PVMS-TCS/PET-UVO reaches lower values than the PET surface. In Chapter 2 we discussed that UVO treatment of PET produced water-soluble low molecular weight organic compounds (LMWOC), which can be removed by water washing and leave behind less hydrophilic PET surfaces. In contrast, the silicon atoms on PVMS-TCS/PET layer exists as silanols and other hydrophilic groups and react with each other to form a thin silica-like layer. The wettabilities of PVMS-TCS/PET-UVO and PVMS-TCS/SiO_x-UVO are nearly identical for the same UV exposure time, which suggests that the properties of both surfaces are dictated primarily by the PVMS-TCS coating.

The surface atomic concentration of carbon, oxygen and silicon for PET, PVMS-UVO and PVMS-TCS/PET was determined by XPS as a function of the UVO exposure time. The oxygen and carbon concentrations for PET (●), PVMS (□) and PVMS-TCS/PET-UVO (▲) increased and decreased, respectively, (cf. Figure 7.17) due to the introduction of hydrophilic moieties (i.e., -OH, carboxyls, and ketones) and the elimination of carbon-containing groups from the sample surface. The decrease of WCA was accompanied with a concurrent increase in the oxygen atomic concentration on the PET-UVO and PVMS-TCS/PET-UVO surfaces as a result of the UVO treatment. Oxygen concentrations of PET-UVO (●), PVMS-UVO (□) and PVMS-TCS/PET-UVO (▲) increased for the 5 minutes of UVO treatment and leveled-off at ≈38%, ≈51% and ≈54% for PET, PVMS-TCS, and PVMS surfaces, respectively. The oxygen concentration of the PET films after the UVO exposure was lower than that of the PVMS-UVO and PVMS-TCS/PET-UVO samples. The UVO treatment induced chain scission and caused removal of oxidized small PET fragments from the PET surface, which

prevented further increase in PET modification, as eluded to earlier in the text. Before the UVO treatment, the PVMS-TCS/PET surface contained more oxygen than the PVMS film due to the Si-O-Si bonds formed between the hydrolyzed TCS molecules during spin-coating. However, after the UVO treatment the oxygen concentration in both samples reached approximately the same level due to incorporation of hydrophilic moieties and silanol groups.

The positions of the various peaks obtained in high-resolution XPS (HR-XPS) experiments reveal information about chemical environment of the corresponding atoms. For example, the silicon atom of polysiloxane has two neighboring oxygen atoms with a binding energy (Si 2p) centered at 99.5 eV. In contrast, the silicon atom in silica (SiO_x) has, on average, 4 neighboring oxygen atoms and a binding energy of 103.6 eV (more scientific: tetrahedral coordination of each silicon atom to four oxygen atoms). The Si 2p peaks of unmodified PVMS and PDMS networks are centered at 102.3 eV (normalized with respect to 285 eV C 1s), but this value is shifted to 102.8 eV for the unmodified PVMS-TCS/PET film. This shift is due to the formation of a 3-dimensional Si-O-Si network during the hydrolysis of TCS and subsequent shift in the binding energy towards that of SiO_x . In addition, the examination of HR-XPS Si 2p spectra of PVMS-TCS/PET reveals the conversion of organo-silicon to SiO_x as a result of the UVO exposure, as shown in Figure 7.18. The Si 2p peak-shifts of PVMS-TCS/PET-UVO possess a trend that is similar to the PVMS-UVO network, where the Si 2p peak shifts to higher binding energies up to 10 minutes of UVO exposure and then saturates at ≈ 103.6 eV, which corresponds to ≈ 1.3 eV peak shift. Ouyang et. al.,

reported Si 2p peak shifts of 1.4 and 1.2 eV for PDMS and PDMS-co-PVMS copolymers respectively after 120 minutes of UVO treatment. Therefore, having lower peak shift of 1.3 eV for the UVO modified PVMS-TCS layer is reasonable. The of Si 2p binding energy peak shift of PVMS-TCS/PET-UVO (≈ 1.3 eV) did not reach the value for SiO_x (≈ 4.1 eV) because of the thickness of SiO_x like layer did not reach the sampling depth of the XPS, which is ≈ 10 nm.

The morphology of PET-UVO and PVMS-TCS/PET-UVO surfaces after 0, 2, 8 and 30 minutes of UVO treatment was examined by SEM. Representative SEM images of the PET-UVO and PVMS-TCS/PET-UVO specimens are shown in Figure 7.19. From the images it is clear that the surface topography of the PET films did not change significantly in the first ≈ 2 min of the UVO treatment. After ≈ 8 min, however, the UVO treatment alters the surface topography appreciably. Specifically, discrete, spheroidal grains measuring $\approx 82 \pm 4$ nm in diameter become apparent. The size of these grains increased with increasing UVO exposure time, and reached $\approx 113 \pm 7$ nm in diameter after 30 min of UVO.^[25] This is due to the semi-crystalline nature of PET films, where the crystalline and amorphous regions of PET films possess different etching/degradation rates. In contrast, the surface topography of the PVMS-TCS/PET-UVO does not change significantly during the course of UVO treatment as shown in Figure 7.19b because the etching/degradation rate for PVMS-TCS was uniform throughout the coating.

Hydrophilic functionalities introduced in PET and PVMS-TCS/PET films during the UVO treatment were utilized to attach reactive organosilane precursors, which are known to

chemisorb predominantly to hydroxyl groups on the surface.^[26, 27] As a proof of concept, we used semifluorinated organosilanes based on trichlorosilane head groups; these molecules are known to react very rapidly with the surface-bound –OH groups even at ambient temperatures.^[28] Semifluorinated t-F8H2 SAMs were deposited from vapor on top of the UVO treated samples, as detailed in the Experimental section. The properties of the semifluorinated SAMs on PET-UVO (PET-UVO/tF8H2) and semifluorinated SAMs on PVMS-TCS/PET-UVO (PVMS-TCS/PET-UVO/tF8H2) were characterized by WCA and NEXAFS, as described in detail below.

In Figure 7.20, we plot the WCA of PET-UVO/tF8H2 (●) and PVMS-TCS/PET-UVO/tF8H2 (▲) samples as a function of the UVO treatment time of PET-UVO and PVMS-TCS/PET-UVO substrates. For comparison, the WCA data from t-F8H2 SAMs formed on top of a silicon wafer (■) (SiO_x/tF8H2) are also included. Whereas the WCA of the SiO_x/tF8H2 samples is ≈115° for all UVO times and agrees well with previously reported results^[28], the WCA values of PET-UVO/tF8H2 are consistently lower than those measured on SiO_x/tF8H2. In addition, the WCA values decrease with increasing the UVO treatment time for PET-UVO/tF8H2 except for untreated PET films. This reduction is due to the removal of the LMWOC layer that has reacted with tF8H2 during the ethanol rinsing step (for detailed discussion see Chapter 2 in this Thesis). By comparing the WCA values of PET-UVO (●, Figure 7.16) and PET-UVO/tF8H2 (●, Figure 7.20) at long UVO treatment times it is apparent that some tF8H2 molecules remained on the PET-UVO surface even after washing. The WCA values of the PVMS-TCS/PET-UVO/tF8H2 samples (▲, Figure 7.20)

are nearly identical to those of tF8H2 SAMs on silicon wafers. In addition, PVMS-TCS/PET sample that was not UVO-treated but exposed to tF8H2 had a WCA of $110.9 \pm 1.2^\circ$, which reveals a minute attachment of tF8H2 molecules directly on PVMS-TCS coating, which took place due to the –OH groups already present on spin-coated PVMS-TCS layer on PET as shown by the FT-IR spectra in Figure 7.15.

NEXAFS spectroscopy was utilized to ascertain the population and molecular orientation of the t-F8H2 molecules in the SAMs on top of the PET-UVO and PVMS-TCS/PET-UVO substrates. Partial electron yield (PEY) NEXAFS intensities are independent of the molecular orientation at $\theta = 50^\circ$ (“magic angle”), where θ denotes the angle between the sample normal and the direction of the electric vector of the X-ray beam. At this so-called “magic angle” the PEY NEXAFS intensity provides a measure of the concentration of various chemical species in the sample surface. The PEY spectra collected from PET-UVO/tF8H2 and PVMS-TCS/PET-UVO/tF8H2 samples at the carbon K-edge at $\theta = 50^\circ$ are plotted for different UVO exposure times for PVMS-TCS/PET-UVO (Figure 7.21a) and PET-UVO (Figure 7.21b). The peaks located at 284.4, 286.5, 292.0 and 295.0 eV in the PEY spectra in Figure 7.21 correspond to the $1s \rightarrow \pi^*_{C=C}$, $1s \rightarrow \sigma^*_{C-H}$, $1s \rightarrow \sigma^*_{C-F}$ and $1s \rightarrow \sigma^*_{C-C}$ NEXAFS transitions of the C=C, C-H, C-F and C-C bonds, respectively. In Figure 7.21a, only the peaks of $1s \rightarrow \sigma^*_{C-H}$, $1s \rightarrow \sigma^*_{C-F}$ and $1s \rightarrow \sigma^*_{C-C}$ transitions are present for all the UVO treatment times and the spectra of PVMS-TCS/PET-UVO/tF8H2 for all UVO times were very similar to those measured on tF8H2 SAMs on SiO_x (not shown).

Likewise, the spectra of PET-UVO/tF8H2 (cf. Figure 7.21b) for UVO times shorter than

5 minutes are very similar to the aforementioned spectra of tF8H2 SAMs on SiO_x. However, a new spectral feature located at 285 eV appeared in samples treated for UVO times greater than 4 minutes, which corresponds to the 1s→π* transition of the C=C signal present in PET. This observation reveals that PET has to be present within the first ≈2 nm of the sample surface, a typical probing depth for the PEY NEXAFS signal. In addition, the appearance of the 1s→π*_{C=C} signal brought in a decrease in the intensity of the 1s→σ*_{C-F} peak, which indicated a reduction in the amount of fluorine on the PET-UVO/tF8H2 with increasing UVO treatment time. This result agrees well with the trend in the contact angle data discussed previously (cf. ●, Figure 7.20). The reduction is due to the removal of LMWOC layer from PET-UVO/tF8H2 surface with tF8H2 molecules attached to it, as depicted schematically in Figure 7.22. The PET surface roughens with increasing UVO treatment time (due to increases in the LMWOC layer thickness) and therefore the quality of the SAM deteriorates. In addition, thicker LMWOC are easier to remove as the washing fluid can penetrate through the defects present in the SAM. In contrast, the tF8H2 SAMs were stable on PVMS-TCS/PET-tF8H2 samples regardless of the UVO exposure time for 3 reasons: 1) the surface of PVMS-TCS/PET-UVO contains silanol groups, which forms more stable Si-O-Si bonds with tF8H2 molecules, 2) the PVMS-TCS/PET-UVO surface does not possess any LMWOC layer and 3) the PVMS-TCS/PET-UVO has a smoother surface than PET-UVO.

NEXAFS spectroscopy has been utilized routinely to obtain information about the orientation of molecules on surfaces. We collected the PEY NEXAFS spectra from PET-UVO/tF8H2 and PVMS-TCS/PET-UVO/tF8H2 samples at various orientations of the sample

with respect to the x-ray beam since the orientation of anti-bonding orbitals relative to the electric vector of the polarized x-ray beam affects the intensity of the $1s \rightarrow \sigma^*$ transition signals. The intensity of each peak contains information about the concentration and orientation of the tF8H2 molecules on the surface. In Figure 7.23a we plot the normalized PEY NEXAFS spectra of PVMS-TCS/PET-UVO/tF8H2 as a function of the photon energy around the carbon K-edge for $\theta = 20^\circ$ and 90° for different UVO treatment times. The most important peaks in the spectra are those at 292 and 295 eV, corresponding to the $1s \rightarrow \sigma^*_{C-F}$ and $1s \rightarrow \sigma^*_{C-C}$ signals, respectively. By comparing the relative intensities of the two peaks at various orientations we conclude that the tF8H2 chains are oriented roughly perpendicularly on the substrates (the peak at 292 eV is higher and that at 295 eV is lower at $\theta = 90^\circ$ relative to the intensities collected $\theta = 20^\circ$).^[5, 29] While we do not provide quantitative measure of the orientation in this paper, it suffices to say that a good measure of the degree of perpendicular orientation is the difference between the spectra collected at $\theta = 20^\circ$ and 90° . However, a close examination of the normalized PEY NEXAFS spectra of PET-UVO/tF8H2 in Figure 7.23b reveals that the orientation of the tF8H2 molecules on the surface was lost for long UVO times, because the NEXAFS spectra do not exhibit any orientation in the tF8H2 molecules, although a portion of the tF8H2 SAMs still remains attached to the underlying substrate, as evidenced by the presence of the fluorine signal in the NEXAFS spectra. We note that the fact that no orientation is detected in the specimens does not mean the t-F8H2 chains are not oriented in the SAMs. Because of the roughening of the substrate, the various portions of the SAM may still be oriented but are pointing into different directions.

As mentioned earlier, PVMS-TCS coating was applied to PE, PP, Kapton® and glass substrates. Their wettabilities were determined qualitatively along with bare substrates. The PVMS-TCS coated substrates had similar wettabilities regardless of the underlying substrate, as shown qualitatively in Figure 7.24a. After exposing both the bare and PVMS-TCS coated substrates to UVO for 5 minutes of UVO, we noted that while the wettability of the bare surfaces improved, it was much higher than that of the specimens with the PVMS-TCS overcoat; the latter were nearly completely wettable (cf. Figure 7.24b). It is shown that the surface characteristics of a variety of substrates are governed by the PVMS-TCS coating regardless of the underlying substrate.

7.3.3. SURFACE INITIATED POLYMERIZATION ON PET, PP AND SiO_x SURFACES

Coupling of the azo-based free radical polymerization (FRP) initiators to PVMS-TCS led to FRP-functionalized PVMS-TCS copolymers (PVMS-TCS-azo) as schematically depicted in Figure 7.25. Subsequent spin-coating of the PVMS-TCS-azo copolymer on PET, PP and SiO_x surfaces facilitated the attachment of FRP initiators to the surfaces of the aforementioned materials. FT-IR data of PVMS-TCS-azo coated PP films exhibited the characteristic peaks of azo ($\approx 1510\text{ cm}^{-1}$), amide (≈ 1650 and $\approx 1530\text{ cm}^{-1}$) and $-\text{OH}$ ($\approx 3300\text{ cm}^{-1}$) groups of the initiator.^[24] Subsequent surface initiated polymerization of methyl methacrylate (MMA) in the presence of PVMS-TCS-azo coated PET, PP and SiO_x substrates resulted in tethered poly(methyl methacrylate) (PMMA) chains on these substrates. FT-IR

spectra of PMMA, PET, PP, PVMS-TCS-azo/PET-PMMA and PVMS-TCS-azo/PP-PMMA films are shown in Figure 7.26a. The presence of PMMA is evidenced from the peaks located at 1730, 1270, 1241, 1150 and 1074 cm^{-1} in the PVMS-TCS-azo/PET-PMMA and PVMS-TCS-azo/PP-PMMA spectra. In addition, the initial thickness of PVMS-TCS-azo layer on SiO_x wafer (≈ 100 nm) increased after polymerization of MMA (≈ 185 nm) as measured by ellipsometry. A PMMA layer ≈ 85 nm thick was grown on SiO_x wafer; the photographs of PVMS-TCS-azo/ SiO_x and PVMS-TCS-azo/ SiO_x -PMMA are shown in Figure 7.26b.

7.4. CONCLUSION AND FUTURE WORK

Thin cross-linkable functional copolymer coatings on various surfaces was performed by first coupling trichlorosilane (TCS) molecules with the vinyl groups of PVMS in the presence of Pt(0) catalysts at room temperature and spin-coating the resulting PVMS-TCS onto various substrates. The silane coupling is tunable, quantitative, and controlled by the vinyl:TCS ratio in the reaction mixture. The thickness and modulus of the coating can be altered by varying the vinyl:TCS ratio and the concentration of the copolymer in the spin-coating solution.

The stability of the PVMS-TCS coating on silicon wafer (SiO_x) and spin-coated thin PET film (PET/ SiO_x) on silicon wafer was monitored by thickness measurements via ellipsometry before and after sonication in a variety of solvents. The thickness of the films did not change after sonication, which confirmed the high stability of the coating on SiO_x and PET/ SiO_x .

The same stability test was performed on the UVO-treated films for different periods of time after converting and rendering the coating hydrophilic. No removal of material was observed, which suggests that the coating is stable under relatively harsh environmental conditions. In addition, the coating stability on PP, PE, PET, PA and Kapton® films was investigated with the Scotch Tape Adhesion Test method. The coating was stable on all substrates containing a few –OH groups that served as “anchoring” points for the coating. The stability of the coating on PP and PE improved with a brief UVO treatment of the bare substrates, which introduced –OH functional groups on substrate surface.

Spin-coated PVMS fluid on PDMS network surface resulted in dewetted PVMS films due to autophobicity and thermodynamic incompatibility between PVMS and PDMS. The stability of the spin-coated PVMS-TCS copolymer on PDMS network (PVMS-TCS/PDMS) surface increased with increasing the TCS coupling to the vinyl groups in PVMS. The quality of the PVMS-TCS coating improved with increasing extent of TCS coupling for the same coating thickness due to faster “immobilization” of PVMS-TCS chains on the PDMS network. Higher concentrations of the copolymer in spin-coating solution resulted in thicker and higher quality PVMS-TCS coatings. The surface chemistry of the composite layers was studied with FT-IR and contact angle goniometer. The coating behaved as PVMS network with increasing PVMS-TCS thickness based on the WCA data and IR signal corresponding to vinyl bands. The UVO treatment of PVMS-TCS/PDMS resulted in improved wettability; the WCA values reached the contact angle values of UVO-treated bare PVMS network for the coatings prepared from PVMS-TCS copolymer concentration above 1% (w/w).

Chemical modification of the remaining vinyl groups of PVMS-TCS/PDMS and PVMS network was carried out with a thiol-terminated peptide via thiol-ene addition reaction as a function of the UV exposure time. The final products were characterized with XPS and nanoindentation. After thiol-ene addition reaction, the measured nitrogen concentration of PVMS-TCS/PDMS network was in accord with the nitrogen concentration of the PVMS network. This finding suggested that the PVMS-TCS/PDMS network behaved as a bare PVMS network against thiol-ene addition reaction except that the modulus of PVMS-TCS/PDMS did not increase relative to the PVMS network. Alternatively, the vinyl groups of PVMS were initially modified via thiol-ene addition reaction and then TCS molecules were coupled to the remaining vinyl groups to introduce cross-linkable moieties. Two different thiol molecules, i.e., semifluorinated thiol and thiol terminated PEG, were used, which produced hydrophobic and hydrophilic coatings, respectively, as evidenced by the WCA measurements. Utilization of these coatings would facilitate one-pot preparation of self-cleaning and protein resistant materials without cumbersome sample preparation steps.

The PVMS-TCS coating was also applied on PET films (PVMS-TCS/PET); the FT-IR analysis confirmed that the PVMS-TCS coating contains –OH groups and these –OH groups can be used to perform additional modification via organosilanes or acyl chlorides. The effect of the UVO treatment on PVMS-TCS/PET samples was compared to the PET films. The WCA of PET films reached 40° and leveled-off after 6 minutes of the UVO treatment due to the removal of more hydrophilic PET fragments by evaporation. In contrast, the PVMS-TCS/PET surface became completely wettable in 6 minutes of the UVO treatment,

because the silicon groups on the surface formed a “silica”-like layer. Surface atomic concentrations of PVMS-TCS/PET-UVO and PET-UVO agreed well with the contact angle measurements as a function of the UVO treatment time. Formation of 3-dimensional silicon networks by the cross-linked TCS molecules was verified by examination of Si 2p high resolution XPS spectra and atomic concentration of oxygen on PVMS network and as spun PVMS-TCS coating.

The surface topography of PET-UVO and PVMS-TCS/PET-UVO films was monitored as a function of the UVO time. The PET-UVO surface becomes rougher with increasing the UVO treatment time. Semi-spherical features formed on the PET-UVO surface after 8 minutes and got larger with increasing the UVO exposure times. In contrast, the surface roughness of PVMS-TCS coated PET samples did not change significantly with the UVO treatment. This effect is due to the homogenous etching rate of PVMS-TCS coating when compared to PET surface, which consists of amorphous and semi-crystalline regions with different etching rates.

Semifluorinated SAMs on PET-UVO and PVMS-TCS/PET-UVO were formed on PET-UVO and PVMS-TCS/PET-UVO substrates as a function of the UVO treatment time of the PET and PVMS-TCS/PET films. The SAMs were characterized by WCA measurements and NEXAFS spectroscopy to determine the quality of the semifluorinated surface. WCA measurements revealed that the wettability of PET-UVO/tF8H2 surface was lower than that of the model semifluorinated silica surface ($\text{SiO}_x/\text{tF8H2}$); the WCA values started to decrease with UVO treatment times of PET-UVO substrate greater than 2 minutes. The formation of

the LMWOC layer with increased surface roughness of PET-UVO caused partial removal of semifluorinated SAMs that resulted in a decrease in the WCA, PEY intensity and a loss of tF8H2 orientation on the PET-UVO substrates. The WCAs of PVMS-TCS/PET-UVO/tF8H2 layers were similar to SiO_x/tF8H2 regardless of the UVO treatment time of PVMS-TCS/PET substrate. The tF8H2 molecules on PVMS-TCS-UVO/tF8H2 substrates were oriented even for long UVO exposure times, because the underlying PET substrate was protected with PVMS-TCS layer against UVO treatment.

Decoration of PET, PP and SiO_x surfaces with PVMS-TCS-azo copolymer was performed and confirmed by FT-IR and ellipsometric measurements. Subsequent immersion of PVMS-TCS-azo coated substrates in MMA monomer and applying heat resulted in the formation of surface-tethered PMMA chains. Characterizations with FT-IR and ellipsometry confirmed the presence of PMMA chains attached to PET, PP and SiO_x substrates.

We have shown an alternative route to modify material surfaces by utilizing a universal functional coating and some possible applications of these coatings will be discussed as Future Work. Additional functionalities can be introduced to a variety of surfaces by incorporating nano-objects into the coating. Fumed silica particles and layered silicates are the potential candidates for such inclusions. In addition, exploiting the tunable thickness and modulus of the PVMS-TCS coating with the substrates that can swell will result in biaxial buckles as will be discussed below.

Incorporation of nanoparticles in PVMS-TCS copolymer coating would increase the functionality of the final coating. For instance, embedded fumed silica particles may

increase the hardness of the coating due to the inclusion of these “hard” nano-objects. The ability of fumed silica particles to react with chlorosilane groups of PVMS-TCS copolymer will lead likely to 3-dimensional networks. Incorporating nano-clays (layered silicates, i.e., montmorillonite) into PVMS-TCS coating would both increase the barrier properties and hardness of the coating (cf. Figure 7.27). Specifically, the presence of layered silicates will increase the tortuous path for the gas molecules to diffuse through the coating and thus lower permeation of gases. In addition, the presence of the -OH groups at the montmorillonite platelet edges will allow for reacting the clay platelets with PVMS-TCS copolymer and increase the robustness/hardness of the coating.

Finally, the PVMS-TCS copolymer coatings can be utilized to generate buckles on a variety of samples. For instance, bi-axial buckles can be formed on the substrates that can swell in solvents. Coating the swelled polymeric substrates with PVMS-TCS, exposing the coating to moisture and following solvent removal will form bi-axial buckles on the substrate surface provided there is a different in modulus between the coating and the substrate. Bi-axial buckles on PDMS network films were formed in the past after prolonged UVO treatment. Due to long UVO exposure times, a thin silica-like layer is generated on PDMS giving rise to buckles with many defects and cracks on the surface. It is hard to obtain truly bi-axial strain over the large areas on the substrates; therefore only a small portion of the resulting sample bears “real” bi-axial buckles. However, homogenous swelling of the substrates in a solvent can eliminate this problem. The tunability of the PVMS thickness and modulus would facilitate alteration of the wavelength of the formed buckles. For example, a

piece of PDMS network can be swelled in toluene and immersed in PVMS-TCS copolymer solution. After removing the PVMS-TCS/PDMS specimen from the copolymer solution, exposing it to moisture causes cross-linking of the top layer, which increases its modulus. Subsequent drying of PVMS-TCS/PDMS results in bi-axial buckles over a large area, as shown in Figure 7.28. Combining buckle formation with the aforementioned PVMS-TCS pre-modification routes would allow for facile generation of topographically-corrugated surfaces.

7.5. REFERENCES

- [1] S. J. Clarson, J. A. Semlyen, R. G. Jones, W. Andão, J. Chojnowski, - *Prentice Hall polymer science and technology series*.
- [2] M. J. Owen, *Industrial & Engineering Chemistry Product Research and Development* **1980**, *19*, 97.
- [3] R. G. Jones, W. Andão, J. Chojnowski.
- [4] C. Jalbert, J. T. Koberstein, A. Hariharan, S. K. Kumar, *Macromolecules* **1997**, *30*, 4481.
- [5] J. Genzer, K. Efimenko, *Science* **2000**, *290*, 2130.
- [6] J. T. Koberstein, *Journal of Polymer Science Part B-Polymer Physics* **2004**, *42*, 2942.
- [7] L. Herczynska, L. Lestel, S. Boileau, J. Chojnowski, S. Polowinski, *European Polymer Journal* **1999**, *35*, 1115.
- [8] H. Hillborg, J. F. Ankner, U. W. Gedde, G. D. Smith, H. K. Yasuda, K. Wikstrom, *Polymer* **2000**, *41*, 6851.
- [9] H. Hillborg, M. Sandelin, U. W. Gedde, *Polymer* **2001**, *42*, 7349.
- [10] R. L. Williams, D. J. Wilson, N. P. Rhodes, *Biomaterials* **2004**, *25*, 4659.
- [11] H. Hillborg, U. W. Gedde, *Polymer* **1998**, *39*, 1991.
- [12] H. Hillborg, U. W. Gedde, *Ieee Transactions on Dielectrics and Electrical Insulation* **1999**, *6*, 703.
- [13] K. Efimenko, M. Rackaitis, E. Manias, A. Vaziri, L. Mahadevan, J. Genzer, *Nature Materials* **2005**, *4*, 293.
- [14] H. Hillborg, S. Karlsson, U. W. Gedde, *Polymer* **2001**, *42*, 8883.
- [15] J. R. Vig, *Journal of Vacuum Science & Technology A: Vacuum, Surfaces, and Films* **1985**, *3*, 1027.

- [16] K. Efimenko, W. E. Wallace, J. Genzer, *Journal of colloid and interface science* **2002**, 254, 306.
- [17] W. T. S. Huck, N. Bowden, P. Onck, T. Pardoën, J. W. Hutchinson, G. M. Whitesides, *Langmuir* **2000**, 16, 3497.
- [18] M. Ouyang, C. Yuan, R. J. Muisener, A. Boulares, J. T. Koberstein, *Chemistry of Materials* **2000**, 12, 1591.
- [19] K. Efimenko, J. A. Crowe, E. Manias, D. W. Schwark, D. A. Fischer, J. Genzer, *Polymer* **2005**, 46, 9329.
- [20] M. M. E. Occhiello, G. Morini, F. Garbassi, P. Humphrey, *Journal of Applied Polymer Science* **1991**, 42, 551.
- [21] M. M. F. Garbassi, E. Occhiello, L. Barino, R. Scordamaglia, *Surface and Interface Analysis* **1989**, 14, 585.
- [22] M. Ouyang, R. J. Muisener, A. Boulares, J. T. Koberstein, *Journal of Membrane Science* **2000**, 177, 177.
- [23] J. Stöhr, *NEXAFS spectroscopy*, Springer-Verlag, Berlin ; New York **1992**.
- [24] G. Socrates, *Infrared characteristic group frequencies, tables and charts*, 2nd edition.
- [25] A. E. Ozcam, K. Efimenko, C. Jaye, R. J. Spontak, D. A. Fischer, J. Genzer, *Journal of Electron Spectroscopy and Related Phenomena* **2009**, 172, 95.
- [26] A. Ulman, *Chemical reviews* **1996**, 96, 1533.
- [27] F. Schreiber, *Progress in Surface Science* **2000**, 65, 151.
- [28] J. Genzer, K. Efimenko, D. A. Fischer, *Langmuir* **2002**, 18, 9307.
- [29] J. Genzer, E. Sivaniah, E. J. Kramer, J. G. Wang, H. Korner, M. L. Xiang, K. Char, C. K. Ober, B. M. DeKoven, R. A. Bubeck, M. K. Chaudhury, S. Sambasivan, D. A. Fischer, *Macromolecules* **2000**, 33, 1882.
- [30] M. Alexandre, P. Dubois, T. Sun, J. M. Garces, R. Jerome, *Polymer* **2002**, 43, 2123.

7.6. FIGURES

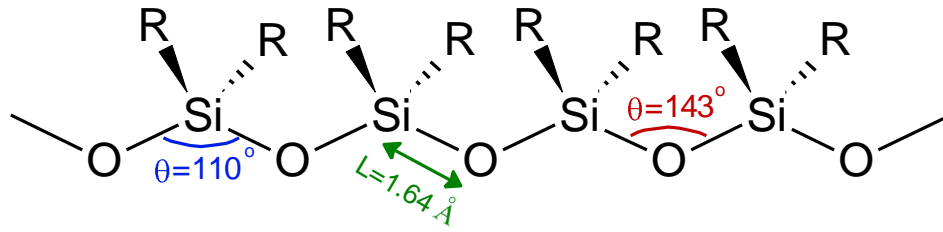


Figure 7.1. The silicone backbone with the bond angles and the bond length. If both R groups are methyl the polymer is called poly(dimethylsiloxane) (PDMS).

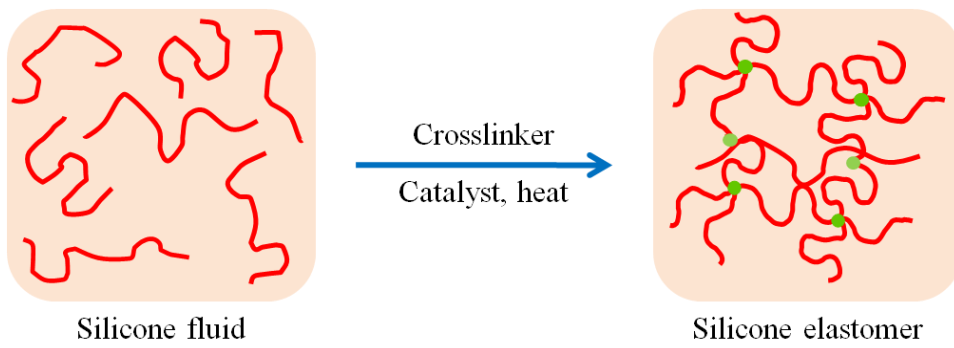


Figure 7.2. Linking silicone chains with each other to form the silicone elastomer networks (SENs).

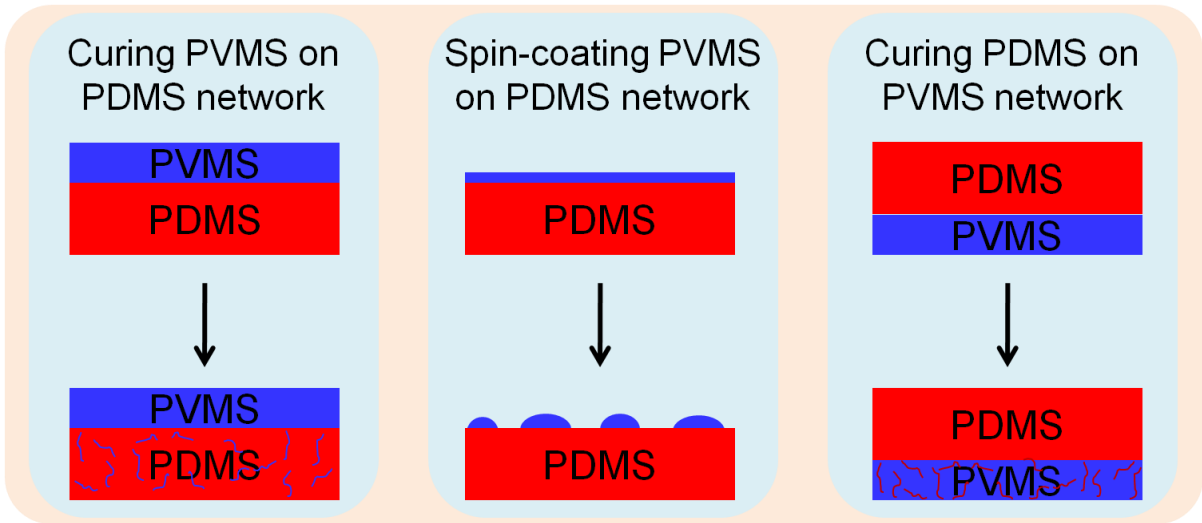


Figure 7.3. Possible routes to form bi-layers of silicone networks.

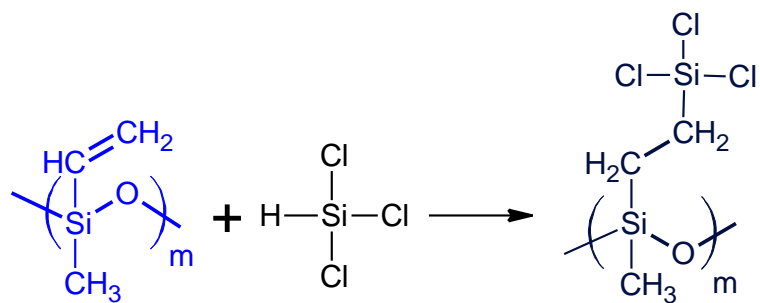


Figure 7.4. Coupling of trichlorosilane (TCS) molecule to vinyl groups of PVMS via the hydrosilylation reaction.

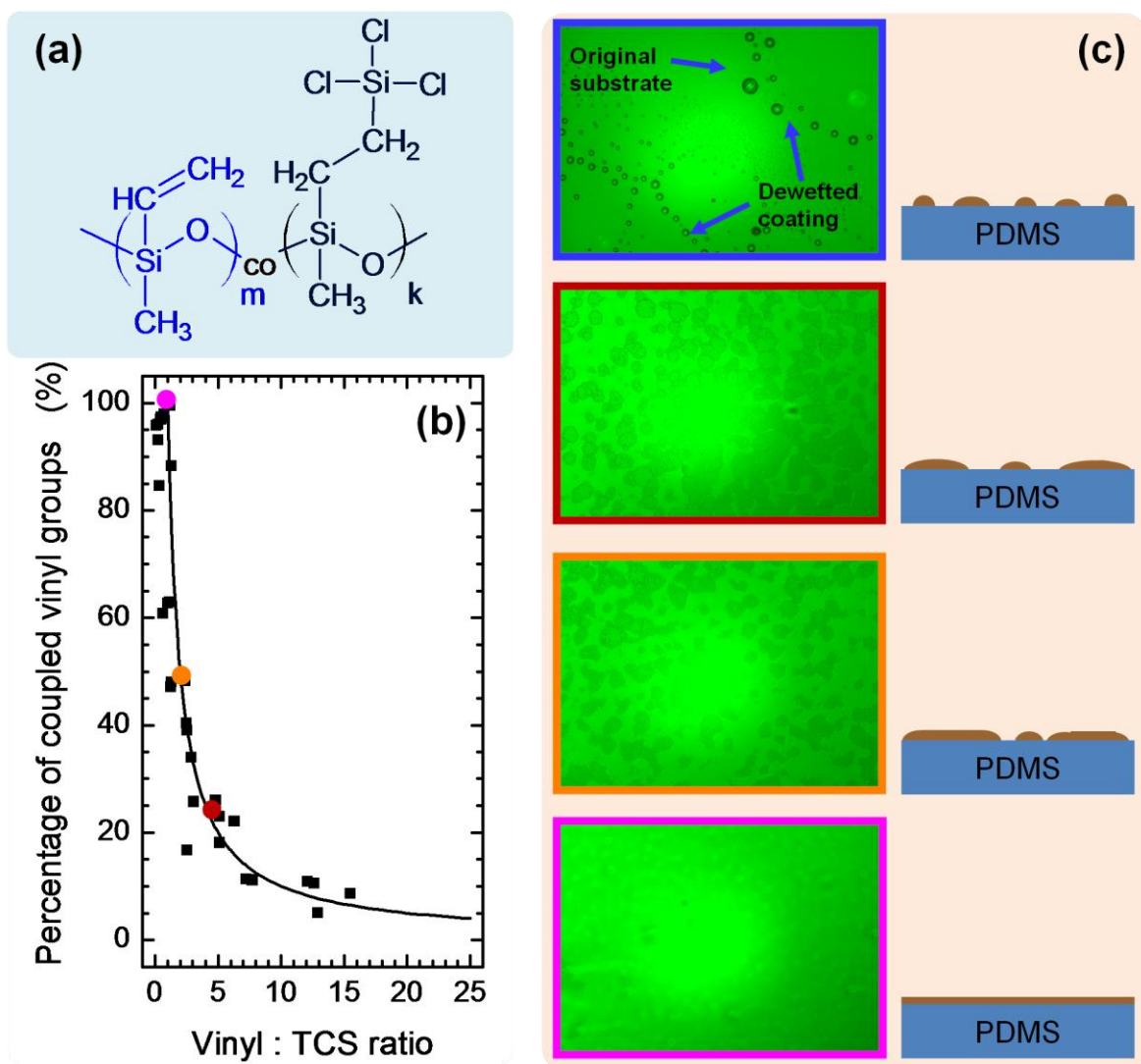


Figure 7.5. The chemical structure of PVMS-TCS/PVMS random copolymer (a), the percentage of reacted vinyl groups with the TCS molecules as a function of the vinyl:TCS ratio (b) and optical images of PVMS-TCS coated PDMS network with PVMS-TCS that has different percentages of the coupled vinyl groups. The red, orange and pink dots in Figure 7.3b correspond to the optical images of the same color frame in Figure 7.3c.

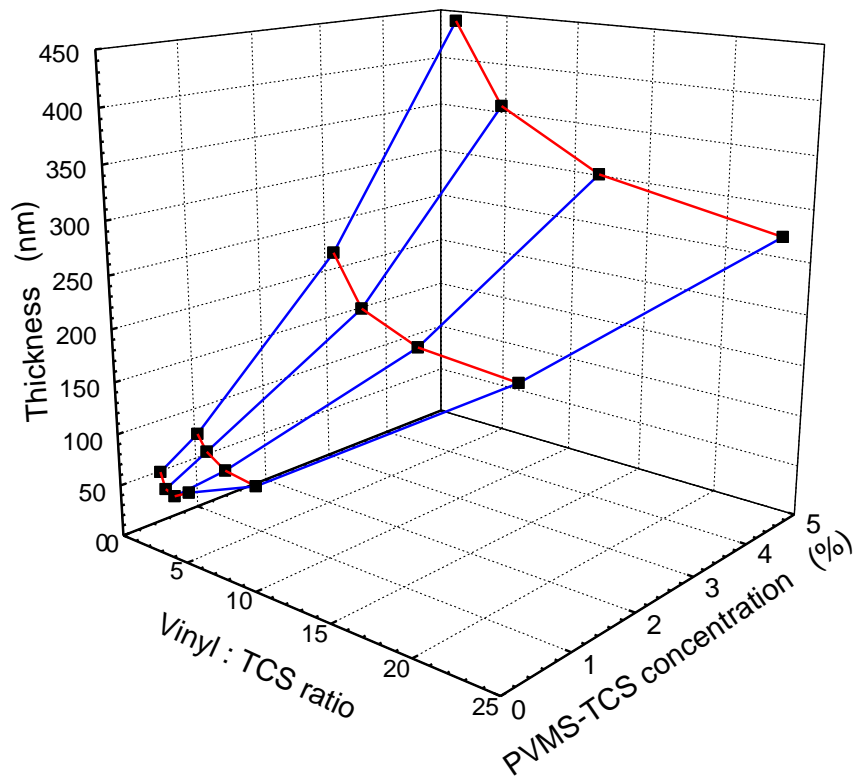


Figure 7.6. The thickness on the PVMS-TCS layer as a function of the concentration of PVMS-TCS in spin-coating solution and vinyl:TCS ratio (■). The lines are meant to guide the eye.

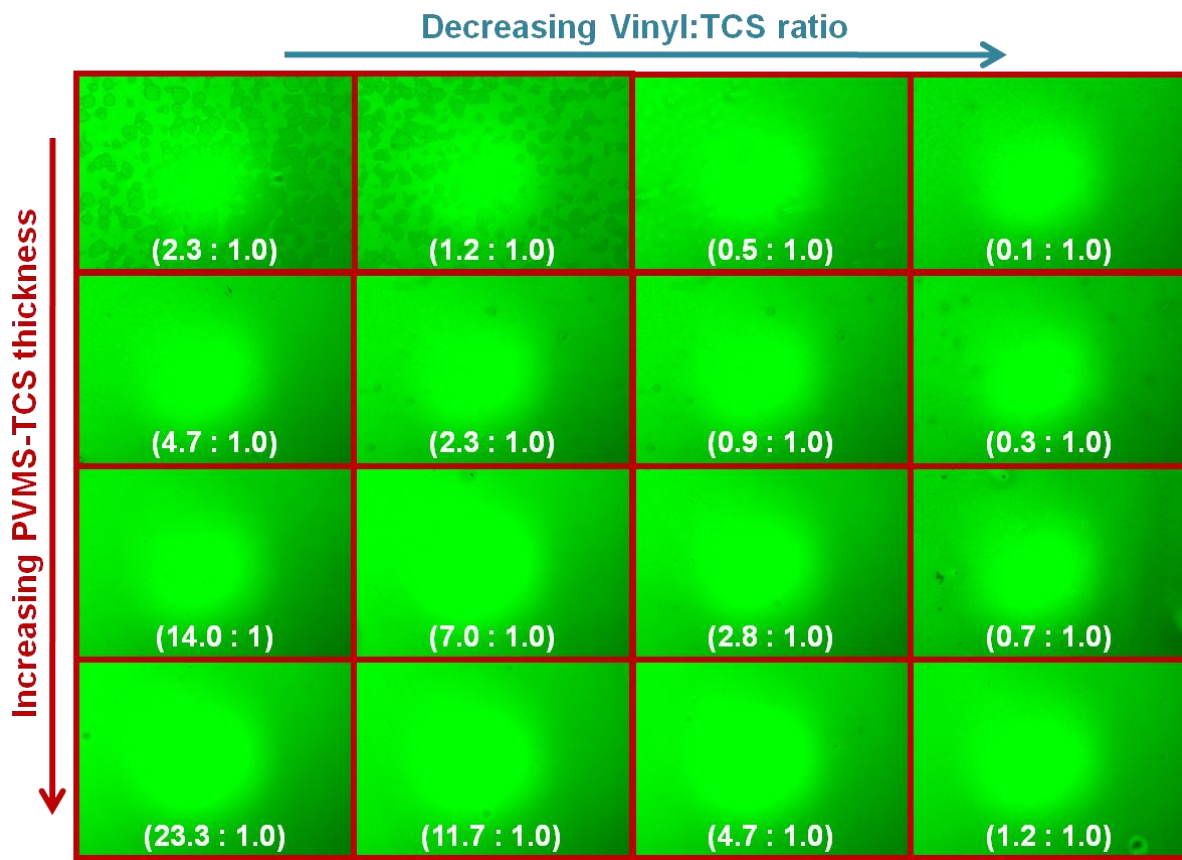


Figure 7.7. Optical microscopy images of spin-coated PVMS-TCS on PDMS network as a function of Vinyl:TCS ratio.

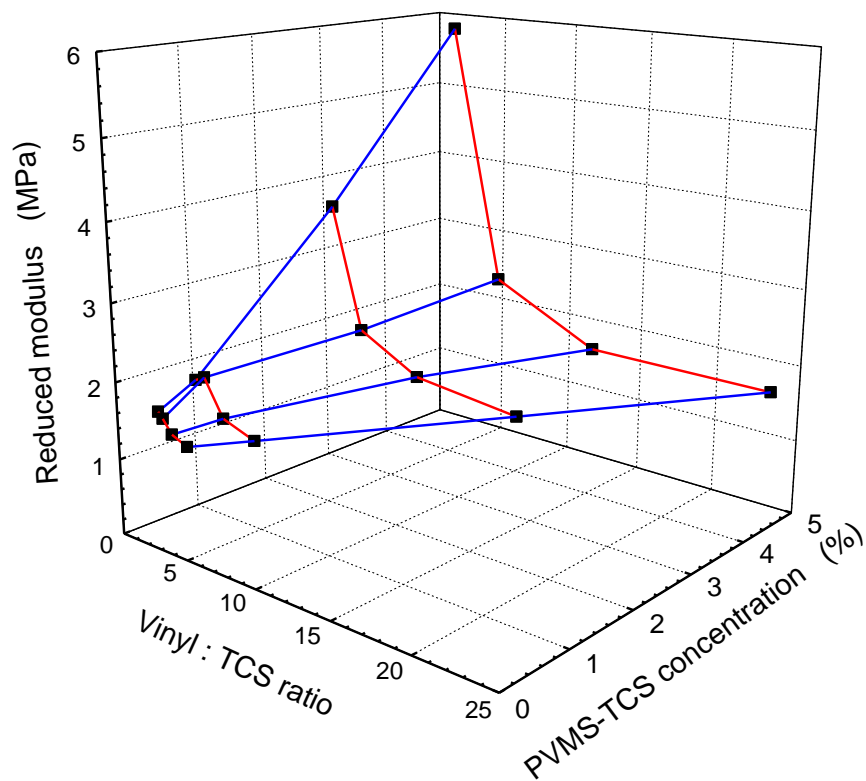


Figure 7.8. The modulus on the PVMS-TCS layer as a function of the concentration of PVMS-TCS in spin-coating solution and vinyl:TCS ratio (■). The lines are meant to guide the eye.

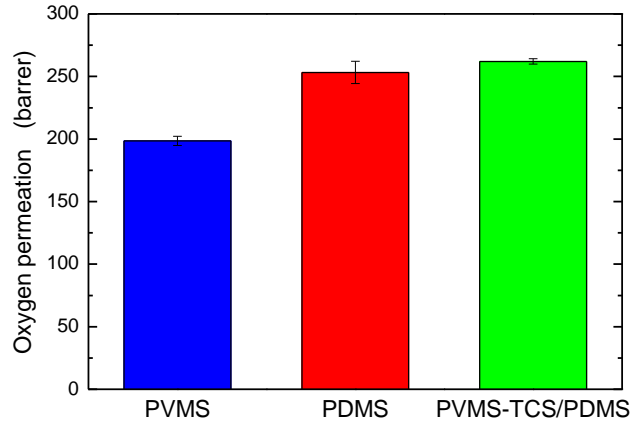


Figure 7.9. Oxygen permeation through the PVMS, PDMS and PVMS-TCS coated PDMS networks. PVMS-TCS layer was ≈ 150 nm, the vinyl:TCS ratio = 7. The values reported represent the average of 3 measurements, the error bars were calculated as “standard error”.

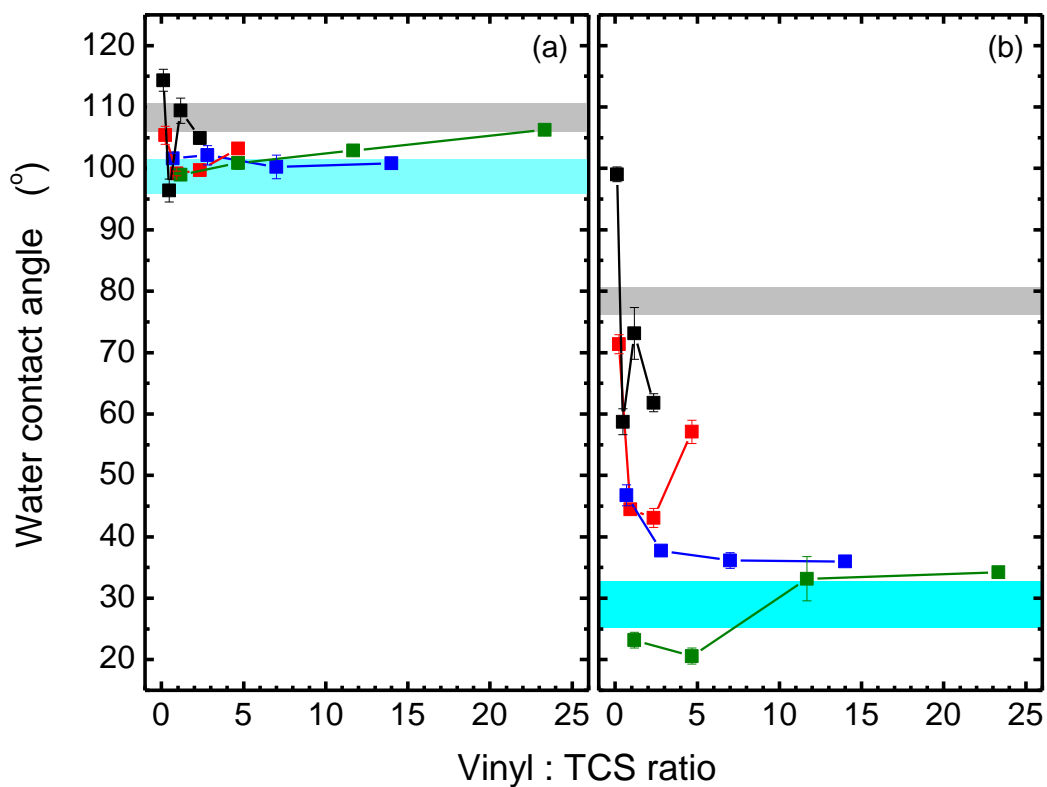


Figure 7.10. Water contact angle of PVMS-TCS coated PDMS networks as a function of vinyl : TCS ratio before (a) and after 10 minutes of UVO treatment for 0.5 (■), 1 (■), 3 (■), and 5% (■) PVMS-TCS concentration in spin-coating solution. The grey and light blue rectangles are the water contact angle range for bare PDMS and PVMS, respectively before and after 10 minutes of UVO treatment.

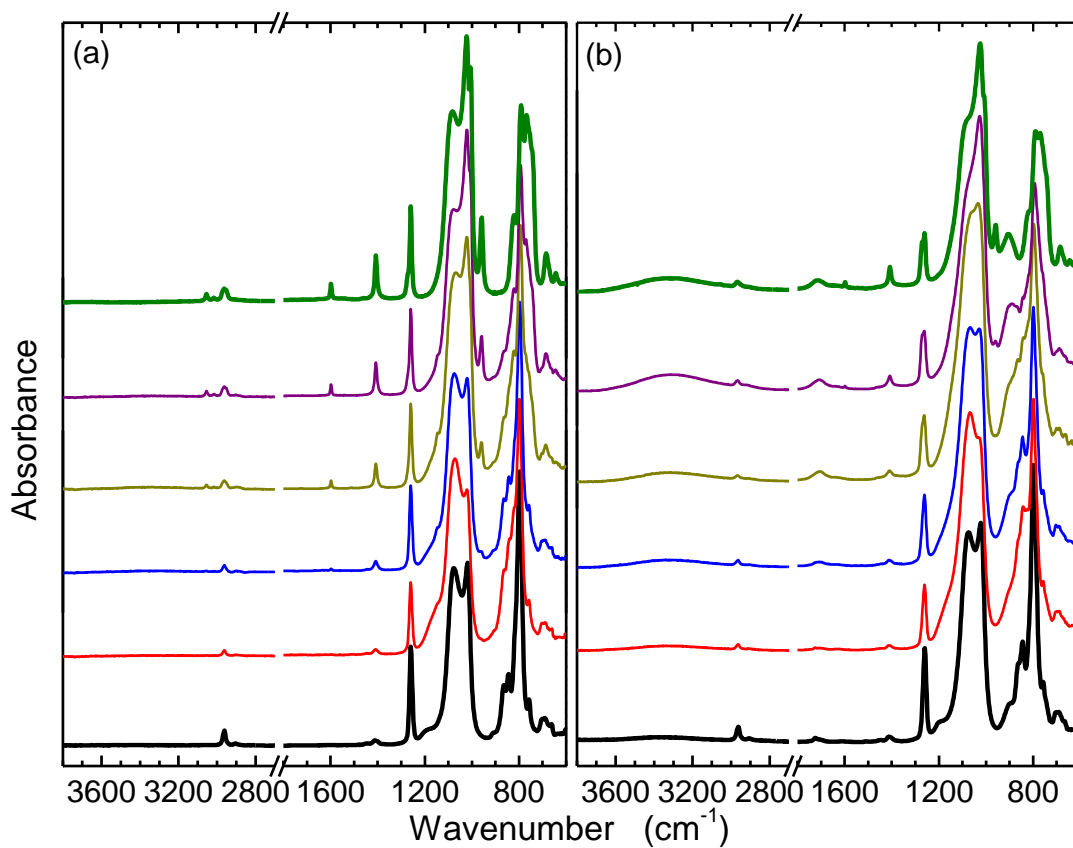


Figure 7.11. FT-IR spectra of PDMS (thick black line), PVMS-TCS/PDMS laminates (from 0.5 (red line), 1 (blue line), 3 (dark yellow line) and 5% (purple line) PVMS-TCS copolymer in spin-coating solution) and bare PVMS (thick olive line) before (a) and after 10 minutes (b) of UVO treatment.

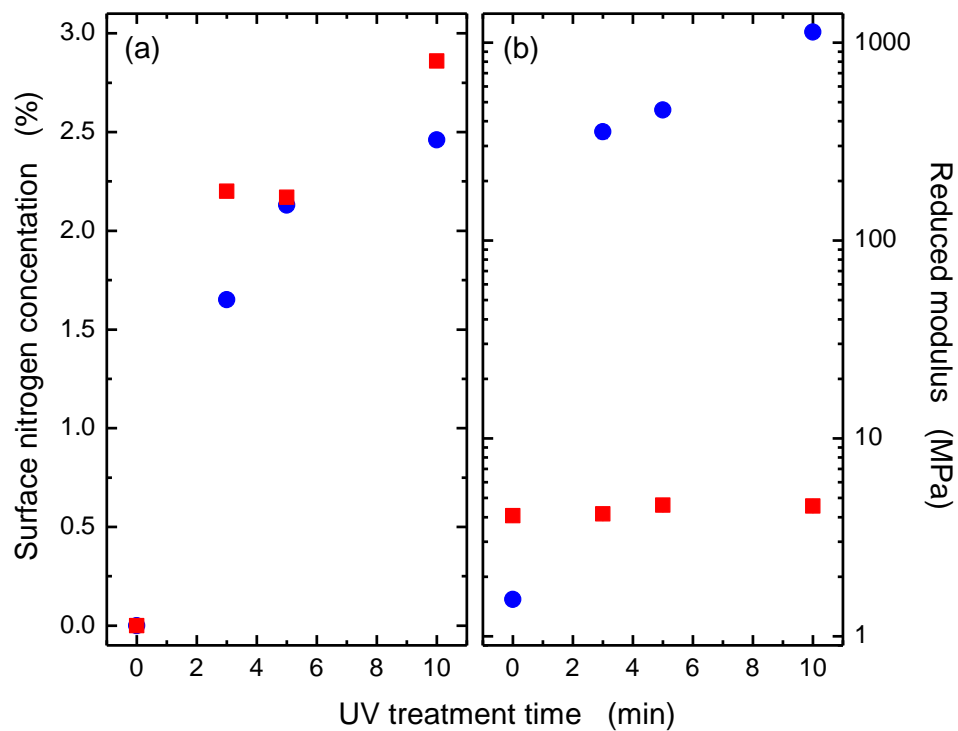


Figure 7.12. Surface nitrogen concentration (a) and modulus (b) of PVMS (●) and PVMS-TCS (■) coated PDMS network after attaching thiol-terminated peptide via thiol-ene addition reaction.

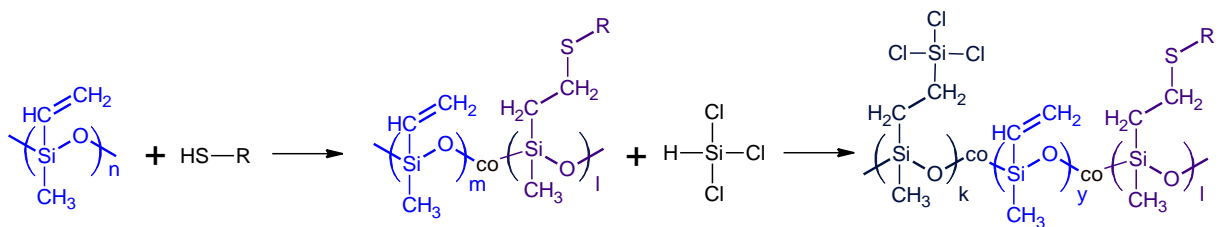


Figure 7.13. Reaction scheme depicting the pre-modification of PVMS-TCS coating.

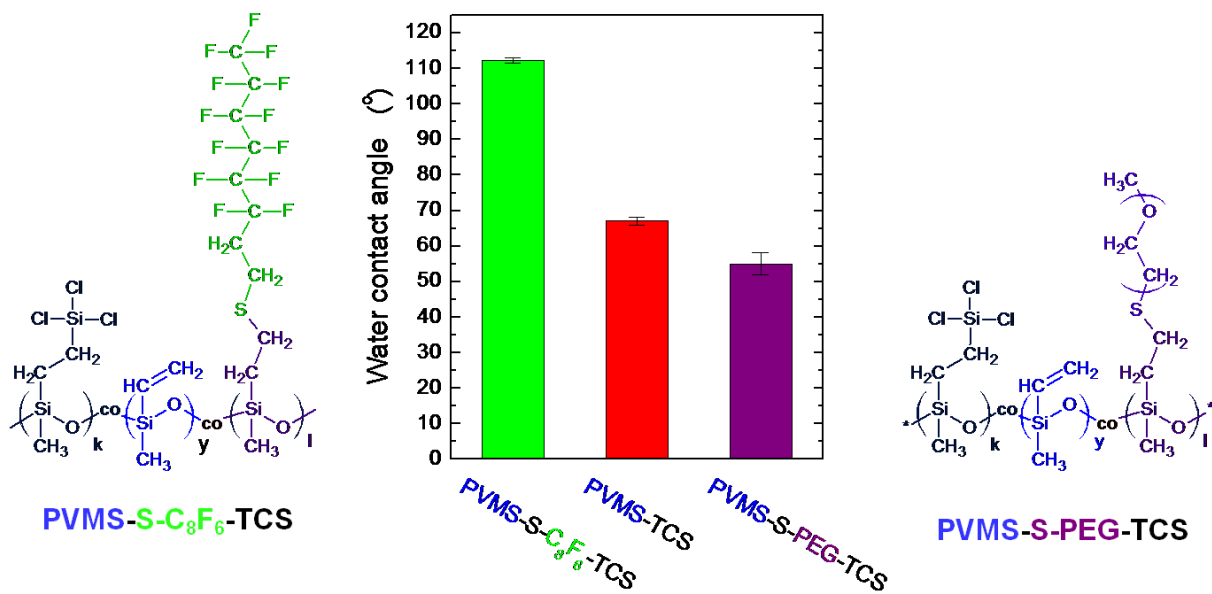


Figure 7.14. Chemical structure of functional coatings and their corresponding wettabilities.

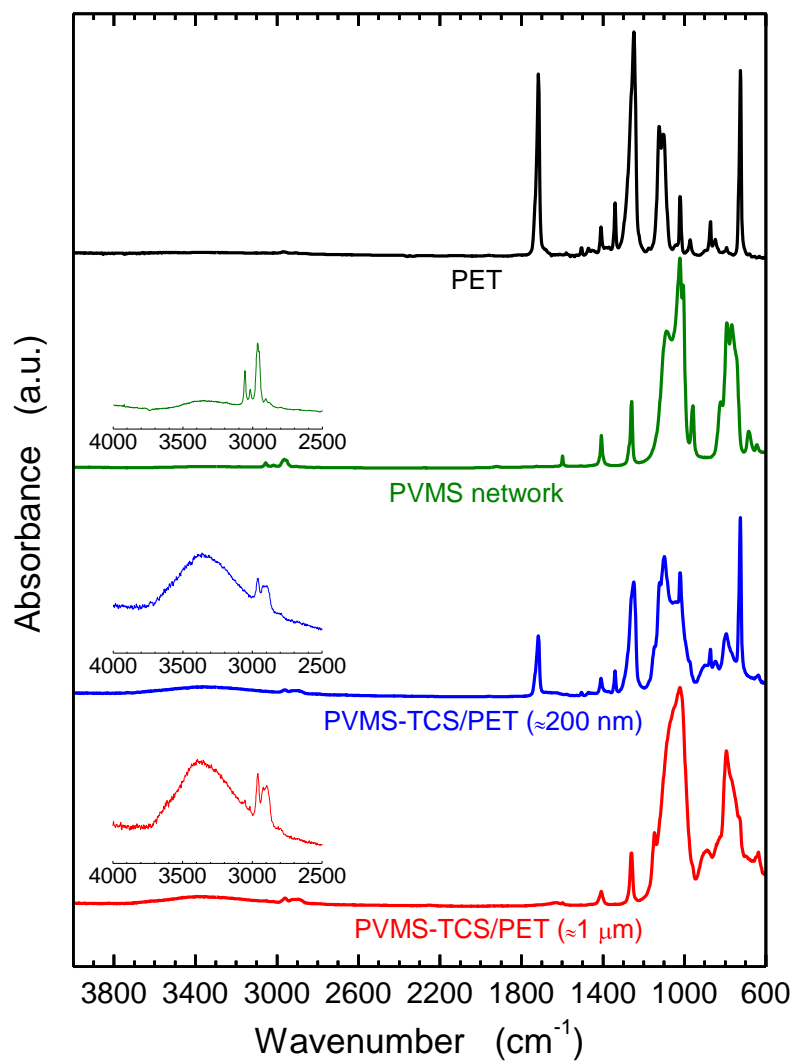


Figure 7.15. FT-IR spectra of PET film (black line), PVMS network (green line), ≈ 200 nm PVMS-TCS layer on PET film (blue line) and ≈ 1 μm PVMS-TCS layer on PET film (red line).

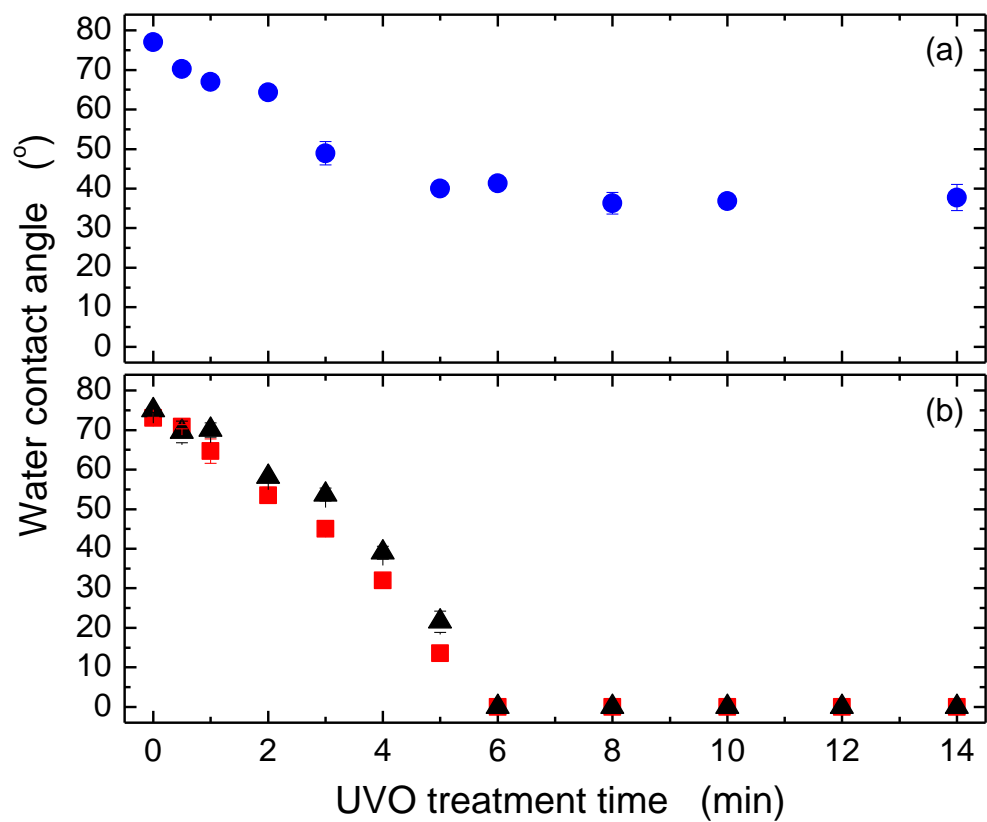


Figure 7.16. Water contact angle of PET films (a), PVMS-TCS/PET and PVMS-TCS/SiOx films (b) as a function of the UVO treatment time.

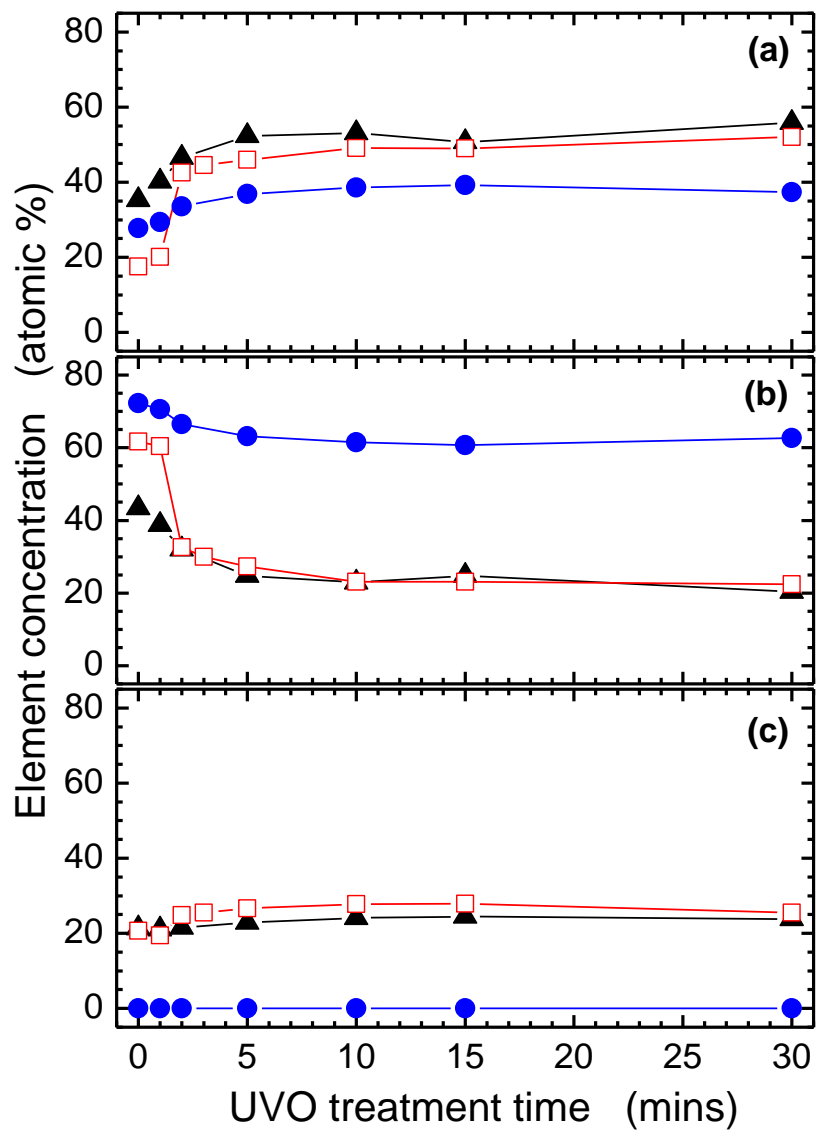


Figure 7.17. Atomic concentrations of oxygen (a), carbon (b) and silicon (c) for PET (●), PVMS-TCS/PET (▲) and PVMS network (□) as a function of the UVO treatment time.

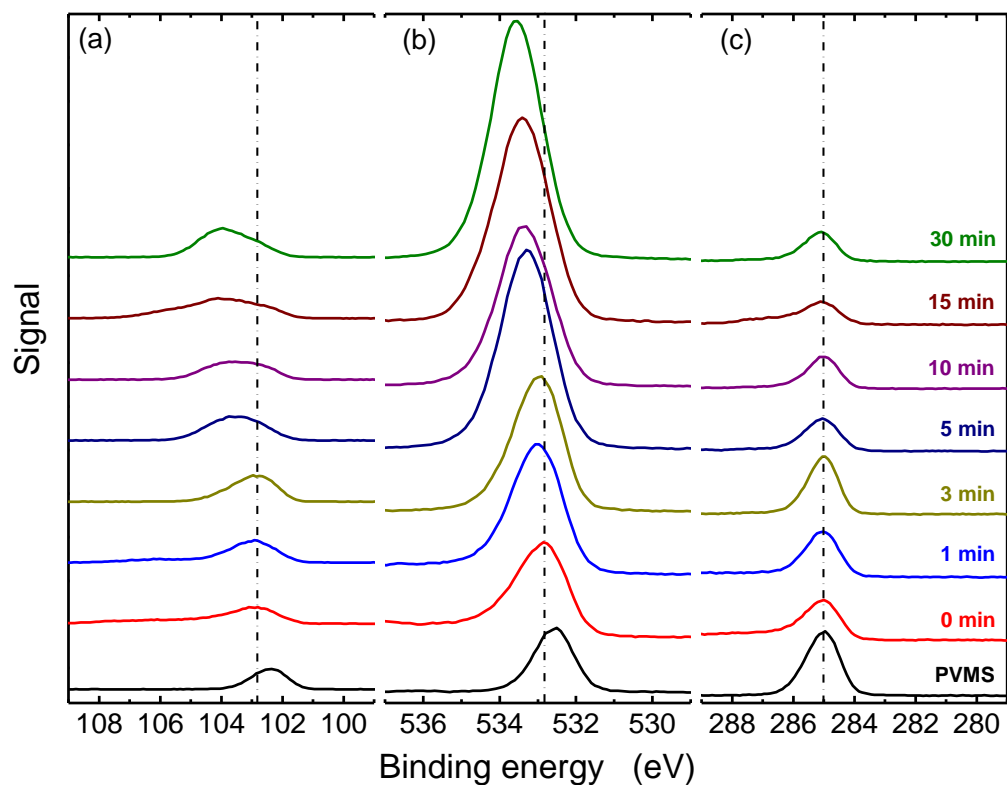


Figure 7.18. HR-XPS silicon (a), oxygen (b) and carbon (c) spectra of bare PVMS (black line) and UVO treated PVMS-TCS/PET as a function of UVO treatment time: 0 (red line), 1 (blue line), 3 (dark yellow line), 5 (navy line), 10 (purple line), 15 (wine line) and 30 (olive line) minutes of UVO treatment. The dashed lines are guides to eye, which are centered at the peak maximas of Si 2p, O 1s and C 1s spectra of PVMS-TCS/PET.

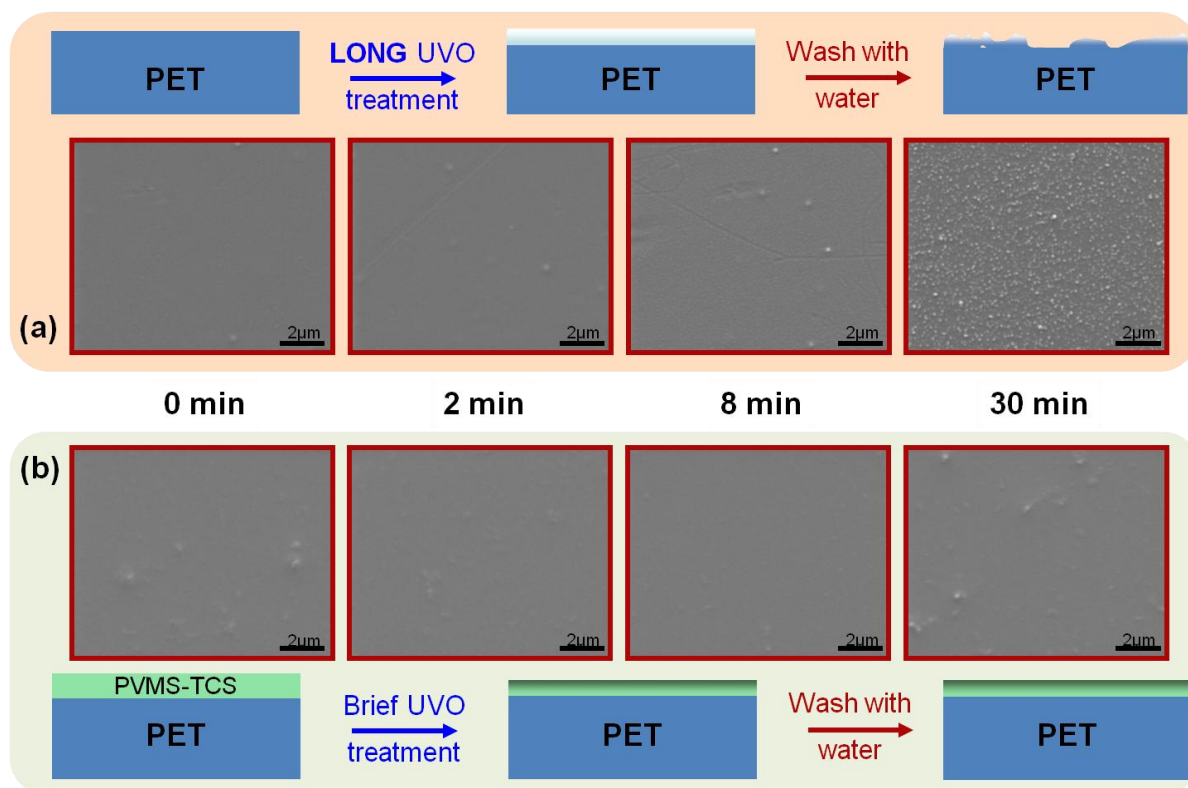


Figure 7.19. Surface topography of PET (a) and PVMS-TCS coated PET films (b) as a function of the UVO treatment time.

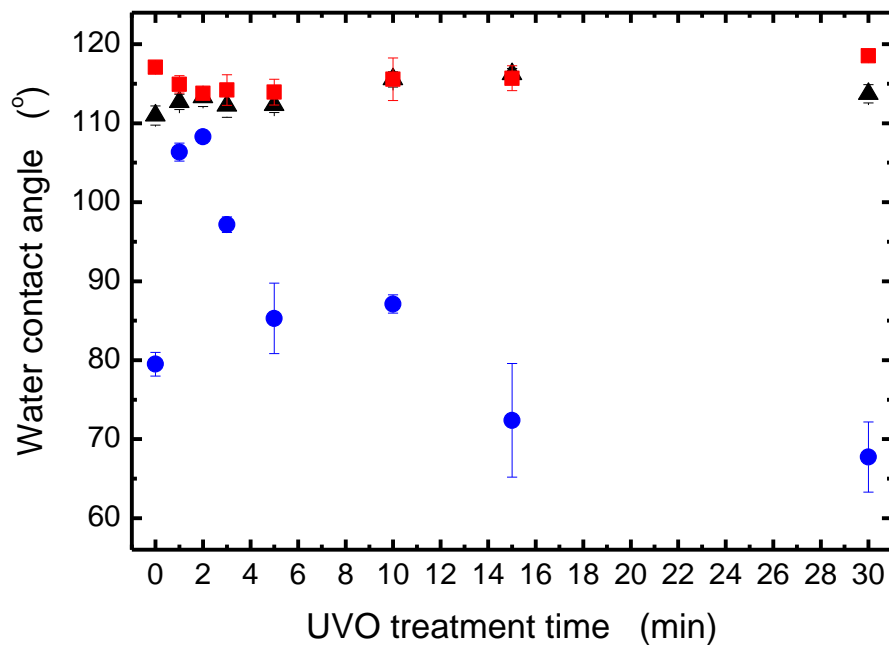


Figure 7.20. Water contact angle of fluorinated PET (●), PVMS-TCS coated PET (▲) and silicon wafer (■) as a function of the UVO treatment time of PET and PVMS-TCS/PET substrates.

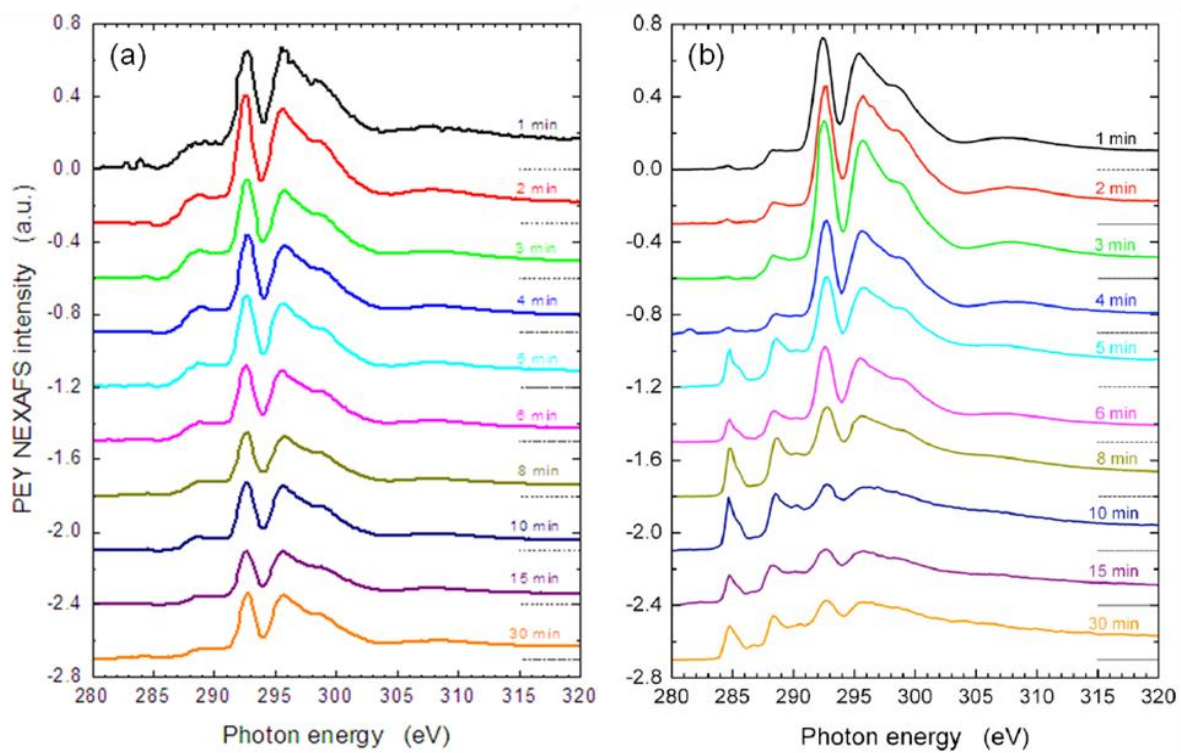


Figure 7.21. Carbon K-edge PEY NEXAFS spectra collected at $\theta = 50^\circ$ from PVMS-TCS/PET modified with UVO for various times ranging from 1 to 30 minutes and covered with tF8H2 SAM. The short dashed line at the post-edge coincides with the pre-edge PEY intensity.

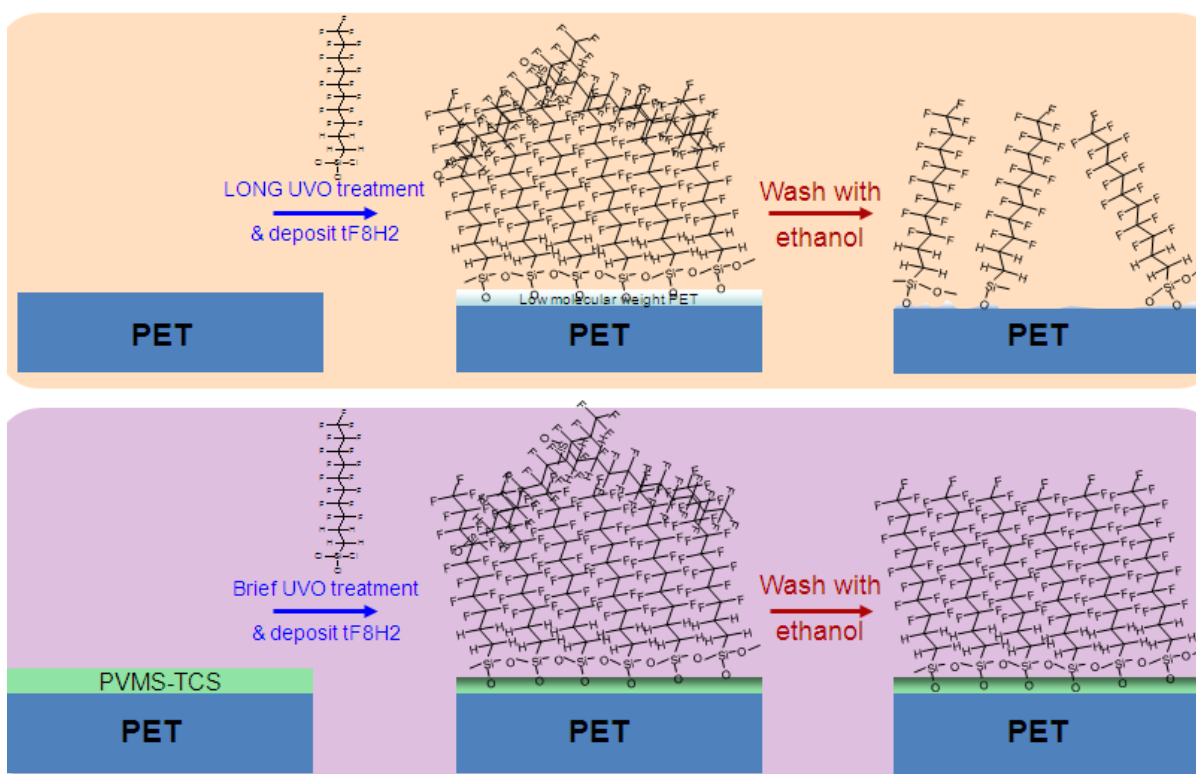


Figure 7.22. Proposed mechanism of removal of fluorinated t-F8H2 silanes for UVO-treated PET.

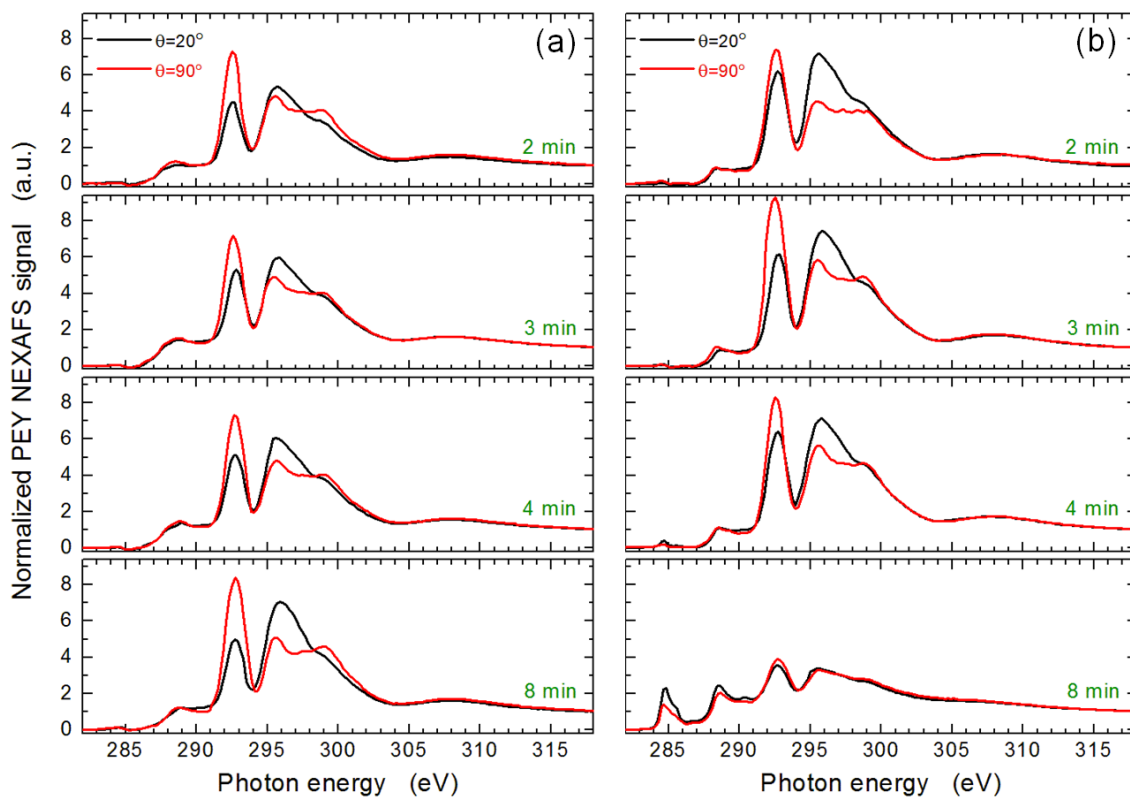


Figure 7.23. NEXAFS spectra of UVO treated and fluorinated PET (a) PVMS-TCS/PET (b) films.

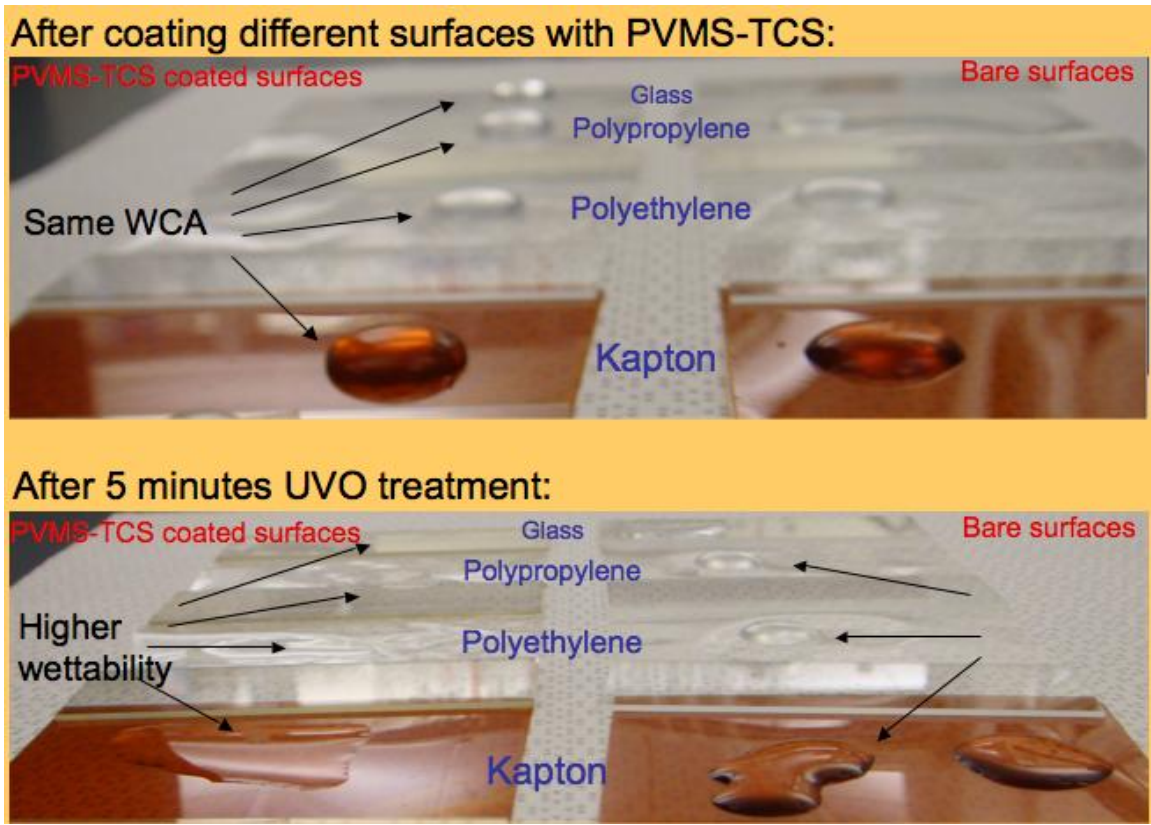


Figure 7.24. Wettability of different material surfaces before and after coating and 5 minutes of UVO treatment.

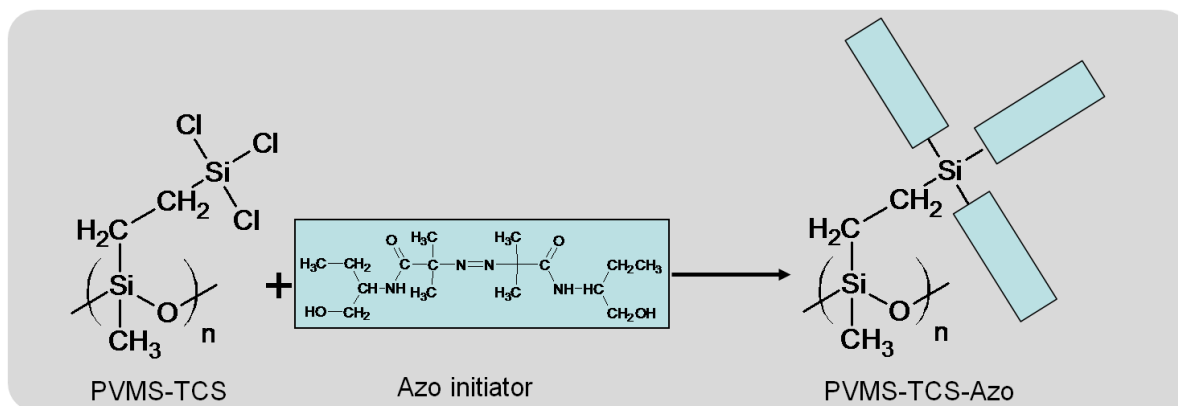


Figure 7.25. Coupling of azo based free radical polymerization initiator to PVMS-TCS.

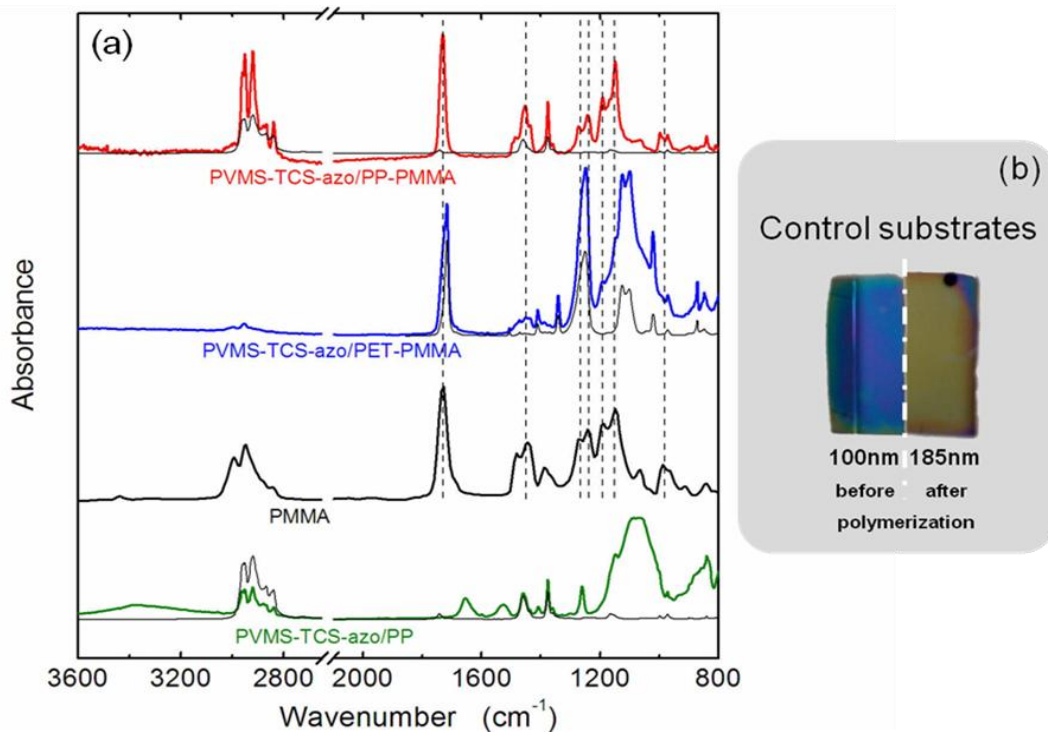


Figure 7.26. FT-IR spectra of PVMS-TCS-azo/PP (green line), PMMA (black line), PVMS-TCS-azo/PET-PMMA (blue line) and PVMS-TCS-azo/PP-PMMA (red line) plotted in graph (a) and surface tethered PMMA chains grown on silicon wafers from PVMS-TCS-azo coating. The thin black lines are the IR spectra of corresponding substrates (PP and PET) and the dashed lines are guide to eye for the IR peaks of PMMA.

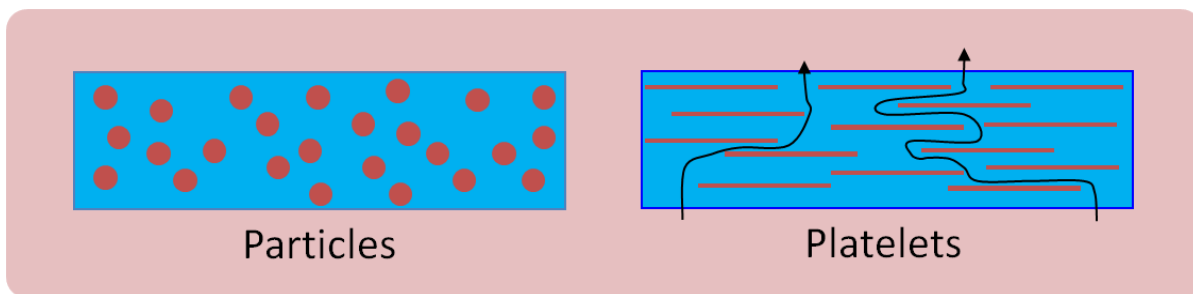


Figure 7.27. Incorporation of nanoparticles in PVMS-TCS copolymer solution would increase the hardness and barrier properties of the coating.

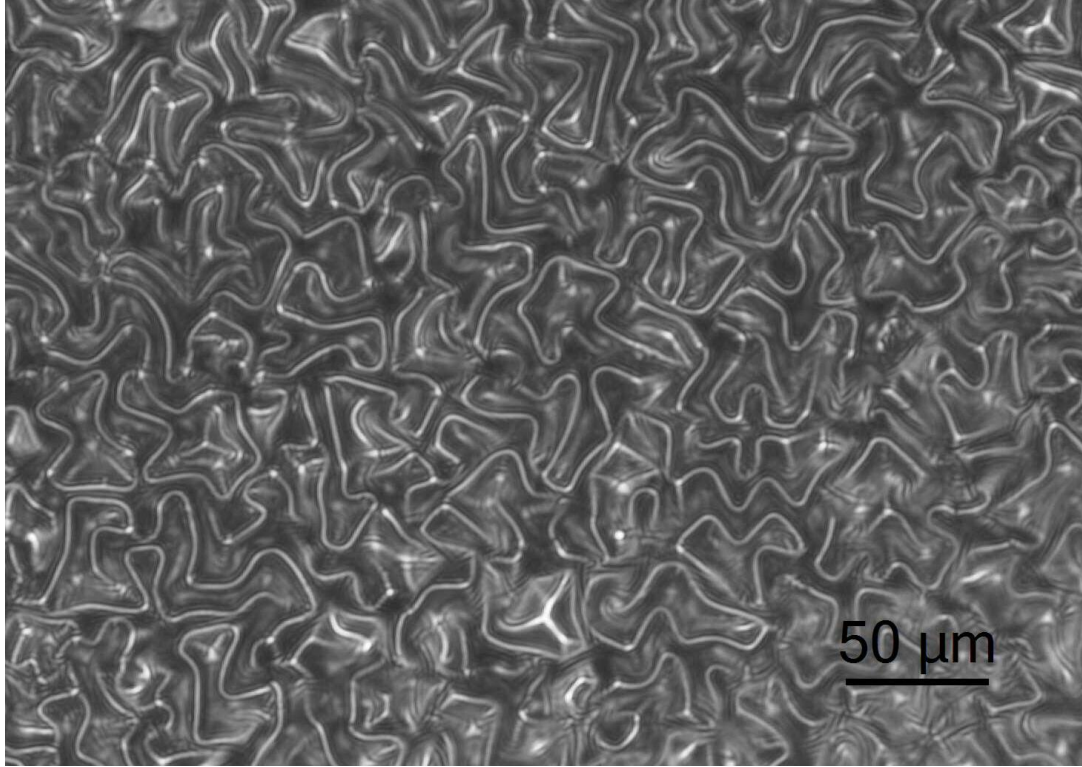


Figure 7.28. Bi-axial buckles formed on PDMS network via immersion of swelled PDMS network in PVMS-TCS copolymer solution.

7.7. APPENDIX

7.7.1. SYNTHESIS OF PVMS

Poly(vinylmethylsiloxane) was synthesized using the step-growth polymerization technique of short hydroxyl-terminated oligomeric vinyl methyl siloxane chains. The precursor monomer for the reaction was obtained by slow hydrolysis of methylvinylchlorosilane in the presence of dilute aqueous solution HCl. The reaction products comprised various methylvinyl siloxane cycles (VD3, VD4, VD5) and linear hydroxyl-terminated chains. The cyclic products were separated by vacuum distillation to obtain linear chains with a yield of $\approx 25\text{-}35\%$ depending on the amount of HCl and water present in the reaction mixture. All polymers used in the experiments were prepared from hydroxy-terminated linear chains. The synthetic procedure involving short linear chains was described in our earlier paper. The solvent-free siloxane polymerization was initiated by a small amount of lithium hydroxide (10 - 20 ppm) at 100°C for various reaction times under constant flow of nitrogen that facilitated the removal of water molecules formed during the reaction. The reaction was terminated by the addition of carbon dioxide, which resulted in α,ω hydroxy-termination of PVMS chains. This method allows the synthesis of a broad range of molecular weight PVMS that can be easily monitored by the change in the viscosity in the reaction apparatus. The final polymer was vacuum filtered using Cellite 545 filtering aid system. The unreacted short oligomeric chains were removed by extraction in methanol. PVMS was first dissolved

in diethyl ether and then added drop wise to chilled methanol. The polymer portion was collected and dried under vacuum for 72 hours. Size exclusion chromatography (SEC) equipped with light scattering and refractive index detectors has verified the complete removal of low molecular weights compounds; the monomer conversion yields were very close to 98%. IR spectroscopy confirmed that the amount of vinyl functional groups remained unchanged throughout the experiment, which suggested that no backbone branching took place during the polymerization. While PVMS of various molecular weights were prepared and characterized, the experiments described hereafter were carried out using only hydroxy-terminated PVMS with molecular weight of 35 kDa.

7.7.2. PREPARATION OF SILOXANE NETWORKS

The α,ω hydroxy-termination of PVMS enables controlled cross-linking reaction at the terminal ends of the chains through alkoxy condensation of silanols in the presence of a Sn catalyst. We have used the poly(vinylmethoxysiloxane) (PVMES) with low molecular weight (≈ 1100 Da) as the crosslinking agent because of the ability to better control over the initial gelation time and elasticity of the final networks. The molar ratio of PVMES to PVMS was kept as (1.7:1) to ensure that condensation reaction exhausted all available silanol groups in the reaction mixture. For network formation, the PVMS chains and the PVMES cross-linker were mixed and the bubbles formed throughout agitation were removed by applying a gentle vacuum. The mixture was then poured into square Petri dishes and pre-

cured for 24 hours at room temperature. After the initial gelation step, the Petri dishes were placed into an oven at 70°C and cured for 72 hours to complete the cross-linking reaction. In order to remove all unreacted components, the PVMS networks were extracted thoroughly in toluene for 48 hours and dried at 50°C for additional 72 hours in order to remove all the solvent. The properties of the final PVMS SENs were tested using rheological techniques and FT-IR to estimate the completion of cross-linking and monitor chemical changes that took place during the cross-linking reaction, respectively.

We prepared a pure model PDMS SEN using ω -vinyl-terminated PDMS with molecular weights of 62 kDa by means of hydrosilylation reaction with tetrakis(dimethylsiloxy) silane (TDSS) in the presence of Pt(II) catalyst. The ratio of PDMS to the crosslinker was kept as 1.7:1 in order to prepare the networks with highest elasticity. The PDMS networks were cast into Petri dishes to yield films having the same thickness as that of the PVMS films. The curing, extraction and drying steps were identical to those employed in the preparation of the PVMS SENs.

CHAPTER 8: COPOLYMERIZATION STUDIES OF FUNCTIONAL THIOIMIDE MOLECULES

8.1. INTRODUCTION

With rapidly increasing population and decreasing supplies of fresh and clean water of the world due in part to heavy metal overload, de-metallation of waters constitutes a pressing scientific and technological issue.^[1-3] Traditionally, processes for water de-metallation have been based on strong interactions of thiolate functional groups with heavy metals.^[1, 4] When insoluble chemical moieties containing thiolate groups are brought in contact with water, heavy metal impurities dissolved in water are chemically bound to the thiolate groups.^[1, 4, 5] The resulting metal-bearing thiolates are isolated, and either worked up by treatment with concentrated mineral acids or disposed off. These rather harsh and costly conditions associated preclude more widespread application of this powerful technology. In this and the next chapter we present a novel method for recovering heavy metals from water. Our process is based on the strong chemical affinity between heavy metals and thiolate moieties. Structural modification of the thiolate-bearing molecules makes our process available not only for scavenging of detrimental metals and toxins (e.g., phosphates, cyanides) but also for reversible use, i.e., repeated scavenging, and release of metals. As will be discussed later, the latter can be accomplished by mild air oxidation of the metalla-complex. Relatively high solubility of small molecule thiolates in water makes their recovery rather difficult.

However, attaching such functionalities to polymeric backbones not only decreases their solubility in water but also enables easy recovery, regeneration and possible reuse.

A large family of model thioimide-based compounds (derivative of disulfides) was synthesized in the laboratory of Dr. Jiří Šrogl at the Institute of Organic Chemistry and Biochemistry of the Czech Academy of Sciences, Czech Republic. The researchers also carried out tests of the compound's reactivity towards metals (Cu, Pb, Cd, Hg, Pd, Zn, Sb, Fe) and cyanide ions. The sulfur-containing functional unit itself features remarkable chemical flexibility. By the subtle red-ox changes in the environment, the functionality can be transformed from electrophile to nucleophile under very mild conditions. For practical applications, it is of great importance that the described transformations are *fully reversible* and all the functionalities show very distinct chemical reactivity under controlled conditions. The aforementioned controlled chemical behavior is the prerequisite for the ultimate cyclic *catch-release* device. Based on the above discussion, new functional materials are being developed in collaboration with the Prague group. Specifically, we plan to incorporate the thioimide chemistries to macromolecules; this process would further enable us to create complex soft matter motifs on a variety of surfaces as schematically depicted in Figure 8.1. Carefully engineered functional coating of this sort can then, in sponge-like manner, scavenge heavy metals like Pb, Cd, Hg, Au, Ag from aqueous wastes or untreated water, and, under controlled conditions, liberate the metals in a different chemical and physical environment.

Thioimide based monomers and post-polymerization modification agents were prepared via changing the R_1 and R_2 functional groups on SN compounds as shown in Figure 8.2. For instance, it is possible to convert the R_1 and R_2 groups to acrylates/acrylamides for polymerizations and alkyl chloride groups for quaternization reactions. In addition, these functional groups can also be selected to assist the solubility of new polymeric materials.

The major aim of this project is to develop synthetic routes towards fabrication of SN-based functional polymers. Two different synthetic pathways, i.e., polymerization and post-polymerization modification will be adopted; those are depicted in Figure 8.3. While direct polymerization involves “one pot reaction”, it may suffer from certain disadvantages due to chemical nature and bulkiness of the SN functional groups; the latter may hinder the polymerization reaction.^[6, 7] In addition, functional groups on SN monomer may interact, terminate the radicals or poison the catalyst, which will prevent chain growth and/or broaden the size distribution of the chains. Therefore, protection of the functional groups or a change in the monomer architecture/chemistry would be necessary for a successful polymerization. Post-polymerization modification (PPM) reaction may overcome the aforementioned difficulties.^[8, 9] A “reactive” polymer precursor that has certain functional groups, which would couple with “matching” functional group of the desired molecule, is synthesized and then the coupling reaction is carried out to obtain the final product. Several post-polymerization modification routes have been described in the literature. The attachment of the SN compound to the “reactive” polymer would be carried out with the suitable technique. We do realize, however, that the PPM reaction may lead to non-uniform distribution of the

newly-attached species along the macromolecule. In this thesis we will investigate both the direct synthesis of thioimide-based polymers (Chapter 7) and PPM of functional polymer backbones with thioimide-based agents (Chapter 8)

We will also study the interactions of these new functional materials with various heavy metals and cyanide ions. To this end, a variety of SN compounds have been prepared and their polymerization and quarternazation behavior studied. The SN compounds for polymerization and post-polymerization modification studies are listed, with some of their advantages and disadvantages, in materials section of this and the following Chapters of this Ph.D. thesis.. .

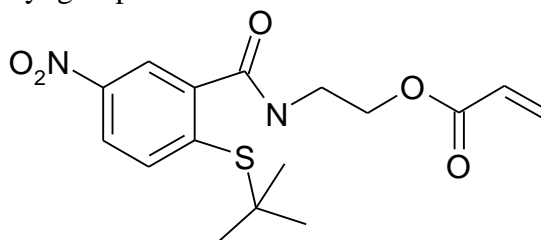
8.2. EXPERIMENTAL

8.2.1. MATERIALS

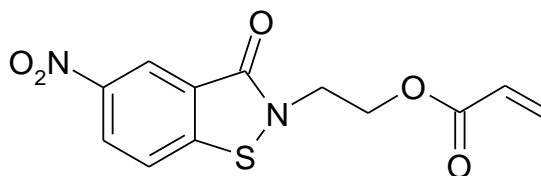
N-Isopropyl acrylamide (NIPAAm), azobisisobutyronitrile (AIBN), aniline, naphthalene, acryl chloride, chlorotrimethylsilane, dimethylformamide (DMF), tetrahydrofuran (THF), dimethylsulfoxide (DMSO), methanol, acetone, dichloromethane (DCM) and diethylether were purchased from Sigma-Aldrich. Phenyacrylamide (PhAAm) was synthesized by reaction aniline and acryl chloride in DCM followed by crystallization. Azo-based free radical polymerization (FRP) initiator for surface initiated polymerization (SIP) was synthesized according to the recipe given in Ref.^[10]

The SN monomers were synthesized in the laboratory of Dr. Jiri Šrogl at the Institute of Organic Chemistry and Biochemistry of the Czech Academy of Sciences, Czech Republic. Each SN monomer is denoted as either SN#U or SN#P, where # represents the generation of the SN monomer, U and P stand for unprotected and protected monomers, respectively. The synthesis of SN1U monomer is summarized in the Appendix to this Chapter.

1. **SN-1-P**: 1st generation SN-protected acrylic monomer. The low hydrolytic stability of the acrylic ester groups and the possibility of steric hindrance during metal adsorption necessitated a change the R₁ and R₂ groups. In addition, the polymerization process may be hindered by the bulky t-butyl groups as we will discuss in the results section.

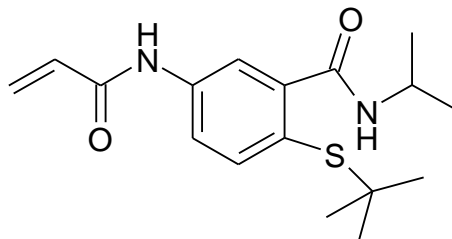


2. **SN-1-U**: 1st generation SN un-protected acrylic monomer. The R₁ and R₂ groups are changed for the same reasons listed above. Besides, the acylchloride functionality is attached to the tertiary amine; this may interfere with the opening and closing of the thioimide ring.

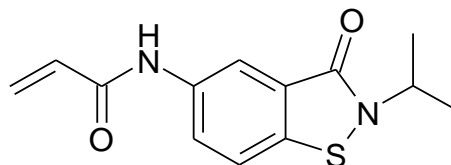


3. **SN-2-P**: 2nd generation SN protected acrylamide monomer. By switching to this chemistry the hydrolytic stability of the monomeric unit increased since the amide bond of acrylamide group is more stable than the acrylate ester group. In addition, the position of the SN group being on the opposite side of the acrylamide group, i.e.,

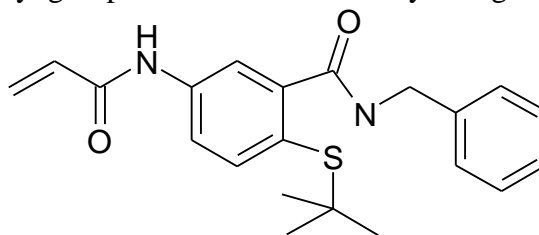
backbone of the polymer lowers the possibility of steric hindrance for metal attachment.



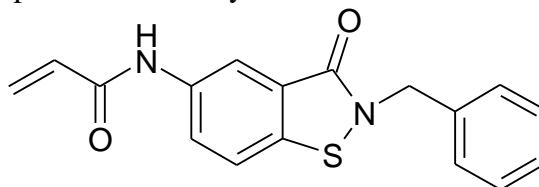
4. **SN-2-U**: 2nd generation SN un-protected acrylamide monomer. This monomer seems the optimum selection with its stability, location of the SN group and the size of the monomeric unit for polymerization.



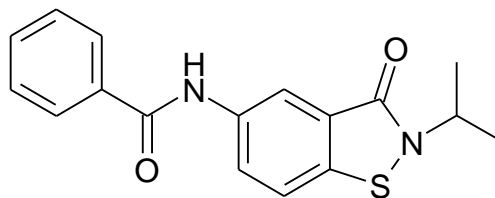
5. **SN-3-P**: 3rd generation SN-protected acrylamide monomer. The replacement of the isopropyl group with benzyl group increases the solubility in organic solvents.



6. **SN-3-U**: 3rd generation unprotected SN acrylamide monomer.



7. **Control SN:** The unprotected SN molecule to study the effect of heat and radicals on the stability of the S-N bond



8.2.2. INSTRUMENTATION

Nuclear magnetic resonance (NMR) spectra were collected with a Bruker Avance 400 MHz NMR spectrometer by using deuterated solvents (see below) for complete dissolution of the polymers. High performance liquid chromatography (HPLC) experiments were conducted using an Acquity UPLC Instrument (Waters Corporation). The elemental analysis of the samples was carried out with PE 2400 Series II CHNS/O (Perkin Elmer, USA, 1999) for C, H, N and SPECTRO iQ II (X-ray-fluorescent analyzer) for other elements. Fourier transform infrared spectroscopy (FT-IR) was employed to monitor chemical changes that took place on the polymer after surface post-modification. The FT-IR spectra were recorded on a Nicolet 6700 spectrometer in transmission mode and the data were analyzed by Omnic software. For each sample 1024 scans were collected after recording a background signal (all with the resolution of 4 cm^{-1}). The thicknesses of polymer brushes on flat substrates were assessed with a variable-angle spectroscopic ellipsometer (VASE) manufactured by J.A. Woollam Co. Ellipsometry measures the difference in the polarization state between the light beams incident onto and reflected from the surface thus providing information about the

dielectric properties and thickness of the film. The film thickness was evaluated using a single layer Cauchy model (Si/SiO_x/brush) before and after each assembly step. Unless otherwise specified, ellipsometric data were collected at an incidence angle of 70° with respect to the surface normal at wavelengths ranging from 400 to 1100 nm in 10 nm increments. The surface chemical composition of the polymer brushes was determined with a Kratos Axis Ultra DLD x-ray photoelectron spectroscopy (XPS) instrument using monochromated Al K α radiation with charge neutralization. Survey and high-resolution spectra were collected with pass energies of 80 and 20 eV, respectively, by using both electrostatic and magnetic lenses. Elemental chemical compositions were determined from spectral regression using Vision and CasaXPS software. Molecular weight and its distribution of the synthesized polymers were determined by size-exclusion chromatography (SEC) coupled with light scattering (Wyatt MiniDAWN) and differential refractive index detection (OptilabREX instruments).

8.2.3. CONTROL EXPERIMENTS WITH MODEL CONTROL-SN COMPOUND

A series of control experiments was conducted to study the stability of the S-N bond on the de-protected SN monomers and to understand the effect of heat and formed radicals on the S-N bond. Therefore, a model de-protected SN compound (control-SN-U) was designed and synthesized, which did not have any labile bonds that could, due to own reactivity interfere, with the screening of the stability test of S-N bond. Specifically, the control-SN-U

was: 1) heated in DMF to the polymerization temperature, 75 °C, and kept at that temperature for 40 hours; 2) heated in DMF at 75 °C in the presence of FRP initiator AIBN, and kept at that temperature for 46 hours; and 3) heated in DMF at 75 °C in the presence of SN3U monomer and kept at that temperature for 22 hours. In addition, SN3U and SN3P monomers were heated in DMF at 75 °C and kept for 40 hours to determine if self polymerization took place in the absence of FRP initiator. All the reaction mixtures were prepared in a Schlenk flask, de-gassed via 3 freeze-thaw cycles with argon and placed in an oil bath at 75 °C for specified amounts of time. Naphthalene was used as a internal calibration standard to determine the relative concentration of the species (monomers and control-SN molecules) in the reaction mixture with HPLC. At specified time intervals, aliquots were taken from the Schlenk flasks with argon purged syringes and run through HPLC.

8.2.4. POLYMERIZATION REACTIONS

8.2.4.1. COPOLYMERIZATION OF SN2P AND PHENYLACRYLAMIDE

Copolymerization of SN2P and PhAAm monomers was carried out in 2 different solvents, i.e., THF and DMF, in the presence of the free radical polymerization (FRP) initiator, azobisisobutyronitrile (AIBN), at 75 °C for 20 hours. The half-life of AIBN is approximately 1 hour at 75 °C^[11], therefore 20 hours of polymerization would be sufficient to consume almost all of the initiator. Initially, THF was used as the solvent for polymerization reaction. Later we switched to DMF to obtain higher molecular weight polymers by

reducing dramatically the chain transfer to solvent. After reaction, the polymerization mixtures were precipitated in cold methanol, which dissolves both monomers but does not dissolve the polymer. The precipitated polymer was dried under reduced pressure and characterized with NMR, FT-IR, SEC, DSC, XPS and TGA.

8.2.4.2. SURFACE INITIATED COPOLYMERIZATION OF SN2P AND PHENYLACRYLAMIDE

Azo-based free radical initiator (cf. Figure 8.4) was deposited onto silicon wafers that were previously cut into pieces of desired dimensions ($\approx 1 \times 3 \text{ cm}^2$) and exposed to UV/ozone treatment for 15 minutes in order to increase the density of surface hydroxyl groups and incubated in free radical initiator solution ($\approx 1 \text{ mM}$ in toluene for 16 hours at $-20 \text{ }^\circ\text{C}$).^[12, 13] The silicon wafers decorated with the initiator were then placed in glass vials containing a mixture of monomers (PhAAm and SN2P) and solvent (DMF). The polymerization mixture was degassed, the vials were sealed and placed in oil bath (75°C) for ≈ 20 hours. After surface-initiated polymerization (SIP), the silicon wafers were taken out of the vials, washed with THF to remove viscous polymer, sonicated for 2+2 minutes, rinsed with THF to remove loosely bound polymer chains and monomers and finally dried under a stream of nitrogen gas. The polymer brushes were then characterized with FT-IR, XPS and ellipsometry (VASE).

8.2.4.3. COPOLYMERIZATION OF NIPAAm WITH SN2U, SN2P, SN3U AND SN3P

NIPAAm was the second co-monomer for the copolymerization studies of SN monomers because of the water solubility and thermo-responsive behavior of parent polymer, PNIPAAm. The copolymerizations of NIPAAm and SN monomers of different compositions were performed in DMF in the presence of AIBN at 75 °C. The monomers, initiator and naphthalene (as a calibration marker) were mixed in a Schlenk flask, de-gassed via 3 freeze-thaw cycles with argon and placed in an oil bath for 20 hours. At specific intervals, samples were taken from the polymerization mixture with argon purged syringes to determine the relative concentration of remaining monomers in the polymerization medium. At the end of the polymerization DMF was evaporated under reduced pressure, the solid portion was dissolved in acetone and precipitated in diethylether 3 times. The precipitated polymer was dried under vacuum and characterized by NMR, SEC, EA and FT-IR.

8.2.5 DEPROTECTION OF PNIPAAm-CO-SN3P COPOLYMERS FROM T-BUTYL GROUPS

The role of the t-butyl group is to protect the thiol group during the monomer synthesis process. Its removal is necessary to capture heavy metals and cyanide ions with the S-N molecule from water. While the de-protection chemistry from t-butyl group for “small” SN molecules was studied by the Šrogl group, de-protection of SN compounds attached to

macromolecular chains was not studied. Therefore, copolymerization of protected monomers with NIPAAm was also carried out to study the de-protection of SN from t-butyl group on the polymer chains. The de-protection reaction was carried out in DCM in the presence of DMSO and chlorotrimethylsilane under the drying tube. The polymer was precipitated after the de-protection reaction in diethylether, dried under vacuum and characterized with NMR and FT-IR.

8.3. RESULTS AND DISCUSSION

8.3.1. CONTROL EXPERIMENTS WITH MODEL CONTROL-SN COMPOUND

The stability of the S-N bond for de-protected monomers is important to protect the functionality of SN compounds to reversibly capture the heavy metals and cyanide ions. Therefore, we designed, synthesized, and tested the model de-protected SN molecules without any reactive groups and exposed this molecule to the conditions, which were used for the polymerization studies.

First, the control SN molecule was kept in DMF at 75 °C in the presence of FRP initiator AIBN (7 times more AIBN compared to the polymerization studies) up to 46 hours under inert atmosphere. Samples taken with argon purged needles were run through HPLC column to determine the relative concentrations of each species and these chromatograms are demonstrated in Figure 8.5. The peaks located at 3.09 and 3.68 minutes of retention time correspond to the control-SN and naphthalene molecules, respectively. The height of the

control-SN peak (3.09 min) decreases slightly with a minor broadening relative to naphthalene peak (3.68 min). The areas under these peaks were determined by integration and their ratios were calculated. The ratios of the peak areas for control-SN and naphthalene are 3.68, 2.99 and 3.16 for the mixture kept at 75 °C for 0, 6, and 46 hours, respectively. The relative amounts of the control-SN molecule decreased by \approx 15-20%, but no other peaks appeared on HPLC chromatograms at the end of the 46 hour period due to the heat and radicals generated from AIBN, which states the stability of control-SN molecules.

The control SN molecule was also added to the polymerization mixture of the SN3U monomer at 75 °C for 22 hours in a Schlenk flask under argon. Aliquots were taken with argon purged needles to determine the relative concentrations of the SN3U monomer, control-SN and naphthalene with HPLC. The chromatograms of the reaction mixture are shown in Figure 8.6 for samples taken after 0, 2, 3.5 and 22 hours of polymerization. The peak for SN3U monomer is located at 2.96 min and its intensity decreases with increasing polymerization time as the SN3U monomer is consumed during the reaction. The ratio of the peak areas for the SN3U monomer and naphthalene decreases from 4.19 to 1.63 after 22 hours of polymerization. The small peak located at 3.11 minute is due to small amount of impurities in the SN3U monomer and it appears as a shoulder for the larger peak located at 3.09 minute that belong to control-SN molecule. The shape of the control-SN peak does not change during the course of polymerization because of its stability at these conditions. The ratio of the area under the peak for control-SN and naphthalene slightly increases from 1.29 to 1.34 after 22 hours of incubation at the polymerization conditions.

In addition, the effect of heat on self-polymerization of SN3U and SN3P monomers was studied in DMF at 75 °C in a Schenk flask under argon. The HPLC chromatograms are plotted in Figure 8.7 for SN3U and SN3P monomers after keeping the monomers for 0 and 40 hours in DMF at 75 °C. The peak areas were determined and their ratios were calculated as 2.87 and 3.33 for SN3U and 3.08 and 2.23 for SN3P monomers before and after the heat treatment, respectively. The relative amount of the monomers changed slightly during this process, but the change for SN3P monomer was more pronounced. It was expected that the change for SN3P would be smaller because of t-butyl protection, which would increase the stability by protection and bulkiness which would provide steric hindrance.

8.3.2. COPOLYMERIZATION OF SN2P AND PHENYLACRYLAMIDE IN BULK

Phenylacrylamide (PhAAM) was selected as a co-monomer due to its structural similarity to 2nd generation SN monomers. It was hypothesized that the copolymerization of PhAAM with the SN compound would lead to random copolymers due to the similarity of the backbone structure of the two monomers. The chemical structures of the monomers and the copolymer are shown in Figure 8.8.

Co-polymerizations were carried out two times in THF to check for reproducibility. The solvent was then switched to DMF to obtain higher molecular weight polymers by reducing the chain transfer to the solvent. The compositions of the polymerizations performed starting polymerization mixtures are summarized in Table 8.1.

8.3.2.1. HOMOPOLYMERIZATIONS OF SN2P AND PHAAM

Homopolymerization of SN2P monomer was also carried out both in DMF and THF to determine the molecular weight that can be obtained for SN2P homopolymer. After polymerization, the attempts to precipitate the “polymer” into cold methanol failed suggesting that the resulting SN2P polymer was not insoluble enough in cold methanol in order to precipitate. The precipitation did not take place likely because the molecular weight of the polymer was not high enough. Therefore, the solvent was evaporated in order to obtain the polymer. Subsequently, SEC samples of SN2P monomer and dried polymerization mixture with same concentration were prepared in THF (mobile phase) to determine the percentage of unreacted SN2P monomer left in the polymerization media. The SEC chromatograms of SN2P monomer (black line) and dried polymerization mixture (red line) are plotted in Figure 8.9, where differential refractive index (DRI) data is shown as a function of the retention time. The SEC chromatogram of SN2P monomer exhibits a single and sharp peak located at the retention time of ≈ 43 minutes; the dried polymer peak has a broad and shorter peak. Since the peak area of polymerization mixture is lower than of the monomer peak, a portion of SN monomer should have polymerized or oligomerized and the unreacted monomer still remains in the polymerization mixture. The protective t-butyl group on SN monomer sterically hinders homopolymerization. The topic will be discussed later in this chapter.

FT-IR spectra of dried polymerization mixture of 100% SN2P (cf. Figure 8.10) do not agree with the SEC data since the intensity of the peaks for the double bond of acrylamide groups almost disappeared after the polymerization process. The C=C stretching vibrations are located at 1640 and 1625 cm^{-1} and the C-H vibrations of C=C bond are located at 985 and 965 cm^{-1} .^[14]

Likewise, the NMR spectrum of the dried polymerization mixture of 100% SN2P (cf. Figure 8.11) does not show the chemical shifts for the protons of the vinyl groups for the SN2P monomer, this observation is in agreement with the FT-IR data. The protons of the vinyl groups of the monomer were expected to be located between 5.9-6.5 ppm; their absence corroborates the FT-IR data suggesting that the oligomeric SN2P molecules are formed during the polymerization process.

Homopolymerization of PhAAm was also performed to obtain poly(phenylacrylamide) (PPhAAm) as a benchmark for the P(PhAAm-co-SN2P) copolymers. PPhAAm was successfully precipitated in cold methanol, recovered, characterized and the polymerization was confirmed.

8.3.2.2. COPOLYMERIZATIONS OF SN2P MONOMER WITH PHAAM

Copolymerization of SN2P monomer with PhAAm in DMF yielded higher molecular weight products compared to the polymerizations carried out in THF due to reduced chain transfer to THF. The increase in the molecular weight was even more obvious during

polymer precipitation process in cold methanol. The copolymers were dried under vacuum and characterized with NMR, DSC, FT-IR, SEC and XPS.

The NMR spectrum of the copolymer containing 9.1% SN2P and 90.9% PPhAAm is shown in Figure 8.12. The presence of the peaks located at 4.20 and 1.25 ppm corresponds to the protons of the tertiary carbon and methyl groups of the isopropyl group originating only from the SN2P repeat units. Therefore, incorporation of SN2P monomer to the growing polymer chain took place during the copolymerization reaction. Similar behavior was also observed for the copolymer containing 4.8% SN2P monomer (data not shown).

The molecular weight and the molecular weight distribution of PPhAAm and the random copolymers (4.8 and 9.1% contents of SN2P) synthesized in DMF are summarized in Table 8.2. The SEC was performed on these samples with THF being the mobile phase and the columns were calibrated with polystyrene standards. The obtained molecular weights of the polymers were close to one another and the polydispersity indices (PDI) were relatively small for FRP polymerization. Interaction of the amide groups of these polymers with the column (Styragel®) during the experiment may be present. It would therefore be beneficial to repeat these experiments after screening the charges between the column material and the polymer.

DSC experiments were carried out to determine the glass transition temperature of the copolymers as a function of the SN2P monomer loading. The second heating curves of the PPhAAm, 4.8 and 9.1 % SN2P containing copolymers are shown in Figure 8.13. The presence of only one glass transition temperature on the thermograms suggests the formation

of random copolymers during the polymerizations. The glass transition temperatures (T_g) of these polymers were determined from the inflection point on the DSC thermogram as 145.0, 151.3 and 164.6 C for PPhAAm, 4.8 and 7.1% SN2P containing copolymers. We could not estimate the T_g of the copolymers using the Fox equation because homopolymerization of SN2P did not yield polymers with high molecular weight. However, the increase in T_g of the copolymers with increasing SN2P loading implies that more SN2P monomers were included to the growing polymer chains.

In addition, XPS was used to qualitatively determine the existence of sulfur in the synthesized polymers to confirm the incorporation of the SN2P monomer to the polymer chains. The polymer powders were placed on cleaned silicon wafers and XPS spectra were collected from both precipitated polymers and shorter polymers/oligomers (left in the decanted portion after precipitation). The data is summarized in Table 8.3 as carbon to nitrogen (C:N) and nitrogen to sulfur (N:S) ratios with theoretical values calculated based on the composition of the copolymer and the number of atoms present on the repeat units. While the C:N ratios obtained experimentally corroborate the theoretical values, the N:S ratios do not agree very well. However, the presence of sulfur on both precipitated and decanted copolymers confirms the inclusion of the SN2P monomer to the copolymer chains during polymerization.

8.3.3. SURFACE INITIATED COPOLYMERIZATION OF SN2P AND PHENYLACRYLAMIDE

8.3.3.1. GROWING PPHAAM AND POLY(PHAAM-CO-SN2P) BRUSHES FROM SILICON WAFERS

Surface initiated polymeriation (SIP) of PhAAm homopolymer and PhAAm-co-SN2P copolymer was performed on silicon wafers by following the FRP scheme. The thickness of polymer brushes was measured by using variable angle spectroscopic ellipsometer at 70° with respect to sample normal; the optical constants and thicknesses were calculated by using the Cauchy model. For both SIP batches the same thickness was obtained for PPhAAm at the end of 20 hours of polymerization and the measured thicknesses and refractive indices of the polymer brushes are shown in Table 8.4. After successfully obtaining PPhAAm polymer brushes, copolymerization was attempted by using 9.1 SN2P and 90.9% PhAAm monomers. At the end of the copolymerization a thickness of 103.7 nm was obtained and this value is very close to the one obtained from PPhAAm brush on silicon wafer. The refractive indices of the PPhAAm and 9.1%SN2P brushes were measured as 1.603 and 1.595, respectively, at the wavelength of 630 nm.

Refractive indices of the monomers and oligomers were simulated by using the ChemSketch software to compare the ellipsometric data with model calculations; they are plotted as a function of the number of the monomeric repeat units in Figure 8.14. The values of the refractive indices increase with increasing number of repeat units and then level off

after ≈ 10 repeat units. The simulated refractive index of PPhAAm is slightly higher than the experimental value obtained with ellipsometer measurements. Therefore the simulated refractive indices are normalized according to the measured refractive index of PPhAAm and these values are summarized in Table 8.4.

Since the calculated refractive index of SN2P monomer/oligomers is smaller than the refractive index of PhAAm monomer/oligomers, a decrease in the refractive index of the copolymer brush was expected. This decrease of measured refractive index of PPhAAm from 1.603 to 1.595 for 9.1% SN2P copolymer may suggest that the SN2P monomer was incorporated in the brush. Assuming the effective mean approximation (EMA) model and calculating the refractive index of the copolymer brush using the normalized values listed in Table 8.5 with a given composition results in a refractive index of 1.600. However, this number is higher than the measured refractive index of the copolymer brush. This may be due to the difference in the polymer brush and starting feed compositions.

The FT-IR spectra of 9.1% SN2P copolymer, PPhAAm brushes on silicon wafer and their difference are shown in Figure 8.15. The positive values for the bands in the difference spectra located at $1670\text{-}1630\text{ cm}^{-1}$ and $1620\text{-}1590\text{ cm}^{-1}$ may be due to the higher amount of amide groups originating from the SN2P monomer (i.e., 2 amides per SN2P monomer, 1 amide per PhAAm monomer). In addition, the peaks in the difference spectra located at 2969 , 1466 , 1387 and 1365 cm^{-1} confirms the presence of t-butyl groups which originate from the SN2P repeat unit.

Characterization of these brushes was carried out using XPS; the data are tabulated in Table 8.6. The theoretical atomic percentages for PPhAAm are in agreement with the experimental values. However, the experimental value of sulfur concentration on 9.1% SN2P brush is lower than the theoretical value. This suggests that the rate of SN2P monomer addition to growing chains was not as fast as PhAAm monomer. An alternative reasoning arises from the unreliable quantification of sulfur with XPS since we only probe first ≈ 10 nm of the 100nm thick brush. Preliminary data obtained from the copolymerization of SN2P with PhAAm and the XPS experiments suggest that the SN2P monomer is incorporated in the PPhAAm brush during the synthesis process.

The viscosity of monomer-solvent mixtures in the vials for SIP increased; the increase in viscosity was due to polymerization in solution, which originates from the unbound portion of the azo initiator. However, the increase in the viscosity for the 9.1% SN2P copolymerization mixture was less pronounced than the increase in the viscosity of the PPhAAm brush polymerization solution. In addition, polymerization of PhAAm in DMF without any initiator added was carried out to determine if PhAAm self-polymerizes thermally. The viscosity of that solution also increased, suggesting that some thermal polymerization took place. SEC chromatograms of these polymerization mixtures are shown in Figure 8.16 for original and normalized peaks; the normalization was carried out by shifting the elution time of PhAAm monomer at 44.5 minutes and the intensity of DMF peak located at 48 minutes. While we could not get quantitative data from these SEC runs; we note that an increase in viscosity and the appearance of a broad peak starting at 34 minutes

for heated PhAAm in DMF imply that thermal polymerization of PhAAm took place in the absence of any initiator.

8.3.4. COPOLYMERIZATION OF NIPAAM WITH SN2U, SN2P, SN3U AND SN3P

The co-monomer PhAAm was switched to *N*-isopropylacrylamide (NIPAAm) to impart water solubility to the copolymer and to take advantage of thermo-responsiveness of PNIPAAm during the *capture-release* process of metal and cyanide ions. The result of homopolymerizations of NIPAAm, SN3U and SN3P monomers will be discussed first and then the results of copolymerization studies of NIPAAm with SN2U, SN2P, SN3U and SN3P will be presented.

8.3.4.1. HOMOPOLYMERIZATION OF NIPAAM, SN3U AND SN3P MONOMERS

Polymerization of NIPAAm, SN3U and SN3P monomers were carried out via FRP to obtain corresponding homopolymers as benchmark samples as summarized in the experimental part.

First, polymerization and characterization of NIPAAm was carried out. After precipitation, the polymer was characterized by ¹H-NMR and water solubility below and above the transition temperature. ¹H-NMR spectrum of the resulting polymer confirms the structure of PNIPAAm (c.f. Figure 8.18, black line). The peaks located at 1.14 (for 6H), 4.00 (for 1H) and 7.16 (for 1H) ppm correspond to hydrogens of the methyl groups of isopropyl,

secondary carbon of isopropyl and amide groups of PNIPAAm respectively. In addition, peaks located at 1.64 and 2.21 ppm correspond to the backbone hydrogens. PNIPAAm was soluble in water at room temperature, but the solution became turbid when the temperature increased above the transition temperature.^[15] The results listed above confirm the formation of PNIPAAm chains.

The polymerization of SN3U monomer was monitored with HPLC as a function of the polymerization time; the HPLC chromatograms are plotted in Figure 8.17. The peaks located at 2.96, 3.12 and 3.68 minute retention time correspond to the SN3U monomer, impurity in the SN3U monomer, and naphthalene, respectively. The ratio of the SN3U monomer to naphthalene decreases with increasing polymerization time due to the addition of the monomers to the growing polymer chain.

Precipitation of the polymerization mixture in diethylether resulted in a gooey material, which was dried under vacuum. ¹H-NMR spectrum of SN3U homopolymer was collected in d-DMF and it is shown in Figure 8.18. The peaks located at 2.15, 5.05, 7.10-8.35 and 10.40 ppm correspond to backbone, benzylic, aromatic and amide hydrogens, respectively. In addition the ratio of integrated peak areas confirm the structure of SN3U homopolymer.

The FT-IR spectrum was collected after embedding the SN3U homopolymer powder in a KBr pellet. Amide I and II bands of the SN3U are located at 1661 and 1537 cm⁻¹, respectively. In addition, the presence of benzisothiazolinone group was confirmed by the IR peaks located at 1592, 1454, 1417, 1089, 1049, 881 and 760 cm⁻¹, they are highlighted in

Figure 8.19. The existence of the benzisothiazolinone groups on the polymeric material demonstrates the presence and stability of SN3U groups after the polymerization reaction.

As opposed to the SN3U monomer, the SN3P monomer did not homopolymerize in DMF based on the HPLC chromatograms. The ratio of peak areas for SN3P to naphthalene did not change significantly during the course of polymerization as shown in Figure 8.20. In addition, SN3P homopolymerization mixture did not precipitate in diethylether; a cloudy solution was formed as it happened for SN2P homopolymerization study. Therefore, we assume that the presence of the bulky t-butyl groups has hindered the addition of SN3P monomer to the growing polymer chains and, consequently, the long polymer chains could not be obtained.

8.3.4.2. COPOLYMERIZATION OF NIPAAAM WITH SN2U, SN2P, SN3U AND SN3P MONOMERS

Copolymerization studies of functional SN monomers were carried out with NIPAAm as the co-monomer in DMF at 75 °C. The relative ratios of NIPAAm to SN monomers were determined by HPLC with naphthalene as an inert marker.

In Figure 8.21 we plot HPLC chromatograms of polymerization mixture containing 10% SN3U and 90% NIPAAm monomers as a function of polymerization time. It is clear that both monomers were added to the growing polymer chain during polymerization since the peak areas for both monomers decreased with respect to naphthalene peak as a function of polymerization time. The NMR spectrum corresponding to 10% SN3U containing monomer is shown in Figure 8.18; characteristic peaks for the aromatic structure, which only result

from SN3U monomer (7.20 ppm), are clearly visible. The FT-IR spectrum of the copolymer containing 10% SN3U exhibits characteristic peaks of the SN3U compound, in agreement with the NMR spectra. Water solubility of the copolymers was studied qualitatively; it was found that it decreased slightly for the copolymers containing SN repeat units.

Earlier in the document it was shown that homopolymerization of SN3P did not take place. We claimed that the bulky t-butyl group on the monomer hindered the addition of the monomer to the growing homopolymer chains. However, HPLC spectra prove the consumption of SN3P monomer during copolymerization of SN3P with NIPAAm as shown in Figure 8.22 for 10% SN3P loading. The SN3P peak located at 3.47 minutes and the intensity of the decreases rapidly and all the SN3P was consumed at the end of the polymerization. The polymerization mixture was able to be precipitated in diethylether due to longer macromolecular chains formed during the polymerization as opposed to protected SN homopolymerizations. The NMR (cf. Figure 8.24, black line) and FT-IR (cf. Figure 8.25 black line) spectra of the SN3P copolymers show characteristic peaks originating from the benzyl and t-butyl groups of SN3P which verify the formation of copolymers.

Increase in the loading of the SN monomers in the copolymerization feed causes a decline in the conversion at the end of the polymerization, as can be seen in Figure 8.23 for 30% SN3P and 70% NIPAAm copolymerization mixture. The intensity of the SN3P peak decreases relative to the naphthalene peak for the first 10 hours, but then the decrease levels-off till the end of the polymerization. In addition, some monomers remained in the Schlenk

flask. Further increase in the SN3P monomer loading reduced monomer consumption, precipitation of the polymers thus took place with lower yields.

8.3.5. DEPROTECTION OF PNIPAAm-CO-SN3P COPOLYMERS FROM T-BUTYL GROUPS

Deprotection reactions of thiol functionality from t-butyl group on SN3P molecules on NIPAAm-co-SN3P copolymer chains were performed via standard deprotection mechanism as summarized in the Experimental section. After deprotection in DCM the copolymer chains were precipitated in diethylether and the samples were characterized with ¹H-NMR, SEC and FT-IR. The deprotection reaction was carried out on copolymers with high contents of SN3P monomer (30 and 50% wt SN3P) in order to detect the chemical changes in the copolymer.

The ¹H-NMR spectrum was collected in d-dichloromethane and it is shown in Figure 8.24. The relative peak areas of methyl hydrogens located at 1.04 ppm to phenyl hydrogens located at 7.1-7.6 ppm decrease after deprotection reaction due to removal of t-butyl groups from the SN3P units on the copolymer chain. In addition, the solubility of the resulting copolymers in organic solvents decreased after deprotection reaction due to the reduction of the concentration of the methyl groups that increase the solubility of the polymer in organic media.

The FT-IR spectra of 50% wt SN3P copolymer before and after deprotection reaction are plotted in Figure 8.25. The disappearance of the peaks corresponding to t-butyl groups at

2969, 1466, 1387, 1365 and 1166 cm^{-1} and the appearance of the peaks for benzisothiazolinone group at 1592, 1454, 1417, 1089, 1049, 881 and 760 cm^{-1} verify successful cleavage of the t-butyl groups.^[14]

The ability to protect the SN compound during the polymerization reaction is important because it helps to preserve the functionality of the molecule after polymerization. For example, in the presence of metal ions the S-N bonds may open and capture these metal ions, which catalyze the polymerization/coupling reactions for ATRP and hydrosilylation reactions. This process may hinder/stop the reaction by catalyst poisoning and prevent polymerization/coupling reactions. The ability of the t-butylmercato group deprotecting after polymerization/coupling reactions would allow for the formation of functional materials by using ATRP or hydrosilylation reaction, which utilize copper salts and platinum complexes, respectively, as catalysts.

8.4. CONCLUSION AND FUTURE WORK

Polymerization of the second generation of protected SN monomer (SN2P) was examined by FRP with PhAAM as the co-monomer in THF and DMF. Copolymerization of SN2P with PhAAM was carried out at different monomer loadings and the synthesized polymers were precipitated in cold methanol except the homopolymerization mixture of SN2P. We claim that the presence of the bulky t-butyl group on the SN2P monomer hindered the addition of the SN2P units to the growing chains. As a result, the length of the

polymer chains did not increase. Therefore the SN2P homopolymerization mixture did not precipitate. However, the copolymerization of SN2P with PhAAm took place, as evidenced from a battery of analytical measurements, including, NMR, DSC, SEC, XPS, and FT-IR. Analyses of these data verified the inclusion of the SN2P monomer to the copolymer. Polymer brushes on silicon wafers were grown via surface initiated polymerization by using a FRP initiator. Homopolymer brushes of PhAAm and copolymer brushes of SN2P-PhAAm (9.1% wt SN2P loading) were formed and the existence of the brushes was verified by ellipsometer, XPS and FT-IR.

In the later phases of the project, a control SN compound (control-SN) was designed and synthesized without any labile groups to determine stability of the S-N bond in the presence of radicals at the polymerization temperature. The concentration of the control-SN was measured relative to naphthalene with HPLC as a function of incubation time. It was found that the control-SN molecule remained intact and S-N bond was stable based on the HPLC data. In addition, the SN monomers were kept in DMF at polymerization temperature in the absence of initiator to determine the thermal polymerization of the monomers. Based on HPLC experiments, the relative ratios of SN monomers and naphthalene did not change considerably

After confirming the stability of the S-N bond, homopolymerization and copolymerization studies of deprotected SN monomers was carried out in DMF. The non-SN co-monomer was switched to NIPAAm because of its water solubility and thermoresponsive behavior, which can be utilized to recover the functional SN copolymers

from water at the end of *catch-release* process of heavy metal and cyanide ions in water. The homopolymerization and copolymerization (NIPAAm as the co-monomer) of both protected and deprotected monomers was monitored by HPLC to determine the remaining monomer concentration in polymerization medium as a function of polymerization time. Investigation of the HPLC chromatograms revealed that the homopolymerization of SN3P did not take place at the end of the polymerization and the polymerization mixture was not able to be precipitated. These findings were in accord with the results of homopolymerization of SN2P monomer. In contrast, the concentration of the SN3U monomer decreased with increasing polymerization time relative to the naphthalene concentration and the SN3U homopolymer precipitated in diethylether. The characteristic peaks for the precipitated SN3U polymer on FT-IR and NMR spectra verified the structure of the SN3U polymer.

Inspection of the HPLC spectra of the copolymerization mixtures of SN monomers with NIPAAm exhibits a decline in the concentration of both protected and de-protected SN monomers along with NIPAAm with respect to naphthalene concentration. This behavior confirms that the both of the SN monomers were incorporated in the growing copolymer chains. Precipitation of the copolymers in diethylether and further characterization with NMR and FT-IR validates the presence of the SN monomers in the copolymer chains.

Deprotection of the protected SN repeat units on the copolymer chains should be carried out in order for these copolymers to be used for collecting metals or cyanide ions from water. Therefore, deprotection reactions were carried out with 30 and 50% SN3P containing copolymers by using the deprotection procedure established for SN monomers.

Characteristic peaks corresponding to t-butyl group disappeared from the NMR and FT-IR spectra collected for SN3P copolymers after the deprotection reaction.

During the aforementioned polymerization studies, it was found that the purity of the synthesized monomers has an important effect on the success of the polymerization. Presence of impurities hinders the polymerization, the concentration of the monomers does not change as a function of polymerization time and therefore the yield decreases. For this reason, special care should be given during crystallization step of the monomers to remove the impurities from the monomers.

The solubility and thermoresponsive behavior of the NIPAAm-SN copolymers in water is an important parameter for practical applications of the copolymers to purify water from heavy metal and cyanide ions. After capturing the impurities from water, the copolymers can be recovered by simply increasing the temperature of water above the transition temperature (T_C) of the copolymer. The T_C of NIPAAm homopolymer is ≈ 32 °C and this value is shown to be altered via tuning the molecular weight or copolymerizing NIPAAm with comonomers. Incorporation of SN monomers in the NIPAAm copolymer is expected to decrease the T_C of the copolymer and this is advantageous since it will reduce the energy input to increase the temperature to recover the copolymers via collapsing and precipitating the copolymer chains.

These are the preliminary data for the basis of a further research in this area. Specifically, we planned to synthesize copolymers containing SN moieties in larger

quantities to test the ability of these copolymers to capture heavy metal and cyanide ions. In addition, the re-usability of the functional copolymers to purify water will be investigated.

8.5. REFERENCES

- [1] M. M. Matlock, B. S. Howerton, D. A. Atwood, *Industrial & Engineering Chemistry Research* **2002**, *41*, 1579.
- [2] R. P. Pohanish, M. Sittig, Knovel, - *Sittig's handbook of toxic and hazardous chemicals and carcinogens\ Y1 - 2008*.
- [3] M. J. Derelanko, M. A. Hollinger, - *Handbook of toxicology\ Y1 - 2002*.
- [4] K. R. Henke, *Water Environment Research* **1998**, *70*, 1178.
- [5] M. M. Matlock, B. S. Howerton, M. Van Aelstyn, K. R. Henke, D. A. Atwood, *Water Research* **2003**, *37*, 579.
- [6] W. Jaeger, J. Bohrisch, A. Laschewsky, *Progress in Polymer Science*, *35*, 511.
- [7] S. Kudaibergenov, W. Jaeger, A. Laschewsky, in *Supramolecular Polymers Polymeric Betains Oligomers*, Vol. 201, **2006**, 157.
- [8] N. K. Boan, M. A. Hillmyer, *Chemical Society Reviews* **2005**, *34*, 267.
- [9] M. A. Gauthier, M. I. Gibson, H. A. Klok, *Angewandte Chemie-International Edition* **2009**, *48*, 48.
- [10] E. Bain, J. Genzer, *Manuscript in preparation*.
- [11] J. Brandrup, E. H. Immergut, E. A. Grulke, *Polymer handbook*, Wiley-Interscience, New York **1999**.
- [12] R. R. Bhat, B. N. Chaney, J. Rowley, A. Liebmann-Vinson, J. Genzer, *Advanced Materials* **2005**, *17*, 2802.
- [13] R. R. Bhat, J. Genzer, *Applied Surface Science* **2006**, *252*, 2549.
- [14] G. Socrates, - *Infrared characteristic group frequencies : tables and charts\ Y1 - 1994*.
- [15] H. G. Schild, *Progress in Polymer Science* **1992**, *17*, 163.

8.6. TABLES AND FIGURES

Table 8.1. Composition of the polymerizations performed

Composition	0% SN2P	4.8% SN2P	9.1% SN2P	20% SN2P	100% SN2P
Solvent					
THF	Yes	Yes	Yes	Yes	Yes
DMF	Yes	Yes	Yes	No	Yes

Table 8.2. Molecular weight and its distribution of the synthesized polymers

	Molecular weight (kg/mol)	PDI
PPhAAm	110K	1.25
4.8% SN2P	110K	1.22
9.1% SN2P	108K	1.22

Table 8.3. N:C and N:S ratios of the copolymers determined with XPS

Samples		C:N ratio	N:S ratio
PPhAAm	Theoretical	7.0	—
	Experimental	8.3	—
4.8% SN2P (precipitated)	Theoretical	7.0	22.0
	Experimental	10.3	36.7
4.8% SN2P (decanted)	Theoretical	7.0	22.0
	Experimental	7.7	74.6
9.1% SN2P (precipitated)	Theoretical	8.9	12.0
	Experimental	8.4	17.0
9.1% SN2P (decanted)	Theoretical	8.9	12.0
	Experimental	10.8	27.7
20% SN2P (decanted)	Theoretical	8.8	6.0
	Experimental	8.5	14.6
100% SN2P (decanted)	Theoretical	7.0	2.0
	Experimental	8.3	2.5

Table 8.4. Measured thickness and refractive index of polymer brushes

Polymerization mixture	Thickness (nm)	$n_{630\text{nm}}$
PhAAm	101.0±0.5	1.603±0.001
9.1% SN2P + 90.9% PhAAm	103.7±0.4	1.595±0.001

Table 8.5. Calculated refractive indexes of monomers

Monomer	Calculated refractive index	Normalized refractive index WRT measured PPhAAm
PhAAm	1.583±0.03	1.603
SN2P	1.556±0.02	1.576
SN2U	1.647±0.03	-

Table 8.6. Atomic percentages of PPhAAm and 9.1% SN2P polymer brush measured with XPS

		C	O	N	S
PPhAAm	# of atoms	9	1	1	0
	theoretical	81.82%	7.09%	7.09%	-
	experimental	81.96%	8.44%	7.61%	0.00
9.1% SN2P	# of atoms	107	12	12	1
	theoretical	81.06%	7.09%	7.09%	0.76%
	experimental	81.44%	8.52%	7.70%	0.34%

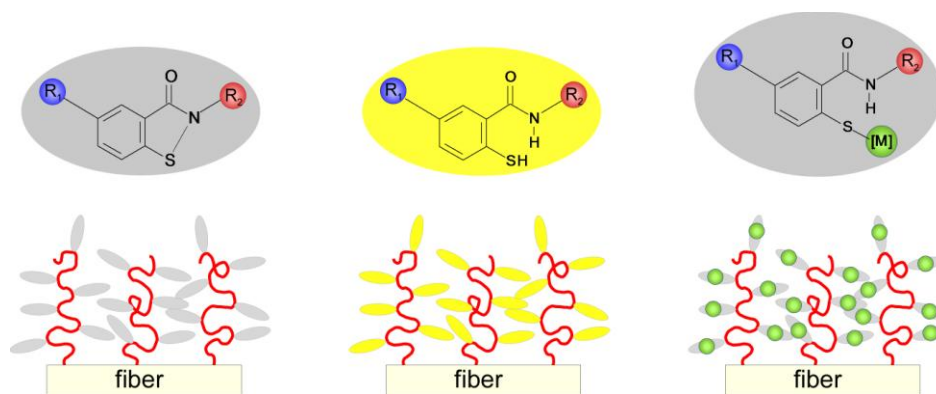


Figure 8.1. Polymers anchored to the surface of a fiber are endowed with thioimide functionality. After oxidation, the ring opens up and the thioimide is ready to scavenge a heavy metal or a toxin (phosphate or cyanide). This process is associated with a color change. Capturing of heavy metals/toxins is associated with de-coloring. The metals/toxins can be removed from the polymeric materials by mild oxidation. The system returns to the original state and can be reused in the recovery process.

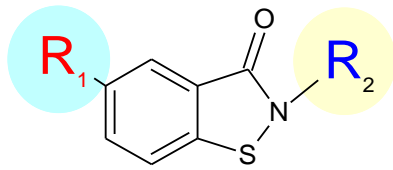


Figure 8.2. Structure of SN compound.

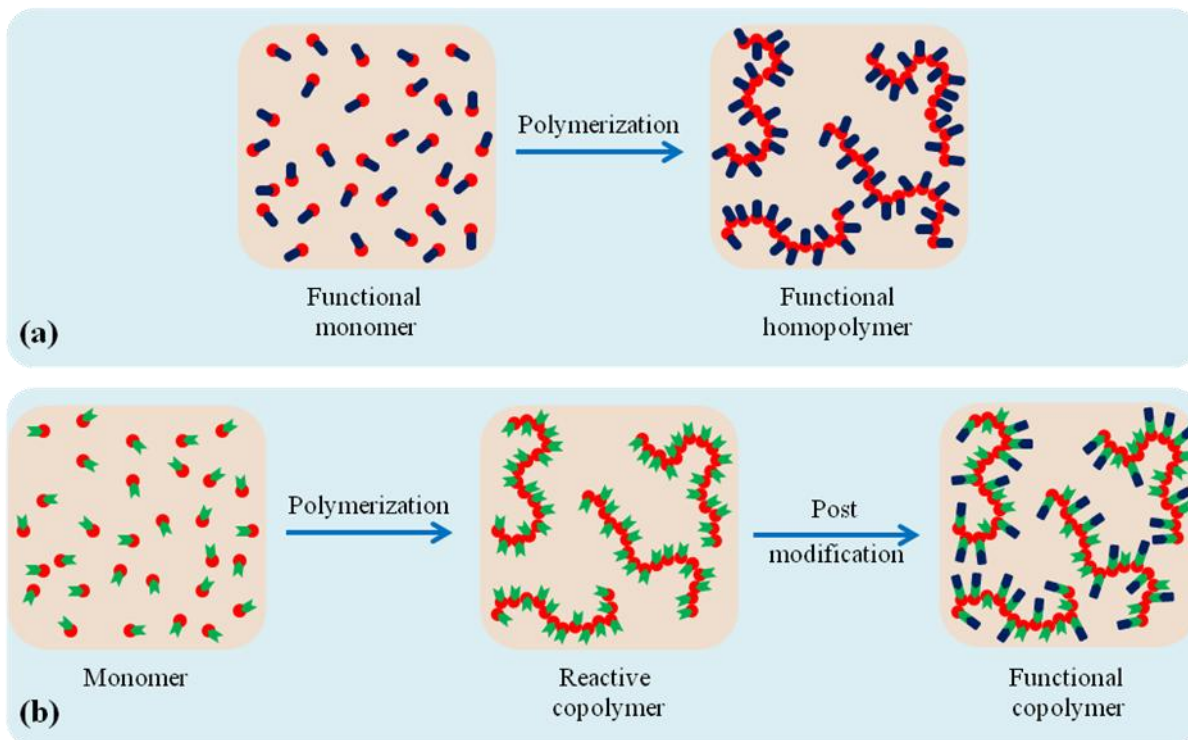


Figure 8.3. Direct polymerization of functional polymer (a) and polymerization of “reactive” polymer for post-polymerization reaction and subsequent attachment of desired functionality.

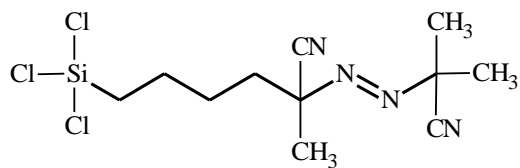


Figure 8.4. Azo-based polymerization initiator for surface-initiated polymerization.

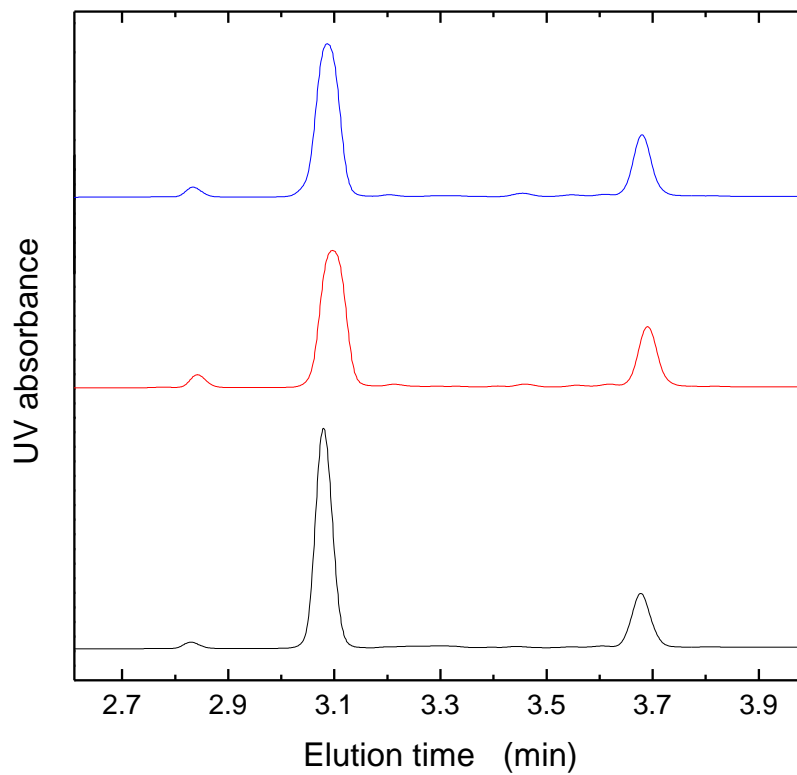


Figure 8.5. HPLC chromatogram of control-SN molecule in DMF in the presence of FRP initiator and naphthalene at 75 °C for 0 hour (black line), 6 hours (red line) and 46 hours (blue line). The peaks located at 3.09 and 3.68 minutes correspond to control-SN and naphthalene respectively.

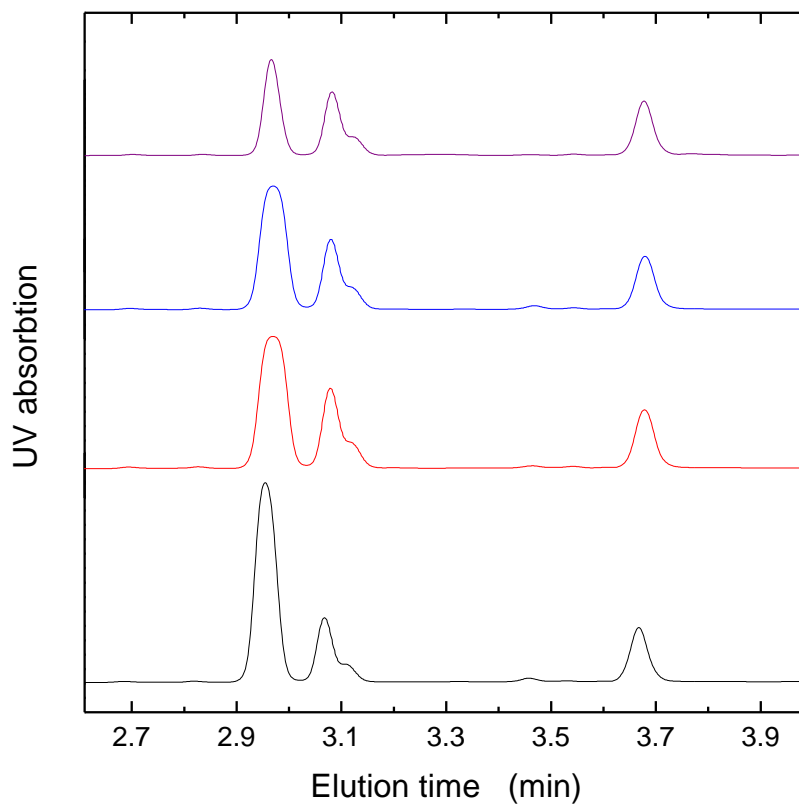


Figure 8.6. HPLC chromatogram of control-SN molecule in DMF in the presence of SN3U monomer, FRP initiator and naphthalene at 75 °C for 0 hour (black like), 2 hours (red line), 3.5 hours (blue line) and 22 hours (purple line). The peaks located at 2.96, 3.09 and 3.68 minutes correspond to SN3U monomer, control-SN and naphthalene respectively.

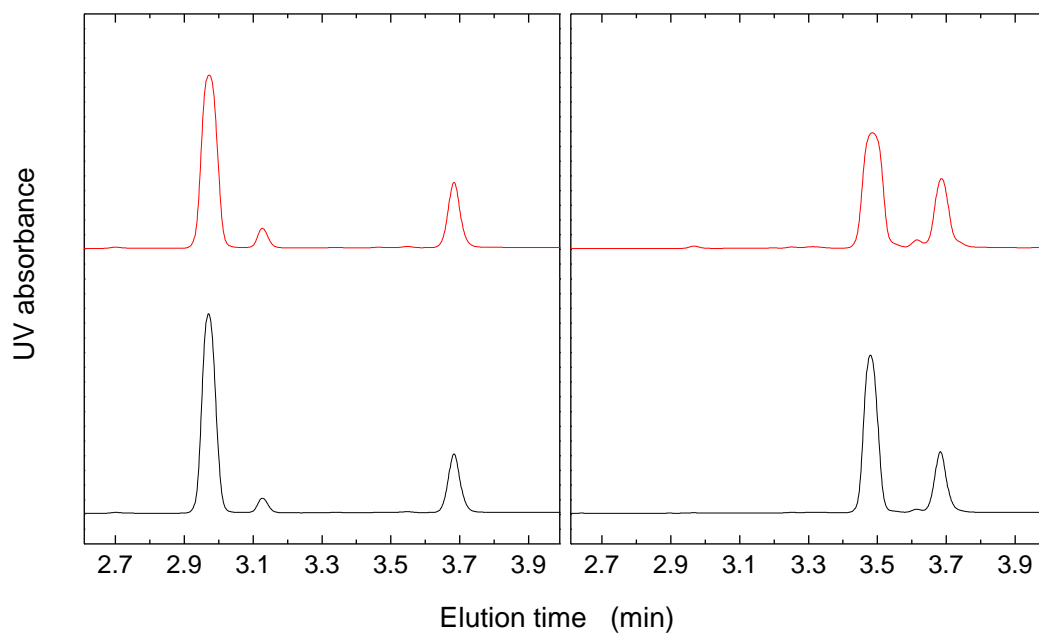


Figure 8.7. HPLC chromatograms of SN3U (left) and SN3P monomers (right) for 0 hour (black line) and 40 hours (red line) in DMF at 75 °C. The peaks located at 2.96, 3.11, 3.49 and 3.68 min correspond to SN3U monomer, impurities in SN3U monomer, SN3P monomer and naphthalene respectively.

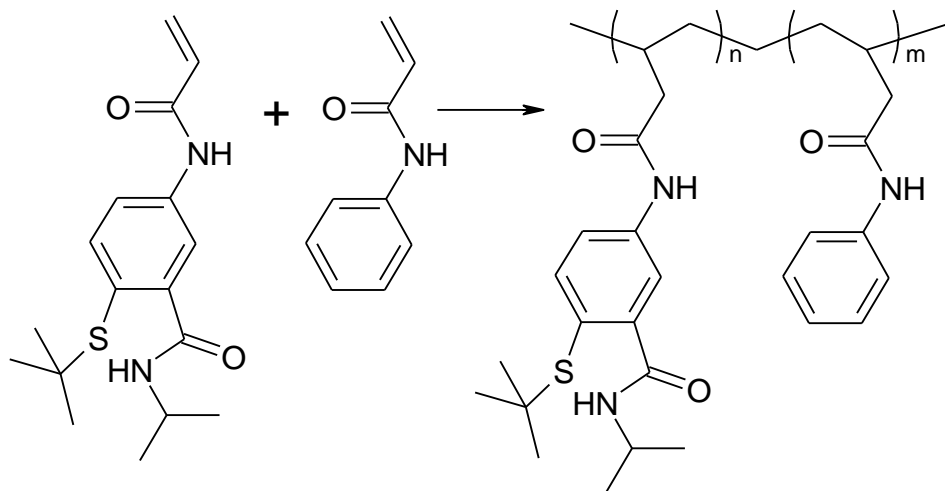


Figure 8.8. Polymerization scheme of SN2P and PhAAm.

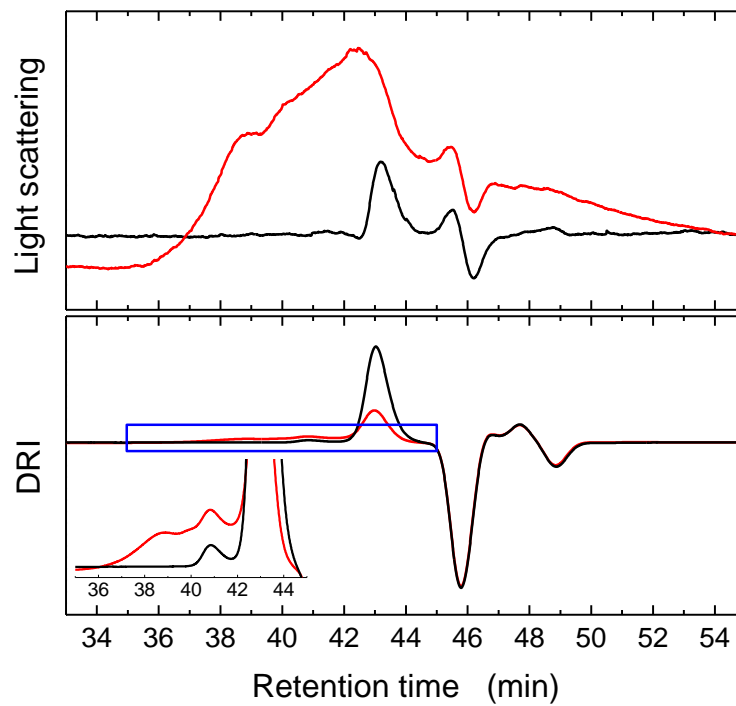


Figure 8.9. Differential refractive index (DRI) and light scattering data of SN2P monomer (black line) and dried polymerization mixture (red line).

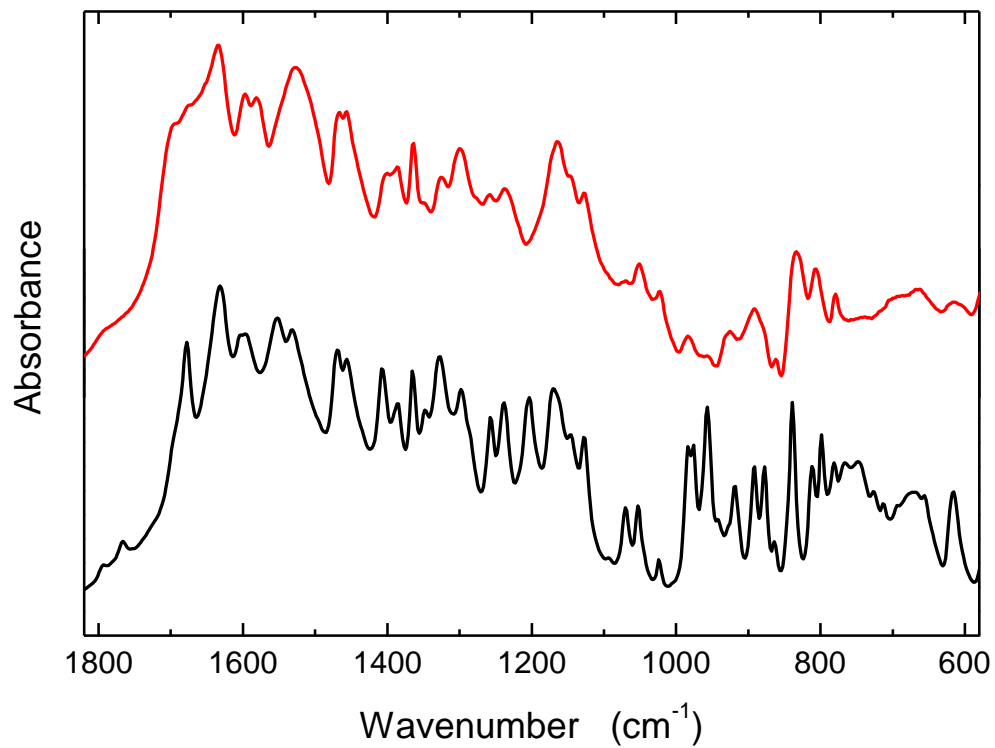


Figure 8.10. FT-IR spectra of SN2P monomer (black line) and dried polymerization mixture of 100% SN2P (red line).

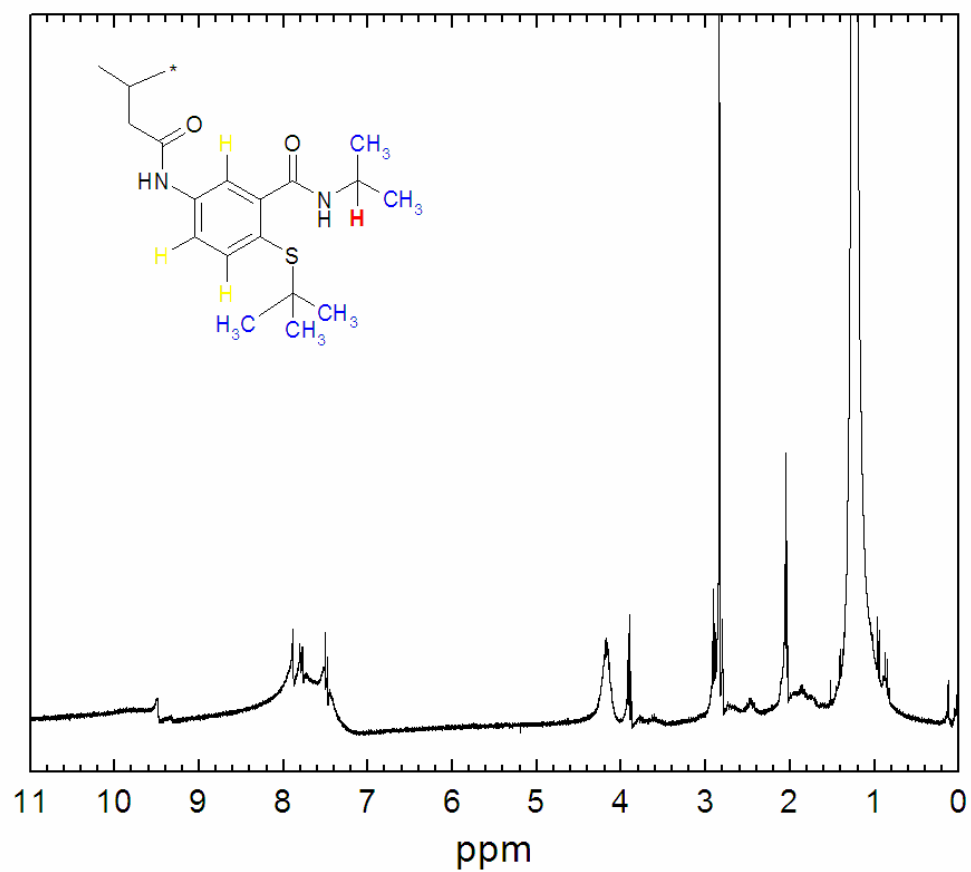


Figure 8.11. NMR spectra of dried polymerization mixture of 100% SN2P collected in d-acetone.

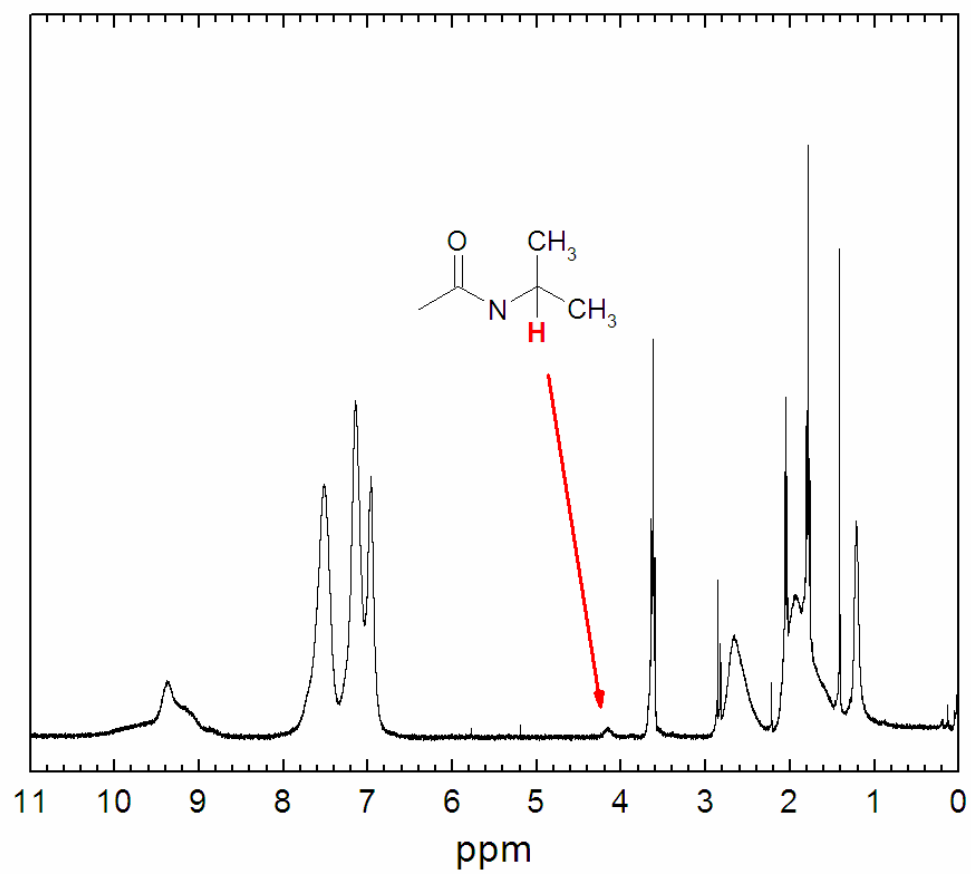


Figure 8.12. NMR spectra of 9.1% SN2P copolymer measured in d-acetone.

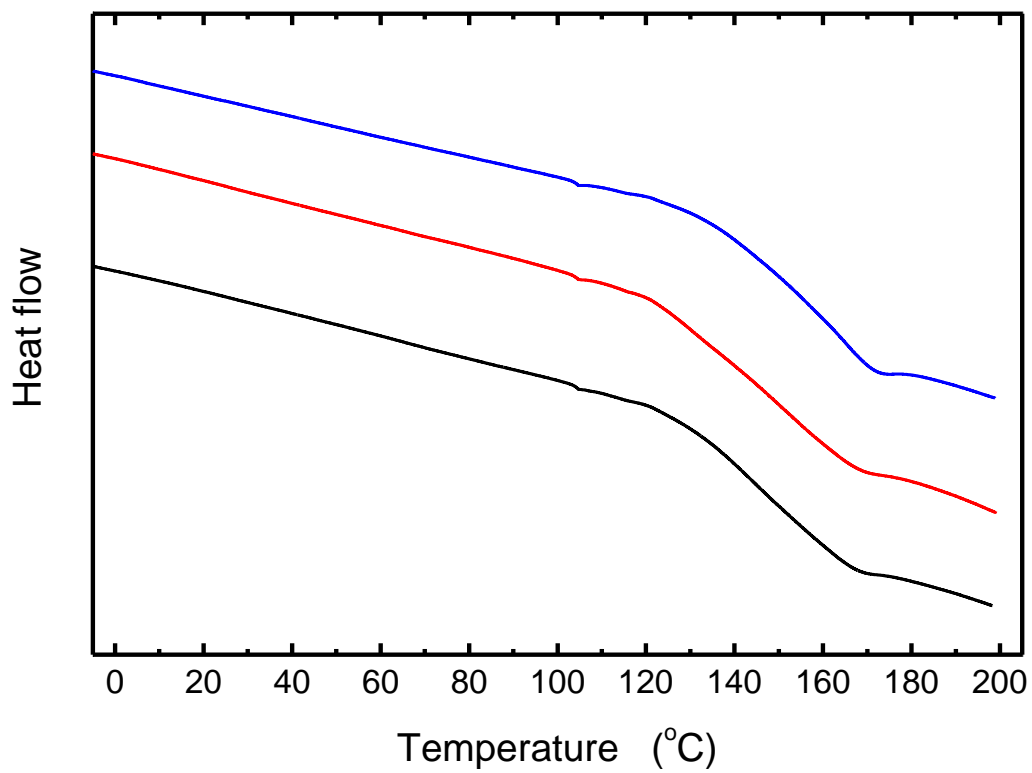


Figure 8.13. DSC thermograms of PPhAAm (black line), 4.8% SN2P (red line) and 9.1% SN2P (blue line) containing copolymers synthesized in DMF at 75 °C (exotherm is up).

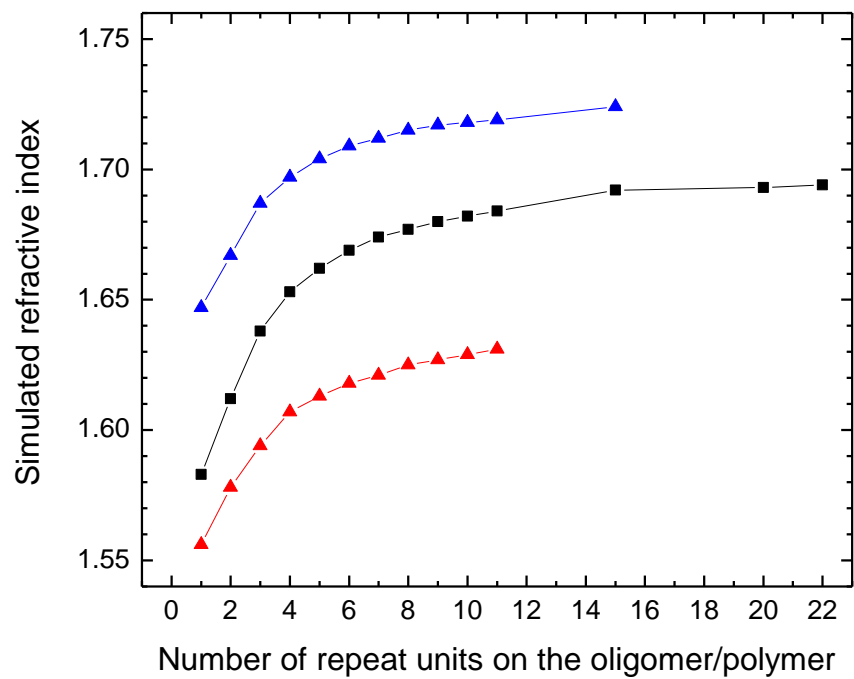


Figure 8.14. Simulated values of refractive indices for SN2P (▲), PhAAM (■) and SN2U (●) as a function of monomeric repeat units.

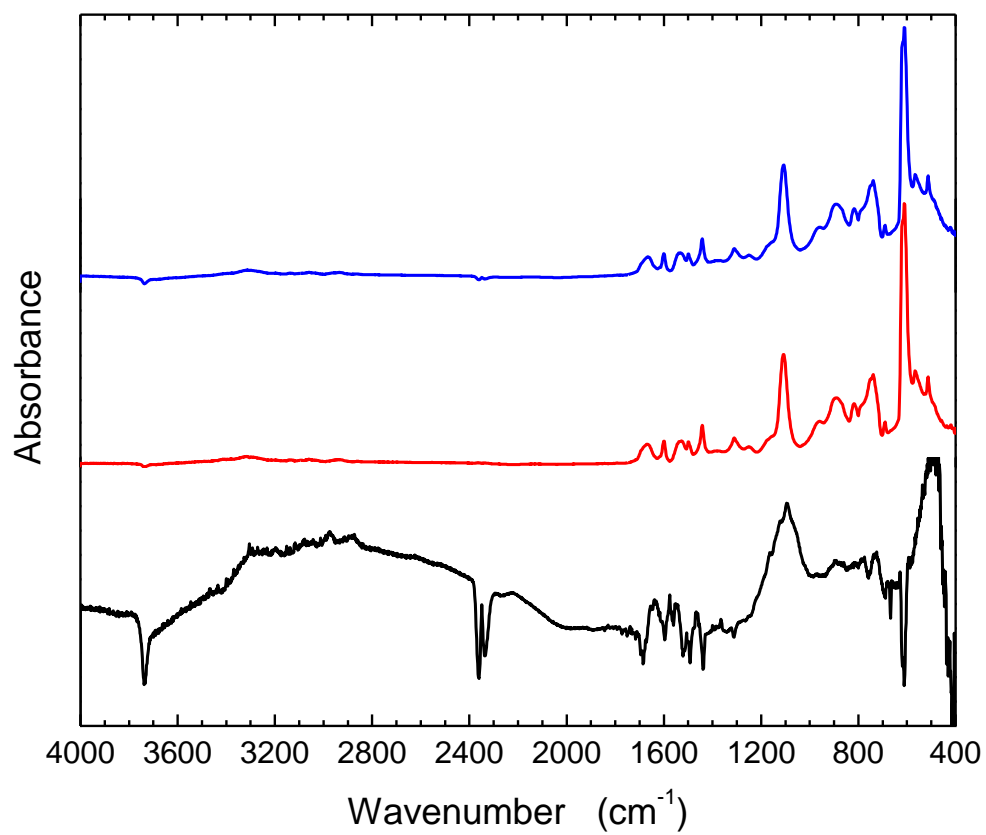


Figure 8.15. FT-IR spectra of 9.1% SN2P-PAAm copolymer, PPhAAm brush and their difference.

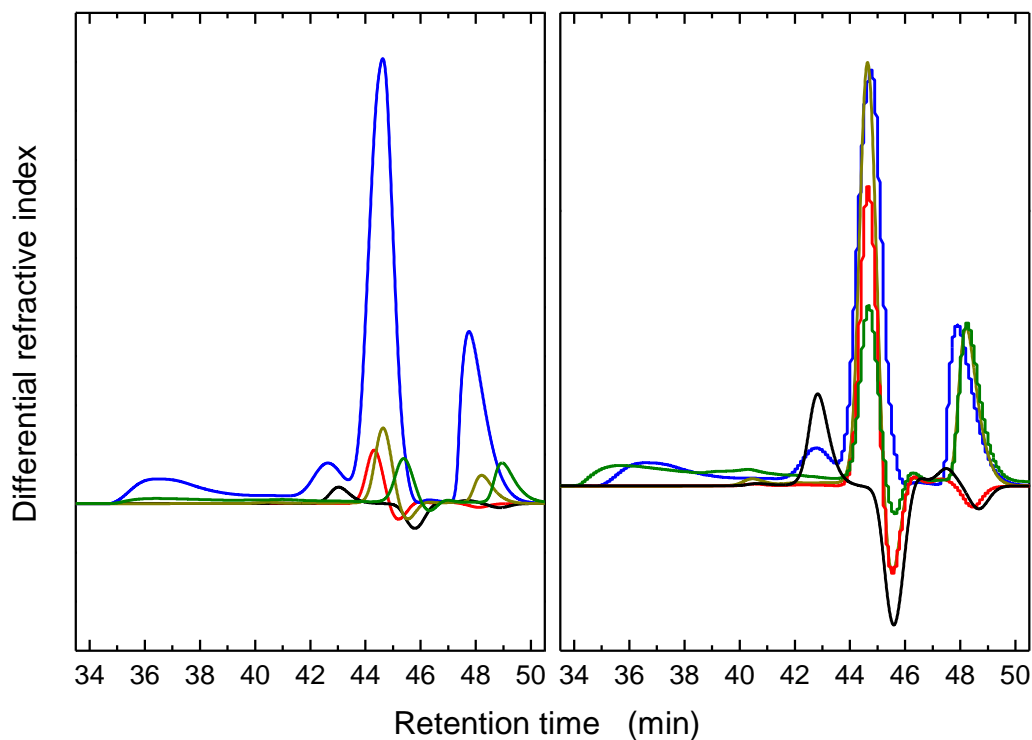


Figure 8.16. Original (left) and normalized (right) SEC chromatograms of the polymerization mixtures from brush growth and monomers. SN2P monomer (black line), PhAAm monomer (red line), from PPhAAm brush polymerization solution (dark yellow line), from 9.1 SN2P brush polymerization solution (blue line) and heated PhAAm solution (olive line).

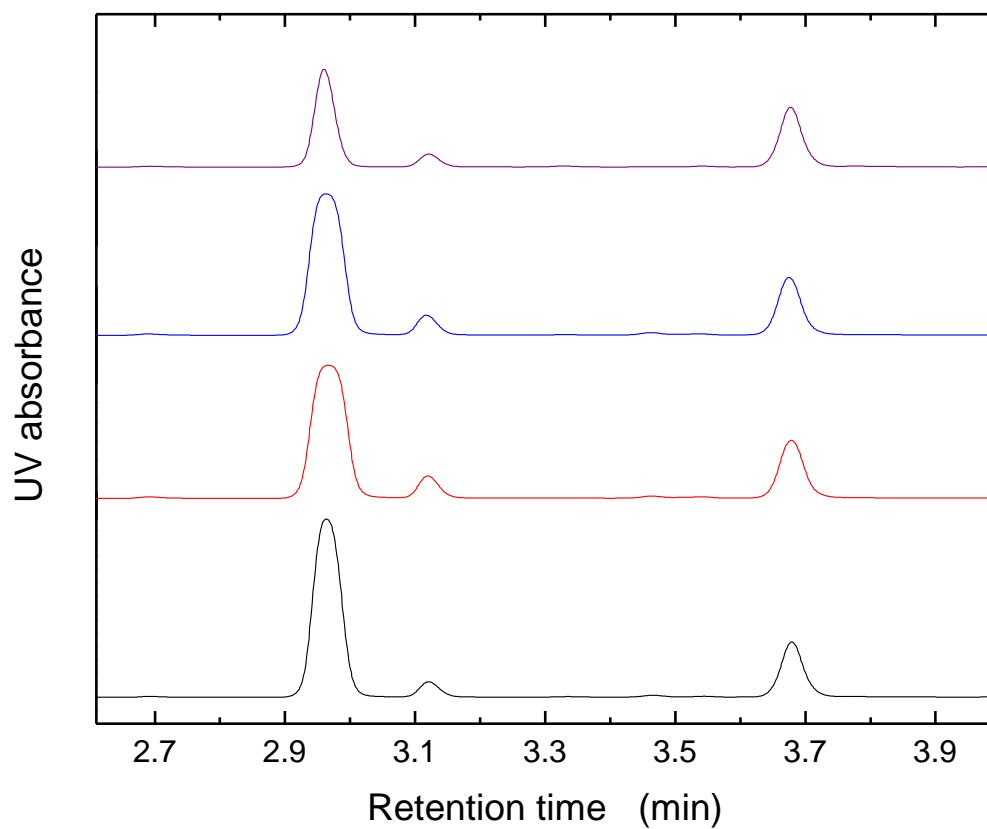


Figure 8.17. HPLC chromatograms of SN3U homopolymerization mixture in DMF at 75 °C for 0 (black line), 2 (red line), 4.5 (blue line) and 24 hours (purple line). The peaks located at 2.96, 3.11, 3.49 and 3.68 min correspond to SN3U monomer, impurities in SN3U monomer and naphthalene respectively.

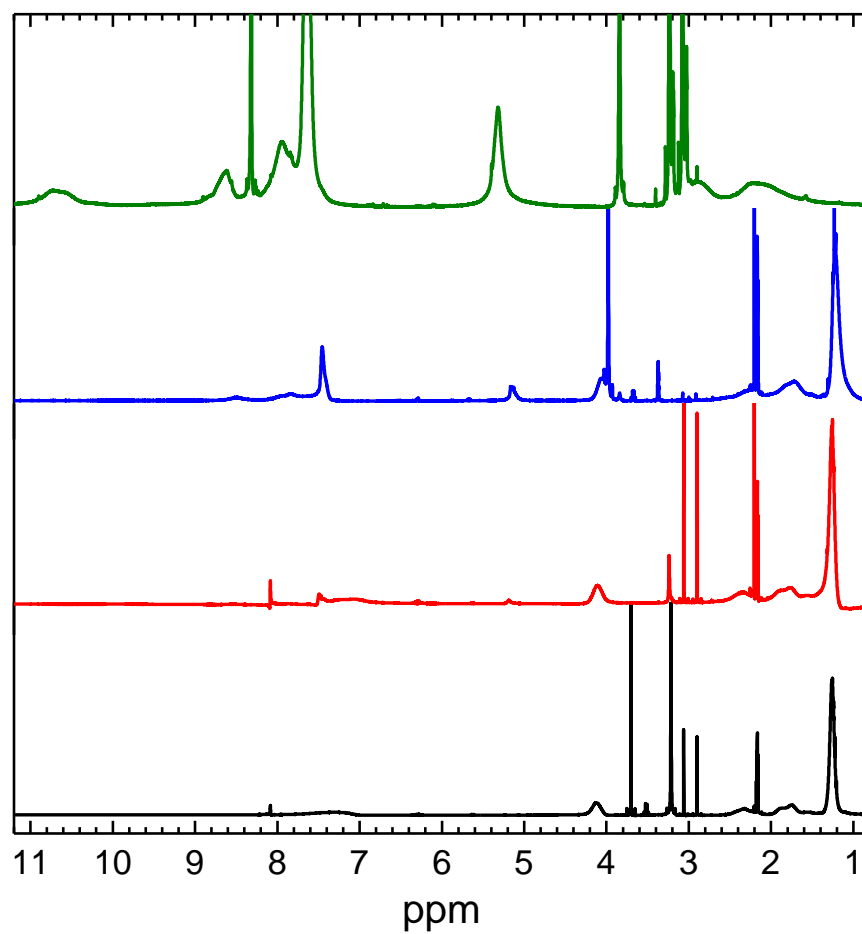


Figure 8.18. $^1\text{H-NMR}$ spectra of PNIPAAm (black line), 10% SN3U (red line), 30% SN3U (blue line) containing copolymer and SN3U homopolymer (green line).

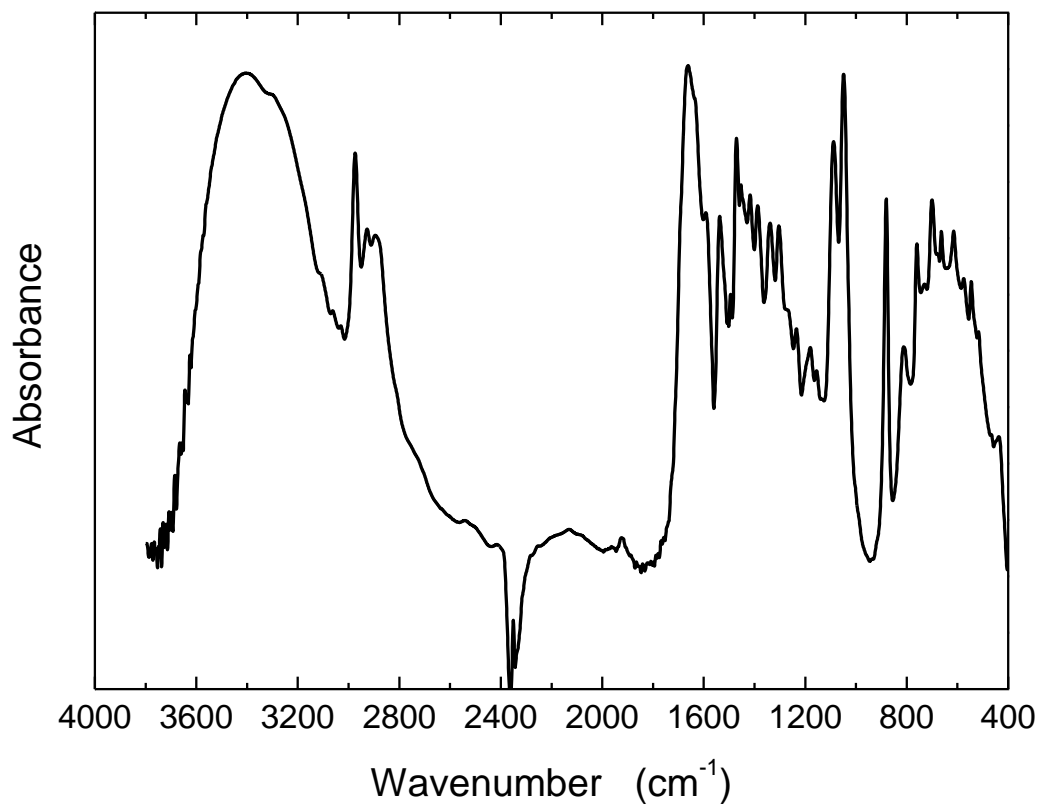


Figure 8.19. FT-IR spectra of SN3U homopolymer.

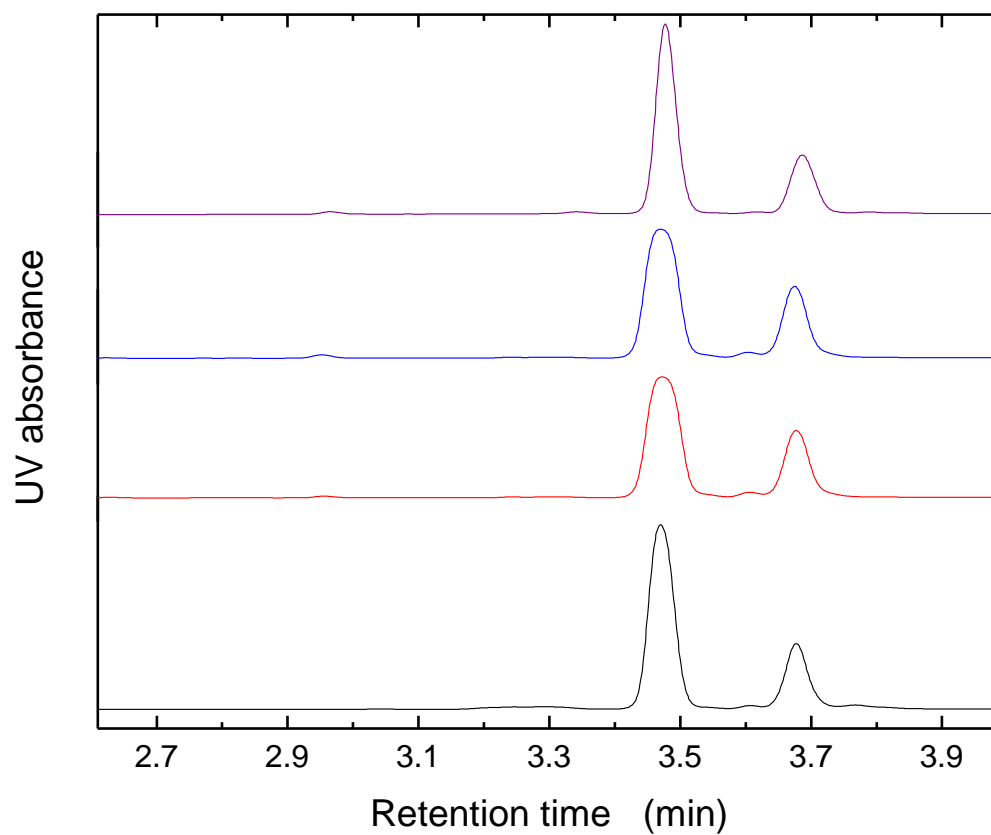


Figure 8.20. HPLC chromatograms of SN3P homopolymerization mixture in DMF at 75 °C for 0 (black line), 2 (red line), 4.5 (blue line) and 24 hours (purple line). The peaks located at 3.47 and 3.68 min correspond to SN3P monomer and naphthalene respectively.

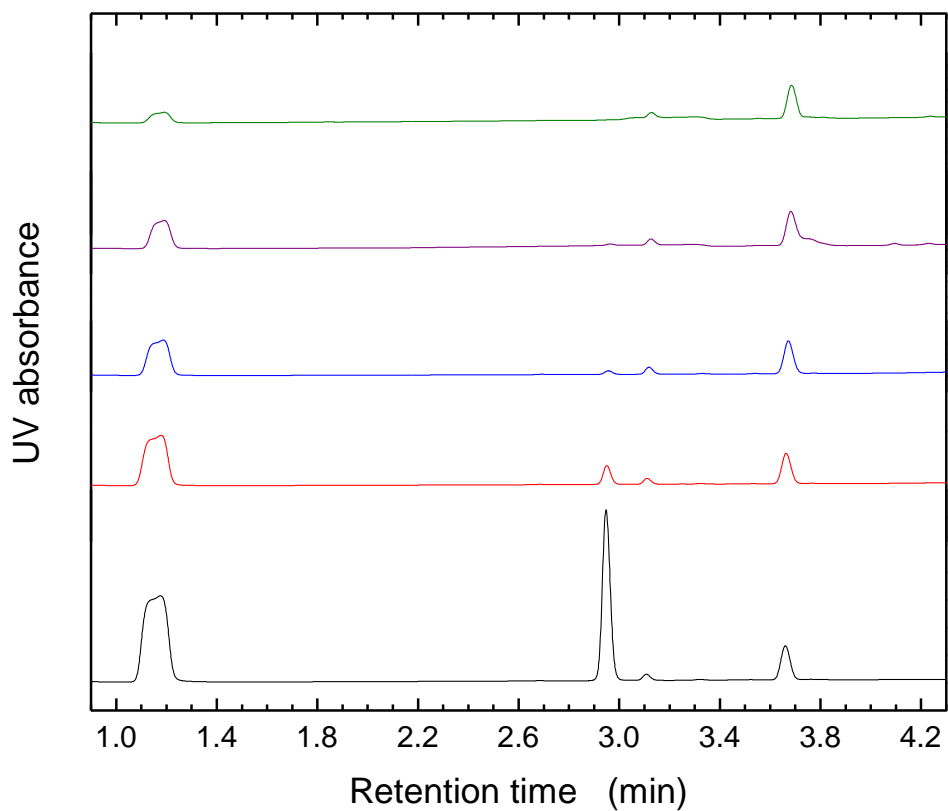


Figure 8.21. HPLC chromatograms of 10% SN3U and 90% NIPAAm polymerization mixture for 0 (black line), 2 (red line), 5 (blue line), 7 (purple line) and 23 hours (olive line). The peaks located at 1.14, 2.98 and 2.68 minutes correspond to NIPAAm, SN3U and naphthalene respectively.

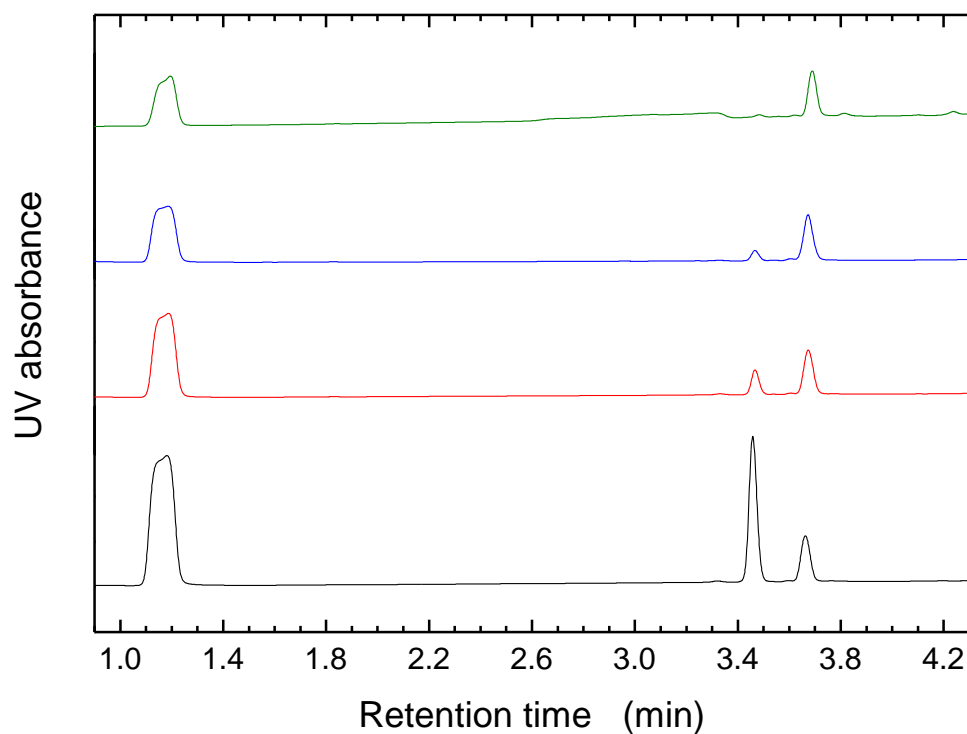


Figure 8.22. HPLC chromatograms of 10% SN3P and 90% NIPAAm polymerization mixture for 0 (black line), 2 (red line), 4 (blue line) and 20 hours (olive line). The peaks located at 1.14, 3.47 and 2.68 minutes correspond to NIPAAm, SN3P and naphthalene respectively.

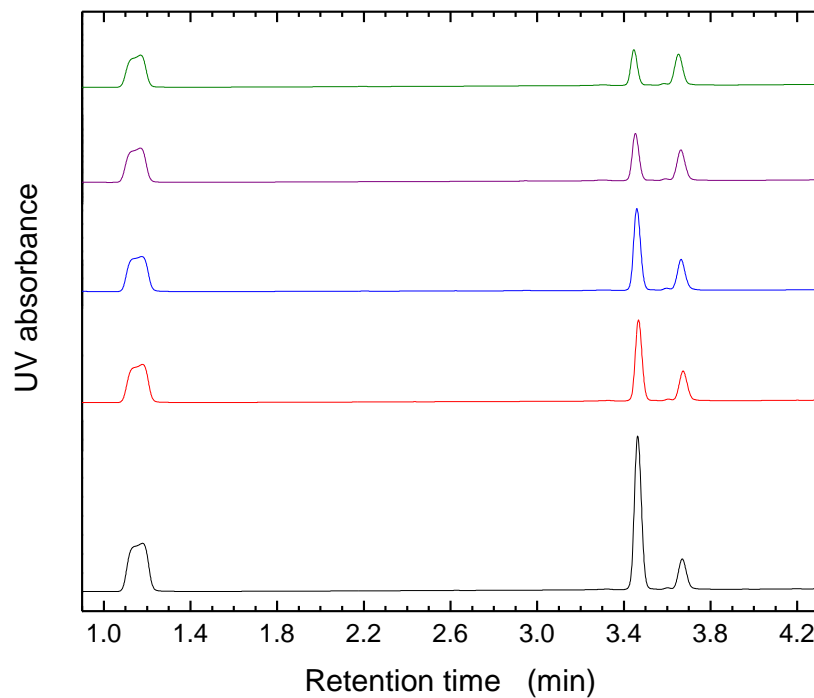


Figure 8.23. HPLC chromatogram of 30% SN3P and 70% NIPAAm polymerization mixture for 0 (black line), 3 (red line), 7 (blue line), 10 (purple line) and 22 hours (olive line). The peaks located at 1.14, 3.47 and 2.68 minutes correspond to NIPAAm, SN3P and naphthalene respectively.

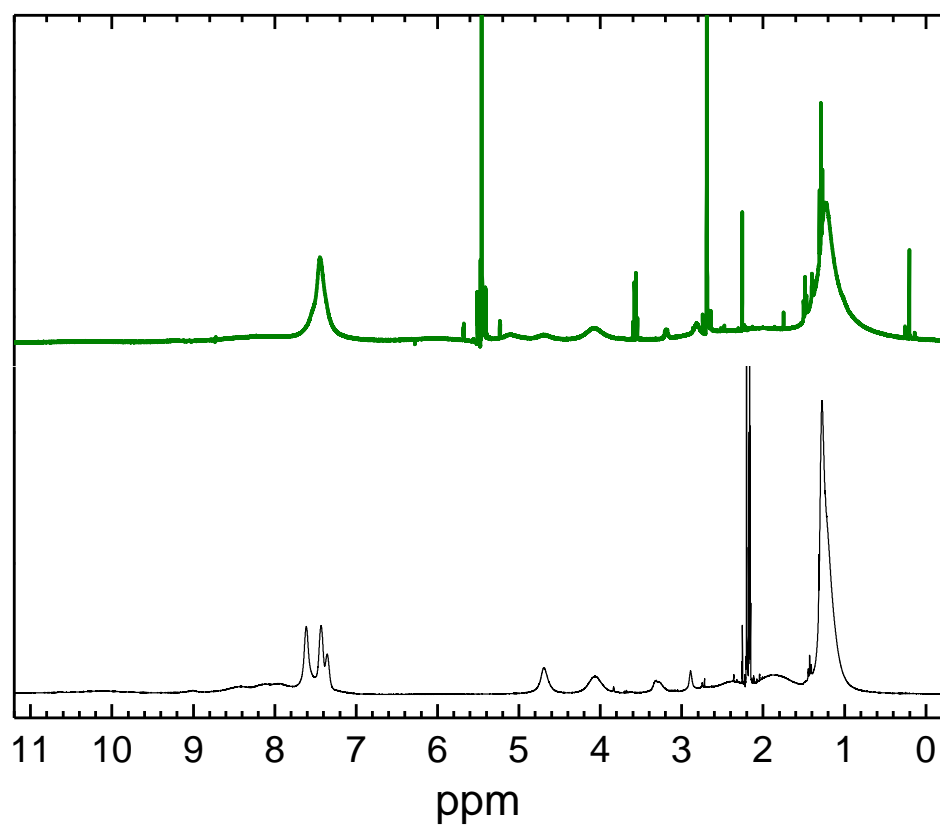


Figure 8.24. ¹H-NMR spectra of 50% wt SN3P containing NIPAAm-co-SN3P copolymer before (black line) and after (red line) deprotection reaction.

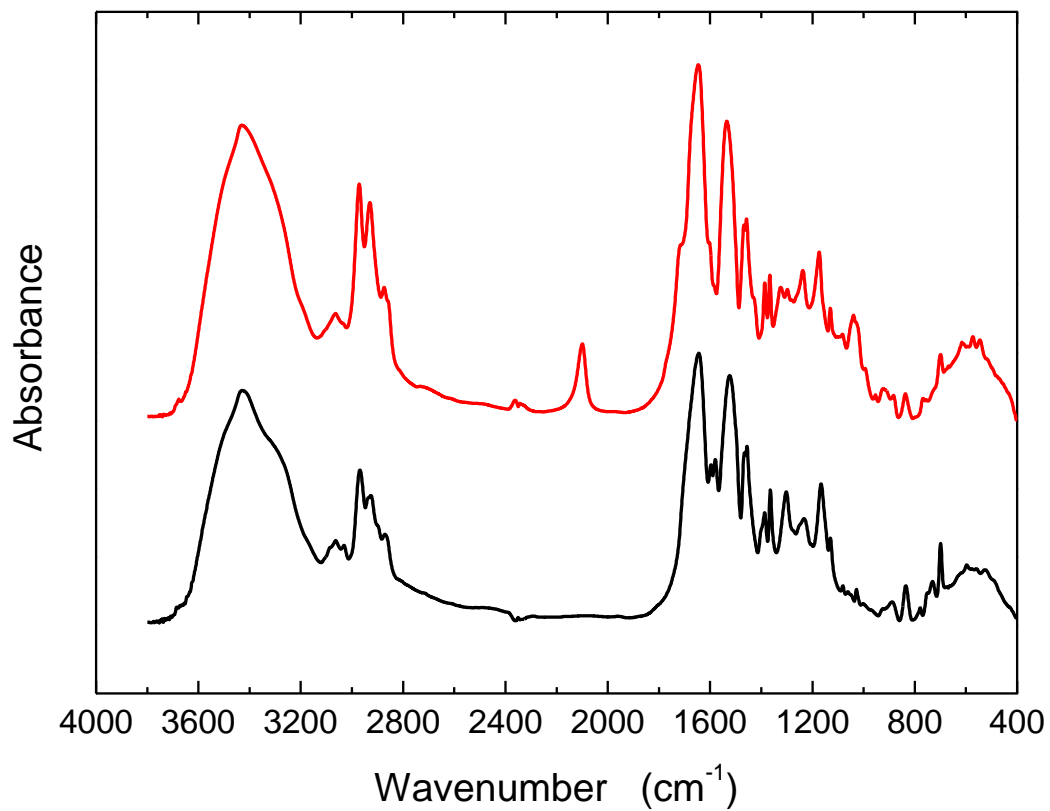


Figure 8.25. FT-IR spectra of 50% SN3P containing NIPAAm-co-SN3P copolymer before (black line) and after (red line) deprotection reaction.

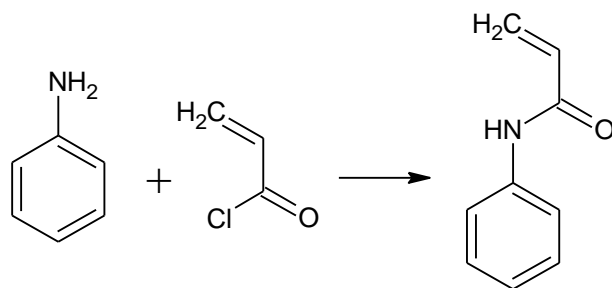


Figure 8. 26. Synthesis of PAAm from aniline and acryloyl chloride.

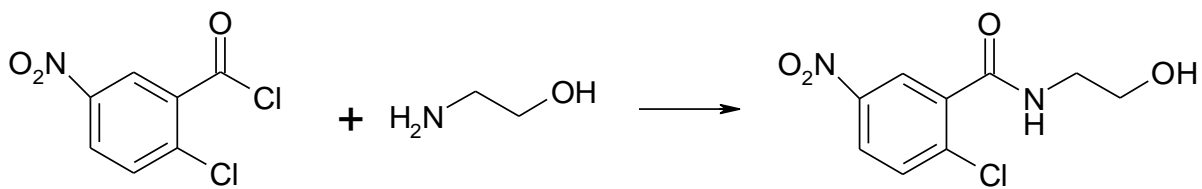


Figure 8.27. Reaction step 1.

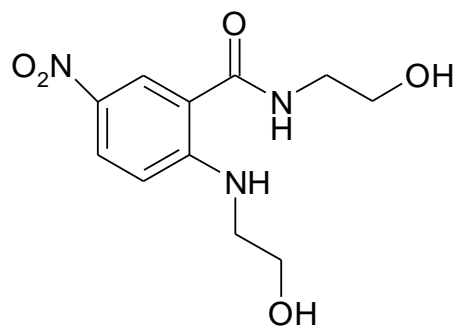


Figure 8.28. Byproduct of reaction step 1.

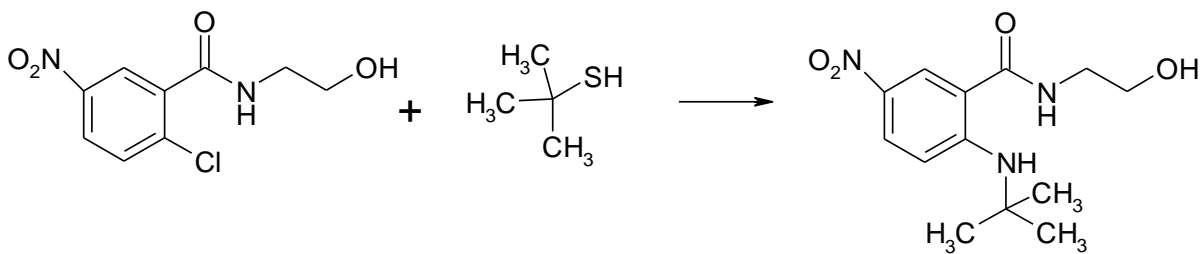


Figure 8.29. Reaction step 2.

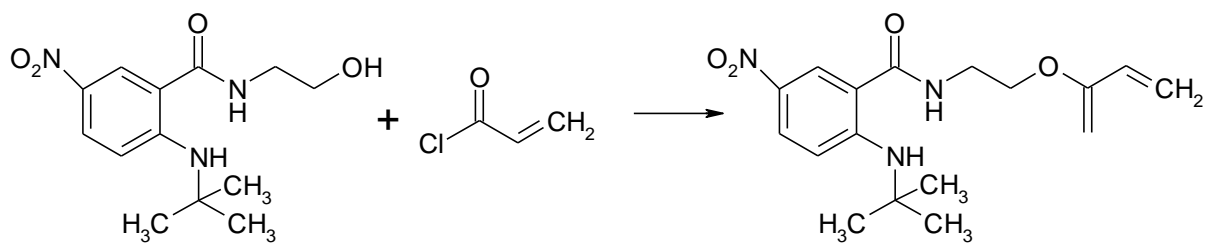


Figure 8.30. Reaction step 3.

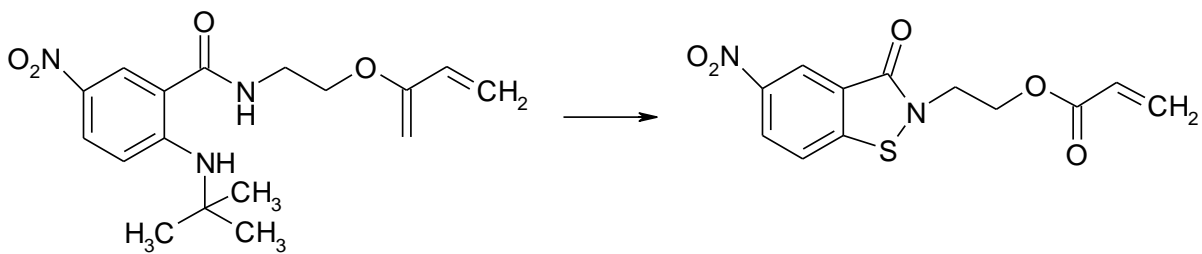


Figure 8.31. Reaction step 4.

8.7. APPENDIX

Phenylacrylamide (PhAAm) was synthesized from aniline and acryloyl chloride in DCM via a 1-step reaction as depicted in Figure 8.26. The last batch of the synthesized PhAAm was not 100% pure. We thus wanted to see the presence of some impurities has an effect on SIP of PhAAm. It appears that the purity of PhAAm has an effect on PhAAm polymerization based on the thickness and brush uniformity on silicon wafer. Therefore, it is necessary to always use pure monomers during the synthesis.

SN monomers were synthesized in 4 steps as described below:

The 1st step in the synthesis of functionalized monomers involves the reaction of 2-chloro-5-nitrobenzoyl chloride (2C5NBC) and 2-aminoethanol at 0 °C in the presence of potassium carbonate (K_2CO_3) (cf. Figure 8.27). 3 equivalents of K_2CO_3 and 2-aminoethanol were mixed in THF and chilled in ice bath. Later, 2C5NBC was added drop-wise and the mixture was stirred at 0 °C for \approx 1hour and at room temperature for 2 hours. Later the reaction the mixture was filtered and the solid K_2CO_3 cake was washed with a small amount of ethyl acetate. After adding a small amount of hexane the filtrate was put in a refrigerator overnight for crystallization. The next day the crystallized filtrate was filtered with glass frit and the product of the 1st step was characterized by HPLC and NMR. The spectrum shows clean product (\approx 98%). The byproduct (cf. Figure 8.28) appears after long reaction times and/or higher reaction temperatures; which was shown by HPLC of the yellow oily sample.

Therefore, keeping the reaction time and temperature at optimum values improve the yield and purity of the product.

The second step of the reaction was performed with the product of 1st step and t-butylthiol (2.5 times in excess) in the presence of NaOH (1.05 times in excess) in DMF to get 2-(tert-butylthio)-N-(2-hydroxyethyl)-5-nitrobenzamide (thio-amide), shown in Figure 8.29. The reaction temperature was set below 0 °C by addition of salt in the ice-water bath. The extent of reaction was monitored by using the HPLC and at the end of the reaction, the mixture was poured into the ice cold 5% hydrochloric acid. The precipitated solid was filtered and washed with water. The t-butylthio-amide was obtained as a yellowish crystalline solid after drying under vacuum.

The acylation reaction of t-butylthio-amide with acryloyl chloride was carried out in dry dichloromethane (DCM) at 0 °C (cf. Figure 8.30). The t-butylthio-amide was dissolved in DCM and acryloyl chloride was added drop wise in the presence of a drying tube.

After obtaining thio-amide the ring was closed in the presence of trimethylsilyl chloride (TMSCl) and dimethylsulfoxide (DMSO) in dry dichloromethane as shown in Figure 8.31 at room temperature for ≈6 hours.

CHAPTER 9: POST-POLYMERIZATION MODIFICATION STUDIES WITH FUNCTIONAL THIOIMIDE MOLECULES

9.1. INTRODUCTION

Direct polymerization of suitable monomers is possibly the most straightforward route to synthesize new functional polymers. However, several problems may appear at various points along the synthetic pathway despite the simplicity of this approach. Some of these issues include the following points: 1) The catalysts or reaction conditions necessary for polymerization may not be compatible with the functional groups present on the corresponding monomer(s). In this case, additional time, effort and reaction steps may be necessary to incorporate protective groups for the polymerization process to take place, which will increase the overall cost. The deprotection step may not proceed to completion and it may also affect the structural integrity of the polymer backbone. In addition, the yield of modified/protected/new monomer may be too small to produce appreciable quantities of the desired polymer. 2) The polymerization may fail to produce sufficiently long polymers with acceptable polydispersity indices even after a successful monomer synthesis. The development of controlled radical polymerization techniques and advances in catalytic polymerization have proven to produce polymers that meet both of these criteria. However, the functional groups present on the monomer may not allow utilization of these polymerization techniques for all the monomers available, because they may participate in

side reactions that can cause a loss of control over the polymerization process. 3) Isolation and/or processing of the synthesized polymers may be inhibited by the desired functionality.

These issues apply not only to bulk polymerization reactions, but also to polymer brush synthesis, where one end of the polymer chain is tethered to a substrate. Indeed, the entropic constraints introduced by surface-initiated polymerizations constitute yet another obstacle that may prevent direct polymerization of a given monomer. With these points in mind, the need for an alternative approach to produce functionalized polymer chains is eminent.

Post-polymerization modification (PPM) represents an alternative synthetic strategy to overcome the aforementioned problems. PPM approach incorporates functionalities into polymer chains by decorating already-synthesized polymers with an appropriate chemical or biological species. In addition, PPM allows for the generation of diverse functional polymer libraries with identical chain lengths (and tailorable chain-length distributions) but different side-chain functionality compared to the parent homopolymer precursor. Therefore, the PPM approach is an appealing and powerful route to study and establish the structure–property relationships in soft materials.

PPM approach is not a new route towards preparing functional materials; several industrial processes take advantage of this approach in bulk polymer production, such as modification of polyolefins.^[1] On smaller scales, a number of single-step, high yielding reactions under mild conditions can produce modified bulk and brush polymers, as highlighted in a recent reviews.^[2, 3] There are several examples of PPM reactions in the

literature, which have been applied successfully to generate functional polymeric materials. Some of the most commonly used PPM reactions involve: “click chemistry”, quaternization, thiol-ene addition reaction, halogenation and reactions between hydroxyl groups and the acid chlorides.

Huisgen 1,3-dipolar cyclo addition reaction, “click chemistry”, is one of the most popular PPM reactions that has appeared in the literature. The reaction between an alkyne and azide groups in the presence of a Cu^{I} catalyst has been applied to a wide variety of polymeric systems with a great success.^[4, 5] This reaction is noted for its mild conditions (including water) and near-quantitative conversion.

Another class of useful reactions employed in post-polymerization modification involves quaternization of amines to quaternary ammonium groups.^[6, 7] Quaternization reactions were employed to modify PDMAEMA, poly(2-vinylpyridine) and poly(4-vinylpyridine) and other functionalities to produce polycations (i.e., permanently charged, so-called, strong, electrolytes) of these polymers. These reactions proceed quickly to high conversions, and can introduce a number of functional groups into the polymer under mild conditions without a catalyst, as well as produce permanent polycations.

Thiol-ene addition reaction is another appealing PPM route that has been used widely to synthesize functional materials.^[8-12] The radical addition of thiols to the carbon-carbon double and triple bonds takes place in the presence of thermal or photosensitive radical initiators. The reaction results in high yields with high tolerance even in the absence of a solvent. For example, the modification of the polymers containing unsaturated carbon-

carbon bond, i.e., poly(propargyl methacrylate)^[13] (PPMA), polyvinylmethylsiloxane^[9] (PVMS) and polybutadiene, were carried out by thiol-ene addition reaction.

Post-functionalization of aryl-containing polymers^[14] has been carried out via halogenation or sulfonation. For instance, sulfonation and bromination^[14] reactions of aryl groups of polystyrene was carried out. Finally, the pendent -OH groups of PHEMA were functionalized with fluorinated mesogens with acyl chloride functionality to study and fabricate protein resistant surfaces.^[15]

In this chapter, we show the applications of quarternization and “click chemistry” to incorporate functional SN post-modification agents to poly(dimethylamino ethyl methacrylate) (PDMAEMA) and poly(propargyl methacrylate) (PPMA), respectively.

9.2. EXPERIMENTAL

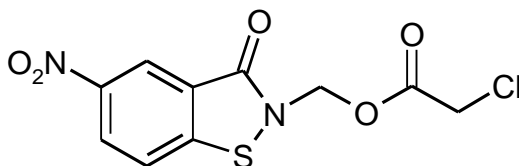
9.2.1. MATERIALS

Dimethylaminoethyl methacrylate (DMAEMA), azobisisobutyronitrile (AIBN), methyl iodide, benzyl chloride, ammonium hexafluorophosphate, anhydrous toluene, dimethylformamide (DMF), acetone, n-hexane and acetonitrile were purchased from Sigma-Aldrich. Propargyl methacrylate (PMA) was acquired from Alfa Aesar. Azo-based free radical polymerization [16] (FRP) and atom transfer radical polymerization^[17] (ATRP) initiators for surface initiated polymerization (SIP) were synthesized according to the recipes

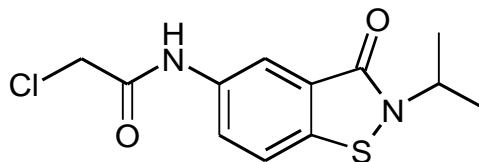
given in Refs. 16 and 17. Poly(ethylene terephthalate) (PET) fibers with attached ATRP initiator were prepared as reported earlier.^[18] Quantofix® cyanide detection kit was purchased from Fisher Scientific.

Various SN agents were synthesized in the laboratory of Dr. Jiří Šrogl at the Institute of Organic Chemistry and Biochemistry of the Czech Academy of Sciences, Czech Republic. Each SN compound for quarternization reaction is denoted as qSN#U, where # represents the generation of the unprotected (U) SN compound that would be attached via quarternization (q). The synthesis of SN based post-modification agents is summarized in the Appendix to this chapter.

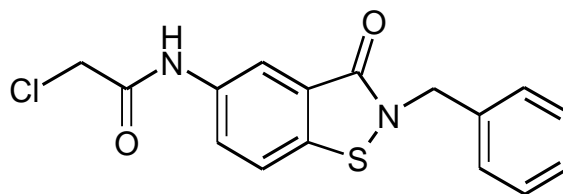
1. **qSN1U compound:** 1st generation SN quarternization agent. The acylchloride functionality is attached to the tertiary amine; this may interfere with the opening and closing of the thioimide ring. Moreover, the ester bond may undergo hydrolytic degradability.



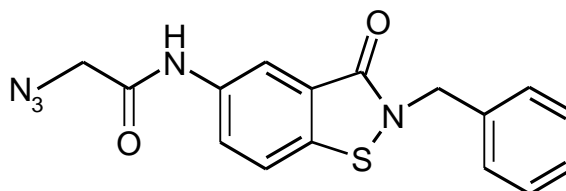
2. **qSN2U compound:** 2nd generation SN quarternization agent. The presence of the amide bond increases hydrolytic stability relative to the SN compound with an ester bond.



3. **qSN3U compound:** 3rd generation SN quarternization agent. The chemistry is similar to qSN2U except the isopropyl group is replaced with a benzyl group to increase the solubility in organic solvents.



4. **Azide-SN3U compound:** Azide-based SN compound. The chemistry is similar to qSN3U since qSN3U was used as a precursor.



9.2.2. INSTRUMENTATION

Nuclear magnetic resonance (NMR) spectra were collected with a Bruker Avance 400 MHz NMR spectrometer by using deuterated solvents (see below) for complete dissolution of the polymers. High performance liquid chromatography (HPLC) experiments were conducted using an Acquity UPLC Instrument (Waters Corporation). The elemental analysis of the samples was carried out with PE 2400 Series II CHNS/O (Perkin Elmer, USA, 1999) for C, H, N and SPECTRO iQ II (X-ray-flourescent analyzer) for other elements. Fourier transform infrared spectroscopy (FT-IR) was employed to monitor chemical changes that

took place on the polymer after surface post-modification. The FT-IR spectra were recorded on a Nicolet 6700 spectrometer in transmission mode and the data were analyzed by Omnic software. For each sample 1024 scans were collected after recording a background signal (all with the resolution of 4 cm^{-1}). The thicknesses of polymer brushes on flat substrates were assessed with a variable-angle spectroscopic ellipsometer (VASE) manufactured by J.A. Woollam Co. Ellipsometry measures the difference in the polarization state between the light beams incident onto and reflected from the surface thus providing information about the dielectric properties and thickness of the film. The film thickness was evaluated using a single layer Cauchy model (Si/SiO_x/Brush) before and after each post-modification reaction. Unless otherwise specified, ellipsometric data were collected at an incidence angle of 70° with respect to the surface normal at wavelengths ranging from 400 to 1100 nm in 10 nm increments. The surface chemical composition of the polymer brushes was determined with a Kratos Axis Ultra DLD x-ray photoelectron spectroscopy (XPS) instrument using monochromated Al K α radiation with charge neutralization. Survey and high-resolution spectra were collected with pass energies of 80 and 20 eV, respectively, by using both electrostatic and magnetic lenses. Elemental chemical compositions were determined from spectral regression using Vision and CasaXPS software. Molecular weight and its distribution of the synthesized polymers were determined by size-exclusion chromatography (SEC) coupled with light scattering (Wyatt MiniDAWN) and differential refractive index detection (OptilabREX instruments).

9.2.3. POLYMERIZATION AND POST-MODIFICATION REACTIONS

9.2.3.1. POLYMERIZATION OF PDMAEMA

Poly(dimethylaminoethyl methacrylate) (PDMAEMA) was synthesized in dimethylformamide (DMF) via FRP initiated by AIBN. Specifically, 10 ml of DMAEMA, 80 ml DMF and 10 mg AIBN were mixed in a Schlenk flask and oxygen was removed via 3-4 freeze thaw cycles. The FRP was carried out under argon for 20 hours at 75 °C. At the end of the polymerization, the reaction was stopped by exposing it to air, which consumed all remaining free radicals. DMF was removed via rotary evaporator and the solid polymer was re-dissolved in acetone and precipitated in n-hexane 3 times.

9.2.3.2. POLYMERIZATION OF PDMAEMA BRUSHES

PDMAEMA brushes were grown on silicon wafers via FRP and/or ATRP and on PET fibers. For FRP, azo-based free radical initiator (cf. Figure 9.1) was deposited on silicon wafers that were previously cut into pieces of desired dimensions (typically 1 x 3 cm²) and exposed to UV/ozone treatment for 15 minutes in order to increase the density of surface hydroxyl groups. The substrates were subsequently incubated in free radical initiator solution (≈ 1 mM in toluene for 16 hours at -20 °C). The silicon wafers decorated with the initiator molecules were then placed in glass vials containing the mixture of DMAEMA and

DMF. The polymerization mixture was degassed, the vials were sealed and placed in oil bath (80°C) for ≈20 hours. After surface-initiated polymerization (SIP), the silicon wafers were taken out of the vials, washed with acetone to remove any free polymer, sonicated for 2 + 2 minutes, rinsed with acetone to remove loosely bound polymer chains and monomers and finally dried under a stream of nitrogen gas. For ATRP, [11-(2-bromo-2-methyl)propionyloxy] undecyltrichlorosilane (BMPUS) was deposited on silicon substrates as described above and the silicon wafers were placed in glass vials. In a Schlenk flask DMAEMA, solvent and the ligand were de-oxygenated via 3 freeze-thaw cycles and CuBr was added to the Schlenk flask followed by an additional freeze-thaw cycle. The ATRP polymerization mixture was transferred to the glass vials containing the initiator-coated silicon wafers. The polymerization was stopped after ≈12 hours by exposing the reaction mixture to oxygen and the wafers were washed, sonicated and rinsed with acetone and dried under a stream of nitrogen gas.

9.2.3.3. POLYMERIZATION OF PROPARGYL METHACRYLATE

Propargyl methacrylate (PMA) was polymerized via FRP in DMF at 75 °C. In a Schlenk flask 4 ml PMA, 30 ml DMF and 6 mg AIBN were mixed, de-oxygenated via 3-4 freeze-thaw cycles and kept in the oil bath for ≈20 hours. At the end of the polymerization the DMF was removed from the polymerization mixture via rotary evaporation. The dried polymer was dissolved in dichloromethane and precipitated 3 times in cold methanol.

9.2.3.4. POST-MODIFICATION OF PDMAEMA WITH SN BASED QUARTEENIZATION AGENTS

The quarternization reactions of PDMAEMA with qSN3U were performed in a round bottom flask in acetonitrile and DMF at 75 °C with a drying tube. Compounds with different extents of quarternization were prepared to study the effect of the SN loading on PDMAEMA. In addition to the quarternization reaction with qSN3U compound, quarternizations of PDMAEMA with methyl iodide and benzyl chloride with same the loading were performed that served as controls. The reaction was monitored with HPLC until all the quarternization agents were consumed and the quarternized polymer was precipitated via addition of hexane and diethylether in the reaction media. The solid was filtered with a glass frits and washed with diethylether. The solid polymer was dried under vacuum.

The Cl⁻ ion on the quarternary PDMAEMA-qSN3U salt (qPDMAEMA-SN3U) was replaced with PF₆⁻ via ion exchange reaction to verify the quarternization reaction and to increase the solubility in organic solvents. The ion exchange reaction between qPDMAEMA-SN3U and ammonium hexafluorophosphate was carried out in DI water and the ion exchanged polymer was collected via filtration. The ion exchanged qPDMAEMA-SN3U salt was dried under vacuum.

9.2.3.5. POST-MODIFICATION OF PDMAEMA BRUSHES WITH SN BASED QUARTERNIZATION AGENTS

PDMAEMA brushes on silicon wafers and PET fibers were quarternized with qSN1U and methyl iodide in acetone at 60 °C for 12 hours. After quarternization reaction, the samples were washed with acetone, sonicated for 2 + 2 minutes in acetone, rinsed with acetone and dried under a stream of nitrogen gas.

9.2.3.6. POST-MODIFICATION OF PPMA WITH ORGANIC AZIDES

The PPMA was post-modified with azide-based SN compound and cyanobenzyl azide via the “click reaction”(cite click papers). The “click reaction” was carried out in the presence of CuMeSal salt in THF under argon. Specifically, 110 mg PPMA, 48.8 mg azide-SN and 15 ml THF were mixed in a Schlenk flask and the reaction mixture was deoxygenated via 3 freeze-thaw cycles; 5 mg CuMeSal was added subsequently to the reaction medium. The “click reaction” was performed at room temperature for 96 hours under argon; HPLC showed that the organo-azides were consumed. The polymers were precipitated in cold methanol and dried under vacuum for further characterization.

9.2.3.7. CAPTURING OF CYANIDE IONS WITH qPDMAEMA-SN

A stock solution of KCN in DI water was prepared with a concentration of 120 ppm. This solution was diluted with DI water to obtain 24 ppm KCN that was used in the purification experiments using PDMAEMA. qPDMAEMA-SN and qPDMAEMA solutions were prepared in DI water with a concentration of 10 mg/ml. The KCN solution and qPDMAEMA-SN were mixed in a separate vial and the mixture was kept at room temperature for 1 hour. The cyanide detection kit was used to determine the remaining concentration of cyanide in the mixture.

9.3. RESULTS AND DISCUSSIONS

9.3.1. POST-MODIFICATION OF PDMAEMA BRUSHES ON SILICON WAFER AND PET FIBERS WITH QSN1U VIA QUARTERNIZATION

We have attached successfully qSN1U to PDMAEMA brushes on PET fibers and silicon wafers and characterized the samples with FT-IR, XPS and ellipsometry. Examination of the IR spectra of PDMAEMA brushes on silicon wafers before and after the attachment of qSN1U revealed characteristic bands corresponding to amide and aromatic nitro groups (cf. Figure 9.2). The new signals located at 1640 and 1600 cm^{-1} correspond to amide I and amide II bands, respectively. New bands also appear at 750, 1100, 1350, and 1525 cm^{-1} , which indicate the presence of aromatic nitro-compounds. In addition, the disappearance of

stretching vibrations of the C-H bond of the $-N(CH_3)_2$ groups located at 2770 and 2820 cm^{-1} confirmed that the quarternization reaction with qSN1U compound took place as shown in Figure 9.2.

Variable angle spectroscopic ellipsometry was employed to determine the thickness and optical constants of PDMAEMA and qSN1U-modified PDMAEMA (qPDMAEMA-SN1U) brushes (Table 9.1). Two different brush thicknesses were used to study the effect of loading of qSN1U on brush thickness. Regardless of the initial brush thickness the relative increase in the thickness was comparable for the two samples.

The ellipsometric thickness data was quantified by using a simple model, which relates the variations in thickness to changes in the overall chemical composition of the polymer brush.^[15] The extent of qSN1U coupling to PDMAMEA brushes was calculated from ellipsometric thickness data by assuming that the grafting density of the PDMAEMA brushes did not change after qSN1U coupling due to chain cleavage. The grafting density of PDMAEMA brushes can be expressed as shown in Equation 9.1:

$$\sigma_{PDMAEMA} = \frac{h_{PDMAEMA} \rho_{PDMAEMA} N_A}{M_{PDMAEMA}} \quad (9.1)$$

where $h_{PDMAEMA}$ is the dry PDMAEMA thickness, $\rho_{PDMAEMA}$ is the PDMAEMA density, N_A is Avogadro's number, and $M_{PDMAEMA}$ is the PDMAEMA molecular weight. The same expression can be written for P(DMAEMA-co-qPDMAEMA/SN) brushes:

$$\sigma_{P(DMAEMA-co-qDMAEMA/SN)} = \frac{h_{P(DMAEMA-co-qDMAEMA/SN)} \rho_{P(DMAEMA-co-qDMAEMA/SN)} N_A}{M_{P(DMAEMA-co-qDMAEMA/SN)}} \quad (9.2)$$

By assuming that the grafting densities of PDMAEMA and P(DMAEMA-co-qPDMAEMA/SN) are equal (i.e., no chain cleavage occurred during the modification process), the thicknesses of PDMAEMA and P(DMAEMA-co-qPDMAEMA/SN) brushes can be related by combining Equations (9.1) and (9.2):

$$\frac{h_{P(DMAEMA-co-qDMAEMA/SN)}}{h_{PDMAEMA}} = \frac{\rho_{DMAEMA}}{\rho_{P(DMAEMA-co-qDMAEMA/SN)}} \frac{M_{P(DMAEMA-co-qDMAEMA/SN)}}{M_{o,DMAEMA}} \quad (9.3)$$

It is possible to simplify Equation 9.3 since the degree of polymerization of the polymer brush does not change after quarternization. Therefore:

$$\frac{h_{P(DMAEMA-co-qDMAEMA/SN)}}{h_{PDMAEMA}} = \frac{\rho_{DMAEMA}}{\rho_{DMAEMA-co-qDMAEMA/SN}} \frac{M_{o,DMAEMA-co-qDMAEMA/SN}}{M_{o,DMAEMA}} \quad (9.4)$$

where $M_{o,DMAEMA-co-qDMAEMA/SN}$ is the “effective” molecular weight of the copolymer unit and $M_{o,DMAEMA}$ is the molecular weight of the DMAEMA. The density and molecular weight of DMAEMA-co-qDMAEMA/SN can be calculated by the following equations:

$$\frac{1}{\rho_{DMAEMA-co-qDMAEMA/SN}} = \frac{w_{qDMAEMA/SN}}{\rho_{qDMAEMA/SN}} + \frac{1-w_{qDMAEMA/SN}}{\rho_{DMAEMA}} \quad (9.5)$$

$$\frac{1}{M_{o,DMAEMA-co-qDMAEMA/SN}} = \frac{w_{qDMAEMA/SN}}{M_{o,qDMAEMA/SN}} + \frac{1-w_{qDMAEMA/SN}}{M_{o,DMAEMA}} \quad (9.6)$$

where $\rho_{qDMAEMA/SN}$, $M_{qDMAEMA/SN}$ are the density and molecular weight, respectively, of the quarternized DMAEMA. These values were calculated from the densities and molecular weights of qSN1U and DMAEMA by using the weighted averages. Finally, $w_{SN/DMAEMA}$ is the weight fraction of quarternized DMAEMA units in the polymer brush.

The densities of PDMAEMA (0.922 g/cm³) and pure qSN1U (1.624 g/cm³) were calculated/estimated with the ChemSketch software and they were used in Equation (9.3) to back-calculate the extent of qSN1U coupling. The $h_{\text{P(DMAEMA-co-qDMAEMA/SN)}}/h_{\text{PDMAEMA}}$ ratios were calculated for different weight fractions of qDMAEMA/SN ($w_{\text{qDMAEMA/SN}}$) values and compared to the thickness ratios obtained experimentally. The weight fraction corresponds to the same experimental and calculated $h_{\text{P(DMAEMA-co-qDMAEMA/SN)}}/h_{\text{PDMAEMA}}$ ratio and was selected as extent of quarternization.

Based on these calculations it was found that $\approx 30\%$ of the PDMAEMA repeat units reacted with the qSN1U molecules. Likewise, the refractive indices of qPDMAEMA-SN1U molecules were also calculated with ChemSketch software and compared with the corresponding experimental values. For instance, the calculated refractive index is found to be between 1.533 and 1.536 when 15-20% of the PDMAEMA repeat units were reacted with qSN1U molecules. These calculated refractive indices of qPDMAEMA-SN1U are in a good agreement with the values obtained from ellipsometric measurements as shown in Table 9.1.

The surface atomic concentrations of nitrogen, sulfur and chlorine measured by XPS are tabulated in Table 9.2. These atomic percentages obtained experimentally are lower than the theoretical estimates calculated based on the extent of reaction values listed above. This may be due to surface contamination by hydrocarbons that may have occurred between the sample preparation and the XPS run. In addition, measuring the concentration of nitrogen and sulfur is a bit more challenging than measuring atomic concentrations of carbon and oxygen because of small photoelectric radius and location of the binding energies. Because of these

limitations, we reasoned that activating the qSN1U compound with fluorinated thiol (cf. Figure 9.3) will make the analysis more accurate due to the 13 fluorine atoms per qSN1U compound and larger photoelectric radius of fluorine.

Hydrolysis of the ester groups in the SN compounds was an issue during KCN capturing studies because of the high pH of KCN solution (in water). Therefore, activation of functional SN groups was carried out by using a fluorinated thiol as shown in Figure 9.3. The samples were characterized with SEC, FT-IR and XPS.

FT-IR spectra were collected for the qSN1U compound (just bare SN compound, not attached to PDMAEMA) before and after modification with the fluorinated thiol. The appearance of new peaks at 1790, 1348, 1220 and 1149 cm^{-1} on the spectra corresponds to the presence of C-F bonds. In addition, the SEC analysis was performed on these compounds to determine if coupling had occurred. The SEC chromatograms are shown in Figure 9.4 as differential refractive index (top plot) and UV absorbance (bottom plot) as a function of retention time. As expected, the retention time for fluorinated qSN1U compound was lower than that for unfluorinated counterpart, indicating an increase in molecular weight of the molecule. The signal for fluorinated qSN1U compound has decreased compared to pure qSN1U compound due to a decrease in the refractive index of the fluorinated material (cf. Table 9.3). The UV signal for fluorinated qSN1U compound did not decrease because the UV absorbance of the material has not changed with the presence of the fluorinated thiol. Based on the elution times the attachment of fluorinated thiol to thio-imide is quantitative since the peak located at 42.5 minutes disappeared.

Calculation of refractive indices of qSN1U, fluorinated thiol, and fluorinated qSN1U (cf. Table 9.3) supports the differential refractive index data obtained with SEC. Since the refractive index of fluorinated qSN1U decreases and approaches that of THF, the contrast between the solvent and modified qSN1U compound is reduced, which causes a reduction in differential refractive index signal.

Attachment of qSN1U compound to PDMAEMA brushes grown on PET fibers was also performed. The presence of qSN1U was confirmed with FT-IR and XPS. A decrease in the intensity of bands located at 2770 and 2820 cm^{-1} suggests that quarternization of PDMAEMA with qSN1U took place. The appearance of a new band at 1600 cm^{-1} confirms the presence of amide groups, which originate from the qSN1U compound as shown in Figure 9.5.

Fluorinated thiol was used to activate the SN groups of the qPDMAEMA-SN1U on PET fibers. The surface compositions of modified fiber mats were determined with XPS and are tabulated in Table 9.4. The fluorinated thiol does not interact with or adsorb on bare PET fibers based on the atomic percentages calculated from the XPS spectra. However, the concentration of fluorine atoms on PDMAEMA brushes on PET fibers is higher than the concentration on bare PET fibers. This may be due to trapped thiols in PDMAEMA brush (as interaction between the fluorinated thiol and PDMAEMA brushes on PET fibers is unlikely). The concentration of fluorine atoms on qPDMAEMA-SN1U brushes on PET fibers is much greater, i.e., $\approx 10\%$, and this is due to the attachment of fluorinated thiols on to qSN1U molecules on PDMAEMA brushes.

Cleavage of PDMAEMA brushes from silicon wafer and/or qSN1U compound from the ester group may be an issue with this type of SN compound. Therefore, it would be beneficial to use 2nd and/or 3rd generation SN compounds for quarternization compound and BMPUS with amide groups to increase the stability of polymer brushes.

9.3.2. POST-MODIFICATION OF PDMAEMA IN BULK WITH qSN3U VIA QUARTERNIZATION

PDMAEMA polymerized via FRP in DMF was characterized via NMR and FT-IR. The ¹H-NMR spectrum of PDMAEMA in deuterated acetone is shown in Figure 9.8. Peaks located at 2.30 (for 6 H), 2.57 (for 2H) and 4.08 ppm (for 2H) corresponds to hydrogens of the methyl groups of tertiary amine, hydrogens of the ethyl group and α -hydrogens of ester group of PDMAEMA respectively. In addition, peaks located at 1.03 (for 3H) and 1.92 ppm (for 2H) corresponds to the backbone hydrogens. (¹H NMR (400 MHz, Acetone): δ 4.08 (d, J = 2H), 2.57 (s, 2H), 2.27 (s, 6H), 1.92 (d, 2H), 1.03 (d, 3H).)

Quarternization reactions of PDMAEMA and qSN3U (cf. Figure 9.6) in the bulk were performed both in acetonitrile and DMF. We aimed to react 30, 50 and 65% of PDMAEMA repeat units with qSN3U. The reactions in both solvents went to completion based on HPLC spectra, where the peak for the qSN3U disappeared at the end the of the quarternization reaction. Therefore, acetonitrile was used as the solvent in large scale reactions to avoid cumbersome removal of DMF that possesses a high boiling point. The presence of qSN3U was verified by FT-IR. The introduction of new IR bands corresponding to phenyl, amide

and benzylisothiazolinone confirmed the attachment of qSN3U to dimethylamino groups of PDMAEMA. Because the solid qPDMAEMA-SN3U salt obtained after quarternization reaction was water soluble the $^1\text{H-NMR}$ spectra were collected in deuterated water. $^1\text{H-NMR}$ also verified the presence of qSN3U attached to PDMAEMA.

In order to increase the solubility of qPDMAEMA-SN3U in organic solvents and validate the quarternization reaction, ion exchange reaction between Cl^- and PF_6^- was performed in water at room temperature (cf. Figure 9.7). The ion exchanged polymer, qPDMAEMA-SN3U- PF_6^- , precipitated as the solution of ammonium hexafluorophosphate in water was added drop-wise into the solution of qPDMAEMA-SN3U. The precipitated polymer was washed with copious amounts of water to remove the ammonium bromide salt, dried under vacuum and characterized with NMR and FT-IR.

The $^1\text{H-NMR}$ of the ion exchanged polymer, whose 50% of PDMAEMA repeat units were quarternized with qSN3U, was collected in deuterated acetone; the corresponding spectrum is shown in Figure 9.8 along with that of the unmodified PDMAEMA. New peaks emerged for secondary amide, aromatic and alkyl hydrogens of benzyl group at 8.01, 7.20 and 5.20 ppm, respectively. In addition, the methyl hydrogens and backbone hydrogens of PDMAEMA are located at 1.20 and 2.20 ppm, respectively. The peaks for methyl hydrogens are broadened due to the quarternization reaction with qSN3U. ($^1\text{H NMR}$ (400 MHz, Acetone): δ 8.01 (s, 1H), 8.53 (s, 1H), 7.72 (d, 3H), 7.33 (s, 6H), 5.07 (s, 3H), 4.46 (d, 11H), 3.76 – 3.07 (m, 10H), 2.83 (d, 10H), 1.07 (d, 9H).)

Chemical changes on PDMAEMA caused by the quarternization reaction were also confirmed by FT-IR. For comparison, FT-IR spectra of ion exchanged qPDMAEMA-SN3U and PDMAEMA are shown in Figure 9.9. The examination of IR spectra reveals the appearance of new peaks for amide I (1660 cm^{-1}), amide II (1549 cm^{-1}), quarternized amine (1473 and 1394 cm^{-1}), benzisothiazolinone (1697 , 1598 , 1456 , 1266 , 1048 and 764 cm^{-1}) and PF_6 (867 , 842 and 559 cm^{-1}) groups. In addition, the intensity of stretching vibrations of the C-H bond of the $-\text{N}(\text{CH}_3)_2$ groups located at 2770 and 2820 cm^{-1} decreased due to the quarternization of PDMAEMA.

9.3.3. POST-MODIFICATION OF PPMA WITH AZIDE-SN3U VIA CLICK REACTION

PPMA homopolymer was synthesized via FRP in DMF at $75\text{ }^\circ\text{C}$ and the polymer was completely soluble in a variety of solvents, which indicated that no cross-linking took place during the polymerization. The NMR and FT-IR data also confirmed the presence of alkyne groups as pendent groups on the polymer. For instance, the NMR peaks located at 2.65 ppm and IR bands located at 3229 and 2128 cm^{-1} confirm the presence of the triple bond after the polymerization (cf. Figures 9.11 and 9.12).

The click reaction between azide group of SN3U and propargyl groups of PPMA was carried out in the presence of Cu^{I} at room temperature for 4 days as shown in Figure 9.8. The disappearance of azide-SN3U peak on the HPLC chromatogram followed by

characterization of precipitated modified polymer with $^1\text{H-NMR}$ and FT-IR confirms that the click reaction took place.

The $^1\text{H-NMR}$ spectra of the PPMA after click reaction was collected in deuterated dichloromethane and the spectrum is shown in Figure 9.11. The new peaks that appear at 11.20, 8.60, 7.55, 5.90 and 4.60 are due to the azide-SN3U molecules attached to the alkyne groups of PPMA. In addition, the ratio of the peak areas corresponding to proton of alkyne groups and protons of the methyl group on the backbone decreases after the click reaction, which shows clearly that the click reaction between PPMA and azide-SN3U took place.

Likewise, the FT-IR spectra verify the click reaction between PPMA and azide-SN3U. The introduction of new IR bands for amide I (1655 cm^{-1}), amide II, (1544 cm^{-1}), benzisothiazoline ($1636, 1598, 1454, 1420, 1265$ and 1052 cm^{-1}) and 1,2,3 triazol ($3108, 1435, 1362, 1137, 961\text{ cm}^{-1}$) groups demonstrates the success of the coupling reaction between PPMA and azide-SN3U (cf. Figures 9.12).

9.3.4. CAPTURING OF CYANIDE IONS WITH qPDMAEMA-SN

We have tested the efficiency of PDMAEMA-SN in capturing cyanides by employing SN-quarternized PDMAEMA brushes on silicon wafers and PET fibers. KCN solution in DI water with a concentration of 1 M was prepared and the aforementioned samples were kept in this solution for designated times. However, the basic nature of 1 M KCN solution ($\text{pH}\approx 11.3$) caused chain cleavage of brushes from the silicon wafers. For this reason, dilute solutions of KCN were prepared and the remaining concentration of KCN in water was

determined with the Quantofix Cyanide Detection kit. As a result of cyanide capturing by the qPDMAEMA-SN3U, the concentration of cyanide in DI water fell from 24 down to ≈ 3 ppm. Control experiments using quarternized PDMAEMA with benzyl chloride with the same level of quarternization did not show any decrease in cyanide concentration. It is therefore apparent that the cyanide ions were captured by the SN3U molecules attached to PDMAEMA chains.

9.4. CONCLUSION AND FUTURE WORK

Post-modification reactions of PDMAEMA and PPMA were performed to create functional polymeric materials for water purification. It was shown that these polymers were successfully modified with the SN compounds. The functionality of SN-modified PDMAEMA was verified by attaching fluorinated thiols and removal of cyanides from water. It has to be stressed that due to limited time only attachment of the 1st generation of SN compound was performed. In spite of its relatively low stability (due to the presence of the ester bond) and possible steric hindrance during the ring opening, our results indicate that the 1st generation compound performed well. It is expected that the higher generation SN compounds will perform even better.

Once optimized, we aim to use these SN-modified macromolecules in water cleaning technologies. Because of the *catch-release* mechanism of SN compounds (or other compounds that are capable of binding to -SH) is reversible, the recovery of these

macromolecules after each cycle is possible. Precipitation of polymers or evaporation of water from the system would not be practical for the recovery of the free polymer chains. Therefore, it is important either to tether the chains on the surface or make them form polymeric networks for practical application of these functional materials to clean water.

Incorporation of multifunctional acrylates, such as 1,4-Butanediol dimethacrylate in polymerization media as a cross-linker is going to result in the formation of polymeric networks, shown schematically in Figure 9.13. These networks are going to act as polymeric sponges; i.e., they will swell in water and capture reversibly cyanide ions, metals or other toxins after post-modification reaction with a SN compound. Such polymeric sponges will eliminate the cumbersome recovery efforts for un-grafted (i.e., free) polymers. It is important to optimize the cross-linking density of these networks by either changing the relative amount or the structure of the cross-linker molecules or by varying the molecular weight of the parent polymer to maximize diffusion through the network and speed up capture and release processes.

Another possible way of generating polymeric sponges is to use multifunctional quarternization agents or organic azides for PDMAEMA and PPMA, respectively, after post-polymerization modification reactions. In this case it is important to have some remaining dimethyl amino or propargyl groups on the linear polymer chains available for cross-linking.

Introduction of living polymerization techniques has allowed for generating polymers with tuned composition and architecture for specific applications. ATRP^[19] and reversible addition-fragmentation chain transfer^[20, 21] (RAFT) polymerization represent two of the most

widely employed controlled radical polymerization (CRP) techniques capable of polymerizing a variety of functional monomers. Several authors reported on the synthesis of homopolymers, random copolymers, gradient copolymers and block copolymers with relatively low (≈ 1.1) polydispersity index by using these CRP techniques. Controlling the architecture of these homopolymers and copolymers is going to allow the control of the location where the functional SN molecules would attach as shown schematically in Figure 9.14. Besides all the aforementioned great benefits, it is possible to end-functionalize these polymers as reported by Matyjaszewski et al^[22] and Lowe et al^[13]. The combination of all these benefits will help fine-tune the position of the SN moiety on the polymer and grafting of these modified polymer chains to a variety of surfaces with different functionalities.

Applying ATRP and RAFT polymerization techniques to grow polymer brushes is another possible way of optimizing the ability of SN functionalized macromolecules to clean water. As mentioned above, these polymerization techniques allow for controlling the architecture of the polymer brushes; controlling monomer distribution along the polymer backbone will facilitate the attachment of the SN molecules to optimal locations along the polymeric matrix. For instance, it is beneficial to have the SN functionalities close to the surface (cf. Figure 9.15) because capture-release of the ions is not going to be hindered by diffusion limitations and steric hindrances.

It is well known that adsorption of biomass on material surfaces causes the decay of functionality over time. The biomass starts accumulating via protein adsorption and protein denaturation; it takes place on any surface proteins come in contact with. Protein adsorption

on various surfaces has been studied extensively over the past several decades; it was shown that^[15, 23] that polymeric coatings containing ethylene glycol units resist biomass adhesion due to the presence of a hydration layer. The presence of the hydration layer between the surface and the protein molecules forms an effective barrier for proteins. Depending on the source, it is inevitable to have protein/biomass free water (sea, river or whatever source of water would be cleaned) and since we plan to use these functional polymeric coatings/networks for water purification it is necessary to consider prevention of protein adsorption. Therefore, designing and synthesizing copolymers containing 2-hydroxyethyl methacrylate (HEMA) or poly(ethylene glycol) methacrylate (PEGMA) using the aforementioned controlled polymerization techniques would help preventing protein adsorption and keep the surface free of adsorbed protein and active during the lifetime of the functional coatings/networks.

9.5. REFERENCES

- [1] N. K. Boen, M. A. Hillmyer, *Chemical Society Reviews* **2005**, *34*, 267.
- [2] R. Barbey, L. Lavanant, D. Paripovic, N. Schuwer, C. Sugnaux, S. Tugulu, H. A. Klok, *Chemical Reviews* **2009**, *109*, 5437.
- [3] M. A. Gauthier, M. I. Gibson, H. A. Klok, *Angewandte Chemie-International Edition* **2009**, *48*, 48.
- [4] P. L. Golas, K. Matyjaszewski, *Chemical Society Reviews*, *39*, 1338.
- [5] W. H. Binder, R. Sachsenhofer, *Macromolecular Rapid Communications* **2008**, *29*, 952.
- [6] W. Jaeger, J. Bohrisch, A. Laschewsky, *Progress in Polymer Science*, *35*, 511.
- [7] S. Kudaibergenov, W. Jaeger, A. Laschewsky, in *Supramolecular Polymers Polymeric Betains Oligomers*, Vol. 201, **2006**, 157.
- [8] M. J. Kade, D. J. Burke, C. J. Hawker, *Journal of Polymer Science Part A-Polymer Chemistry*, *48*, 743.
- [9] J. A. Crowe, J. Genzer, *Journal of the American Chemical Society* **2005**, *127*, 1768.
- [10] J. A. Crowe-Willoughby, J. Genzer, *Advanced Functional Materials* **2009**, *19*, 460.
- [11] C. E. Hoyle, T. Y. Lee, T. Roper, *Journal of Polymer Science Part A-Polymer Chemistry* **2004**, *42*, 5301.
- [12] R. K. Iha, K. L. Wooley, A. M. Nystrom, D. J. Burke, M. J. Kade, C. J. Hawker, *Chemical reviews* **2009**, *109*, 5620.
- [13] B. Yu, J. W. Chan, C. E. Hoyle, A. B. Lowe, *Journal of Polymer Science Part A-Polymer Chemistry* **2009**, *47*, 3544.
- [14] J. J. Semler, Y. K. Jhon, A. Tonelli, M. Beevers, R. Krishnamoorti, J. Genzer, *Advanced Materials* **2007**, *19*, 2877.

- [15] S. Arifuzzaman, A. E. Ozcam, K. Efimenko, D. A. Fischer, J. Genzer, *Biointerphases* **2009**, *4*, FA33.
- [16] E. Bain, J. Genzer, Manuscript in preparation.
- [17] K. Matyjaszewski, P. J. Miller, N. Shukla, B. Immaraporn, A. Gelman, B. B. Luokala, T. M. Siclovan, G. Kickelbick, T. Vallant, H. Hoffmann, T. Pakula, *Macromolecules* **1999**, *32*, 8716.
- [18] A. E. Ozcam, K. E. Roskov, J. Genzer, R. J. Spontak.
- [19] K. Matyjaszewski, J. H. Xia, *Chemical reviews* **2001**, *101*, 2921.
- [20] J. Chiefari, Y. K. Chong, F. Ercole, J. Krstina, J. Jeffery, T. P. T. Le, R. T. A. Mayadunne, G. F. Meijs, C. L. Moad, G. Moad, E. Rizzardo, S. H. Thang, *Macromolecules* **1998**, *31*, 5559.
- [21] Y. K. Chong, T. P. T. Le, G. Moad, E. Rizzardo, S. H. Thang, *Macromolecules* **1999**, *32*, 2071.
- [22] K. Matyjaszewski, N. V. Tsarevsky, *Nature Chemistry* **2009**, *1*, 276.
- [23] R. R. Bhat, B. N. Chaney, J. Rowley, A. Liebmann-Vinson, J. Genzer, *Advanced Materials* **2005**, *17*, 2802.

9.6. TABLES AND FIGURES

Table 9.1. Thickness and optical constants of PDMAEMA brushes before and after attaching qSN1P

	PDMAEMA before qSN1P		PDMAEMA after qSN1P		Thickness increase (%)
	Thickness (nm)	$n_{630\text{nm}}$	Thickness (nm)	$n_{630\text{nm}}$	
Sample 1	207.46±3.96	1.503±0.000	261.98±5.13	1.547±0.003	26.27±0.26
Sample 2	107.04±4.36	1.506±0.001	132.83±5.11	1.537±0.000	24.11±0.32

Table 9.2. Atomic concentrations of qSN1U modified PDMAEMA brushes on silicon wafer and theoretical atomic percentages

		Atomic percentage (%)				
		Carbon	Oxygen	Nitrogen	Sulfur	Chlorine
qPDMAEMA-SN1U – 1	Experimental	68.44	24.97	5.37	0.41	0.81
qPDMAEMA-SN1U – 2	Experimental	68.72	25.12	5.26	0.31	0.58
15% qSN1U coupling	Theoretical	68.75	19.79	9.38	1.04	1.04
11% qSN1U coupling	Theoretical	69.49	19.49	9.32	0.85	0.85

Table 9.3. Calculated refractive indices and molecular weights of qSN1U, fluorinated thiol and THF

Monomer	Calculated refractive index ^{a)}	Molecular weight (Da)
qSN1U	1.652 ± 0.02	302.7
C8F6SH	1.321 ± 0.02	380.2
qSN1U-C8F6SH	1.479 ± 0.03	682.9
THF	1.416 ± 0.02	-

^{a)} The errors were reported by ChemSketch

Table 9.4. Atomic percentages of samples after exposed to fluorinated thiol in ethanol

		Atomic percentage (%)				
		Carbon	Oxygen	Nitrogen	Fluorine	Sulfur
PET	theoretical	71.40	28.60	-	-	-
C ₈ F ₆ SH-PET	experimental	76.17	23.33		0.50	0
C ₈ F ₆ SH-PDMAEMA/PET	experimental	67.42	18.44	7.00	6.99	0.15
C ₈ F ₆ SH-qPDMAEMA-SN1U/PET	experimental	62.68	19.48	7.02	10.32	0.50

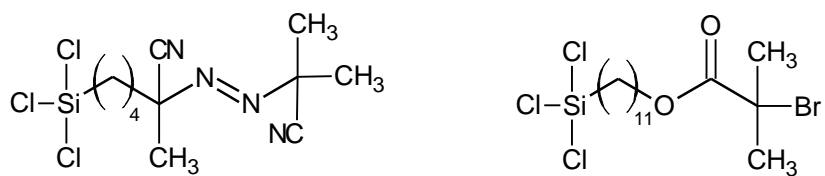


Figure 9.1. Free radical and atom transfer radical polymerization initiators for surface initiated.

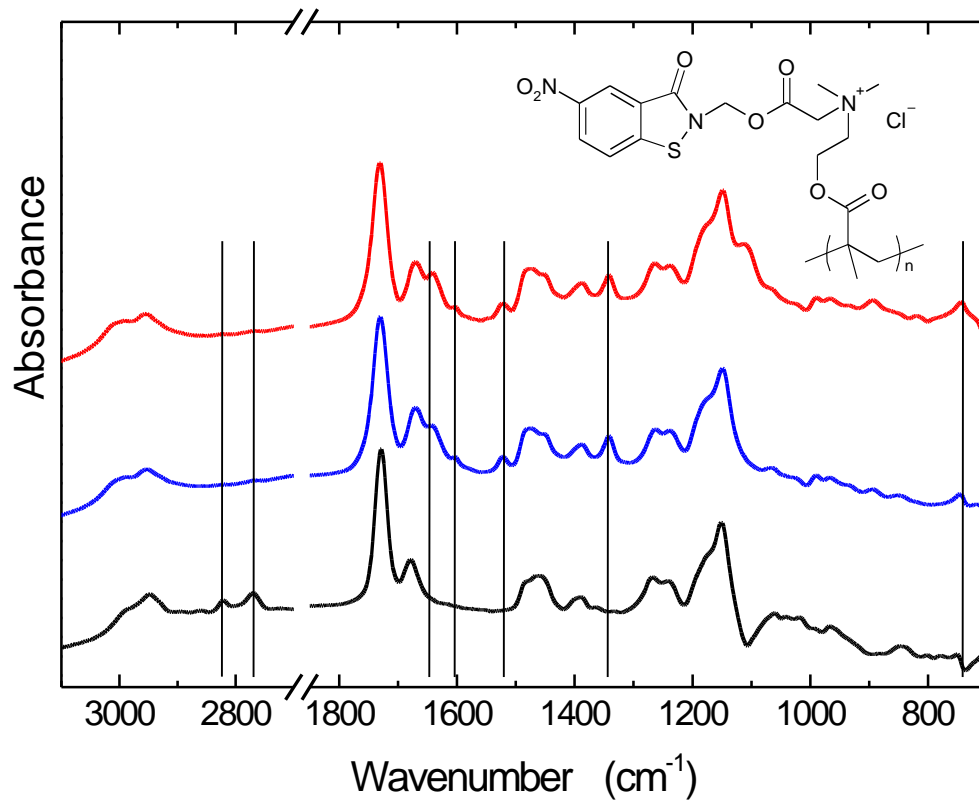


Figure 9.2. FT-IR spectra of 100nm PDMAEMA brush on silicon wafer (black line), qSN1U attached to 100nm (blue line) and 200nm (red line) PDMAEMA brush on silicon wafer.

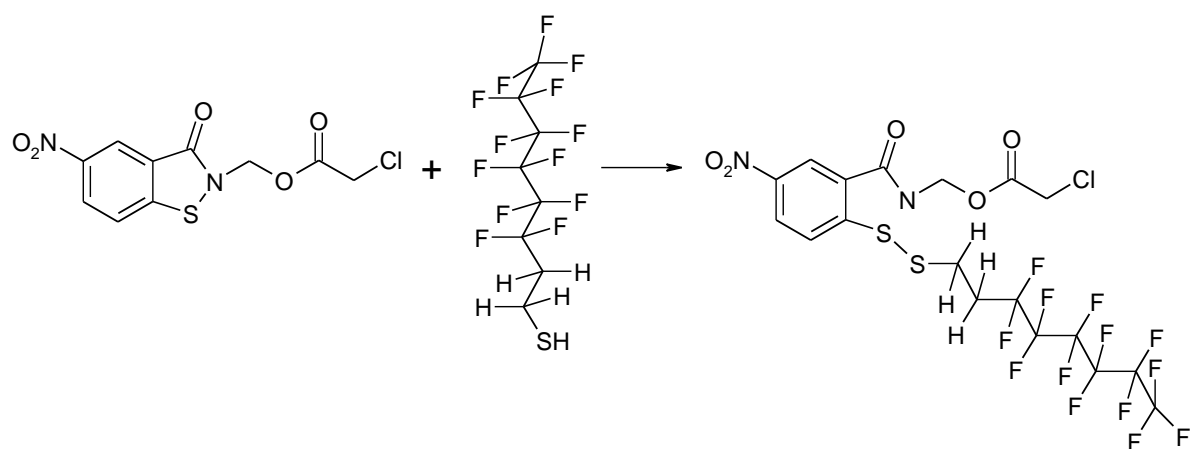


Figure 9.3. Reaction scheme of activating SN bond of qSN1U.

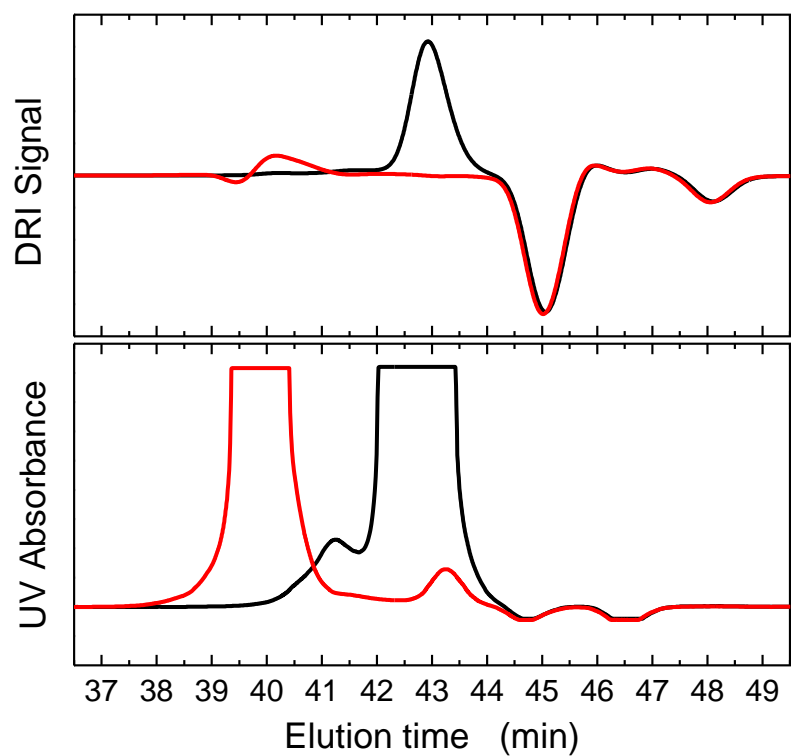


Figure 9.4. Differential refractive index and UV absorbance data of qSN1U (black line) and qSN1U after attachment of fluorinated thiol (red line).

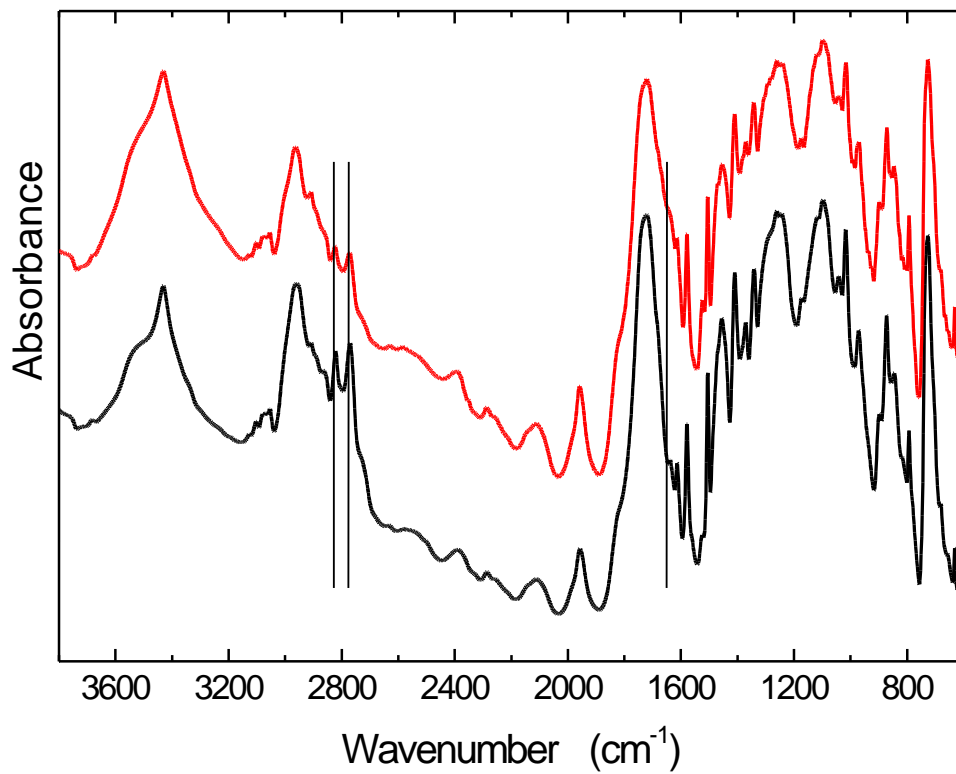


Figure 9.5. FT-IR spectra of PDMAEMA brushes on PET fibers before (black line) and after qSN1U modification (red line).

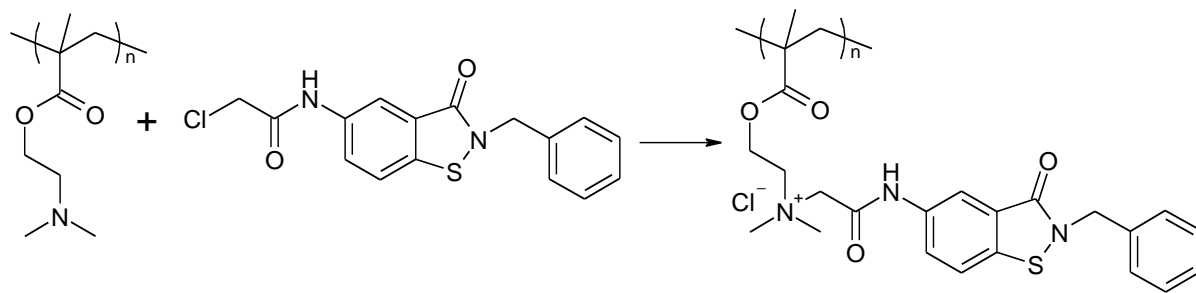


Figure 9.6. Reaction scheme of quaternization reaction of PDMAEMA and qSN3U.

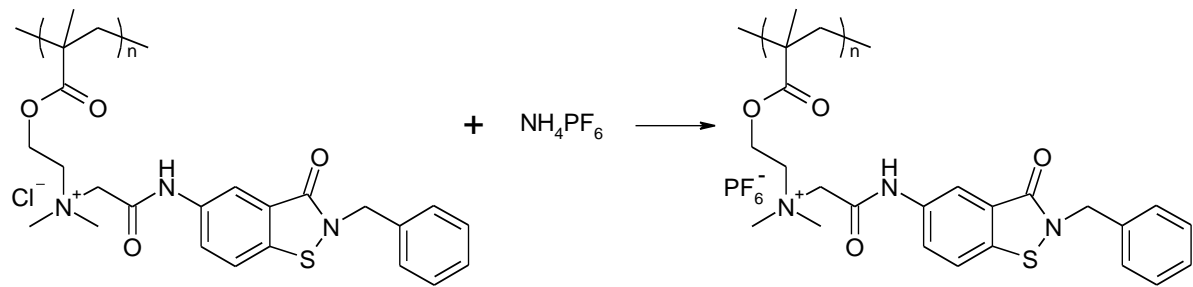


Figure 9.7. Reaction scheme of quaternization reaction of PDMAEMA and qSN3U.

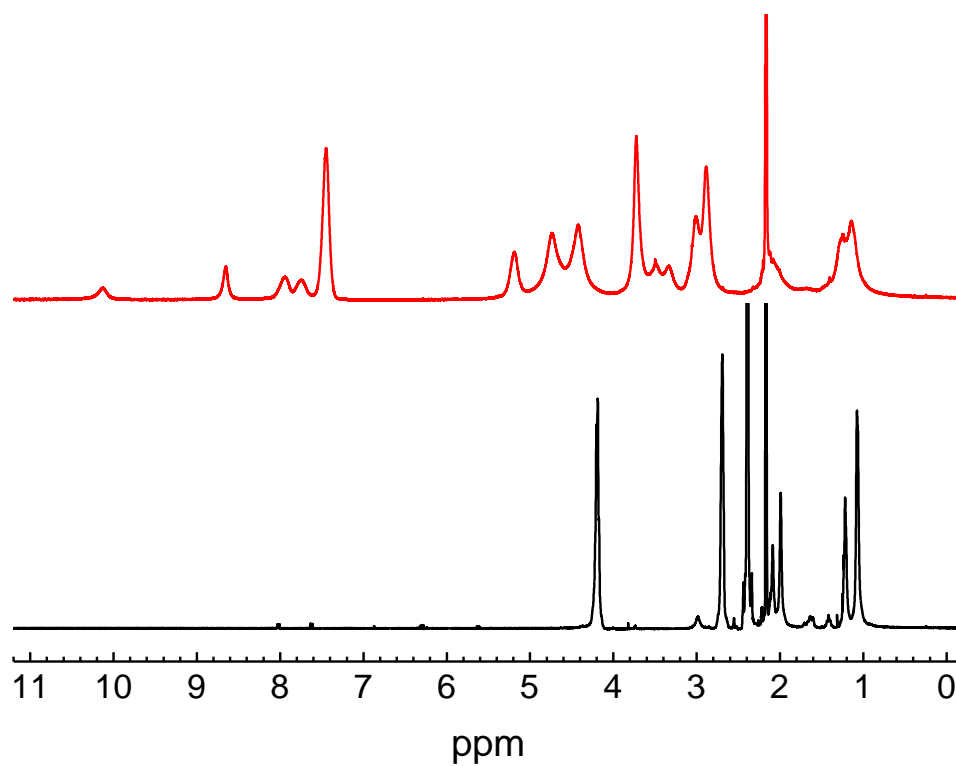


Figure 9.8. ¹H-NMR spectra of PDMAEMA before (black line) and after (red line) quaternization reaction with qSN3U.

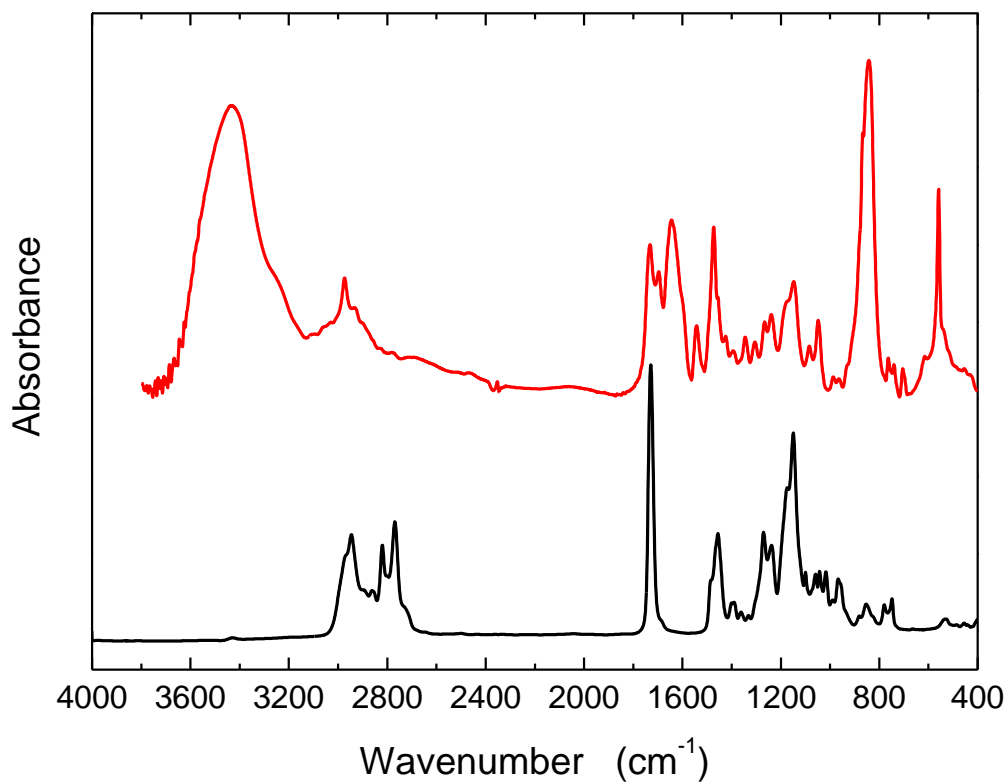


Figure 9.9. FT-IR spectra of PDMAEMA (black line) and quarternized and ion exchanged PDMAEMA (red line).

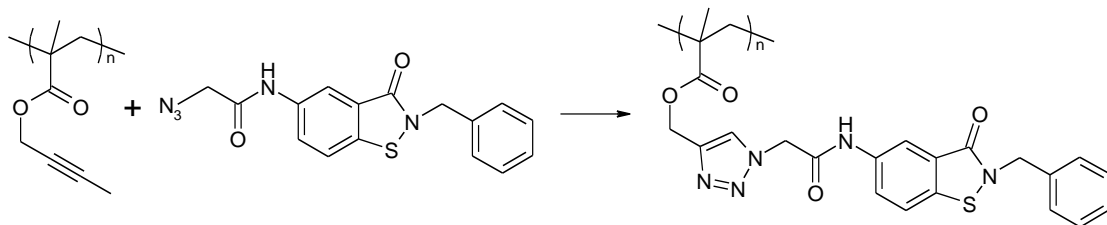


Figure 9.10. Reaction scheme of click reaction of azide-SN3U with PPMA.

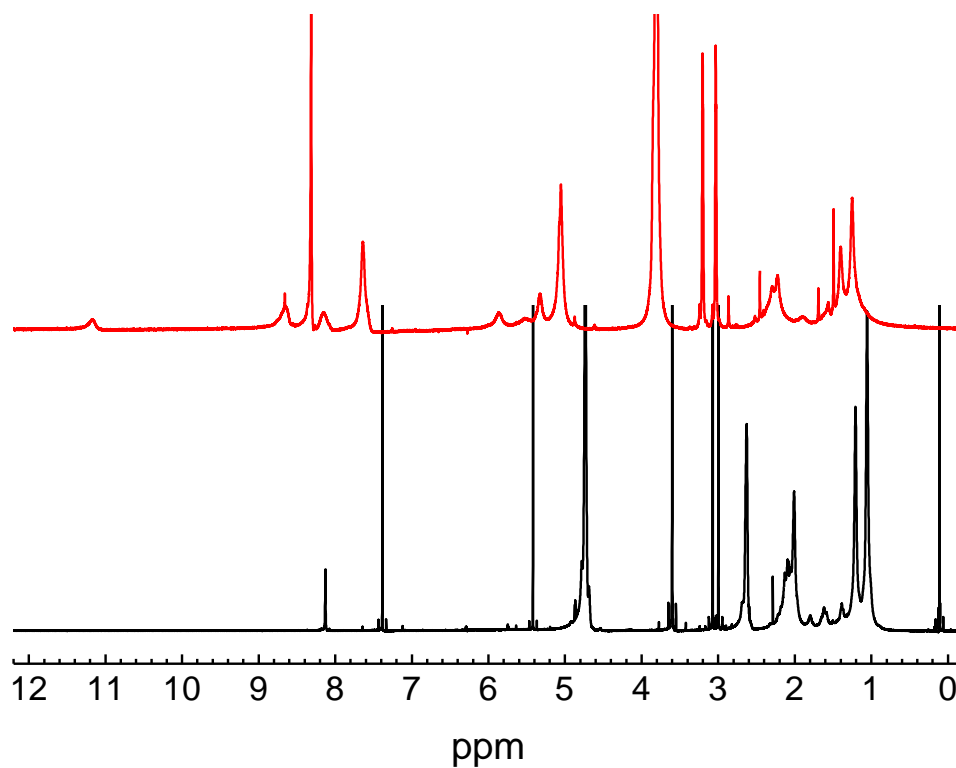


Figure 9.11. NMR spectra of propargyl methacrylate before (black line) and after click reaction with azide-SN3U (red line).

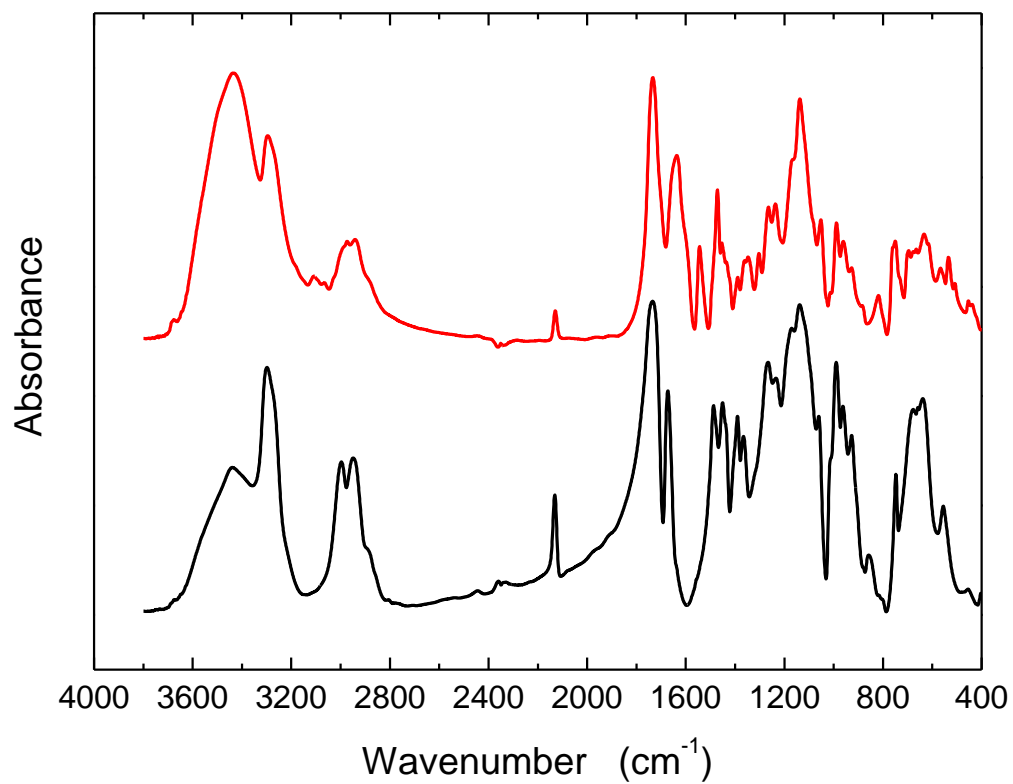


Figure 9.12. FT-IR spectrum of PPMA before (black line) and after the click reaction with azide-SN3U (red line).

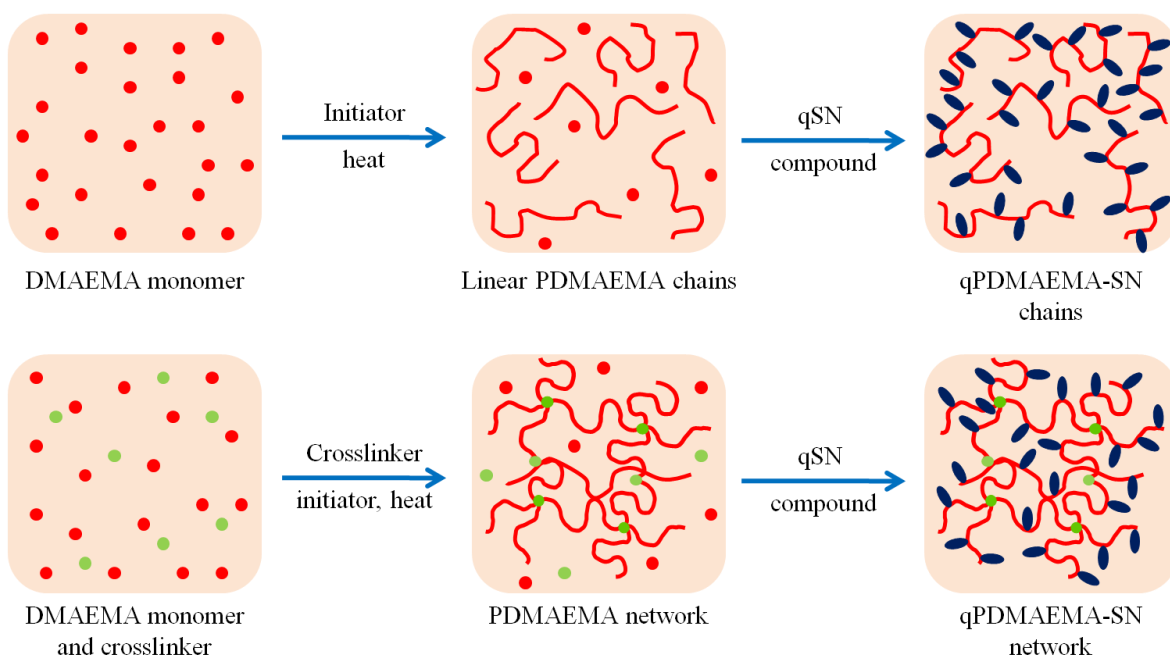


Figure 9.13. Formation of free polymer chains (a) and polymer networks (b) and their post-modification to obtain functional copolymers for water purification.

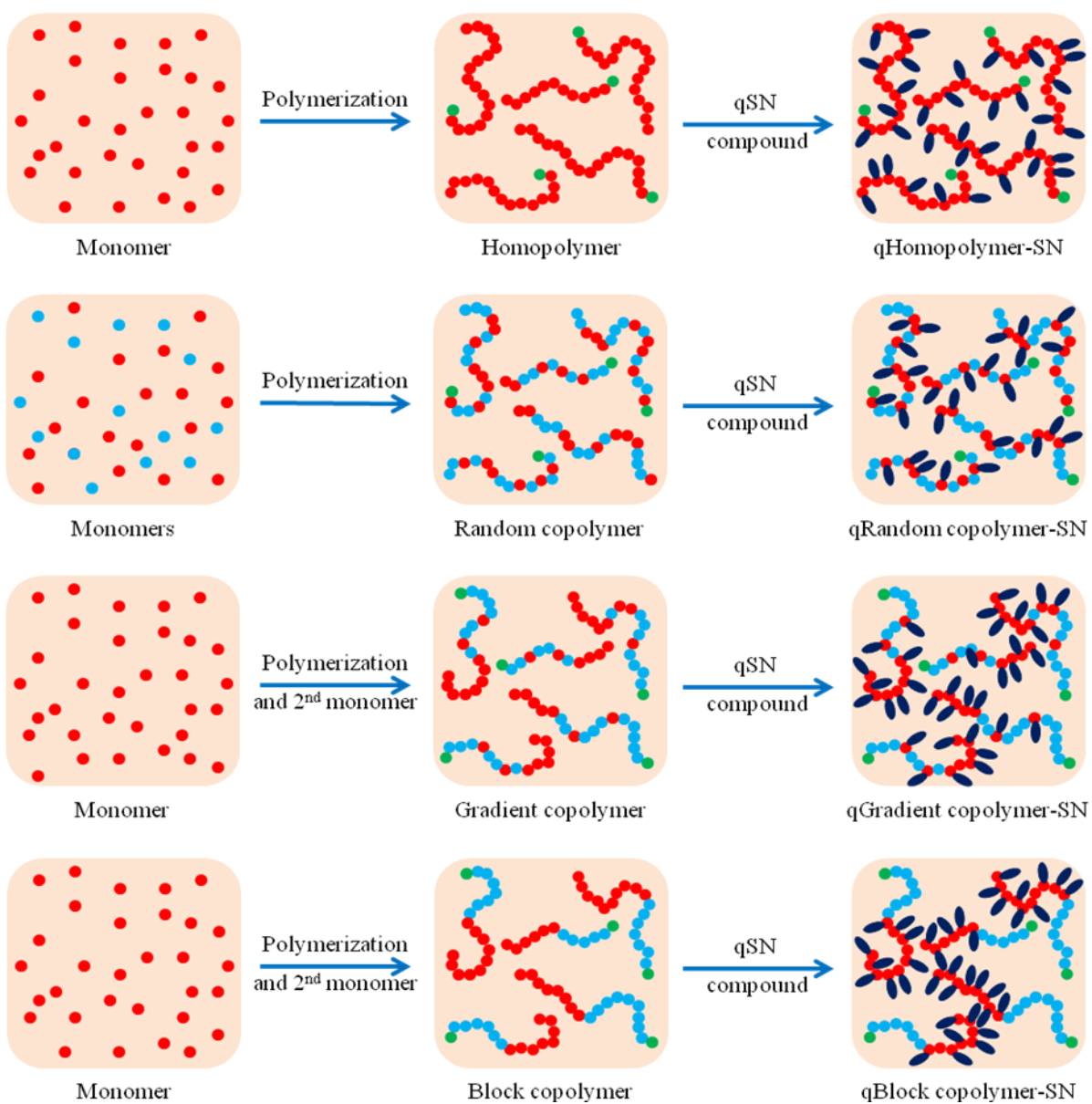


Figure 9.14. Possible polymer architectures that can be used to be used with post-modification reactions.

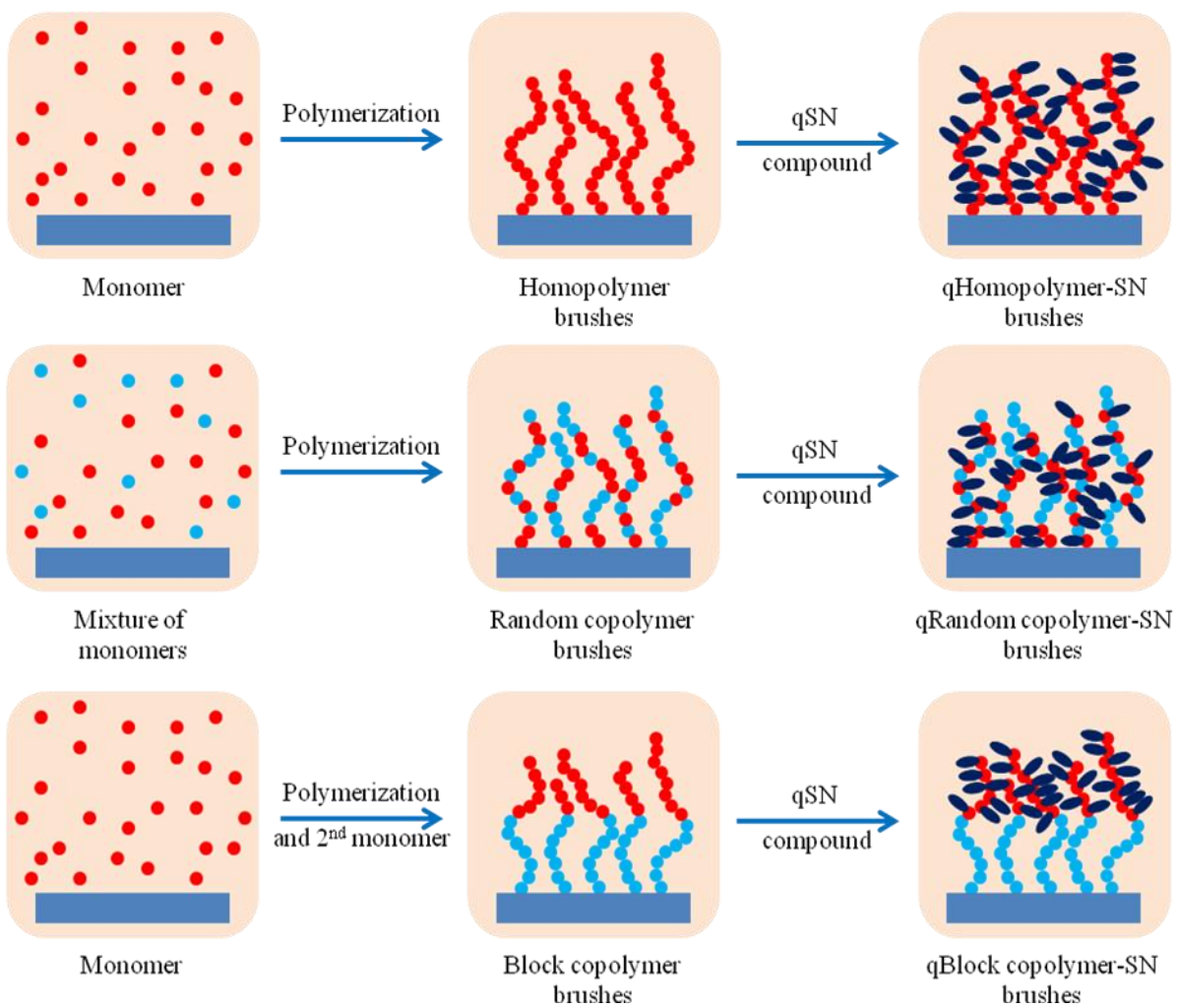


Figure 9.15. Homo-polymer, random copolymer and block copolymer brushes for post-modification reactions.

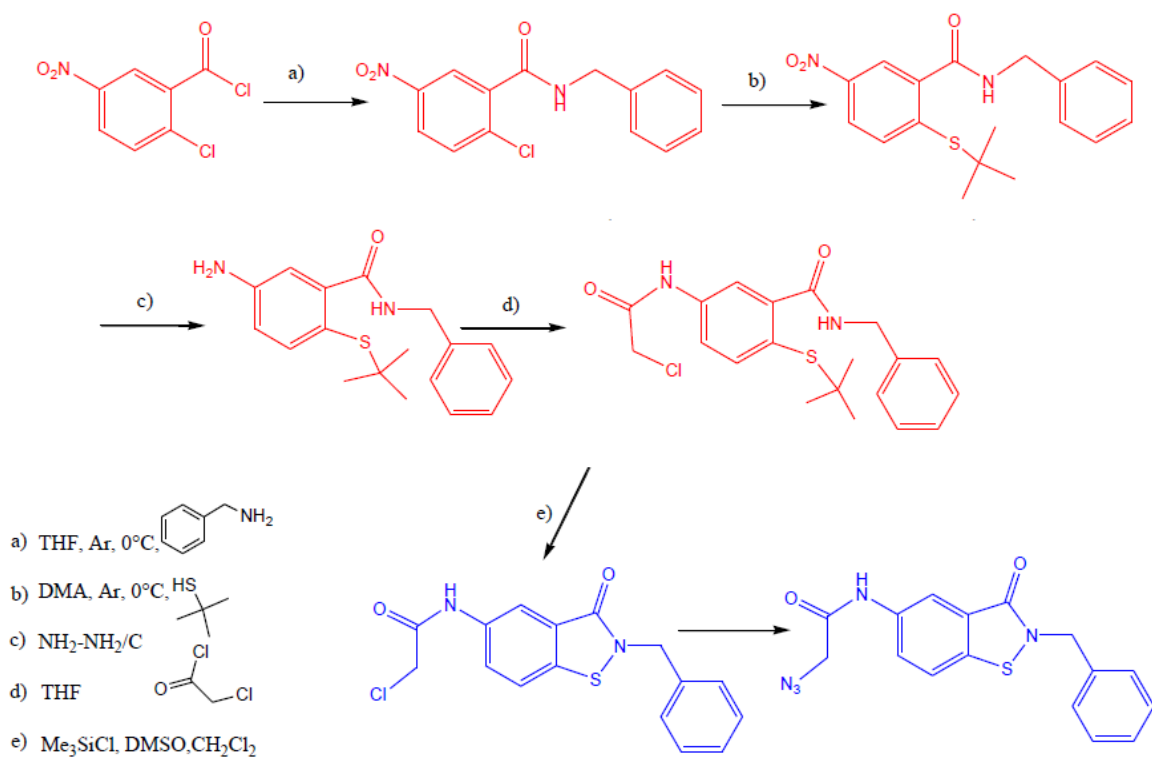


Figure 9.16. Reaction schemes of SN post modification compounds.

9.7 APPENDIX

9.7.1. SYNTHESIS OF N-BENZYL-2-CHLORO-5-NITROBENZAMIDE

Benzylamine (34 mmol) was stirred in 25 ml of pyridine. The flask was cooled to 0 °C and the reaction mixture was stirred under argon. Then the 2-chloro-5-nitrobenzoic chloride was added to the solution. The yellow suspension was isolated by ice/5% HCl mixture. The compound was filtered and dried under vacuum. (reaction “a” in Figure 9.16)

9.7.2. SYNTHESIS OF N-BENZYL-2-TERT-BUTYLSULFANYL-BENZAMIDE

N-Benzyl-2-chloro-5-nitrobenzamide (20.2 mmol) was suspended in 25 ml of dry dimethylacetamide (DMA). The flask was cooled to 0 °C and the reaction mixture was stirred under argon. Then the *tert*-butylthiol was added to the suspension followed by the addition of sodium hydroxide. The substance was isolated was added to the suspension ice/5% HCl mixture. The compound was filtered and dried under vacuum. (reaction “b” in Figure 9.16)

9.7.3. SYNTHESIS OF 5-AMINE-N-BENZYL-2-TERT-BUTYLSULFANYL-5-NITROBENZAMIDE

N-Benzyl-2-*tert*-butylsulfanyl-5-nitrobenzamide (18.58 mmol) was dissolved in 200 ml of dry ethanol. The flask was heated to 80 °C and the reaction mixture was stirred under argon. Subsequently carbon black (7 g) and hydrazine hydrate (55.7 mmol) were added to the solution. The carbon black was then filtered out through Celite 45 and the yellow solution was evaporated under reduced pressure. (reaction “c” in Figure 9.16)

9.7.4. SYNTHESIS OF N-BENZYL-2-TERT-BUTYLSULFANYL-5-(2-CHLORO-ACETYLAMINO)-BENZAMIDE

5-Amine-*N*-benzyl-2-*tert*-butylsulfanylbenzamide (68.4 mmol) was dissolved in dry THF. The flask was cooled to 0 °C and the solution was stirred under argon. The chloroacetylchloride was subsequently added to the solution. The resulting crystals were filtered and dried under vacuum. (reaction “d” in Figure 9.16)

9.7.5. SYNTHESIS OF N-(2-BENZYL-3-OXO-2,3-DIHYDRO-BENZO[d]ISOTHIAZOL-5-YL)-2-CHLORO-ACETAMIDE

N-Benzyl-2-*tert*-butylsulfanyl-5-(2-chloroacetylamino)benzamide was suspended in 200 ml of dry dichloromethane. The flask was cooled to 0° C and the reaction mixture was stirred under argon. The chlorotrimethylsilane (Me₃SiCl) and dimehtylsulfoxide (DMSO)

were added to the solution. The resulting crystals were filtered and the solid was dried under vacuum. (reaction “e” in Figure 9.16)

CHAPTER 10: SUMMARY AND OUTLOOK

10.1. SUMMARY

The two central themes of this Ph.D. dissertation include: 1) devising novel means of modification of surfaces of poly(ethyleneterephthalate) (PET) and silicone elastomer networks (SENs), and 2) the synthesis of thioimide-based copolymers to create functional materials. Specifically, the surface properties of PET and SENs were altered to attach nano-objects (i.e., particles and clay platelets) and to create soft hydrophilic substrates, respectively. In addition, novel thioimide functionality was incorporated into polymer chains to be employed in water purification technologies that remove heavy metals and cyanides from water.

Both physical and chemical routes were utilized to modify the PET surface. Initially, ultra-violet/ozone (UVO) treatment was exploited to increase the wettability of self-standing PET and spin-coated PET on silicon wafers. The increase in the surface energy, variations in chemical composition, and alteration of the topography of the UVO modified PET films were monitored by water contact angle (WCA), x-ray photoelectron spectroscopy (XPS) and atomic force microscopy (AFM), respectively. The UVO-treated PET films were modified chemically with semifluorinated silanes allowing further functionalization of the PET surface.

The irregular shapes and sizes of rPET flakes make uniform surface modification by UVO treatment challenging. For this reason we use chemical treatment technologies to modify these rPET flakes. The interaction between the surface of the rPET flakes and layered silicate platelets is a key property in achieving proper dispersion of layered silicates in the PET matrix. The layered silicate platelets possess a negatively charged surface due to isomorphic substitution of Al^{3+} with Mg^{2+} . We used aminolysis to increase the attractive interaction between the rPET surface and the layered silicate platelets. It was shown earlier that although monofunctional and “small” amines degrade PET, multifunctional and “large” amine-containing molecules do not cause significant damage to the parent material. Therefore, poly(allylamine hydrochloride) (PAH) and polyethyleneimine (PEI) were used as a “molecular glue” to attach the clay platelets onto the rPET surface. The adsorption of PAH and PEI onto spin-coated PET films was monitored by WCA (wettability) and spectroscopic ellipsometry (thickness) measurements. The measured thicknesses of both adsorbed polyelectrolytes were <1 nm regardless of the deposition time; the PEI modified PET surfaces resulted in lower WCA values compared to their PAH counterparts. Subsequent adsorption of Na^+ montmorillonite (Na^+ MMT) platelets resulted in thickness increases of ≈ 3 and ≈ 2 nm for the PEI and PAH modified substrates, respectively. These thickness increases correspond to approximately 1 to 2 layers of clay platelets stacked together. Upon adsorption of the clay platelets, the PEI-based substrates exhibited lower WCA than those for PAH based specimens indicated a higher platelet coverage in the PEI case. Therefore PEI was selected to modify the rough and irregular rPET flake surface. Attachment of Na^+ MMT clay

platelets on rPET flakes coated with PEI chains was confirmed with XPS. Melt-processing of Na⁺ MMT modified rPET flakes was carried-out to form rPET/clay nanocomposites. However, degradation of PET in extruder took place during melt-processing as revealed by melt rheology and FT-IR experiments.

We also modified successfully PET fibers produced by electrospinning solutions of rPET in hexafluoroisopropanol. The surface of the PET fiber mats was first altered by attaching 3-aminopropyltriethoxysilane (APTES) molecules via the amidation reaction between the ester group of PET and the primary amine group of the APTES molecules. Hydrolysis of the ethoxysilane groups of the APTES molecules yielded silanol groups on the PET fiber surface. Covalent attachment of a silane-based atom transfer radical polymerization (ATRP) initiator allowed the “grafting from” polymerization of several functional monomers, i.e. , *N*-isopropylacrylamide (NIPAAm), 2-(dimethylamino)ethyl methacrylate (DMAEMA) and 2-hydroxyethyl methacrylate (HEMA), from the surface of the PET fiber. The thermoresponsive behavior of the PNIPAAm modified PET fibers was demonstrated by performing WCA measurements and coating the fibers with gold nanoparticles below and above the transition temperature of PNIPAAm. The grafted PDMAEMA and PHEMA brushes were modified by post-polymerization reactions involving quarternization and acylation, respectively. Alkyl bromides and alkyl iodides were used as quarternization agents for PDMAEMA. The antibacterial properties of modified PET fiber mats were tested against *E. coli*; it was shown that longer alkyl chains were more effective at killing the bacteria compared to shorter alkyls. The protein resistance of PHEMA modified PET fibers

was probed before and after acylation by exposing the fibers to fibrinogen solutions. We showed that the presence of PHEMA brushes on PET fibers hindered fibrinogen adsorption.

Mechanical alloying of PET flakes and Na⁺ MMT was carried out in steel containers in the presence of steel balls. The mechanical milling of rPET and vPET caused a reduction in the polymer molecular weight with increasing milling time. The extent of crystallization of the mechanically milled PET samples increased with increasing milling time; we attributed this to the decrease in molecular weight of the PET samples, which facilitated the formation of crystals due to easier packing of polymer chains. The extent of crystallization of alloyed PET/clay mixture, however, did not seem to change with increasing milling time. X-ray diffraction and transmission electron microscopy experiments revealed exfoliation, intercalation and dispersion of Na⁺ MMT clay platelets in the rPET matrix, which took place in solid state at a concentration of 5% (w/w) Na⁺ MMT in PET.

Chemical tunability of the vinyl groups of PVMS allowed us to attach cross-linking functionalities via hydrosilylation reaction. Specifically, trichlorosilane (TCS) molecules were coupled to the vinyl group of PVMS in the presence of Pt(0) catalyst, which resulted in the formation of PVMS-TCS random copolymers. The silane coupling is tunable, quantitative, and controlled by the vinyl:TCS ratio in the spin-coating solution. The thickness and modulus of the coating can be altered by varying the vinyl:TCS ratio and the concentration of the copolymer in the spin-coating solution. The stability of the spin-coated PVMS-TCS coating was examined by measuring the thickness of the film before and after sonication in toluene, THF, chloroform, acetone, ethanol, methanol and water. Post-

modification of the PVMS-TCS film accomplished by the thiol-ene addition reaction of the remaining vinyl groups with thiol-terminated peptides in the presence of photoinitiator molecules and under UV light ($\lambda=365$ nm). Characterization of the modified surface with XPS confirmed attachment of model peptide molecules on the PVMS-TCS surface. In addition, “pre-modification” of PVMS was carried out with fluorinated thiols and thiol-terminated PEG molecules before TCS coupling reaction and the remaining vinyl groups were coupled with TCS molecules. Spin-coating the aforementioned copolymer solutions facilitated the formation of hydrophobic and hydrophilic coatings, respectively. Finally, coupling azo-based free radical polymerization initiator to PVMS-TCS copolymer was carried out. Decoration of PET, PP and SiO_x surfaces with PVMS-TCS-azo copolymer was performed and confirmed by FT-IR and ellipsometry measurements. Subsequent immersion of PVMS-TCS-azo coated substrates in MMA monomer solutions and applying heat resulted in the formation of surface-tethered PMMA chains. Characterization with FT-IR and ellipsometry confirmed the presence of PMMA chains attached to PET, PP and SiO_x substrates.

Functional thioimide-based molecules (SN compounds, synthesized by the Srogl Research Group) were copolymerized to prepare polymers that can reversibly capture and release heavy-metal and cyanides from water. The copolymerization of SN monomers with phenylacrylamide and NIPAAm yielded functional copolymers that were characterized by NMR, FT-IR, HPLC, DSC, and TGA. In addition, surface-initiated copolymerization of SN monomer and phenylacrylamide yielded polymer brushes that incorporated the SN

functionality. Post-modification polymerization reactions of PDMAEMA and poly(propargyl methacrylate) (PPgMA) were carried out with quarternization-SN and azide-SN compounds. Successful modification of PDMAEMA and PPgMA was confirmed with HPLC, NMR and FT-IR. The SN-modified PDMAEMA was used to study the cyanide capturing ability from water. It was successfully demonstrated that the SN-modified PDMAEMA lowered the concentration of cyanide ions in water from 24 down to 3 ppm.

10.2. OUTLOOK

Detailed description of future experiments pertaining to each topic has been provided at the end of each chapter in this Ph.D. Thesis. The following description only summarizes the key points pertaining to each research theme.

To establish the optimal conditions leading to the formation of rPET/clay nanocomposites we first need to determine the cause of rPET degradation during melt processing in during extrusion. For instance, we need to consider the stability of polyelectrolytes and the reaction of free amine groups of polyethyleneimine with the ester bonds during melt processing. The reported degradation temperature of high molecular weight (60 kDa) PEI is around 300°C, which is higher than the PET extrusion temperature (≈ 280 °C). However, elevated temperatures in conjunction with intense shear may lead to PEI degradation during extrusion and may emit undesirable amine derivatives, which can accelerate the degradation of rPET during extrusion (and can also be hazardous for food and

beverage applications). During extrusion, free amine groups may react with the ester bonds thus decreasing the molecular weight of rPET and reduced number of free amine groups may lower the interactions between clay and modified rPET surface. Since the interactions between the inorganic filler and the polymer matrix play an important role for mechanical property enhancement, the mechanical properties of fabricated nanocomposites may not be improved due to “lowered” interactions between the clay surface and rPET. Therefore, careful consideration of these and related issues must be investigated in systematic fashion to enable future development and potential commercialization of this route to rPET/clay nanocomposites for use in food packaging. Special attention thus needs to be paid to surface modification procedures and optimizing the conditions by which the rPET surface is modified prior to clay attachment. Post-extruded composites prepared in this fashion will be characterized by XRD to determine if the clays remain ordered (non-exfoliated), DSC to determine polymer crystallinity and thermal transitions, TGA to probe the degradation behavior and clay loading, TEM to assess the composite morphology, gas permeation to measure the permeability of CO₂ and O₂, and extensional rheometry to establish the mechanical properties.

The effect of fiber diameter affecting the curvature of the fiber surface on polymerization rate and polydispersity of polymer brushes should be studied by carrying out “grafting from” polymerization from PET fibers having various diameters ranging from nanometers to micrometers. In addition, the attachment of metal nanoparticles to PNIPAAm chains can be repeated with different fiber diameters to determine the effect of convex-ness of the surface

on nanoparticle uptake. The “non-leaching” character of surface tethered polymer chains would allow repeated employment of modified PET fibers for antibacterial and protein resistant applications. Therefore, the efficiency and stability of the modified PET fiber mats should be determined and tested for multi-use filter applications.

Incorporation of nanoparticles in PVMS-TCS copolymer film would increase the functionality of the final coating. For instance, mechanical properties of the coating may be improved by embedding fumed silica particles into the coating due to the inclusion of these “hard” nano-objects. Likewise, incorporating nano-clays (layered silicates, i.e., montmorillonite) into PVMS-TCS would both increase the barrier properties and hardness of the coating. Specifically, the presence of layered silicates will increase the tortuous path for the gas molecules to diffuse through the coating and thus lower permeation of gases. The functional “hard” and “impermeable” coatings can be utilized to produce scratch resistant surfaces and gas-barrier films for packaging applications, respectively.

In addition, the PVMS-TCS copolymer coatings can be utilized to generate buckles on a variety of substrates provided that the substrate swells in a solvent. For instance, biaxial buckles can be formed by swelling the substrate, coating it with PVMS-TCS, exposing the specimen to moisture, and removing the solvent from the base material. The properties of the buckled substrate (i.e., wavelength and amplitude) will depend on the mismatch in the modulus of the top (PVMS-TCS) and bottom layers, the thickness of the PVMS-TCS coating and the corresponding Poissons’ ratios. A proof of concept for this strategy, we have used PDMS as a substrate, swelled it in toluene and immersed into PVMS-TCS copolymer

solution. Removing the PVMS-TCS/PDMS specimen from the copolymer solution and exposing it to moisture caused cross-linking of the top PVMS-TCS layer that resulted in increased modulus. Subsequent drying of PVMS-TCS/PDMS resulted in bi-axial buckles that extended over large sample areas. Combining buckle formation with the aforementioned PVMS-TCS chemical pre-modification would allow for facile generation of chemically-tailored topographically-corrugated surfaces.

In addition, we plan to grow and characterize tethered functional polymer chains via PVMS-TCS-azo on a variety of surfaces with different functional monomers and polymerization durations, which will allow generation of surface tethered polymer chains without cumbersome sample preparation steps.

The measurement of molecular weight and polydispersity index of the thioimide functionalized copolymers was not possible because these copolymers interact with the styrene-divinylbenzene packing of the size exclusion chromatography column. We plan to screen the interaction between the polymer and column packing by using inorganic salts (for instance: LiBr) in the mobile phase. In addition, the *catch-release* behavior of thioimide functionalized macromolecular chains with heavy metal and cyanide ions will be determined. In addition, the architecture of the copolymers can be varied via controlled radical polymerization techniques, which will facilitate a better control of the location of functional SN molecules on the polymer chain. This is of paramount importance because it will determine the efficacy of the final product by determining the rate of particle collection by controlling the mass transfer. Finally, utilization of PDMAEMA brushes on PET fibers will

allow the covalent attachment of SN compounds to modified PET fibers via quarternization reaction. These fibers can be then used as multi-use filters for a continuous process of water purification.